

# Ion-scattering spectroscopy of III–V semiconductor surfaces

by

Nicholas Simon Kaijaks

BSc (Hons) MSc



A thesis submitted for admission to the degree of  
Doctor of Philosophy

University of Warwick  
Department of Physics

March 2000

## Contents

Acknowledgments . . . . .	v
Declaration . . . . .	vi
Summary . . . . .	vii
Abbreviations and common symbols . . . . .	viii
<b>1 Introduction</b>	
1.1 Motivation . . . . .	1
1.2 An overview of surface science . . . . .	4
1.2.1 Ultra-high vacuum (UHV) . . . . .	4
1.2.2 Surface science analytical techniques . . . . .	5
1.2.2.1 Low energy electron diffraction (LEED) . . . . .	5
1.2.2.2 Auger electron spectroscopy (AES) . . . . .	6
1.2.2.3 Medium energy ion scattering spectroscopy (MEIS) . . . . .	7
1.2.2.4 Coaxial impact collision ion scattering spectroscopy (CAICISS) . . . . .	7
1.2.2.5 High resolution electron energy loss spectroscopy (HREELS) . . . . .	8
1.2.2.6 Surface x-ray diffraction (SXRD) . . . . .	8
1.2.2.7 Reflection high energy electron diffraction (RHEED) . . . . .	9
1.2.2.8 Scanning tunnelling microscopy (STM) . . . . .	9
1.3 Experimental work . . . . .	10
1.4 Structure and content of the thesis . . . . .	11
1.5 References . . . . .	12
<b>2 III–V semiconductor surfaces</b>	
2.1 Introduction . . . . .	13
2.2 Bulk structure . . . . .	14
2.3 Semiconductor surface structure . . . . .	19
2.3.1 Relaxation and reconstruction . . . . .	19
2.3.2 Reconstruction mechanisms . . . . .	20
2.3.3 Dimerization . . . . .	22
2.4 Growth techniques . . . . .	24
2.4.1 Bulk growth . . . . .	25
2.4.2 Epitaxial growth . . . . .	26
2.5 References . . . . .	27

<b>3</b>	<b>Experimental techniques</b>	
3.1	Introduction . . . . .	29
3.2	Ion-surface interactions . . . . .	29
3.2.1	Charge-exchange mechanisms . . . . .	30
3.2.2	Collision and inelastic energy loss . . . . .	32
3.3	Sample preparation techniques . . . . .	33
3.3.1	Argon ion-bombardment and annealing (IBA) . . . . .	34
3.3.2	Atomic hydrogen cleaning (AHC) . . . . .	37
3.4	Analysis techniques . . . . .	39
3.4.1	Low energy electron diffraction (LEED) . . . . .	39
3.4.2	Auger electron spectroscopy (AES) . . . . .	43
3.4.3	Ion scattering spectroscopy (ISS) . . . . .	44
3.4.3.1	Introduction . . . . .	44
3.4.3.2	Interaction potentials . . . . .	45
3.4.3.3	Shadow cones . . . . .	46
3.4.3.4	Mass resolution . . . . .	49
3.4.4	Impact-collision ion scattering spectroscopy (ICISS) . . . . .	51
3.4.5	Coaxial impact-collision ion scattering spectroscopy (CAICISS) . . . . .	53
3.4.6	Medium-energy ion scattering spectroscopy (MEIS) . . . . .	55
3.5	References . . . . .	60
<b>4</b>	<b>Computational techniques</b>	
4.1	Introduction . . . . .	63
4.2	VEGAS simulation . . . . .	63
4.2.1	Double-alignment geometry . . . . .	63
4.2.2	Hitting and detection probabilities . . . . .	65
4.2.3	The single-row approximation . . . . .	66
4.2.4	The complete crystal method . . . . .	68
4.2.5	Ion track correlation and connection . . . . .	70
4.3	Structural optimization . . . . .	72
4.4	Computational developments . . . . .	74
4.4.1	VEGAS . . . . .	74
4.4.2	Visualization . . . . .	76
4.5	References . . . . .	78

<b>5</b>	<b>GaSb(001) surface reconstructions</b>	
5.1	Introduction . . . . .	79
5.2	GaAs(001) surface reconstructions . . . . .	79
5.3	GaSb(001) reconstructions . . . . .	88
5.4	Experimental work . . . . .	91
5.4.1	The Warwick CAICISS system facilities . . . . .	91
5.4.2	The MEIS facility at CLRC Daresbury . . . . .	93
5.4.3	Experiments . . . . .	96
5.5	Results and discussion . . . . .	98
5.5.1	Efficacy of atomic hydrogen cleaning . . . . .	98
5.5.2	Thermal decomposition of GaSb(001) . . . . .	100
5.5.3	GaSb(001)–(1×3) reconstruction . . . . .	103
5.5.4	GaSb(001)–c(2×6) reconstruction . . . . .	108
5.5.5	GaSb(001)–c(6×4) reconstruction . . . . .	117
5.5.6	Summary . . . . .	125
5.6	References . . . . .	126
<b>6</b>	<b>Surface preparation and the (4×2) reconstruction of InAs(001)</b>	
6.1	Introduction . . . . .	128
6.2	Experimental details . . . . .	128
6.3	Structural analysis of InAs(001)–(4×2) . . . . .	129
6.4	Beam damage induced by ion bombardment of InAs(001) . . . . .	137
6.5	Summary . . . . .	144
6.6	References . . . . .	145
<b>7</b>	<b>Conclusions and future work</b>	
7.1	Conclusions . . . . .	146
7.2	Future work . . . . .	151
	Index . . . . .	ix

## Acknowledgments

First thanks must be to Chris McConville, a supervisor whose good humour, patience and encouragement have never failed, even when times were at their worst. A great debt is owed to Team Surface; in particular to Salim Al-Harthi, Ian Gee, David Brown, Steve Driver and Rob Johnston. I always knew I could rely on their healthy cynicism and cunning diversionary tactics at 10.30am, 3.30pm (and the odd time before, after and between) to keep me from my work. Thanks also to Adrian Lovejoy for putting out fires (almost literally).

Next, the most recent alumni of the 422 Institute, Richard Dixon and Gavin Bell, deserve congratulations, both for managing to escape, and for their excellent advice; perhaps I should have taken it... Another ex-member, Tim Noakes, deserves hearty thanks for useful discussions (as they say), both in the good old days on CAICISS, and latterly at Daresbury, where Paul Bailey, too, deserves plaudits for his IGOR Pro macros that made data analysis **so** much easier ('Release the MEIS!'). A hearty 'feck' for Paul Quinn, whose VEGAS front-end gave me the impetus to develop the code myself.

I thank EPSRC for provision of a studentship, and for grants to use the excellent MEIS facility at CLRC Daresbury Laboratory, as well as Andrew Mowbray at MCP Wafer Technology Ltd who generously provided the samples used in the project. Also thanks to David Wright who generously allowed me study leave from Warwick Business School.

On a more personal level, I also thank Gill Frost, formerly of the University's counselling service, who helped me work through the two successive housing disasters that beset me in my second year, and to Colin, Stuart, Sue and Rona, who offered me a second home. Finally, thanks to my mother, without whom (I can confidently write) I would never have got this far, and to Ros, mia cara, whose support (both emotional and financial!) deserves an award itself. I would like to dedicate this thesis to my grandmother, Julianna Emilija, who died on 31st July 1998, aged 93. By teaching me Richard Scarry's *ABC*, Nanny started me on the long road they call 'education'. I hope that it has proved worthwhile.

## Declaration

I declare that this thesis contains an account of my research carried out in the Department of Physics at the University of Warwick and at the MEIS Facility, CLRC Daresbury Laboratories between October 1995 and September 1998 under the supervision of Dr C.F. McConville. The research reported here has not been submitted either wholly or partially at this or any other academic institution for admission to a higher degree. As far as possible, the research has been undertaken in accordance with University safety policy.

The experimental data using MEIS reported in chapters 5 and 6 were obtained with the assistance of Mr S. Al-Harhi and Dr T.C.Q. Noakes. In chapter 5, CAICISS experimental data were obtained with Dr R.J. Dixon whilst HREELS data were produced by Dr G.R. Bell. Computational and visualization work was performed by the author. Parts of this work have been presented at an international conference (IVST-13) at Birmingham 1998, and several papers have been published or are in preparation:

*Atomic hydrogen cleaning of polar III–V semiconductor surfaces*

G.R. Bell, N.S. Kaijaks, R.J. Dixon and C.F. McConville: *Surf. Sci.* **401** (1998) 125

*A novel  $c(6\times 4)$  reconstruction of the atomic hydrogen-cleaned GaSb(001) surface*

N.S. Kaijaks, S. Al-Harhi, T.C.Q. Noakes, P. Bailey and C.F. McConville  
(in preparation)

*Surface reconstructions of atomic hydrogen-cleaned GaSb(001) observed by medium energy ion-scattering spectroscopy*

N.S. Kaijaks, S. Al-Harhi, T.C.Q. Noakes, P. Bailey and C.F. McConville  
(in preparation)

*Atomic structure of the InAs(001)– $(4\times 2)$  reconstruction studied by medium energy ion-scattering spectroscopy*

N.S. Kaijaks, S. Al-Harhi, T.C.Q. Noakes, P. Bailey and C.F. McConville  
(in preparation)

## Summary

Medium energy ion-scattering spectroscopy (MEIS), low energy electron diffraction (LEED), Auger electron spectroscopy (AES) and coaxial impact collision ion-scattering spectroscopy (CAICISS) have been used to characterize a number of III–V semiconductor surface structures produced by cleaning with atomic hydrogen. MEIS has also been used to characterize sub-surface damage of samples prepared by argon ion-bombardment and annealing (IBA).

Annealing under a flux of atomic hydrogen radicals ( $H^*$ ) has been shown to enable desorption of surface contaminants such as oxides and hydrocarbons. This atomic hydrogen cleaning technique has been used repeatedly to form both recognized and novel reconstructions of the (001) surface of gallium antimonide. The process of thermal decomposition of  $H^*$  cleaned GaSb(001)–(1×3) was examined using CAICISS and AES. Reconstruction to the c(2×6) phase was observed, followed by non-congruent sublimation of Sb and finally surface degradation. A number of GaSb(001) reconstructions have been characterized by MEIS, LEED and AES. These reconstructions included the 1×3 and c(2×6) surfaces and a previously unreported c(6×4) structure. Models for these reconstructions have been compared and analyses made to determine best-fit structural parameters using software developed by the author. The experimental data for the (1×3) reconstruction was found to be in good agreement with a model based on single Sb dimer chains separated by Ga atoms. It was found that the c(2×6) data was consistent with a bilayer model based on antiphase Sb dimers. However, MEIS results suggested significant staggering of the surface Sb dimers. Structural parameters for the dimerization of these reconstructions have been determined. Models for the c(6×4) reconstruction were considered, and a closer fit found for a model based on Sb dimer chains with staggered antiphase second layer Sb dimers.

A (4×2) reconstruction of the (001) surface of indium arsenide was prepared by AHC and analysed by MEIS, LEED and AES. Three previously proposed models have been compared and evaluated. It was found that a model based on In dimer pairs separated by second layer dimers was relatively inconsistent with the MEIS data recorded. A model based on single In dimers separated by second layer two-dimer chains was consistent with MEIS results, but structural parameters determined were nonphysical. A model without dimerization in the second layer was found to be in best agreement with the experimental results, as well as being physical and consistent with previously reported STM data. Structural parameters for this model were determined. A study of the effects of argon ion-bombardment and annealing (IBA) on the  $H^*$  cleaned InAs(001) surface was performed using MEIS, LEED and AES. The degree of sub-surface damage induced by the bombardment process has been analysed with reference to the energy of the ion beam. It was found that a layer with a high defect density was produced by IBA with a depth directly dependent on the incident ion energy. No such sub-surface damage was found in samples prepared by AHC.

## Abbreviations and common symbols

2D	two dimensional
3D	three dimensional
AES	Auger electron spectroscopy
AFM	atomic force microscopy
AHC	atomic hydrogen cleaning
ALICISS	alkali impact-collision ion scattering spectroscopy
AN	Auger neutralization
CAICISS	coaxial impact-collision ion scattering spectroscopy
CLRC	Central Laboratories of the Research Councils
CVD	chemical vapour deposition
DRS	direct recoil spectroscopy
ECM	electron counting model
EPSRC	Engineering and Physical Sciences Research Council
FWHM	full width at half maximum
H*	atomic hydrogen (radicals)
HEIS	high energy ion scattering spectroscopy
HREELS	high resolution electron energy loss spectroscopy
IBA	ion bombardment and annealing
INS	ion neutralization spectroscopy
ISS	ion scattering spectroscopy
LEED	low energy electron diffraction
LEED I–V	low energy electron diffraction intensity variation
LEIS	low energy ion scattering spectroscopy
MBE	molecular beam epitaxy
MEIS	medium energy ion scattering spectroscopy
MOCVD	metal-organic chemical vapour deposition
MOMBE	metal-organic molecular beam epitaxy
NICISS	neutral impact-collision ion scattering spectroscopy
PES	photoemission (spectroscopy)
RBS	Rutherford backscattering spectroscopy
RHEED	reflection high energy electron diffraction
SIMS	secondary ion mass spectrometry
STM	scanning tunnelling microscopy
SXRD	surface x-ray diffraction
TOF	time-of-flight
UHV	ultra high vacuum
VEGAS simulation!)	(not an abbreviation, merely a pun on generic Monte Carlo simulation!)
XPS	x-ray photoelectron spectroscopy
$\epsilon_0$	permittivity of free space ( $8.85 \times 10^{-12} \text{ Fm}^{-1}$ )

## 1 • Introduction

### 1.1 Motivation

Since 1912, when the first observation of x-ray diffraction proved that crystals are composed of a periodic array of atoms, the science of the solid state has matured to provide an enormous breadth of knowledge of the chemistry and physics of materials. One small, but very significant, chapter in this knowledge concerns semiconductors, a class of material which has, since the 1960s, grown to become central to modern life in the developed world. The scientists and engineers working today in the semiconductor industry strive to develop practical electronic devices which are smaller, faster and more efficient than ever before, and it is to this end that intensive research into the fundamentals of III–V semiconductor materials continues apace worldwide.

Gallium arsenide (GaAs) is the most studied III–V semiconductor material. It has come to play a major role in the electronics industry, usurping silicon and germanium as the material of choice for many optoelectronic and laser devices. This is partly because the technologies of GaAs production (particularly by epitaxial growth) and processing are relatively well-developed, but primarily as a result of its direct band gap transition. The existence of a direct transition, not present in Si and Ge, enables many useful optoelectronic properties, not least enhanced photon yield. Hence GaAs has become a particularly important material for devices such as sensors, light-emitting and laser diodes, as well as for traditional solid-state devices such as fast-switching (GHz) transistors.

However, the wavelengths accessible using the direct band gap transitions of GaAs alone are inherently limited. There are several other III–V materials with similar narrow band gaps to GaAs (e.g. InAs, InSb, GaSb, AlAs), which offer the potential not only for use in single material devices, but also for band gap engineering. By employing techniques such as the epitaxial growth of heterogeneous layer structures or production of non-stoichiometric alloy semiconductors, a wider range of band gaps (and thus wavelengths) are accessible, enabling more varied and general optoelectronic devices to be designed.

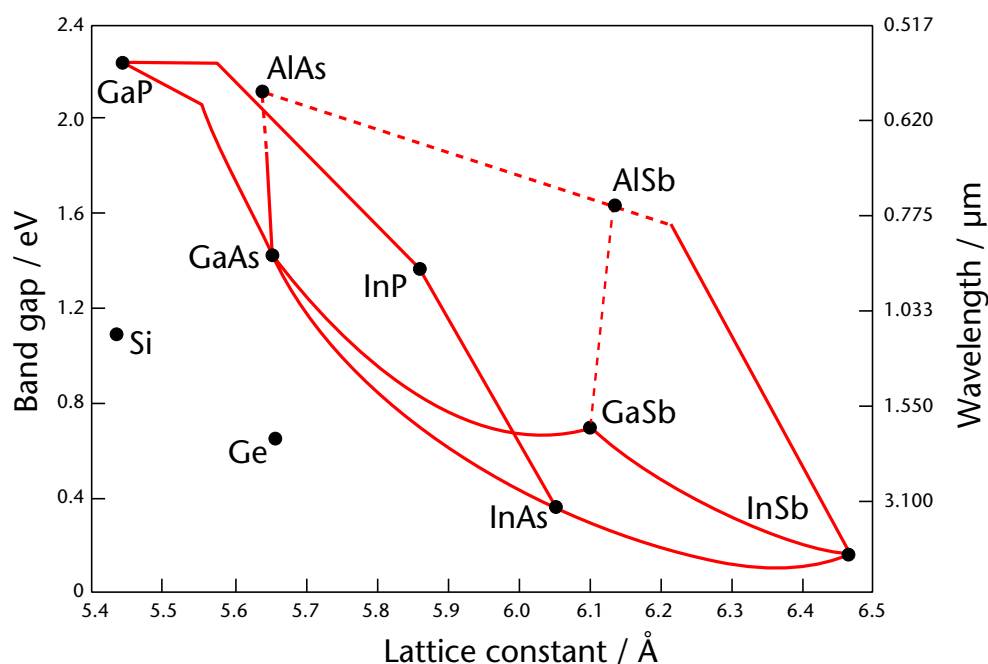


Figure 1.1: Room temperature lattice constants, band gaps and their corresponding wavelengths for some binary III–V semiconductors which crystallize in the zincblende structure. Lines show the range of parameters available from ternary compounds. Si and Ge are also shown for comparison [after Tien<sup>1</sup>].

It can be seen in figure 1.1 that GaAs and AlAs have very closely-matched lattice constants (0.04 % difference). Hence, any pseudobinary alloy of these three elements should be relatively free of strain, which would otherwise result in dislocations and other crystal defects which may degrade the electronic properties of a device. By adding judicious quantities of Al to GaAs, compounds with a range of band gaps from 1.44–2.21 eV can be formed. Similarly, there is a so-called ‘6.1 Å’ family of III–V semiconductors, consisting of InAs, GaSb and AlSb. Construction of appropriate ternary and quaternary compounds from these three narrow band gap III–V semiconductors can enable engineering of high-speed and optoelectronic devices with band gaps of  $\sim 0.3$ –1.7 eV, although there is some residual lattice mis-match between these materials. Together, this range of III–V materials covers wavelengths across the visible spectrum and into the infrared.<sup>2</sup> Recently, GaN based materials (e.g. GaInN and GaAlN) with relatively wide band gaps (around the range  $\sim 1.9$ –6.2 eV) have proved successful for optoelectronic devices in the blue and ultraviolet regions.<sup>3,4</sup> These nitrides crystallize in a wurtzite, rather than a zincblende structure. Although these represent a new and interesting class of semiconductor they are not discussed in this thesis.

As technology develops, electronic devices are growing closer in scale to the atomic arrays that form them. As a result, their function is increasingly reliant on the local crystallographic and electronic structure of their material surfaces and interfaces. It is therefore crucial to the design of devices to understand the properties and behaviour of the material surfaces that form them, both in growth and in action on the atomic scale. In the case of short-period heterostructures engineered for a specific band gap, the interfaces between layers constitute a significant fraction of the total volume. Hence, it is to be expected that the structure and stoichiometry of the growth surface will have a significant impact on device performance.<sup>5</sup> The ideal of smooth, abrupt interfaces may well be affected by the atomic surface structure in different ways. For example, some reconstructions of the surface may favour anisotropic growth morphologies<sup>6</sup>, whilst the III/V ratio of some reconstructions may lead to non-stoichiometric interfaces that cannot be compositionally abrupt.<sup>7</sup> Clearly, there is an identified technological need for the study of III–V semiconductor surfaces and interfaces. Whilst a great deal has been accomplished in the study of GaAs, much remains to be learnt about the surfaces of other III–V semiconductors, such as GaSb and InAs. These materials, examined in this research, are promising in themselves for applications such as high-speed transistors, wireless communications, infra-red detectors and laser diodes<sup>8</sup>, as well as in band gap engineered heterostructure devices. An interesting environmental application is in atmospheric gas detectors, since the common pollutants CO, HCl, CO<sub>2</sub> and O<sub>3</sub> all have strong absorption lines in the 2–5  $\mu\text{m}$  band.<sup>9</sup>

Additionally, narrow band gap III–V semiconductor materials pose many interesting problems to fundamental science, in the fields of solid-state physics, chemistry and particularly surface science. The solid surfaces of all materials, including III–V semiconductors, present a discontinuity in the ideal symmetry of a crystalline solid. Atoms on the topmost layer have lost their neighbours above them and are therefore in a different environment from their bulk-situated counterparts. By this argument, the surface can be viewed as the most extreme ‘defect’ of a bulk material. Re-arrangement of the surface

atoms with respect to their bulk positions may occur in order to minimize the surface energy, resulting in significant changes to the physical and electronic properties of the material. It is therefore evident that the surface profoundly affects the measured physical and electronic properties of materials, and that bulk models can only loosely describe the properties of the surface. This is particularly true for interactions with other atomic and molecular species and has implications for industrial processes including heterogeneous catalysis, thermionic emission, crystal growth, brittle fracture and electrical contacts. It might also be said that an understanding of the fundamental surface science of III–V semiconductors brings its own technological benefits.

## 1.2 An overview of surface science

As noted above, an understanding of the surface is of vital concern to those wishing to exploit the properties of semiconductors in device design and fabrication, as well as being of academic interest. It is appropriate now to consider both the techniques required and the special problems involved with study of surfaces in general. For a fuller description, the reader is referred to some of the many specialist texts available.<sup>10,11</sup>

### 1.2.1 Ultra-high vacuum (UHV)

To successfully study the properties of a surface on the atomic scale, the surface must be atomically clean for the duration of an experiment. Hence, the rate of arrival of potential contaminants at the surface must be kept to a minimum for a period of several hours.

From the kinetic theory of gases it is relatively straightforward to determine that at a pressure of  $\sim 10^{-6}$  mbar, a surface will be covered by one monolayer (ML) of a reactive species in around one second, if all incident atoms adhere to (or *adsorb on*) the surface.

From an experimental perspective it is clear that better vacua are required to ensure that samples remain clean on a practical time-scale. A pressure of around  $10^{-9}$  mbar will give a monolayer adsorption time of the order of an hour. It is only since the early 1960s, when commercial high-vacuum pumps, stainless-steel vessels and components became available, that the pressure regime known as *ultra-high vacuum* (UHV), of around  $10^{-9}$ – $10^{-11}$  mbar has

been regularly attainable. Such vacua, used in modern surface science, reduce the problems of ambient contamination. Nonetheless, UHV still implies major constraints on the types of experimental work possible. In particular, it is essential to be able to clean the sample surfaces within the vacuum system to a level compatible with UHV; whilst UHV guarantees that samples will be negligibly influenced by ambient atoms, it does not guarantee that the sample itself will not introduce contamination. UHV cleaning techniques are discussed in more detail in Chapter 3. However, for a general discussion of vacuum physics, the reader is again referred to appropriate texts.<sup>12,13</sup>

### 1.2.2 Surface science analytical techniques

A range of UHV-compatible techniques have been developed over the years to study surfaces. These techniques are broadly sensitive to at least one of the following; crystallography, periodicity, morphology, chemical state, elemental composition, vibrational and electronic structure. They may give information on the surface properties over a short or long range, and may characterize both surfaces and their adsorbates. It is therefore usually necessary to use a combination of two or more techniques to fully characterize a surface. These myriad techniques are discussed fully elsewhere.<sup>10</sup> The following are either used in this work or have been frequently used to characterize III–V materials and are cited in later chapters. This brief description is more fully expanded upon in chapter 3 for those techniques used in the experimental work in this thesis.

#### 1.2.2.1 Low energy electron diffraction (LEED)

Low energy electron diffraction (or LEED) gives information on the long-range translational periodicity of a surface in the form of the *reciprocal lattice*. Electrons are accelerated through a potential of around 50–200 eV, and are directed onto the surface at normal incidence. Diffracted and backscattered electrons are filtered by a retarding grid (or optics) to remove inelastically scattered electrons. The short inelastic scattering mean-free-path of low energy electrons ensures surface specificity. The remaining elastically scattered electrons hit a hemispherical phosphorescent screen, forming a visible diffraction pattern of

spots representing the reciprocal lattice. An important point to note is that LEED only indicates the periodicity of the surface, not the atomic positions. In the case of a surface with a small amount of adsorbate studied solely with LEED, it is not possible to determine either the sites to which adsorbate atoms are bound or even whether the substrate atoms have moved.

LEED may also be used quantitatively, whereby the intensities of the diffracted spots are measured as a function of incident electron energy, typically over a range of about 40–300 eV. This quantitative LEED technique is known as LEED I–V and a structural solution is only possible by comparison with simulations of I–V curves for each diffracted spot and for a range of possible models using a calculated reliability factor (*R-factor*) analysis. The solution may then be honed by iteration. This approach requires considerable computing power, and is best suited to surfaces where some knowledge of the structure has already been gained by complementary techniques.

#### 1.2.2.2 Auger electron spectroscopy (AES)

Auger electron spectroscopy (AES) give surface compositional information integrated over a depth of two to three atomic layers. A beam of electrons (typically 3–5 keV in energy) is incident on the sample surface and an energy-resolving detector is used to record the energy spectrum of electrons ejected from the surface. An incoming electron may remove a core level electron from a surface atom, thus creating a hole. One mechanism of relaxation from this state is for a higher-level electron to fill the vacancy, imparting the energy within the same energy level to release an *Auger electron*. The Auger electron energy is independent of the incident beam energy and is characteristic of the differences between the energy levels of the specific atom. AES, like LEED, requires only a low energy electron source, and is therefore an analytical technique well-suited to smaller laboratories.

### 1.2.2.3 Medium energy ion scattering spectroscopy (MEIS)

Medium energy ion scattering spectroscopy (MEIS) is an ion scattering spectroscopic (ISS) technique able to offer both compositional and real-space crystallographic information. It uses a beam of light ions (typically  $H^+$  or  $He^+$ ) at around 100 keV, incident along a low-index crystallographic direction of the sample. A classical analysis of the intensity of scattered ions as a function of scattering angle and energy enables compositional depth-profiling as well as confirmation of surface crystallographic structure by geometric means. *Ab initio* structure determination is obtained by *R*-factor analysis of Monte Carlo spectral simulations for model surfaces. One major advantage of MEIS over techniques such as LEED and surface x-ray diffraction is that the data affords a real-space representation of the structure. This means that structural analysis is often more straightforward. Indeed, basic structural information can be gleaned for some surfaces without the need for simulation. However unlike LEED, the requirement for a relatively high energy, stable ion source means that MEIS is only possible at dedicated major facilities.

### 1.2.2.4 Coaxial impact collision ion scattering spectroscopy (CAICISS)

Coaxial impact collision ion scattering spectroscopy (CAICISS) is similar to MEIS, but uses lower energy ions (1–10 keV) and a simple  $180^\circ$  backscattering geometry. Typically, the time-of-flight is measured using a pulsed ion beam in order to determine the energy loss in collision, which is characteristic of the target composition. By rotation of the sample through one or more axes, the structure of the sample can be profiled geometrically, since the  $180^\circ$  backscattering ensures that only central collisions are detected. The low energy of CAICISS results in increased surface specificity whilst, geometrically, spectral simulation is straightforward. There is, however, more complication in some aspects of simulation, due to the increased likelihood of multiple scattering events and surface neutralization. Unlike MEIS though, its simple geometry means that CAICISS can be used as a ‘bolt-on’ technique, requiring only line-of-sight with the sample. The low-energy ion source is simpler in design and operation, making CAICISS well-suited for the smaller laboratory.

#### 1.2.2.5 High resolution electron energy loss spectroscopy (HREELS)

High resolution electron energy loss spectroscopy (HREELS) relies on the inelastic energy loss of a near-monochromatic electron beam (of energy 1–100 eV with a spread of  $\sim 1$ –10 meV FWHM) due to coupling with the long range dipole electric fields induced by excitations within the lattice. As a result, HREELS is a non-invasive technique; electrons need not even penetrate the surface and the effective probing depth is controlled by simply varying the incident electron energy. Energy analysis is performed about a strong ‘quasi-elastic’ peak (typically 4–15 meV FWHM), where the incident and detected energies are equal. On the energy-loss side of this peak, features can be observed due to generation of low energy surface excitations (usually  $< 400$  meV). These excitations may occur as a result of adsorbate vibrational modes; however, they may also be due to collective excitations of the lattice or charge carriers close to the surface (surface phonons and surface plasmons respectively). Whilst HREELS can probe both types of excitation, analysis of the plasmon excitations in doped semiconductor surfaces is particularly useful for deduction of information about carrier concentration, mobility and electronic damage.

#### 1.2.2.6 Surface x-ray diffraction (SXR D)

Surface x-ray diffraction (SXR D) uses glancing incidence and exit geometries ( $\sim 0.5^\circ$  from the surface) to obtain surface specificity. By measuring the intensity of diffracted x-ray beams across a wide range of azimuthal angles, information on atomic position parallel to the surface can be obtained, whilst measuring the intensity change over a range of polar angles for a given azimuth gives information on atomic positions normal to the surface. This requires high precision goniometry and a stable, bright, synchrotron x-ray source. These experimental complexities are offset by the relative simplicity of structural analysis which can essentially use a kinematical approximation to obtain real space information by Fourier transform of reciprocal space data instead of the trial-and-error approach to *ab initio* analysis required for LEED. The application of SXR D has therefore been particularly useful in semiconductor surface analysis, where large surface unit cells are commonplace.

### 1.2.2.7 Reflection high energy electron diffraction (RHEED)

Reflection high energy electron diffraction (or RHEED) is an alternative to LEED, offering surface specificity with high energy electrons ( $\sim 10\text{--}30$  keV). Grazing incidence and exit angles are used, although less glancing than SXRD, typically being  $1\text{--}2^\circ$ . The small overall scattering angle maintains a relatively large elastic scattering cross-section. Although the inelastic scattering mean-free-paths of the high energy electrons are relatively long compared to LEED, the grazing angle ensures that elastically scattered electrons come only from the surface region. In RHEED, relatively simple electron optics are required and the geometry is less intrusive than LEED for use during growth and deposition; LEED optics must typically be sited normal to the sample surface. Furthermore, for analysis of growth, RHEED is particularly useful, since the nature of the pattern is affected by surface morphology far more than that of LEED and specular intensity measurements can be used to determine monolayer growth rate. Disadvantages are that although the diffraction pattern formed is indicative of the surface symmetry, rotation of the sample is required to establish the surface periodicity in two dimensions. Changes of periodicity in the plane of incidence are not reflected by changes in the diffraction pattern. Overall, RHEED is better suited for surface assessment during growth rather than quantitative structural analysis.

### 1.2.2.8 Scanning tunnelling microscopy (STM)

Scanning tunnelling microscopy (STM) is a technique reliant upon the wave-like nature of electrons. If two conductors are brought close together (to a separation of the order of  $4 \text{ \AA}$ ) and a potential applied between them, then the overlap of the electron wavefunctions permits quantum mechanical tunnelling and a current flow across the gap. At low temperatures and voltages, if the current is kept constant (to within a few per cent), then the gap should remain constant to within around  $0.01 \text{ \AA}$ . In STM, an atomically sharp electrode tip is scanned mechanically in a raster pattern to cover the surface. By altering the height of the tip above the surface using a feedback loop to maintain a constant tunnelling current, the electronic morphology of the surface can be determined.

Alternatively, the tunnelling current can be recorded for a constant height. This is faster to measure, but more complex to interpret since the tunnelling current is related to the surface morphology by a convolution of the electronic structures of tip and surface. Interpretation can become more difficult still in semiconductors where the tunnelling probability may vary from atom to atom. However, this distinction can be useful in elucidating surface atomic arrangements. For example in GaAs, the Ga atoms tend to have empty electron states. Thus if the STM polarity is such that the tip is the cathode, tunnelling will essentially only occur into Ga atoms (hence, empty state imaging). Reversing the polarity results in tunnelling only from electron-rich As atoms to the tip, resulting in so-called filled-state images. Thus by a simple reversal of polarity, the group III and group V elements can be isolated and imaged separately with atomic spatial resolution.

### **1.3 Experimental work**

The work described in this thesis was performed primarily in order to learn more about the surface atomic structures of two different III–V semiconductor (001) surfaces: gallium antimonide (GaSb) and indium arsenide (InAs). A number of different reconstructions of the GaSb(001) surface have been analysed with MEIS, AES and LEED in order to gain information about their crystallography. In particular, a new, stable  $c(6\times 4)$  surface phase was observed for the first time. This structure has been analysed and a surface structural model proposed. The more common  $(1\times 3)$  and  $c(2\times 6)$  GaSb(001) reconstructions were also observed and analysed to determine structural parameters for qualitative models already proposed. Additionally, CAICISS and AES were used to examine, in real-time, the thermal decomposition of the  $(1\times 3)$  reconstruction. The effect of argon ion-bombardment on the InAs(001) surface was also examined using CAICISS, MEIS and AES, and a study made to compare the damage induced by bombardment at a number of incidence energies. The structure of its  $(4\times 2)$  reconstruction was also examined and different models compared in order to determine a best-fit structural solution. Aside from the materials aspects, another aim of the work was to use and evaluate a combination of techniques for surface preparation and analysis. The primary preparation technique used was atomic

hydrogen cleaning (AHC), a relatively novel technique which has already been shown to produce less damaged surfaces than the more common technique of argon ion bombardment and annealing (IBA). The final aim of the work was to assess the suitability of a promising structural technique such as MEIS for the study of the common III–V binary semiconductor surfaces.

#### **1.4 Structure and content of the thesis**

This thesis has been prepared in accordance with the guidelines of the University of Warwick<sup>14</sup> and its Department of Physics<sup>15</sup>. The corpus of the thesis is structured in eight chapters, the first of which gives an overview of the field of work, the techniques used, and the specific experiments performed. Chapter 2 is concerned with some of the relevant theoretical properties of the materials under investigation. It has been written to cover a broad range of fundamentals of crystalline and electronic structure at a level appropriate for a reader from any physical science discipline to understand the work performed. The chapter focuses on the physical structure of surfaces, but also includes a brief description of relevant sample growth processes, including both bulk and epitaxial techniques. Chapter 3 is devoted to a theoretical examination of the experimental techniques used, describing methods of both surface preparation (including IBA and AHC) and surface analysis (including LEED, AES, MEIS and CAICISS). It begins by discussing ion–particle interactions which are central to most of these techniques. Chapter 4 describes computational techniques and work performed. This includes the theoretical basis of the VEGAS simulation software used to model MEIS experiments and a discussion of reliability factors for determining the quality of fit between experimental data and simulation. Developments in simulation and visualization by the author are discussed. Chapters 5 and 6 are experimental chapters devoted to GaSb and InAs respectively, each beginning with an introduction to the specific material system under analysis and the experiments performed, before presenting the experimental results and discussion thereof. The work is drawn to a conclusion in Chapter 7, which also describes possible approaches and areas for future work. The thesis is completed by a full index.

## 1.5 References

- <sup>1</sup> P.K. Tien, private communication cited in T.H. Chiu and W.T. Tsang: *J. Appl. Phys.* **57** (1985) 4572
- <sup>2</sup> T.C. McGill and D.A. Collins: *Proc. 6th Int. Conf. on Narrow Band Gap Semiconductors*, eds. R.A. Stradling and J.B. Mullin (IOP, 1993) S1
- <sup>3</sup> S.N. Mohammad and H. Morkoc: *Progr. Quantum. Electr.* **20** (1996) 361
- <sup>4</sup> S.P. Denbaars: *Proc. IEEE* **85** (1997) 1740
- <sup>5</sup> A.G. Milnes and A.Y. Polyakov: *Solid State Electron.* **36** (1993) 803
- <sup>6</sup> V. Bressler-Hill, S. Varma, A. Lorke, B.Z. Nosho, P.M. Petroff and W.H. Weinberg: *Phys. Rev. Lett.* **74** (1995) 3209
- <sup>7</sup> M. Yano, H. Yokose, Y. Iwai and M. Inoue: *J. Cryst. Growth* **111** (1991) 609
- <sup>8</sup> D.H. Chow, R.H. Miles, T.C. Hasenberg, A.R. Kost, Y.H. Zhang, H.L. Dunlap and L. West: *Appl. Phys. Lett.* **67** (1995) 3700
- <sup>9</sup> W.F. Micklethwaite, R.G. Fines and D.J. Freschi: *III-Vs Rev.* **9** (1996) 51
- <sup>10</sup> D.P. Woodruff, T.A. Delchar: *Modern Techniques of Surface Science* (Cambridge, 1994) *et loc. cit.*
- <sup>11</sup> M. Prutton: *An Introduction to Surface Science* (Oxford, 1994) *et loc. cit.*
- <sup>12</sup> N.W. Robinson: *The Physical Principles of Ultra-High Vacuum Systems and Equipment* (Chapman & Hall, 1968)
- <sup>13</sup> T.A. Delchar: *Vacuum Physics and Techniques* (Chapman & Hall, 1993)
- <sup>14</sup> *Guide to Examinations for Higher Degrees by Research* (University of Warwick Graduate School, 1996)
- <sup>15</sup> *Preparation of PhD Theses, PHYS/PG/3* (Department of Physics, University of Warwick, 1995)

## 2 • III–V semiconductor surfaces

### 2.1 Introduction

The field of III–V semiconductor surface crystallography has developed dramatically over the past fifteen years, the impetus for this growth being provided mostly from the advent of scanning tunnelling microscopy (STM). This technique enabled, for the first time, direct imaging of a semiconductor surface.<sup>1</sup> The ability of STM to resolve local electronic structures on the atomic scale with minimal surface damage or interference<sup>2</sup> has enabled researchers to study many surface properties of semiconductors, from geometric and electronic structure of clean, ordered surfaces to analysis of local features (such as defects, steps and impurities), interfacial interactions and growth.<sup>3</sup> In addition, semiconductors lend themselves well to STM, since with predominantly covalent bonding and spatially-localized electron orbitals, analysis is much simpler than for the majority of metal surfaces. Through STM and other techniques, we now have a much more detailed understanding of the fundamentals of semiconductor surfaces, required for device development.

Although useful in visualising crystal structures, STM cannot provide crystallographic solutions, as the tunnelling current that generates the image is primarily influenced by the density of electronic states (of both the sample and the tip) rather than actual atomic positions. Other techniques, such as surface x-ray diffraction, ISS and LEED are more appropriate, and the use of the latter two in this work is described in the following chapters. Since surface science is a broad church, readers may come from chemistry, physics or materials science backgrounds, where depth and breadth of knowledge and terminology may differ. This chapter therefore begins with a relatively simple introduction to the electronic and physical structure of both the bulk and the surface, in order to understand the application of these techniques and assess the properties of semiconductor surfaces. Since growth *per se* is not discussed elsewhere, the chapter concludes with a brief overview of semiconductor crystal growth in order to understand how the ideal of single crystal materials is approached in the preparation of the real samples used in this work.

## 2.2 Bulk structure

The work in this thesis concentrates on single crystal III–V semiconductor materials, where the atomic structure is representable as a three-dimensional *lattice*, each *unit cell* of which contains one or more atoms forming the *motif* (also sometimes known as the *basis*) of the crystal. The lattice may be defined in terms of primitive translation vectors  $\mathbf{a}$ ,  $\mathbf{b}$  and  $\mathbf{c}$  such that any two lattice points are connected by a lattice translation vector

$$\mathbf{t} = h\mathbf{a} + k\mathbf{b} + l\mathbf{c} \quad 2.1$$

where  $h$ ,  $k$ ,  $l$  are integers. All physical properties of the crystal are invariant under  $\mathbf{t}$ . For example, the electron number density  $n(\mathbf{r})$  is a periodic function of  $\mathbf{r}$  (itself defined in terms of  $\mathbf{a}$ ,  $\mathbf{b}$  and  $\mathbf{c}$ ) such that  $n(\mathbf{r} + \mathbf{t}) = n(\mathbf{r})$ . It can be defined as a Fourier series

$$n(\mathbf{r}) = \sum_{\mathbf{g}} n_{\mathbf{g}} \exp(i\mathbf{g} \cdot \mathbf{r}) \quad 2.2$$

where  $\mathbf{g}$  is a *reciprocal lattice vector* with dimensions of  $[\text{length}]^{-1}$

$$\mathbf{g} = h\mathbf{a}^* + k\mathbf{b}^* + l\mathbf{c}^* \quad 2.3$$

The *reciprocal lattice* is the Fourier transform of the real crystal lattice. The primitive translation vectors of the reciprocal lattice  $\mathbf{a}^*$ ,  $\mathbf{b}^*$ ,  $\mathbf{c}^*$  are related to those of the real lattice  $\mathbf{a}$ ,  $\mathbf{b}$ ,  $\mathbf{c}$  by

$$\mathbf{a}^* = \frac{m(\mathbf{b} \times \mathbf{c})}{\mathbf{a} \cdot \mathbf{b} \times \mathbf{c}}, \quad \mathbf{b}^* = \frac{m(\mathbf{c} \times \mathbf{a})}{\mathbf{a} \cdot \mathbf{b} \times \mathbf{c}}, \quad \mathbf{c}^* = \frac{m(\mathbf{a} \times \mathbf{b})}{\mathbf{a} \cdot \mathbf{b} \times \mathbf{c}} \quad 2.4$$

It is important to note that there are two distinct values of the factor  $m$  in common use. A value of 1 is favoured by crystallographers, whilst a value of  $2\pi$  is more commonly used by physicists. The latter definition ( $m = 2\pi$ ) is used in this thesis. Each vector is therefore orthogonal to two of the axis vectors of the real crystal such that

$$\begin{aligned} (\mathbf{a}^* \cdot \mathbf{a}) &= (\mathbf{b}^* \cdot \mathbf{b}) = (\mathbf{c}^* \cdot \mathbf{c}) = m \\ (\mathbf{a}^* \cdot \mathbf{b}) &= (\mathbf{b}^* \cdot \mathbf{c}) = (\mathbf{c}^* \cdot \mathbf{a}) = 0 \end{aligned} \quad 2.5$$

The reciprocal lattice is a useful concept as it has a number of geometric properties which ease crystallographic calculations. Each vector  $\mathbf{g}$  of the reciprocal lattice is normal to a set of real lattice planes, and hence if the components of  $\mathbf{g}$  have no common factor, then  $|\mathbf{g}|$  is inversely proportional to the spacing of the real lattice planes normal to  $\mathbf{g}$ . *Miller indices* can therefore be defined as a physical means of labelling lattice planes by their reciprocal lattice vectors. For example, the Miller indices  $(1\bar{1}\bar{2})$  define the real lattice planes whose related primitive reciprocal lattice vectors have indices  $h=1$ ,  $k=-1$ ,  $l=-2$ . Planes of equivalent symmetry are denoted by braces, e.g.  $\{1\bar{1}\bar{2}\}$ , whilst the indices of a direction in a crystal are denoted by square brackets. In cubic crystals the direction  $[hkl]$  is normal to planes  $(hkl)$ . Directions of equivalent symmetry are denoted by angle brackets;  $\langle 100 \rangle$  represents the set including  $[001]$ ,  $[010]$ ,  $[00\bar{1}]$  etc. The reciprocal lattice is particularly useful as it gives the form of crystal diffraction patterns such as those formed in LEED. This is discussed further in the next chapter.

A crystal takes its form as a result of the forces acting between its constituent atoms, arising predominantly from the electric charges of the electrons furthest from the nuclei, i.e. the valence electrons. In bonding with a neighbouring atom, their free energy is reduced by sharing (covalent bonding) and exchange (ionic or polar bonding) of valence electrons. In most III–V semiconductors, the bonds have largely covalent character. The three valence electrons of the group III (*trivalent*) atoms are shared with the pentavalent group V atoms, resulting in complete outer energy shells for both atoms, and a stable electronic structure. The bonds can be visualized as a concentrated electron cloud between the atoms, equivalent to a pair of spin–opposite electrons, polarized by the residual charge on the pentavalent atoms.

The orbitals (i.e. wavefunctions) of the electrons have shapes dependent on the angular momentum quantum number  $l$ . For historical reasons, orbitals with  $l = 0$  are called s-orbitals, and those with  $l = 1$  are p-orbitals. The boundary surfaces (within which there is a high probability of finding the electron) are spherically symmetrical for s-orbitals and shaped like a dumb–bell for p-orbitals, as shown in figure 2.1.

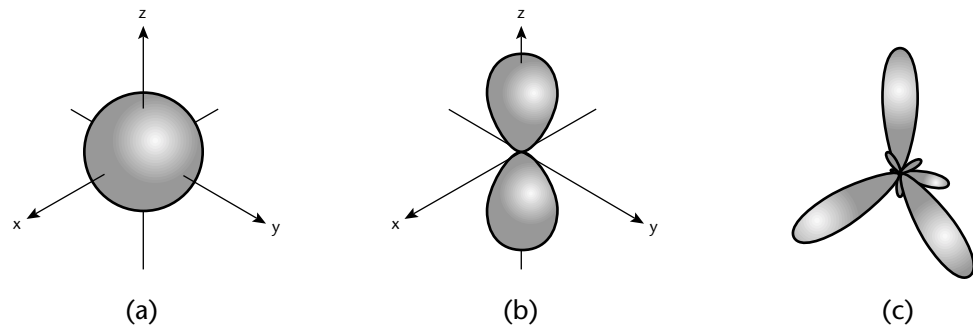


Figure 2.1: Boundary surfaces (95% probability) for (a) a 1s-orbital (b) a  $2p_z$ -orbital and (c) an  $sp^3$  hybrid orbital. Note that the two orthogonal p-orbitals are not shown in (b) for clarity.

In most III–V bonding, electrons from the s- and p-orbitals of the two elements combine in a ratio of 1:3 to form hybrid  $sp^3$  orbitals co-ordinating with the four nearest neighbour atoms. These hybrid orbitals are tetrahedral, with a bond angle of  $109.47^\circ$  resulting in a simple face-centred cubic (FCC) lattice with a two-atom motif of a group III atom at  $(0,0,0)$  and a group V atom at  $(\frac{1}{4}, \frac{1}{4}, \frac{1}{4})$ , as shown in figure 2.2.<sup>4</sup> It may perhaps be more easily visualized as a pair of interpenetrating primitive FCC lattices, with motifs of a single group III and group V atom respectively. This is named the zincblende structure after a common structure found in a ZnS ore.

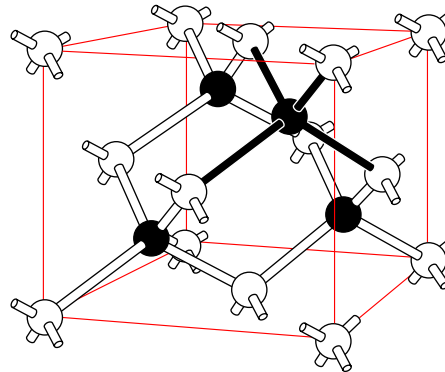


Figure 2.2: Ball and stick model of the zincblende atomic structure. Open circles represent cations (e.g. In, Ga) and closed circles anions (e.g. As, Sb). If both species are identical, then the structure becomes that of diamond. The black 'sticks' indicate the tetrahedral coordination of the atoms in the zincblende structure.

The  $\{111\}$ ,  $\{110\}$  and  $\{100\}$  surfaces of zincblende compound semiconductors are the most commonly studied. The  $\{110\}$  surfaces pass through equal numbers of group III and group V atoms, and are the natural cleavage planes of III–V compounds. Hence,  $\{110\}$  surfaces are termed non-polar and can be prepared by cleavage *in-vacuo*. By contrast, the

$\{111\}$  and  $\{100\}$  polar surfaces are bulk-terminated by atoms of one element alone, and cannot be produced by cleaving. Ideal, unreconstructed  $\{100\}$  III–V semiconductor surfaces are therefore classified as either group III- or group V-terminated.<sup>5</sup> It is only these polar surfaces that undergo surface reconstruction (discussed in §2.3.1 below). It should also be noted that an alternative definition of a polar surface is used in some literature, where  $(hkl) \neq (\bar{h}\bar{k}\bar{l})$ .

Having considered the bond-approach to the crystal, it is appropriate to consider a band-approach. The covalently-bonded crystal described above is essentially a large molecular structure formed by hybrid orbitals. In the extreme of an infinite periodic crystal, the orbitals are grouped together across the lattice forming a continuum of energy states called an energy band. The valence band is the band of energies occupied by the valence electrons whilst the next highest energy band, with many free energy states available, is the conduction band. In a metal, the valence band is full and the conduction band partially filled, with no gap between the bands. For an insulator, there is a *band gap*, so large that it is impossible for an electron within the valence band to gain enough kinetic energy to reach the conduction band. The separation of the two bands varies in a four-dimensional relationship between the energy  $E$  and the three vector directions of momentum  $\mathbf{k}$ . In a semiconductor the band gap minimum is narrow enough (typically of the order of an electronvolt) to enable a significant number of electrons to be thermally excited to the conduction band. This behaviour is the key to the useful electronic properties of semiconductors.

This band gap transition may be *direct* if the conduction band minimum and the valence band maximum coincide in  $\mathbf{k}$  such that electron transitions are possible with zero momentum change (as occurs with gallium arsenide). The energy gap is  $E_g = \hbar\omega_g$  where  $\omega_g$  is the frequency of the photon generated by the transition. This is shown diagrammatically in figure 2.3. In an *indirect* band gap material (such as silicon or GaP), the minimum energy gap is separated by a substantial wavevector  $\mathbf{k}_c$ . Direct photon transition cannot satisfy conservation of wavevector, since  $\mathbf{k}_{photon}$  is negligible at these energies.

Therefore, a lattice vibration (*phonon*) with wavevector  $\mathbf{k}_{phonon}$  and frequency  $\Omega$  is required to achieve the momentum change required, such that

$$\mathbf{k}_{photon} = \mathbf{k}_c + \mathbf{k}_{phonon}; \quad \hbar\omega = E_g + \hbar\Omega \quad 2.6$$

The solution of the band structure of a real three-dimensional crystal is non-trivial, and it is not relevant to the work in this thesis to examine the quantitative relationship in greater depth. The reader is instead referred to other works.<sup>6,7,8,9,10</sup> Since the band structure defines the optical and electronic properties of the crystal, it is clear that its control and understanding are crucial to the development of devices based on semiconductors such as gallium antimonide and gallium phosphide. However, to fully understand the electronic structure of a surface it is germane to appreciate its physical structure as well.

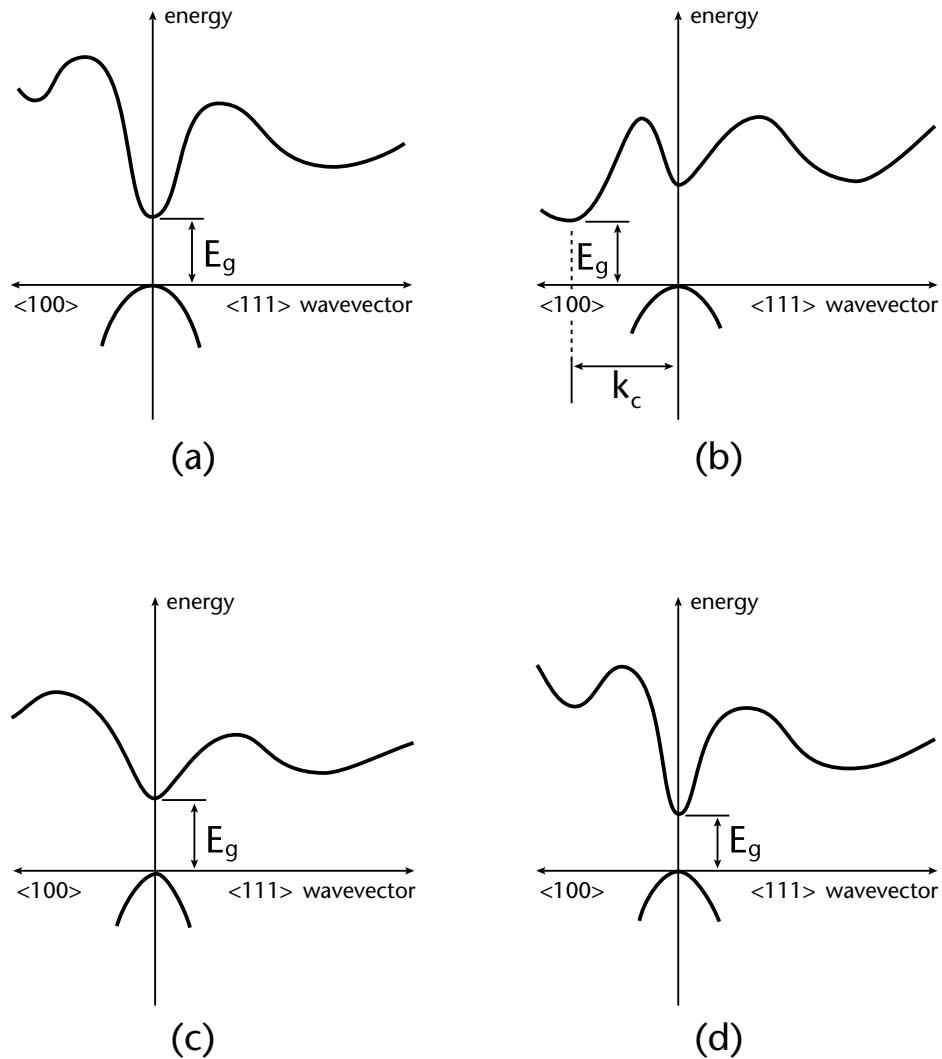


Figure 2.3: Band structures for four III–V semiconductors; (a) GaAs, (b) GaP, (c) GaSb and (d) InAs. All have direct transitions except (b) GaP [after Levinshtein et al<sup>11</sup>]

## 2.3 Semiconductor surface structure

### 2.3.1 Relaxation and reconstruction

When a surface forms, the interactions between atoms in the topmost layer (and the layers below) are modified due to the absence of neighbouring atoms on one side. In order to achieve electronic and physical stability, the surface atoms are usually rearranged and/or displaced to minimize the surface energy and the number of dangling bond states. This rearrangement may take the form of a simple compression, or more normally expansion, of the atomic planes parallel to the surface known as surface *relaxation*, as shown in figure 2.4. Relaxation does not in itself affect the lateral periodicity and is therefore inaccessible to surface electronic analytical techniques such as STM. It is, however, measurable using physical techniques such as ISS.

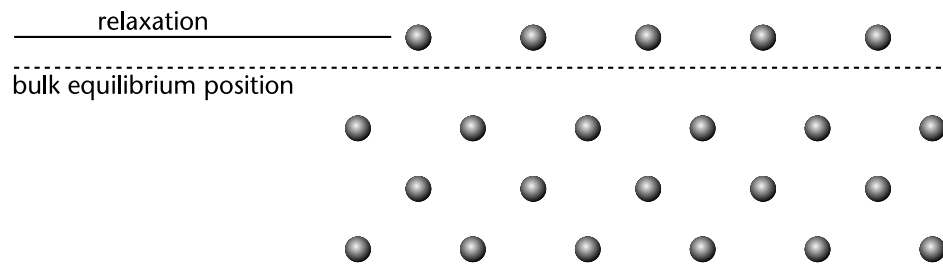


Figure 2.4: Surface relaxation (viewpoint within the surface plane), where the outermost atomic layer has shifted outwards to reduce surface free energy.

Surface *reconstruction* is generally a more complex process where the surface atoms not only relax normal to the surface, but also undergo a rearrangement of the surface periodicity. Reconstructed surfaces have lowered translational symmetry and often exhibit different chemical compositions to that of the bulk. To describe the translational symmetry of the reconstruction it is common to use Wood notation.<sup>12</sup> If the primitive surface mesh formed by bulk termination of the surface has basis vectors  $\mathbf{a}$  and  $\mathbf{b}$ , and the reconstructed surface mesh has primitive basis vectors  $m\mathbf{a}$  and  $n\mathbf{b}$ , then the surface is said to have an  $(m \times n)$  reconstruction. A centred or  $c(m \times n)$  reconstruction has an additional mesh point at the centre of the primitive  $(m \times n)$  mesh. For (001) surfaces of III–V semiconductors,  $\mathbf{a}$  and  $\mathbf{b}$

lie along the  $[110]$  and  $[1\bar{1}0]$  directions respectively, such that  $|\mathbf{a}| = |\mathbf{b}| = L/\sqrt{2}$  where  $L$  is the bulk lattice parameter. Common reconstructions of these surfaces include  $(4\times 2)$ ,  $c(8\times 2)$ ,  $c(4\times 4)$ ,  $(2\times 4)$  and  $c(2\times 8)$ . Some example reconstructions are shown in figure 2.5. By convention, the form  $(n\times m)$  where  $n > m$ , as in  $(4\times 2)$  and  $c(6\times 4)$ , refers to group III terminated surfaces (those terminating with some fraction of a monolayer of group III atoms) whilst  $(m\times n)$  forms, like  $c(2\times 8)$ , refer to group V terminated reconstructions. Different registries (translations between the substrate and surface meshes) are possible for a given  $(m\times n)$ , and it is important to note that many techniques which can give surface periodicity information (like LEED and STM) are unable to distinguish between them.

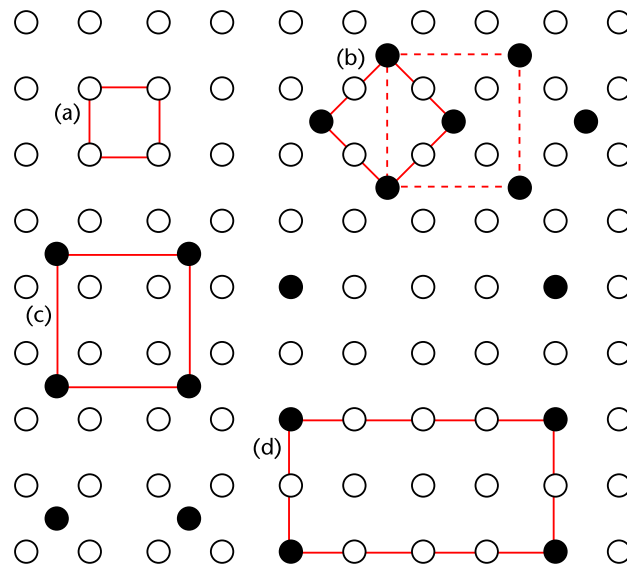


Figure 2.5: Surface reconstructions from a viewpoint normal to the surface plane. The open circles show the substrate periodicity,  $(1\times 1)$  in Wood notation, also highlighted as (a). The closed circles show top layer (ad)atoms forming a range of different reconstructions. (b) shows a reconstruction which can equivalently be described as  $(\sqrt{2}\times\sqrt{2})$   $R45^\circ$  or (dashed line) as  $c(2\times 2)$ , (c) shows a primitive  $(2\times 2)$  and (d) shows  $(4\times 2)$  periodicity.

### 2.3.2 Reconstruction mechanisms

In a zincblende structure III–V semiconductor, the interatomic bonds are tetrahedral in nature, each consisting of two spin-paired electrons forming a hybrid  $sp^3$  orbital. On forming a surface these bonds are broken, leaving unpaired, energetically unstable dangling bonds. Such a surface has a large free energy and reconstruction occurs to reduce this to at least a local minimum. For a surface formed by crystal cleavage alone, it is most likely that a simple rehybridization of the dangling bonds will occur. However, for an annealed III–V

semiconductor surface, the reconstruction may also involve some change in surface stoichiometry. A variety of nearly degenerate structures are therefore possible. Numerous theoretical and experimental studies over the the past ten years have led to the proposal of a number of semi-empirical qualitative ‘principles’ which apply to almost all semiconductor reconstructions.<sup>13,14,15,16,17</sup> These can be summarized for III–V compounds:

- i) Surfaces tend to be ‘autocompensated’ (as defined below).
- ii) For a given surface stoichiometry, the surface atomic geometry is determined primarily by a rehybridization-induced lowering of the energies of bonds (filled-state anion dangling bonds or other surface bonds such as dimers).
- iii) The surface structure observed will be the lowest free-energy structure kinetically accessible under the preparation conditions.

The first principle is a result of the requirement that (ignoring defects) the surface of a compound semiconductor must be electronically neutral. This limits the range of possible surface stoichiometries. An *electron counting model* (ECM) can be applied to determine the allowable surface compositions.<sup>18,19,20</sup> This model is based on the hypothesis that the number of available electrons must exactly fill all dangling bond states in the valence band, whilst conduction band states must be empty, thus forming a semiconducting surface. This criterion is named the non-metallicity condition and it is possible only for surfaces which are relaxed. Such a relaxed, charge neutral surface is said to be autocompensated.

Having thus far accounted for surface stoichiometry, the second principle determines the viability of a surface geometry. Consider a pair of dangling bonds with a total of two electrons between them. Since anions are more electronegative than cations, anion dangling bond states lie at lower energy than cation states (by a significant fraction of the band gap). It is therefore energetically most favourable to transfer charge, completely emptying the cation states and filling the anion states. The charge transfer may be further stabilized by an outward anion relaxation and inward cation relaxation thus further reducing the free energy. In more complex situations such as dimerization, as described in §2.3.3, a similar argument applies to surface (non-dangling) bonds.

The final principle is straightforward thermodynamics, although critically it does account for the process used to prepare the surface. Different ‘stable’ reconstructions can be produced by different approaches and therefore represent only *local* minima in free energy. Factors determining the reconstruction exhibited include the temperature and III/V flux ratio during MBE growth, and the temperature, time and presence of group V flux during post-growth annealing. The energy difference between these different reconstructions is often very small<sup>21,22</sup>; indeed several domains of different reconstructions may co-exist on the same surface. One-dimensional disorder may also occur, wherein a random half-unit mesh shift can occur in the dimer direction resulting in a mixture of  $c(2m \times n)$  and  $(m \times n)$  domains.<sup>23</sup> Overall, it must be recognized that the ECM does not uniquely determine the surface reconstruction. It can only be used as a guide to help identify viable models.

### 2.3.3 Dimerization

It is often energetically favourable for a pair of adjacent dangling bonds to rehybridize, bending the back bonds to the second layer whilst forming a new bond with bulk-like length between the adjacent top layer atoms.<sup>5</sup> This pair of atoms is termed a *dimer*, although it is threefold co-ordinated unlike a conventional molecular dimer (with one-fold co-ordination). Symmetric (and asymmetric) dimerization reduces the number of dangling bonds to one per atom. The dimers may then be stabilized either by raising the anion and lowering the cation (as for dangling bonds), or by further hybridization with the remaining dangling bonds on the atoms.

Whilst dimerization clearly introduces two-fold periodicity into the reconstruction, it is also quite possible to introduce other periodicities through parallel dimer rows, missing dimers or missing second layer atoms. Indeed, such structures are often required to satisfy the reconstruction principles and the ECM given above. For example, without missing dimers, many semiconductor surfaces cannot be autocompensated due to excess charge.

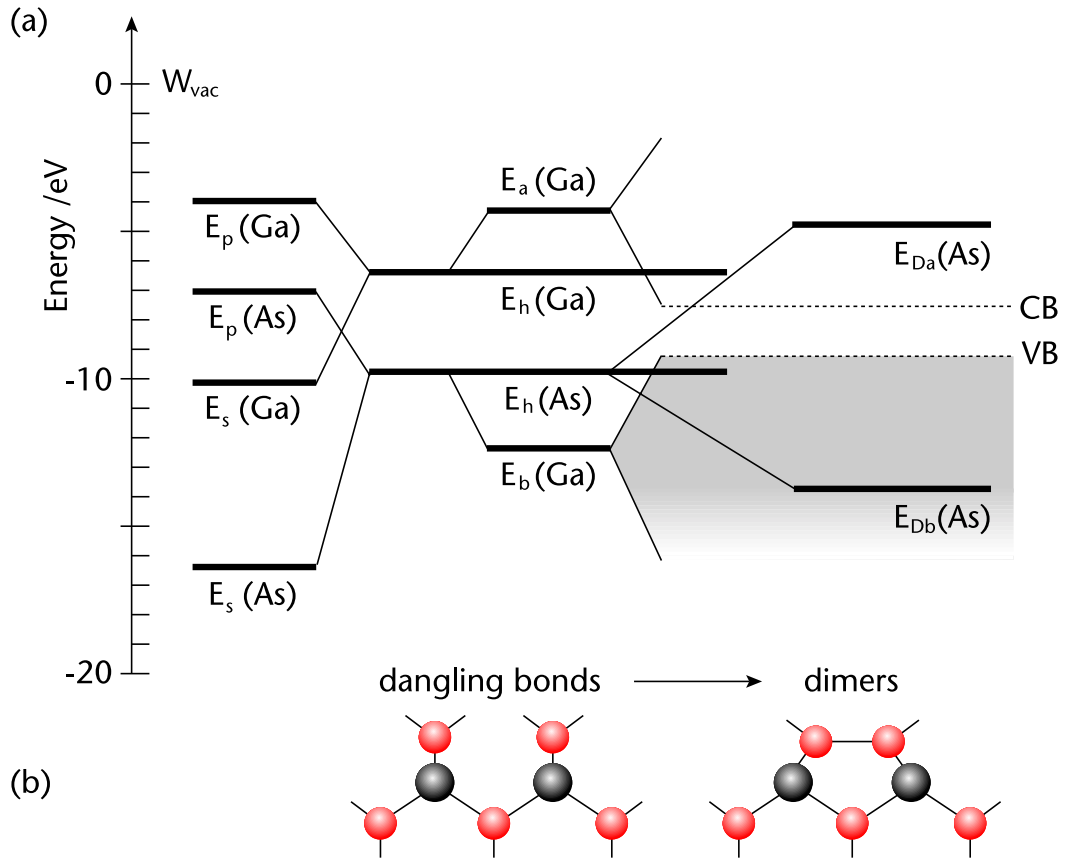


Figure 2.6: (a) A schematic of the energy levels of the GaAs(001)-As terminated surface. Beginning with  $s$  and  $p$  states for the Ga and As,  $sp^3$  hybrids form a bonding ( $E_b$ ) and antibonding ( $E_a$ ) combination which broaden into valence (VB) and conduction (CB) bands. At the (001) surface, two of the As hybrids are unbonded  $sp^3$  hybrid dangling bonds. Subsequent dimerization produces an As–As dimer bonding ( $E_{Db}$ ) and antibonding ( $E_{Da}$ ) combination, leaving one As dangling bond per atom at the hybrid energy  $E_h$ . Since this energy is below VB and the equivalent Ga dangling bond energy is above CB, charge transfer from Ga to As must (for autocompensation) occur to produce a filled lone-pair orbital [figure after Xue<sup>16</sup>]. (b) is a simple schematic of dimerization (viewpoint in surface plane).

As a working example of the ECM, consider a Group V (anion) terminated surface unit cell consisting of  $D$  dimers with every  $N$ -th dimer missing (i.e. a  $2 \times N$  reconstruction).<sup>16</sup> Start by counting the electrons required for the  $2 \times N$  reconstruction. Each anion dimer requires six electrons (two for dimer bonding and four for the two dangling bonds per atom), hence there must be  $6D$  electrons per surface unit. Next,  $8D$  electrons are needed to bond these  $D$  dimers to the second layer cations (two electrons for the four bonds from each dimer). The total number of electrons required would therefore be  $14D$ . Now count the electrons available for bonding. The top layer anions provide  $2V_n D$  electrons (where  $V_n$  is the number of valence electrons on the anion). The second layer cations have  $2V_p \times N/2 = V_p N$  electrons available ( $N/2$  since half the second layer electrons are already bonded to the third layer,  $V_p$  is the number of cation valence electrons). According

to the ECM, the numbers of available electrons and required electrons must be equal, i.e.

$$14D = 2V_nD + V_pN \quad 2.7$$

For the GaAs(001) surface (with energy levels as shown in figure 2.6 above),  $V_n = 5$ ,  $V_p = 3$ , and therefore  $4D = 3N$ . The smallest unit cell which satisfies this condition is the  $2 \times 4$  cell with three dimers ( $D = 3$ ) and every fourth dimer missing ( $N = 4$ ). If deeper layer atoms are involved in reconstruction, the calculation inevitably becomes more complex. Despite this, and a (very) few reported exceptions<sup>24</sup>, the ECM has proved a useful tool in the solution of semiconductor surface structures.

It is clear that there are many possible structural models for III–V compounds, and an evaluation of their validity is far from trivial, although the principles cited above are a significant aid. However, establishing a model's validity is only a partial solution of a surface structure. The quantitative determination and optimization of structural parameters, and evaluation of their precision are equally important, and are described in greater detail in the following chapters.

## 2.4 Growth techniques

Whilst it is not of direct relevance to the experimental work presented in this thesis, it is salient to briefly describe the growth process used to prepare the samples used in this study, as from the first principle quoted above, it affects the surface structure produced thereafter. There are two main types of growth technique relevant to the semiconductors used here: bulk crystal growth and epitaxy. Both are capable of producing highly pure single crystals, with impurity levels less than one part in  $10^{10}$ , as required both for accurate quantitative surface structural analysis and for reliable device fabrication. As this section can only provide a brief introduction, the reader is referred to appropriate texts.<sup>25,26,27,9</sup>

### 2.4.1 Bulk growth

The Czochralski method is one of the best proven techniques for the growth of large semiconductor crystals, commonly used for silicon growth. It is analogous to the classic experiment where a seed crystal of copper sulphate is placed in a supersaturated copper sulphate solution and allowed to cool. In Czochralski growth, a molten mass of raw material (the melt) is kept at a controlled temperature only slightly above the melting point. If the material has a tendency to evaporate or decompose (for example, evolving arsenic from GaAs), the melt must be kept under an inert gas pressure or liquid-encapsulated under a layer of appropriate molten glass. Into the melt is placed a small seed crystal onto which atoms from the melt attach themselves, whilst maintaining the crystallinity of that seed. The crystal is slowly rotated and pulled out of the melt to ensure uniformity of growth, resulting in a boule that may be several centimetres in diameter and tens of centimetres in length. Although boules are often cut normal to the direction of growth to give circular wafers, some are grown at odd orientations (e.g. InSb is grown along a  $\{211\}$  axis), and cut to the desired plane. This can cause problems of inhomogeneity in the doping profile across individual wafers. Bulk-grown crystals will typically require further refinement by local melting to diffuse impurities and defects towards one end of the crystal (so-called zone refining). Consider that close to the phase boundary, there is a distribution coefficient

$$k = \frac{C_{solid}}{C_{liquid}} \quad 2.8$$

where  $C_{solid}$  and  $C_{liquid}$  are the concentrations of impurity in the solid and liquid phases respectively. As  $k < 1$  (indeed typically 0.1), then by moving a crystal slowly through a furnace, a zone of it is melted, the position of this zone travelling along the crystal. At any point, the solid at the back of the zone will be  $k$  times as impure as the melted material—i.e. purer. After repeating this process  $n$  times, the impurity concentration at the first-melted end of the crystal will be

$$C_{solid} = k^n C_{original} \quad 2.9$$

By such a process, the impurity concentration can be reduced to a few parts in  $10^{10}$  in relatively few passes. This zone refining process is akin to the Bridgman method of crystal growth, commonly used for GaAs, where the melt is placed in a furnace with a shallow temperature gradient along its length. The furnace is then slowly cooled whilst maintaining the same temperature gradient, thus crystallizing the melt from one end. This crystal may be further zone-refined if desired.

### 2.4.2 Epitaxial growth

After cutting, grinding and electropolishing, it is possible to use sections from a bulk-grown boule as substrates for growing extremely pure, thin layers of semiconducting material layer-by-layer. These layers are called epilayers (from the Greek *epi-*, prefix for upon, with *taxis*, arrangement) giving the name epitaxial growth to the generic technique. Techniques such as molecular beam epitaxy (MBE) and metal-organic CVD (MOCVD) are used to produce the sharply-defined layers needed for band gap engineering applications. MBE is essentially crystallization by condensation or reaction of a molecular gas with a surface under UHV conditions. The molecular gases are produced by vaporization of the materials in their own locally-heated shuttered crucibles, known as Knudsen cells or *k-cells*. The rate of growth is dependent on factors including the molecular flux (itself dependent on the k-cell temperature), the time for which the shutter is open to allow the gas to exit, and the substrate temperature. By having k-cells containing both elements for a given III–V semiconductor, the molecular flux ratio can be controlled. This controls the stoichiometry and (along with the substrate annealing conditions) hence the reconstruction of the growth surface. The use of UHV ensures that the substrate remains free of contamination during growth, and secondly, that all growth occurs as a result of molecular (as opposed to viscous or diffusive) flow. Hence, molecules incident upon the substrate have not interacted with other molecules en route and those which do not ‘stick’ or *adsorb* on the surface are rapidly pumped away. The result is a growth technique capable of producing high purity materials and surfaces with extremely abrupt interfaces and controlled composition, and indeed multilayered structures with

negligible interlayer penetration, without the thermal energy and atomic diffusion inherent in bulk-growth techniques. A further advantage of UHV is that it allows real-time monitoring techniques such as reflection high energy electron diffraction (RHEED) and quadropole mass spectroscopy to be used *in-situ*. There are, however, two notable drawbacks to MBE. Firstly, samples must be kept in UHV if the purity of surface is to be maintained. Since this is not always practical, contamination can be avoided *ex-situ* by growing an amorphous film of group V material onto the surface before removal from vacuum. This protective *capping layer* can later be desorbed thermally or *decapped* in UHV to reveal the clean, well-ordered underlying surface.<sup>28,29,30</sup> A second drawback is that MBE is an expensive and relatively slow process.

MOCVD uses an organometallic vapour source at much higher pressures, where viscous flow is the primary mechanism for gas adsorption. Like vapour-phase epitaxy it is a chemical process, so is faster than MBE and can be performed on a relatively large substrate. However, since MOCVD is performed at near-atmospheric pressure, the accuracy of deposition is lower and UHV surface science techniques (other than optical techniques) cannot be used. Metal-organic molecular beam epitaxy (MOMBE) is designed to be a good compromise between the two. In all epitaxial growth techniques, the surface structures formed and even the mechanism of growth on the atomic scale can be highly sensitive to the existing surface structure, orientation and stoichiometry. Surface-sensitive techniques are therefore essential for their evaluation and analysis.

## 2.5 References

- <sup>1</sup> G. Binnig, H. Rohrer, Ch. Gerber, E. Weibel: *Phys. Rev. Lett.* **50** (1982) 120
- <sup>2</sup> G. Binnig, H. Rohrer: *Helv. Phys. Acta.* **55** (1982) 726
- <sup>3</sup> R. Wiesendanger: *Scanning Probe Microscopy and Spectroscopy: Methods and Applications* (Cambridge, 1994)
- <sup>4</sup> C. Kittel: *Introduction to Solid State Physics* (5th edn., Wiley, 1976)
- <sup>5</sup> W. Mönch: *Semiconductor surfaces and interfaces* (Springer, 1993)
- <sup>6</sup> J.M. Ziman: *Principles of the Theory of Solids* (2nd edn., Cambridge, 1972) *et loc. cit.*
- <sup>7</sup> S.M. Sze: *Physics of Semiconductor Devices* (Wiley, 1981)
- <sup>8</sup> S.M. Sze: *Semiconductor devices, physics and technology* (Bell, 1985)
- <sup>9</sup> L. Solymar and D. Walsh: *Electrical Properties of Materials* (6th edn., Oxford, 1998)
- <sup>10</sup> W.T. Wenckebach: *Essentials of Semiconductor Physics* (Wiley, 1999)
- <sup>11</sup> M.E. Levinshtein and S.L. Rumyantsev, Y.A. Goldberg, A.Y. Vul' and

- M.P. Mikhailova in: *Handbook Series on Semiconductor Parameters*, eds. M.E. Levinshtein S. Rumyantsev and M. Shur (World Scientific, 1996)
- <sup>12</sup> E.A. Wood: *J. Appl. Phys.* **35** (1964) 1306
- <sup>13</sup> D.J. Chadi, in: *The structures of surfaces III, Springer Series in Surface Sciences 24*, eds. S.Y. Tong, M.A. van Hove, K. Takayanaga, S.D. Xie (Springer, Berlin, 1991) 532
- <sup>14</sup> C.B. Duke: *Chem. Rev.* **96** (1996) 1237
- <sup>15</sup> J.P. LaFemina: *Surf. Sci. Rep.* **16** (1992) 133
- <sup>16</sup> Q. Xue, T. Hashizume, T. Sakurai: *Progress in Surf. Sci.* **56** (1997) 1
- <sup>17</sup> C.B. Duke, in: *Physical Structure, Handbook of Surface Science 1*, ed. W.N. Unertl (Elsevier, North Holland, 1996) 229
- <sup>18</sup> M.D. Pashley: *Phys. Rev.* **B40** (1990) 10481
- <sup>19</sup> D.J. Chadi: *J. Vac. Sci. Technol.* **A5** (1987) 834
- <sup>20</sup> H.H. Farrell, J.P. Harbison, L.D. Peterson: *J. Vac. Sci. Technol.* **B5** (1987) 1482
- <sup>21</sup> M. Lannoo: *Mater. Sci. Eng.* **B22** (1993) 1
- <sup>22</sup> J.-M. Jin, L.J. Lewis: *Surf. Sci.* **325** (1995) 251
- <sup>23</sup> C.F. McConville, T.S. Jones, F.M. Leibsle, S.M. Driver, T.C.Q. Noakes, M.O. Schweitzer, N.V. Richardson: *Phys. Rev.* **B50** (1994) 14965
- <sup>24</sup> L.J. Whitman, P.M. Thibado, S.C. Erwin, B.R. Bennett, B.V. Shanabrook: *Phys. Rev. Lett.* **79** (1997) 693
- <sup>25</sup> W.D. Lawson, S. Nielsen: *Preparation of Single Crystals* (Butterworth, 1958)
- <sup>26</sup> E.H.C. Parker (ed): *The Technology and Physics of Molecular Beam Epitaxy* (Plenum, 1985) *et loc. cit.*
- <sup>27</sup> J.Y. Tsao: *Materials Fundamentals of Molecular Beam Epitaxy* (Academic, 1993) *et loc. cit.*
- <sup>28</sup> Z.J. Gray-Grychowski, R.G. Egdell, B.A. Joyce, R.A. Stradling and K. Woodbridge: *Surf. Sci.* **186** (1987) 482
- <sup>29</sup> S.A. Clark, C.J. Dunscombe, D.A. Woolf, S.P. Wilks and R.H. Williams: *J. Vac. Sci. Technol. B* **12** (1994) 551
- <sup>30</sup> S.A. Clark, J.W. Cairns, S.P. Wilks, R.H. Williams, A.D. Johnson and C.R. Whitehouse: *Surf. Sci.* **336** (1995) 193

## 3 • Experimental techniques

### 3.1 Introduction

In this chapter, the interactions between ions and surfaces are discussed, as they underpin all the surface science techniques used in this work. The mechanisms for charge exchange are considered, as are the sources of energy loss. Sample preparation is discussed, in particular the techniques of argon ion-bombardment and annealing (IBA) and atomic hydrogen cleaning (AHC). Finally, the theoretical basis for the analytical techniques of LEED, AES and ISS are considered.

### 3.2 Ion-surface interactions

Amongst all the surface cleaning and analysis techniques used in this study, the majority rely on an understanding of the interaction between ions and surfaces. There are a variety of possible results of such interactions, and the likelihood of each is dependent on many different factors. The most important of these are the energies, masses and angles of incidence of the incident ions and the masses and crystal structure of the substrate atoms. To illustrate the importance of ion energy, consider the profile of a generalized sticking probability  $P$  as shown in figure 3.1.

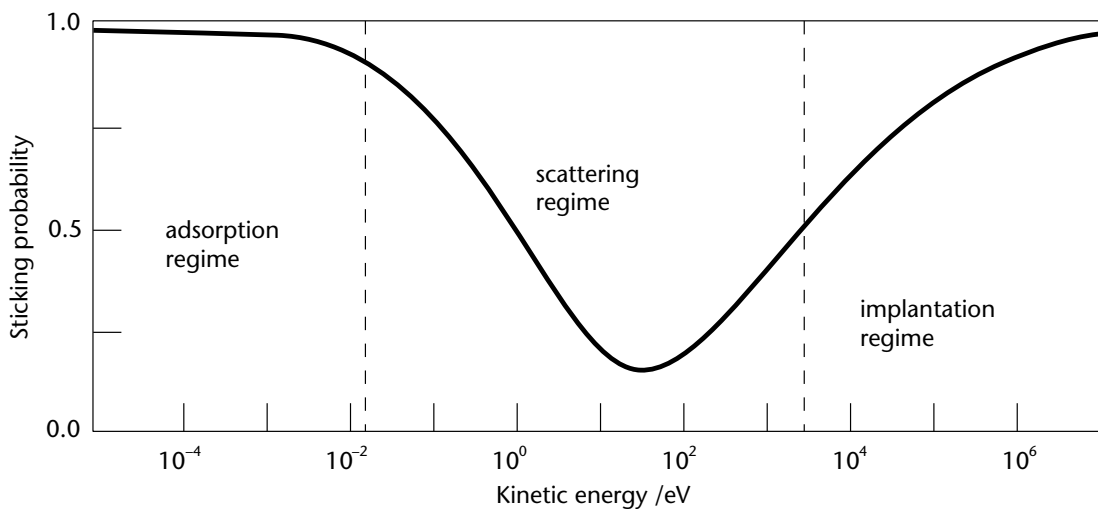


Figure 3.1: A generalized plot of the relation between particle-sticking probability and incident ion energy [after Rabelais and Marton<sup>1</sup>].

$P$  is defined as the ratio of the number of atoms that are deposited or stick to the surface to the number of incident ions. For very low ion energies (below  $\sim 500$  eV) condensation and chemisorption are the primary interactions, and sticking is common. Above this energy, scattering and sputtering processes predominate, with implantation increasing with energy.<sup>1</sup> It is these latter regimes that are of interest for the ion-scattering spectroscopies and cleaning techniques used in this study.

### 3.2.1 Charge-exchange mechanisms

Since ions are rarely in charge equilibrium with the surface, the first interaction of an incident ion approaching a surface normally involves charge-exchange and neutralization. There are several mechanisms for charge exchange, including resonant ionization, resonant neutralization, Auger neutralization, Auger de-excitation, quasi-resonant neutralization (also known as non-adiabatic tunnelling) and radiative neutralization. Some of these are shown schematically in figure 3.2.

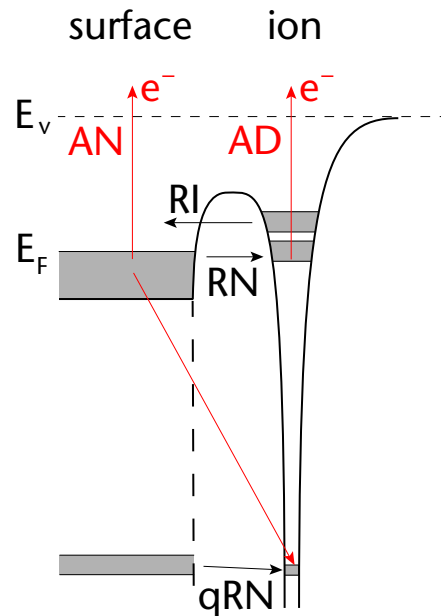


Figure 3.2: A schematic diagram of some charge exchange processes between a solid surface and the potential well of an ion.  $E_F$  is the Fermi energy of the surface, the vacuum energy is  $E_v$ . Excited states of the ion are shown as shaded areas. Resonant charge exchange processes are shown in black: resonant neutralization (RN), resonant ionization (RI) and quasi-resonant neutralization (qRN); whilst in red are Auger neutralization (AN) and Auger de-excitation (AD).

In resonant neutralization, the hole state of the ion forms a broadened energy level straddling the Fermi level, which allows an electron in the surface to tunnel to and thus neutralize the ion, without energy loss. It is similarly possible to (re-)ionize the incident species if an electron from a state just above the Fermi level tunnels (back) to the surface (resonant ionization). Quasi-resonant neutralization is an equivalent process to resonant neutralization, whereby an electron from an occupied core-level state of the surface tunnels to fill a deep hole state of the ion. This is normally followed by an appropriate energy relaxation within the surface.

If the surface does not have an occupied conduction band state close to the ion hole state, a conduction band electron may tunnel into the potential well of the ion, and then fall to a deeper hole state. In doing this, it donates its excess energy to another surface conduction band electron which is ejected from the surface (Auger neutralization). This electron is known as an *Auger electron*, and has a characteristic energy which is used in analytical techniques such as ion neutralization spectroscopy (INS) and Auger electron spectroscopy (AES). A related charge-exchange process is Auger de-excitation, which takes place not in ions but in excited neutral atoms. As in Auger neutralization, a conduction band electron from the surface fills a deep hole state in the incident particle. The excess energy results in the emission of an Auger electron from the excited state of the atom.

All of these charge-exchange processes are fast ( $\tau \sim 10^{-14}$  s) compared to the duration of the interaction as a whole and are relatively independent of incident ion energy. As a result, an ion may be neutralized and then re-ionized (indeed more than once) during both incoming and outgoing trajectories. The processes are competitive, and have varying probabilities. For example, resonant neutralization and resonant ionization are dominant for alkali metal ions, whilst Auger neutralization dominates for noble gas ions. Quasi-resonant neutralization is rarer and leads to interesting results, as its probability oscillates with time as a function of the scattered particle velocity, whilst the ion is in the vicinity of the surface.<sup>2</sup> The excited atom produced by resonant neutralization of an ion may be de-excited by either Auger de-excitation or a combination of resonant ionization followed by

Auger neutralization. It is usually assumed that the neutralization rate has an exponential dependence<sup>3</sup> on the separation of the ion and the surface  $s$  so that the rate is of the form

$$R_n = A \exp(-as) \quad 3.1$$

The probability of neutralization in a time interval  $dt$  is therefore  $Rdt = (R/v_{\perp}) ds$  where  $v_{\perp}$  is the component of the ion velocity normal to the surface. Integrating along a trajectory from an infinite distance to a minimum spacing  $s_{min}$  leads to an escape probability

$$P_{ion} = \exp \left[ \int_{s_{min}}^{\infty} \left( \frac{A}{v_{\perp}} \right) \exp(-as) ds \right] \quad 3.2$$

For energetic ions (>500 eV), it is usual to approximate  $s_{min}$  to zero, so that

$$\begin{aligned} P_{ion} &= \exp(-A/av_{\perp}) \\ &= \exp(-v_0/v_{\perp}) \end{aligned} \quad 3.3$$

where  $v_0$  is a characteristic velocity dependent on both the ion and surface species. It is clear from this that any process which increases the interaction period will greatly increase the probability of neutralization. This has ramifications for the surface specificity of ISS techniques which are discussed in §3.4.3.

### 3.2.2 Collision and inelastic energy loss

In the collision phase, the regime where the electron orbitals of the two particles overlap, several processes are possible. For low energy collisions, as described earlier, reaction may lead to adsorption on the surface. At higher energies, scattering or implantation are more likely. The probability of implantation increases with smaller ions, higher energies and incidence angles closer to crystallographic axes, as these conditions enable the ions to penetrate deeper into the crystal where inelastic energy loss is more likely. This loss mainly occurs through two mechanisms: electronic and nuclear stopping. Electronic stopping originates from the Coulombic interaction between the ion and substrate electrons, which can cause neutralization and excitation of the ion (as already described for ion approach).

The system is subsequently de-excited, usually by emission of photons or electrons resulting in inelastic energy loss. During nuclear stopping, the incident ion elastically transfers momentum and energy to the substrate atoms. This can be modelled by a simple binary collision model with the nuclei interacting as screened repulsive Coulombic potentials. The resulting recoil of the substrate atoms is the cause of sputtering, the process of ejection of surface atoms used for the analytical techniques of secondary ion mass spectrometry (SIMS) and direct recoil spectroscopy (DRS)<sup>4</sup> as well as in IBA cleaning, described further in §3.3.1. Those ions which are not implanted in the substrate, but are instead scattered and escape the surface, are used in ion-scattering spectroscopy (ISS) for analysis of the substrate, as described in §3.4.3.

### 3.3 Sample preparation techniques

*In-vacuo* cleaning of surfaces is required to produce a well-ordered surface with a low level of contamination before investigation. There are several common methods used for *in-situ* cleaning, including crystal cleavage, annealing, ion bombardment and chemical reaction.

For zincblende structure III–V semiconductors, cleavage along  $\{110\}$  crystallographic planes is a useful technique for sample preparation. However, there are limitations to the number of times a sample can be cleaved, and reproducibility (for example, of step density) from cleave to cleave can vary greatly. There can be difficulties in cleaving and manipulating samples *in-vacuo*, and it is not possible to cleave polar  $\{111\}$  and  $\{100\}$  surfaces. Chemical etch methods are not ideal, as one element of most binary compounds (including III–V semiconductors) will tend to be preferentially etched. Heating to desorb adsorbed gas molecules from a surface can be useful, but many contaminants are bound too strongly to the surface to desorb at temperatures below the melting point of the substrate material. For III–V compound semiconductors there is the additional problem of *non-congruent sublimation*. Both group III and group V elements sublime and are adsorbed as a result of thermal excitation. There is a congruent sublimation temperature  $T_{cs}$  below which the equilibrium partial pressure of the group III element, and hence the sublimation

rate, should be higher than that for the group V element (shown in table 3.1 for the compounds used in this work).<sup>5</sup> Hence, it is to be expected that at elevated temperatures below  $T_{cs}$  there will be a surfeit of the group V species. However, the group V element tends to form molecular dimers ( $V_2$ ) which are less thermodynamically stable than the usual molecular species ( $V_4$ ). Therefore, dimers recombine to form tetramers with higher partial pressures and they themselves sublime. The result is congruent sublimation. Above  $T_{cs}$  the desorption rate of group V atoms is higher, producing a net surface excess of group III atoms. Even if the temperatures required to desorb contaminants are below the melting point for the compound, they may result in non-congruent sublimation, altering if not effectively destroying the surface of interest.

Compound	GaAs	GaP	GaSb	InAs
$(T_{cs} \pm 5)$	868 K	853 K	728 K	660 K

Table 3.1: Congruent sublimation temperatures ( $T_{cs}$ ) for GaAs and III-V semiconductors used in this study [data from Wood<sup>5</sup>].

### 3.3.1 Argon ion-bombardment and annealing (IBA)

In the ion bombardment phase of IBA, 0.5–5 keV  $Ar^+$  ions are incident on the sample surface. Such ions have a large screened Coulombic interaction cross-section with the surface atomic nuclei. These nuclear stopping collisions can be modelled as classical binary collisions<sup>6</sup>, causing a cascade through neighbouring atoms. If the cascade is sufficiently small, the collisions can be modelled as separate binary events, and the energy transfer described by a linear Boltzmann transport equation.<sup>7</sup> For a critically high energy cascade, this collision linearity is replaced by the recoil of a local volume of atoms, known as a spike<sup>8</sup>, which results in a high density of defects and a major rearrangement of the crystal structure to accommodate it (such as amorphization). If the collision cascade intersects with the surface, top layer (surface and adsorbate) atoms are ejected in a process called *sputtering*.

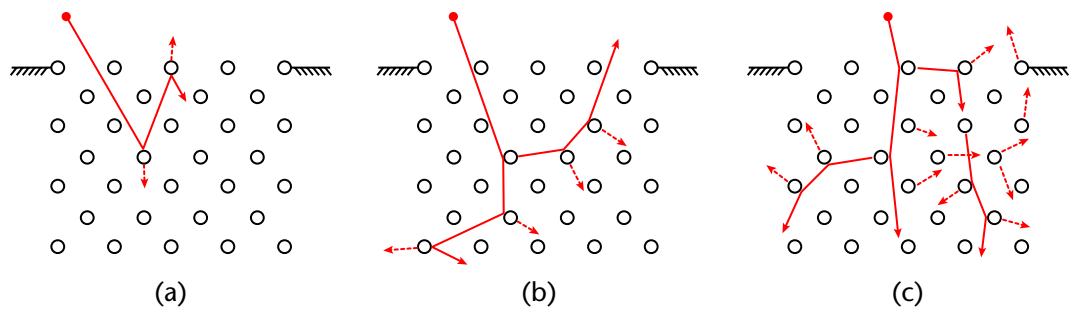


Figure 3.3: Three regimes of sputtering induced by elastic collisions. (a) Single knock-on: Recoil atoms receive sufficient energy to be sputtered, but not enough to induce collision cascades. (b) Linear cascade: Sufficient energy is gained by the recoil atoms for a linear collision cascade to occur. The density of recoil atoms is low enough for binary collisions to dominate, and collisions between moving atoms are infrequent. (c) Spike: The density of recoil atoms is so high that the majority of atoms within a local volume (the spike volume) are in motion [after Malherbe<sup>9</sup>].

The sputtering process itself causes significant damage to both surface and sub-surface, and hence ion bombardment is normally followed by annealing. During annealing, defects such as dislocations tend to migrate to the surface where they combine and/or dissipate, thus tending to restore the physical order of the sample. Unfortunately, the annealing process also leads to some preferential surface segregation of bulk impurities and implanted incident atoms, which must be removed by further cycles of bombardment and annealing. Generally, several cycles of IBA are required to prepare a relatively pure sub-surface region and a damage-free surface.

The erosion due to sputtering is often quantified by the sputter yield, a measure of the number of target atoms removed per incident ion. The sputter yield is affected by a number of factors including the temperature, ion flux and in particular, the incident ion energy and incidence angle. Sputter yield measurements have been performed by many different groups, for a number of III–V compounds (although the greatest concentration have been on GaAs surfaces).<sup>9</sup> Some trends are shown in figure 3.4. Although it is clear that there is significant experimental variation, the sputter yield within an experiment is essentially constant for incidence angles of 0–50° to the GaAs(001) surface normal. As the angle becomes more grazing, the yield falls rapidly as the ions *skim* the surface, scattering from multiple surface atoms with little energy transfer to the near-surface.<sup>10</sup> The effect of ion energy is, as can be expected, of decreasing damage with lower energies.

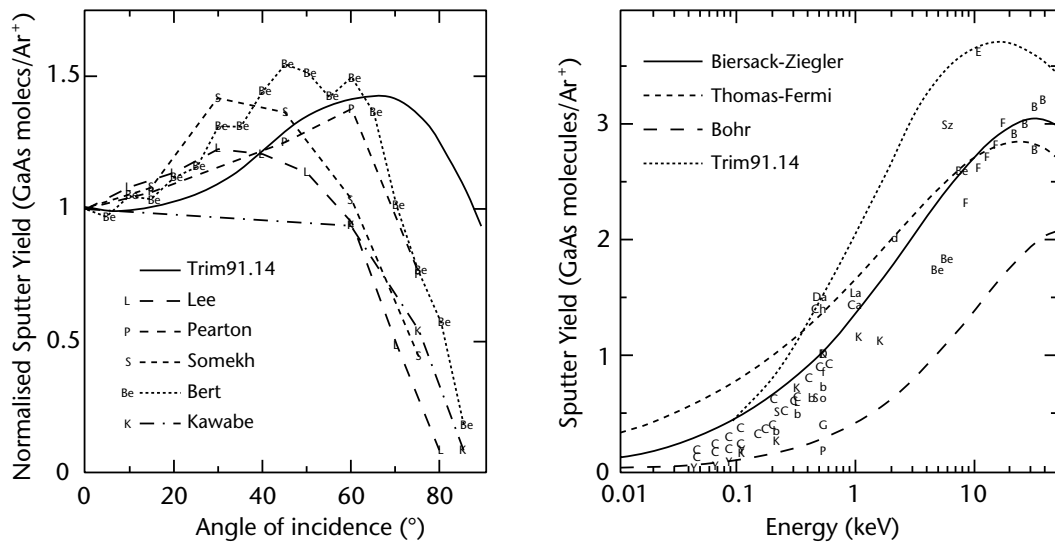


Figure 3.4: Sputter yields for GaAs(001) as a function of (a) incidence angle relative to surface normal and (b) ion energy [both compiled by Malherbe<sup>9</sup>]. The different letters indicate data points from different experimental reports. In (a), the solid curve represents the theoretical results obtained using TRIM<sup>6</sup> whilst in (b), curves represent theoretical results obtained using a number of different stopping power calculations.

Although the effects of sputtering can be reduced by cyclic IBA, there remain other effects which must be considered. Preferential sputtering may occur during ion bombardment (the species depending on factors including mass and nuclear stopping cross-section), and the anneal cycle of IBA may result in non-congruent sublimation of group V species from the surface, as described for thermal cleaning above. Both bombardment and annealing will alter the surface stoichiometry. Amorphization occurs when most atoms in a region are displaced from their lattice sites, destroying the crystalline order of the surface. For the energy regime used in IBA cleaning, a shallow amorphous layer is produced, confined to the top few nanometres of the surface and easily repaired by annealing. However, point defect diffusion and implantation of incident ions in the bulk both result in a residual damaged layer at much greater depth for all but the lowest of energies (<100 eV), which remains detectable even after annealing. Also, the surface topography after IBA may exhibit unusual features on the sub-micron scale such as rippling, droplets and columnar features known as cones, formed during recrystallization of the amorphous surface region. Finally, electronic (radiation) damage occurs, where point defects induced by IBA become electrically active, acting as donors or acceptors. This can significantly alter the electronic properties of the material, with obvious implications for device fabrication.

### 3.3.2 Atomic hydrogen cleaning (AHC)

A relatively novel technique uses atomic hydrogen ( $H^*$ ) for cleaning. It has been demonstrated that irradiation with hydrogen radicals in a plasma produced by electron cyclotron resonance (ECR) mediates the desorption of oxides and hydrocarbons, two of the most persistent semiconductor surface contaminants. In particular they have been shown to permit desorption at a lower temperature than by heating *in vacuo* alone.<sup>11,12,13,14,15,16</sup> However, ECR sources are expensive, physically incompatible with typical MBE equipment and most critically, produce ionized and energetic particles which are as liable to cause sputter damage to the substrate as traditional techniques. Hence, another technique was developed, using atomic hydrogen generated by thermal dissociation of room-temperature molecular hydrogen by a hot tungsten filament. This results in a flux of non-energetic  $H_2$  and  $H^*$  incident on the sample, which has been shown to be effective in cleaning a range of semiconductors, including GaAs<sup>17</sup>, InP<sup>18</sup>, GaSb<sup>19</sup>, InAs and InSb<sup>20</sup>.

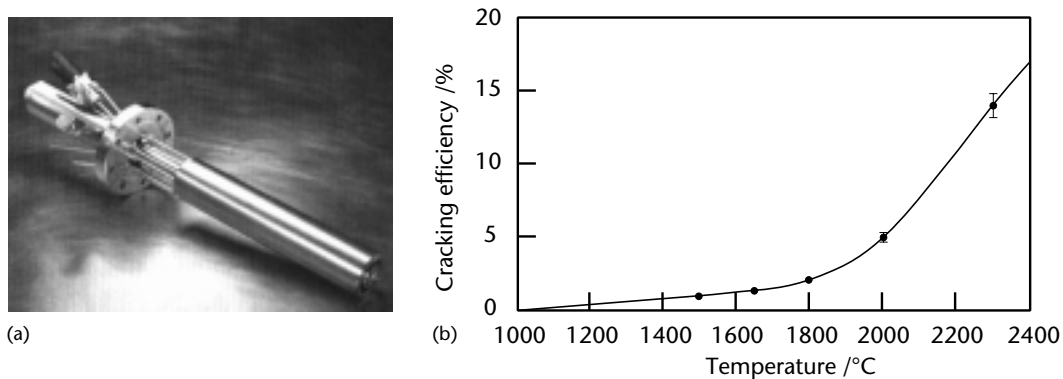
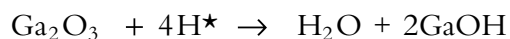
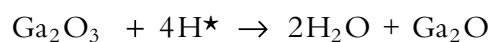
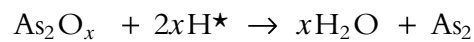


Figure 3.5: (a) The EPI atomic hydrogen source, and (b) its measured cracking efficiency<sup>21</sup>

The cracking efficiency of the source is less than an ECR plasma source<sup>21</sup>, being typically 6–7% at a typical operating filament temperature of  $\sim 2100$  K, but the negligible kinetic energy of the beam means that the source can be used for relatively long periods without causing sputtering damage to the sample. The only caveat is that care must be taken to avoid localized heating of the sample by the hot filament.

Since the work in this study began, a novel atomic hydrogen source has been reported using electron-stimulated desorption (ESD).<sup>22</sup> In this design, H<sub>2</sub> adsorbs dissociatively onto and then permeates through a thin metal alloy membrane into the UHV chamber at room temperature. There it is struck by a 1500 eV electron beam, producing a flux of neutral H<sup>•</sup> with energy ~ 1 eV. This design has a higher cracking efficiency than a thermal source, and is cold, reducing local temperature variation within the chamber. Future studies might benefit from consideration of such an ESD source design.

The physical mechanism for AHC is still uncertain, but is believed to be the same for all these source designs. Consider the air-exposed GaAs surface, which consists of a layered native oxide structure, with a mixture of Ga and As oxides outermost, Ga<sub>2</sub>O<sub>3</sub> near the interface and elemental As immediately below the native oxide and above the bulk GaAs.<sup>23</sup> The native oxide layer contains significant carbon, predominantly in the form of hydrocarbons. IBA appears to result in the conversion of these hydrocarbons into strongly bonded Ga carbides. These carbides are persistent even after high-temperature annealing and induce a depletion layer at the substrate-epilayer interface after MBE, with inevitable implications for device fabrication.<sup>24</sup> By comparison, the mechanism for atomic hydrogen cleaning (AHC) of GaAs appears to be a two-stage process; the chemically active hydrogen radicals are readily adsorbed onto the surface, reacting with oxides and carbon to form water and methane. These are then thermally desorbed on annealing at a relatively low temperature, resulting in efficient cleaning of the surface.<sup>25</sup>



It has been shown that the use of atomic hydrogen can also enable the desorption of the persistent carbides introduced by IBA, although at a slower removal rate.<sup>22</sup> The use of gentle annealing also increases the desorption rate of any hydrogen atoms which remain adsorbed on the clean surface.

### 3.4 Analysis techniques

Two fundamental areas of interest in the study of surfaces are their elemental composition and atomic structure. There are several techniques which may be used to examine these tasks. Techniques such as Auger electron spectroscopy (AES) can be used to determine elemental composition by analysis of electronic transitions. Low energy electron diffraction (LEED) uses reciprocal space imaging to analyse surface symmetry, whilst ion-scattering techniques image the surface structure in real space. All of these techniques have been used, and are discussed below. Further background information can be found elsewhere.<sup>26</sup>

#### 3.4.1 Low energy electron diffraction (LEED)

LEED is a technique based on the wave-like behaviour of electrons.<sup>27,28</sup> For simplicity, consider an electron as a plane wave described by an incident wavevector  $\mathbf{k}$  in terms of a unit vector  $\mathbf{s}$

$$\mathbf{k} = (m/\lambda)\mathbf{s} \quad 3.4$$

where  $m = 2\pi$  (defined earlier in §2.2). Since the wavelength of the electron  $\lambda$  (in Å) is related to its kinetic energy  $E$

$$\lambda = \sqrt{150.4/E} \quad 3.5$$

then above a certain energy the wavelength is short enough that the electron may be diffracted by a three-dimensional periodic array of scatterers, such as a bulk crystalline solid. For elastic scattering of electrons, energy and momentum are conserved. Hence, the wavevector  $\mathbf{k}'$  of the diffracted electrons must meet the following conditions

$$k^2 = k'^2 \quad 3.6$$

$$\mathbf{k}' - \mathbf{k} = \Delta\mathbf{k} = \mathbf{g} \quad 3.7$$

where  $\mathbf{g}$  is any reciprocal lattice vector (as defined in equation 2.3). This is essentially an expression of Bragg's law of diffraction,  $2d \sin \theta = n\lambda$ , where  $d$  is the spacing between adjacent lattice planes ( $hkl$ ).<sup>29</sup> Thus, measurement of the diffraction of an electron beam

can lead to deduction of the reciprocal lattice and hence by inversion of equation 2.3, to the real lattice. Equation 3.7 can be expressed alternatively to give the Laue equations by taking scalar products with  $\mathbf{a}$ ,  $\mathbf{b}$ ,  $\mathbf{c}$

$$\mathbf{a} \cdot \Delta\mathbf{k} = mh, \quad \mathbf{b} \cdot \Delta\mathbf{k} = mk, \quad \mathbf{c} \cdot \Delta\mathbf{k} = ml \quad 3.8$$

These equations can be readily interpreted geometrically such that  $\Delta\mathbf{k}$  must lie on a certain cone about the direction of  $\mathbf{a}$ , on a cone about  $\mathbf{b}$  and on a cone about  $\mathbf{c}$ . There can only be a single energy  $E$  and direction of  $\mathbf{k}$  that intercepts all three cones and satisfies all three equations.

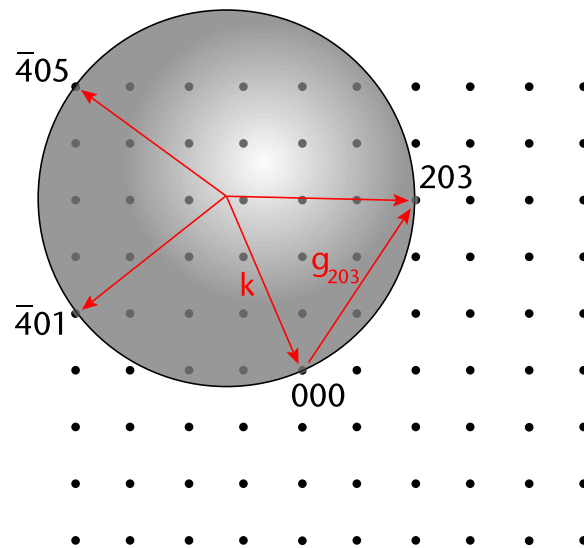


Figure 3.6: The Ewald construction for bulk diffraction. The incident wavevector  $\mathbf{k}$  is drawn in the direction of the incident beam (which in this case lies in the plane of the page), and three diffracted wavevectors  $\mathbf{k}'$  in the  $(h0l)$  plane are shown. The  $\mathbf{g}_{203}$  reciprocal lattice vector is also marked. Other points may intersect the sphere in other planes parallel to the page.

The Ewald construction enables a convenient graphical representation of this solution. A 3D reciprocal lattice is drawn with the incident wavevector  $\mathbf{k}$  terminating at an arbitrary lattice point. A sphere is drawn with radius  $k$  about the origin of  $\mathbf{k}$ . Since the scattered wavevector  $\mathbf{k}'$  has the same magnitude as  $\mathbf{k}$  (after equation 3.6), a diffracted beam will only be formed where this sphere intersects other points on the reciprocal lattice.

In the case of surface diffraction as in LEED, the system is only periodic in 2D (parallel to the surface), such that only the wavevector component parallel to the surface  $\mathbf{k}_{\parallel}$  is conserved by the addition of a reciprocal net vector  $\mathbf{g}$ . The Ewald construction may be

easily adapted to represent this situation. Whilst it remains a 3D construction (since the incident and diffracted beams lie in three dimensions), there is a relaxation of the conditions for diffraction, such that the reciprocal lattice points are replaced by reciprocal lattice ‘rods’ perpendicular to the surface and passing through the reciprocal lattice points.

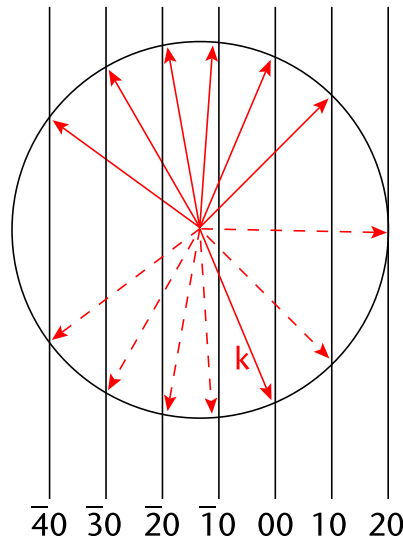


Figure 3.7: The Ewald construction for surface diffraction. The incident wavevector  $k$  is labelled. There are clearly many more possible diffraction conditions than for the bulk, due to the reduced symmetry. The wavevectors marked by dashed lines indicate those beams which propagate into the crystal and are therefore not observed.

In a typical LEED experiment, a beam of electrons is accelerated through around 100 eV and impinges on the sample surface normal. The elastic mean-free-path of the electrons  $\Lambda_{in}$  is given by

$$I = I_0 \exp\left(-x/\Lambda_{in}\right) \quad 3.9$$

where  $x$  is the distance travelled into the sample. A schematic plot of  $\Lambda_{in}(E)$  is shown in figure 3.8. For most materials, this has a minimum of about 20 Å near 100 eV.<sup>30</sup> Clearly, the beam will be severely attenuated after travelling through only a few surface layers.

These inelastically scattered electrons are filtered by a retarding electrostatic grid, and the remaining elastically back-diffracted electrons accelerated to strike a phosphorescent screen forming a visible diffraction pattern which is therefore due only to contributions from the top few surface layers.

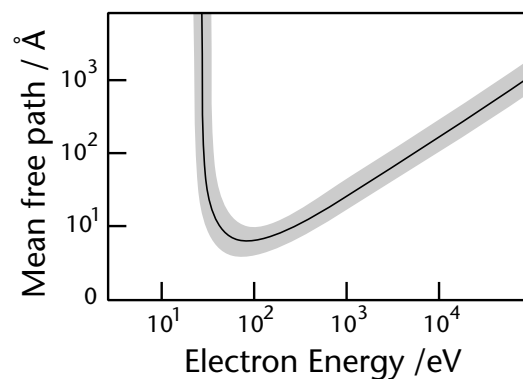


Figure 3.8: The electron mean-free-path for a range of incident electron energies. Most materials have  $a\lambda_m$  which lies in the shaded area [after Quinn<sup>30</sup>].

LEED is used to determine the structure and periodicity of surfaces, with the sharpness and regularity of the LEED pattern as a monitor of the crystalline quality of the surface. The geometric form of the pattern, being the intersection of the reciprocal lattice rods with the screen, shows a portion of the 2D surface reciprocal space structure. Features in the pattern corresponding to the ideal unreconstructed surface are known as integer order spots, as they would arise from a  $(1 \times 1)$  surface mesh. Features at smaller spacings (in reciprocal space) are termed fractional order spots, and are due to larger real space periodicities. Analysis of the diffraction pattern therefore enables elucidation of the surface symmetry and perhaps thence of the arrangement of atoms within the surface unit cell. To analyse the LEED pattern of a reconstructed surface, the first step is to identify the possibility of rotated domains—where both  $(m \times n)$  and  $(n \times m)$  overlayers co-exist on different regions of the surface. The actual LEED pattern is the incoherent sum of the individual LEED patterns from the different domains. Once this is done, possible surface reciprocal lattice vectors  $\mathbf{a}^*$ ,  $\mathbf{b}^*$  are identified and thus the surface symmetry can be related to the unreconstructed bulk surface. This task becomes increasingly complex with higher order periodicities.

Quantitative LEED uses analysis of the variation in diffracted spot intensity (and thus of the profiles of the reciprocal lattice rods) with beam energy to gain information about the surface structure. This is far from trivial since accurate prediction of intensities requires a full quantum mechanical treatment of the dynamic multiple scattering process which

actually occurs in LEED. Generally, *ab initio* structural solution is not possible, and an iterative approach is required, starting from an assumed structure based on a kinematic approximation, which is modelled, compared to experimental data and refined. The process becomes extremely complicated for large unit cells, such that surface cells containing more than a ten atom motif are rarely soluble. The results are not always unambiguous, and a careful approach to evaluating the reliability of a given model fit is necessary. The calculation of trustworthy *R*-factors is crucial, and various forms have been proposed for the fitting of LEED I-V profiles. *R*-factor determination is equally important in the evaluation of surface structures calculated using MEIS, and is therefore discussed more fully in the following chapter. There is a great body of knowledge of LEED which it is not appropriate to discuss further in this thesis. Readers are therefore referred to other texts instead for further information.<sup>31</sup>

### 3.4.2 Auger electron spectroscopy (AES)

The technique of Auger electron spectroscopy allows qualitative and quantitative chemical analysis of surface layers, using a three electron process, analogous to that described in §3.2.1. The sample is bombarded with 3–30 keV primary electrons, which results in core level electrons  $E_1$  being emitted as secondaries, ionising the sample. Electrons from more external levels  $E_2$  fall to fill the hole thus created, giving the energy  $(E_1 - E_2)$ . This excess energy is passed to a third electron from energy level  $E_3$  which is ejected, doubly-ionising the atom. The *Auger electron* has kinetic energy  $E \approx E_1 - E_2 - E_3$  which is both independent of the incident beam energy and characteristic of the electron energy levels and therefore of the chemical composition of the sample surface. This kinetic energy may also undergo chemical shifts of a few eV due to differences in the local electronic environment, such as variations in the hole-hole interaction energy, giving useful chemical state information. The low energy of the emitted Auger electrons ensures a low mean-free-path ( $\lambda = 0.5\text{--}3$  nm) and thus good surface specificity (within  $3\lambda$  of the surface). As with LEED, the detailed theory of AES is unnecessary for the comprehension of this thesis. For more information, the reader is directed elsewhere.<sup>26</sup>

In practice, calculations of binding energies are rarely performed today. Instead reference is made to collections of ‘fingerprint’ AE spectra, collated from all elements for the purpose of species identification.<sup>32</sup> Generally, the derivative of the integral spectrum is used as the peaks are often more pronounced and the background of secondary inelastically-scattered electrons is reduced.<sup>33</sup> Additionally, the types of experimental apparatus used for AES lend themselves to derivative-mode data-collection. By accounting for variations in elemental sensitivity (due to varying interaction cross-section) it is possible to determine quantitative compositional information for the sample by measurement of the relative intensities of the spectral peaks. The surface-fraction of a given element can be estimated as

$$P_Z = \frac{I_Z}{S_Z} \left| \sum_j \frac{I_j}{S_j} \right. \quad 3.10$$

where  $I_j$  is the peak-to-trough height of the derivative intensity and  $S_j$  is the elemental sensitivity factor for element  $j$ . Inevitably, the accuracy of this calculation depends on the accuracy of the sensitivity factor and its consistency when comparing standard elemental samples with the element *in-situ* experimentally. Such considerations must be taken into account when look-up tables of sensitivity factors are produced. An assumption must also be made about the homogeneity of the near-surface region. For example, an overlayer of one species will inevitably attenuate the signal of any underlying species.

### 3.4.3 Ion scattering spectroscopy (ISS)

#### 3.4.3.1 Introduction

Ion scattering spectroscopy (ISS) is a term covering a varied set of techniques which provide information about elemental composition and surface structure.<sup>34</sup> However, the interpretation of ISS data is often easier than for other techniques due to its conceptual simplicity. ISS uses ions of known energy and species incident on a solid surface in a vacuum, and some form of ion or neutral detector to measure the flux of elastically scattered ions at a fixed scattering angle  $\theta$ . At low energies (in the range of around 100 eV to 10 keV), the penetration depth of the incident ions and the mean-free-path for inelastic

collisions are small, whilst the neutralization rate is high, resulting in good surface specificity, as very few multiply-scattered ions are detected. This explains the use of low energy ion scattering (LEIS) as a fundamental technique for surface analysis. At higher incident energies (10–200 keV), in the medium energy ion scattering (MEIS) regime, surface specificity is obtained by aligning the incident beam along low-index crystallographic directions such that deeper atoms are shadowed by the repulsive interaction potential of the atoms nearest the surface.

#### 3.4.3.2 Interaction potentials

Since the interaction time of a scattering event is small when compared to the period of phonon vibration in a solid, it is generally adequate to use a single elastic binary-collision model to describe the collision between an ion and a surface. This allows the interaction to be considered as a classically conservative transfer of energy and momentum between two hard spheres, as between billiard balls. However, to understand how ISS can be used in surface structure analysis, it is necessary to consider the interacting forces between the incident ion and the target atom. When a primary ion of nuclear charge  $Z_1e$  approaches a surface atom  $Z_2e$ , it will experience a repulsive force due to a Coulombic interaction potential. However, in the low–medium energy regime ( $< \text{MeV}$ ), the ion will also experience electronic screening, and hence the interaction potential will decrease faster than  $1/r$ . Most common interaction potentials therefore use a Coulombic term in  $1/r$  multiplied by a screening function  $\xi(r/a)$

$$V(r) = \frac{Z_1 Z_2 e^2}{4\pi\epsilon_0 r} \cdot \xi\left(\frac{r}{a}\right) \quad 3.11$$

Here  $a$ , in  $\text{\AA}$ , is a function called the screening length. One common screening function is the Molière approximation of the Thomas–Fermi atomic model<sup>35,36</sup> (TFM), which uses either the Firsov<sup>37</sup> or Lindhard<sup>38</sup> screening length. The TFM model superseded Bohr and Born–Mayer potential functions, more accurately predicting the results of actual ion scattering experiments.

$$\xi_{TFM}\left(\frac{r}{a}\right) = 0.35 \exp\left(\frac{-0.3r}{a}\right) + 0.55 \exp\left(\frac{-1.2r}{a}\right) + 0.1 \exp\left(\frac{-6.0r}{a}\right) \quad 3.12$$

$$a_{Firssov} = \frac{0.4685}{(\sqrt{Z_1} + \sqrt{Z_2})^{2/3}} \quad 3.13$$

$$a_{Lindhard} = \frac{0.4685}{(Z_1^{2/3} + Z_2^{2/3})^{1/2}} \quad 3.14$$

In the LEIS energy regime, the screening lengths in the TFM approximation are often also reduced by an empirical factor which is constant ( $C = 0.6$  to  $0.8$ ), or by the expression<sup>39</sup>

$$C = 0.54 + 0.045(\sqrt{Z_1} + \sqrt{Z_2}) \quad 3.15$$

As an alternative, the entirely empirical Ziegler-Biersack-Littmark (ZBL) function has been developed<sup>6</sup>

$$\begin{aligned} \xi_{ZBL}\left(\frac{r}{a}\right) = & 0.0281 \exp\left(\frac{-0.2016r}{a}\right) + 0.2802 \exp\left(\frac{-0.4029r}{a}\right) + \\ & 0.5099 \exp\left(\frac{-0.9423r}{a}\right) + 0.1818 \exp\left(\frac{-3.2r}{a}\right) \end{aligned} \quad 3.16$$

$$a_{ZBL} = \frac{0.4685}{Z_1^{0.23} + Z_2^{0.23}} \quad 3.17$$

Both the theoretical TFM and empirical ZBL interaction potential functions give similar results for most LEIS experiments, and have been modified to give either more simplicity in calculation<sup>40</sup> or more accurate agreement with experiment<sup>41</sup>. Once the interaction potential has been modelled, it can be used to gain quantitative information on surface structure by evaluation of the shape of shadow cones.

### 3.4.3.3 Shadow cones

When an ion beam is incident on a surface, scattering occurs due to the interaction potential, with the amount of deflection dependent on the impact parameter  $p$ , which is the distance between the trajectory of the ion and a parallel line through the centre of the target atom. This results in a region behind the target atom known as a *shadow cone*, into which incident ions cannot penetrate. This limits ion penetration into the bulk by ‘hiding’ sub-surface atoms, as shown in figure 3.9.

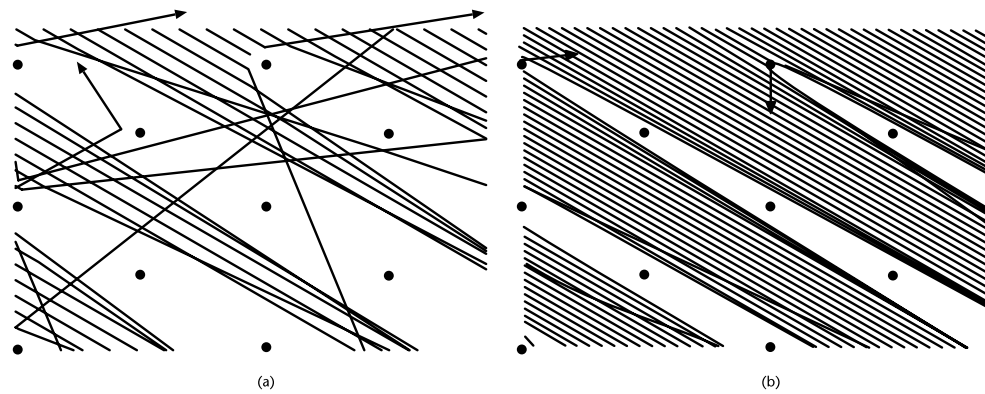


Figure 3.9: A computer-generated schematic of sub-surface shadow cones. The shadow cone ‘hides’ atoms below the surface from direct illumination by the incident ions (entering from top left). In (a) LEIS, the cone is relatively wide. This ensures surface specificity regardless of the incidence angle. Note also that multiple subsurface scattering events may occur, resulting in indirect illumination of sub-surface ions. In (b) MEIS, the cone is much narrower and it is necessary to align the incident beam along a low-index crystallographic direction to ensure that sub-surface atoms are shadowed. With ‘random’ alignment, much deeper atoms will still be illuminated by MEIS.

Analysis of the flux distribution close to the shadow cone edge shows that an effect known as focussing occurs. This can be explained qualitatively by considering that a uniform density of incident ions results in a depleted region behind the cone. However, as the majority of ions are forward-scattered, the trajectories must be accumulated close to the shadow cone edge. This focussing effect gives rise to an intensity peak, analogous to sheets of rain pouring off the edges of an umbrella.

For a screened Coulombic interaction potential, the shadow cone has a radius of

$$R = 2\xi\sqrt{\frac{Z_1Z_2e^2l}{E}} \quad 3.18$$

at a distance  $l$  behind the atom, where  $E$  is the incident ion energy and  $\xi$  is a precalculated screening factor. For a simple Coulombic potential, as used in high energy interactions (such as in RBS),  $\xi$  has a unity value.

In practice however, it is not even necessary to plot the shadow cone to deduce the local structure, as the only necessary factor is the relationship between the interatomic spacing and the surface critical incidence angle. The surface critical incidence angle  $\psi_c$  is the grazing angle at which the shadow cone of a surface atom just masks its neighbour, as shown in figure 3.10.

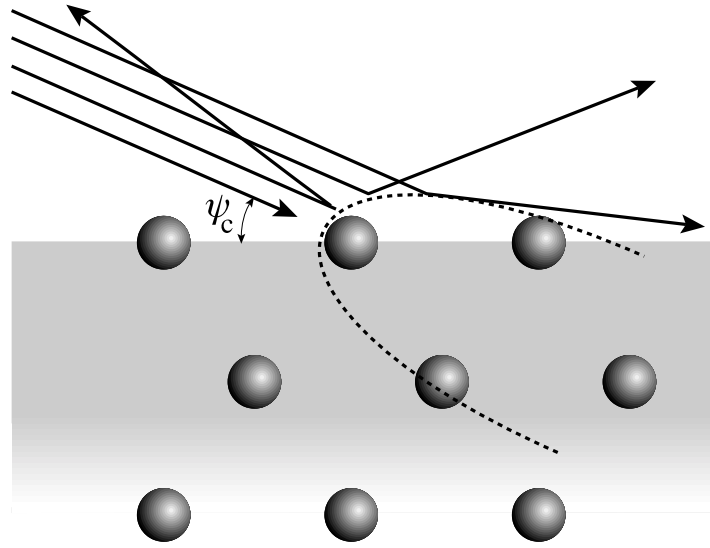


Figure 3.10: A schematic of a shadow cone at the surface critical incidence angle. The adjacent surface atom is just in shadow.

Experimentally, this angle is clearly resolved as a result of the focussing effect described above. However, since the intensity peak has a finite width, an arbitrary percentage drop-off is normally chosen to actually define the critical angle. This critical angle has been empirically related to the interatomic spacing  $d$  using both TFM and ZBL interaction potentials<sup>42</sup>

$$\begin{aligned} \ln \psi_{c \text{ TFM}} = & 4.6239 + \ln\left(\frac{d}{a}\right)(-0.0403 \ln A - 0.6730) \\ & + \ln A(-0.0158 \ln A + 0.4647) \end{aligned} \quad 3.19$$

$$\begin{aligned} \ln \psi_{c \text{ ZBL}} = & 4.7334 + \ln\left(\frac{d}{a}\right)(-0.0250 \ln A - 0.7205) \\ & + \ln A(-0.0094 \ln A + 0.3647) \end{aligned} \quad 3.20$$

where  $A = Z_1 Z_2 e^2 / 4\pi\epsilon_0 E_0 a$ . For a fixed target and incident ion combination at a given energy,  $A$  is constant and these equations reduce to a simple power law, a fact which is extremely useful for interpretation of experimental work.

In both LEIS and MEIS, performing azimuthal scans at near-grazing polar angles will yield surface symmetry information, whilst polar scans along high symmetry azimuths will give surface-substrate registration and relaxation information. The effect of blocking, where shadow cones prevent the exit of backscattered particles, also provides structural

information in both energy regimes. With scattering angles less than  $180^\circ$ , intensity changes cannot always be positively assigned to either shadowing or blocking, making interpretation more difficult.<sup>43</sup> This is one reason for the development of  $180^\circ$  backscattering impact-collision ISS (ICISS)<sup>44</sup> as described in §3.4.4. The use of controlled alignment of shadow cones ensures surface specificity in MEIS, and in §3.4.6 this is explored further, in particular with reference to so-called double-alignment geometries.

#### 3.4.3.4 Mass resolution

One important issue so far neglected is the ability of ISS to give elemental compositional information. An elastic ion scattering event is described by its momentum and energy transfer. For an incident ion of mass  $M_1$ , energy  $E_0 = \frac{1}{2}M_1u^2$  and stationary target ion of mass  $M_2$ , the collision results in the scattered ion having energy  $E_1 = \frac{1}{2}M_1v^2$  whilst the target ion has energy  $E_2 = \frac{1}{2}M_2w^2$ . This is shown in figure 3.11(a).

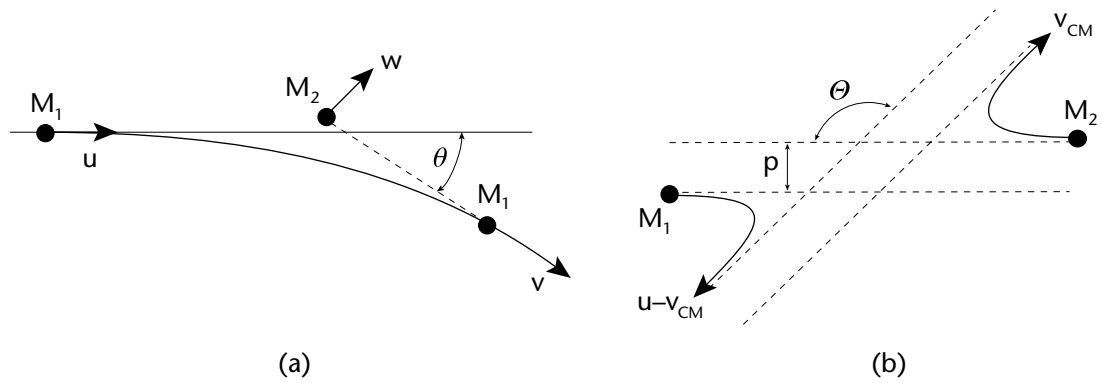


Figure 3.11: A schematic diagram of single-scattering geometry for an ion incident on a surface atom in (a) laboratory and (b) centre-of mass frames. In (a) the incident ion has initial velocity  $u$ , scattering angle  $\theta$ , and final velocity  $v$ . The target atom is initially at rest, and recoils with velocity  $w$ . In (b) the CM system moves with velocity  $v_{cm}$  relative to the laboratory frame, with scattering angle  $\theta$ . The impact parameter is  $p$ .

By considering conservation of energy and momentum parallel and perpendicular to the angle of incidence, it is possible to evaluate the energy of the scattered ion

$$\frac{1}{2}M_1u^2 = \frac{1}{2}M_1v^2 + \frac{1}{2}M_2w^2 \quad 3.21$$

$$M_1u = -M_1v \cos(180 - \theta) + M_2w \cos(180 - \theta) \quad 3.22$$

$$0 = M_1v \sin(180 - \theta) - M_2w \sin(180 - \theta) \quad 3.23$$

Eliminating  $w$

$$\frac{v}{u} = \frac{M_1 \cos \theta \pm (M_2^2 - M_1^2 \sin^2 \theta)^{\frac{1}{2}}}{M_1 + M_2} \quad 3.24$$

and hence the ratio of the scattered to incident energies, known as the kinematic factor, can be calculated

$$K = \frac{E_1}{E_0} = \frac{[\cos \theta \pm (A^2 - \sin^2 \theta)^{1/2}]^2}{[A + 1]^2} \quad 3.25$$

where  $A = M_2/M_1$ , the ion mass ratio. As the energy ratio depends only on the mass ratio for a given scattering angle, peaks in a spectrum of scattered ion intensity versus energy will directly reflect the elemental mass composition of the target. Quantitative information can be obtained from the scattered ion intensity which can be related to the incident ion intensity and the number and types of particles interacting, given the scattering cross-section  $\sigma$ . This cross-section increases with atomic number of the target and with decreasing energy and scattering angle. However, for LEIS, its determination is not trivial. Further discussion of  $\sigma$  is therefore postponed until §3.4.6 on MEIS.

It is possible to deduce an expression for the mass resolution of ISS.<sup>45</sup> For light ions (where  $A > 1$ )

$$\frac{M_2}{\Delta M_2} = \frac{E_1}{\Delta E_1} \cdot \frac{2A}{A + 1} \cdot \frac{A + \sin^2 \theta - (A^2 - \sin^2 \theta)^{1/2} \cos \theta}{A^2 - \sin^2 \theta + (A^2 - \sin^2 \theta)^{1/2} \cos \theta} \quad 3.26$$

For 180° backscattering (as in ICISS and variants), all collisions must be central. Equations 3.25 and 3.26 therefore reduce to

$$\frac{E_1}{E_0} = \frac{(A - 1)^2}{(A + 1)^2} \quad 3.27$$

and

$$\frac{M_2}{\Delta M_2} = \frac{E_1}{\Delta E_1} \cdot \frac{4A}{A^2 - 1} \quad 3.28$$

This is the condition for maximum energy transfer, and hence the maximum mass resolution. However, this is also the condition for minimum scattering cross-section, and for maximum energy spread in scattered ions. Mass resolution is obviously limited by primary ion energy spread and detector resolution, but also by spread due to thermal vibration in scattered ions. Although the phonon energy  $E_{phon}$  is too low to cause a shift in the energy of the scattered ions, it does result in a measurable line width, such that<sup>46</sup>

$$\Delta E_1 = \frac{8(A - 1)(AE_0 E_{phon})^{1/2}}{(A + 1)^2} \quad 3.29$$

In the case of CAICISS (discussed in §3.4.5), a worst case estimate for the maximum energy spread in 180° backscattering of 2 keV Ne<sup>+</sup> from Cu suggests  $\Delta E_2/E_1 \sim 2.6\%$ .

#### 3.4.4 Impact-collision ion scattering spectroscopy (ICISS)

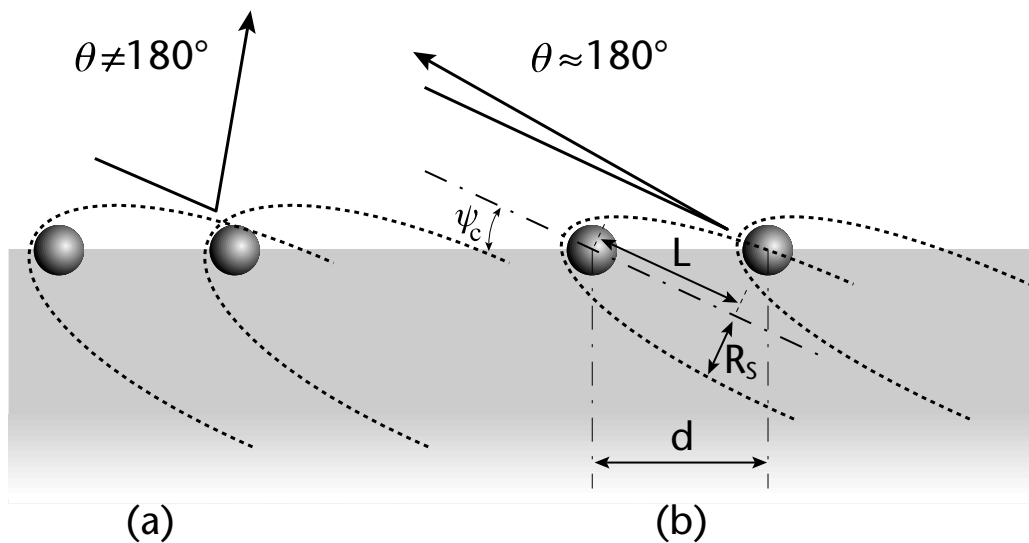


Figure 3.12: A schematic diagram showing the difference between (a) generic ISS and (b) ICISS. In (b) the critical angle for the onset of backscattering from the nearest neighbour can be simply related to the shadow cone size experimentally, according to the relations given in the text.

In ICISS only central impact-collisions, where the scattering angle is 180°, are considered. This results in several simplifications to generic ISS. Firstly, in this regime it can be assumed that no blocking occurs, as on a simple level, an ion should always be able to exit a surface along the same trajectory by which it entered. This equivalence of inbound and exit trajectories is known as the principle of time-reversal as the direction of travel of the

ion is reversible. Equations 3.27 and 3.28 are evidently greatly simplified from their generic equivalents, enabling faster calculation and simulation. Also, since the impact is central, the impact parameter must be zero. This allows more accurate surface structure determination than generic LEIS, as the edge of the shadow cone at the critical angle locates the centre of mass of the shadowed atom. Under these circumstances, the critical angle  $\psi_c$  has a simple geometric relation to the shadow cone radius  $R_S$  at a distance  $L$  from its apex, and the interatomic spacing  $d$  as shown in figure 3.12(b)

$$R_S = d \sin \psi_c \quad 3.30$$

$$L = d \cos \psi_c \quad 3.31$$

In practice, the scattering angle used in ICISS is usually less than  $180^\circ$  for ease of experimental apparatus design, since it is impossible for both ion source and detector to coincide. A physically separated constant-output ion source and electrostatic energy analyser are used with a scattering angle of around  $165^\circ$ , where most of the arguments for using a high scattering angle still apply, and hence ICISS quickly became a popular technique for structural determination after its proposal in 1981.<sup>43</sup> Over the following five or so years, consideration of the high neutralization probability in ISS led directly to the development of ALICISS, using alkali ions<sup>47</sup>, and NICISS, using a pulsed ion source and channel-plate detector to measure both neutrals and ions in a time-of-flight (TOF) measurement (hence also known as TOF-ICISS).<sup>48</sup> These developments of the technique also had the advantage of decreasing the ion flux and hence the surface damage<sup>49</sup>, whilst retaining sensitivity to backscattered particles from subsurface layers. The addition of an electrostatic double-deflection unit could divert both incoming and outgoing ions onto a true  $180^\circ$  backscattering trajectory. In addition to elemental surface studies, variants of ISS have been used in compositional studies of adsorbates (e.g. CO–Ni(001)<sup>50</sup>, O/H–W(111)<sup>51</sup> and O–Ir<sup>52</sup>), catalysts (e.g. MoO<sub>3</sub>–TiO<sub>2</sub><sup>53</sup>) and alloy surfaces (e.g. CuNi<sup>54</sup> and PtNi<sup>55</sup>), whilst there have been many structural analyses of pure and adsorbed metal and semiconductor surfaces using ISS and ICISS, reviewed elsewhere.<sup>47,56</sup>

### 3.4.5 Coaxial impact-collision ion scattering spectroscopy (CAICISS)

CAICISS is a technique developed by Aono and co-workers at the RIKEN Laboratory in Tokyo in 1988. The technique achieves true  $180^\circ$  backscattering using an annular channel-plate detector coaxial with the incident ion beam produced by a pulsed source of several keV in energy.<sup>57</sup> In addition to the improved detection and reduced flux resulting from the use of a TOF system, the coaxial design results in a true scattering angle within less than  $1.5^\circ$  of the theoretical ideal of  $180^\circ$ . This makes simulation of the scattering simpler and more accurate even than in ICISS, with the additional advantage of being less intrusive experimentally, requiring only line-of-sight to the sample via a single port on a vacuum chamber. This geometrical simplicity also allows *in situ* observation of surface processes such as epitaxial growth on semiconductor surfaces.<sup>58,59</sup>

For ICISS, it was assumed that blocking effects could be ignored, due to the principle of time-reversal. Whilst this assumption is adequate for the relatively loose interpretation of  $180^\circ$  backscattering used in ICISS, it is not appropriate for CAICISS. For true  $180^\circ$  scattering at the critical angle, incident ions will be focussed onto atoms by the shadow cones of their neighbours. Since no collision is entirely elastic, this will result in the backscattered ion having a slightly reduced energy. Therefore on exit, the blocking cone of the original focussing atom will be slightly wider than the shadow cone on entry. Focussing by blocking actually dominates the backscattering process.<sup>60</sup> As the scattering angle is reduced from  $180^\circ$ , there is a point where shadowing and blocking produce an equal intensity-enhancing effect. This double-focussing effect is at a maximum for an angle dependent on the energy loss in the collision. For typical CAICISS experiments this occurs at around  $179^\circ$  and provides even more peak enhancement at the critical angle than from generic ISS.<sup>49</sup> Below this angle is the domain of ICISS, where shadowing dominates, as expected anyway from the naïve assumption of time-reversal. The double-focussing condition is only attainable using an electrostatic double-deflector as in NICISS or with an annular detector as in CAICISS, making these particularly sensitive techniques for the interpretation of surface structure.

Another group, headed by Rabelais, has designed equipment to perform both CAICISS and DRS simultaneously, described as time-of-flight scattering and recoiling spectrometry (TOF-SARS)<sup>61</sup>, although physically the technique has CAICISS at its core. Several groups have used ICISS for structural analysis of metal surfaces. Niehus has investigated Cu(110)-O and Cu(110)-(2×3)-N, NiAl(111), Pt(111), Pt(110)-(2×1), Au(110)-(1×2), Ni(110)-(2×1)-O and Pd(110)-(1×2)-H.<sup>49,62,63,64</sup> Rabelais and co-workers have extensively studied Pt(110)-(1×2) and -(1×3) reconstructions<sup>65</sup> and Ni(110), Ni(110)-(1×2)-H and Ni(110)-(2×1)-O surfaces.<sup>66</sup> Nakanishi has investigated mixed metal surfaces including Cu(100)-Ag and Cu(100)-Au.<sup>67</sup>

In semiconductor research, Aono and others have focused largely on metal adsorbates on silicon surfaces. Particular interest has been focussed on observation of Ag island growth in real-time on the Si(111)-( $\sqrt{3} \times \sqrt{3}$ )R30°-Ag reconstruction, and the effect thereupon of H adsorption/desorption.<sup>68</sup> Rabelais and co-workers have examined clean and H-terminated Si(100)<sup>69,70</sup> as well as Ge epilayers.<sup>71</sup> In addition, Katayama *et al* have used the real-time CAICISS signal to manage the MBE growth process through control of the incident molecular flux.<sup>72</sup> Our group has studied a number of surfaces including clean and Sb-adsorbed surfaces of Si(100) and Ag(111).<sup>73,74</sup>

Little structural work on III-V semiconductors has been performed using ICISS, with *in-situ* growth studies being more common. Aono has also examined S and (NH<sub>4</sub>)<sub>2</sub>S<sub>x</sub> passivation of InAs(100).<sup>67,75</sup> Tamura has studied As-terminated GaAs(100)<sup>76</sup>, growth of GaAs on Si and highly mismatched InAs substrates.<sup>77</sup> These CAICISS studies have led to the conclusion that the As dimer length on GaAs(001) is 10% shorter than the bulk lattice spacing. Tamura has since reported the value of CAICISS in monitoring real-time MBE growth dynamics for an range of III-V compound semiconductors.<sup>78,79</sup> As mentioned in §3.4.4 above, there are fuller reviews of ICISS, as well as of ISS and its applications elsewhere, to which the reader is referred for a more detailed historical overview.<sup>34,56</sup>

### 3.4.6 Medium-energy ion scattering spectroscopy (MEIS)

MEIS in its present form has been developed as a high-resolution variant of Rutherford backscattering (RBS) of light ions. For general information on MEIS, there are some useful review articles.<sup>80,81</sup> In its standard form, RBS uses relatively high energy (10–2000 keV) ions primarily to depth profile bulk samples. Since at high energies the elastic scattering cross-section is small, energy loss due to multiple atom scattering is rare. More common is energy loss through electronic excitation, which occurs at an essentially linear rate with depth. Hence, the backscattered yield depends on the composition at a depth proportional to the energy loss. MEIS and RBS share the advantage over LEIS that the interaction potential is simpler and there are fewer neutralization effects. However, as stated earlier, for surface studies with MEIS it is necessary to use specific alignment geometries.

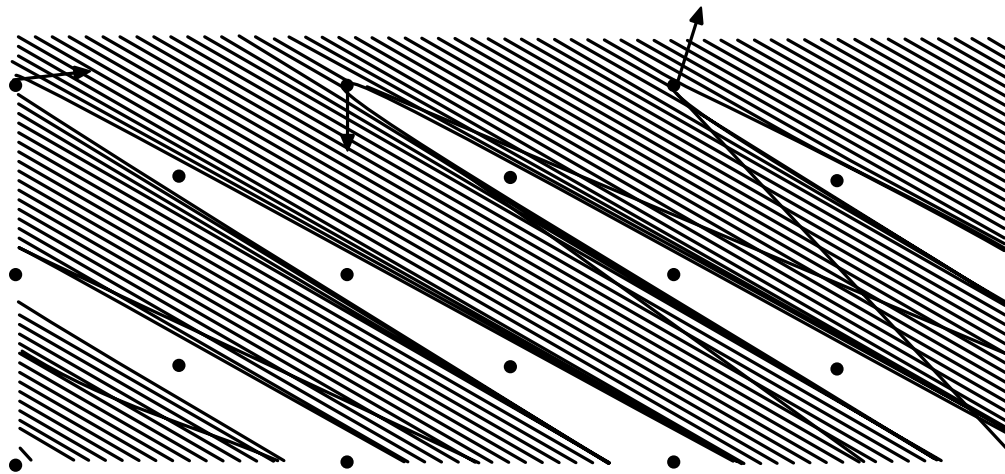


Figure 3.13: Computer-generated trajectories for an ion beam incident on a crystal along a low-index direction. Note the narrow shadow cones and near-perfect shadowing, with only a few low impact parameter collisions leading to backscattering [after van der Veen<sup>80</sup>].

A low-index crystallographic alignment of the incident beam will mean that surface atoms shadow deeper atoms. In the example shown in figure 3.13 of an ideal, static, bulk-like lattice, only the top layer atoms are illuminated by the ion beam; layers below are not visible. Shadowing can be used to determine the surface structure by rocking the crystal about the incident beam direction  $\beta$  and measuring the change in the ion yield. However,

in the case of a simple top layer relaxation, as shown in figure 3.14, the change in the interlayer spacing results in an angular change  $\delta\beta$  in the shadowing direction. The backscattered surface yield  $N$  will therefore exhibit asymmetry about the bulk shadowing direction, directly related to the magnitude of the relaxation. Similar (but more complex) asymmetries and yield variations with angle are observed in more complex reconstructions.

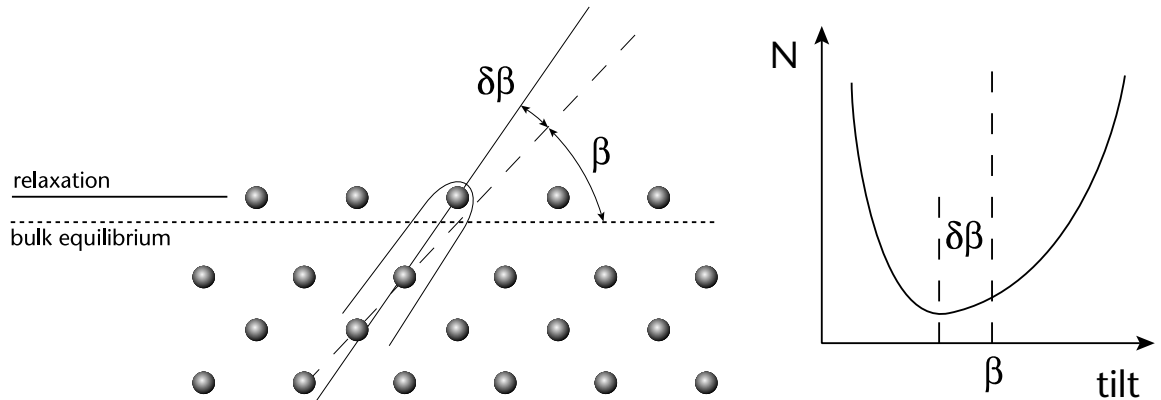


Figure 3.14: Top layer relaxation leads to an angular shift  $\delta\beta$  in shadowing direction from that of the bulk  $\beta$ , resulting in an asymmetric variation of backscattered yield with crystal tilt angle.

It should be noted that in a real crystal, thermal vibrations alter the shadow cone positions such that some deeper atoms may be illuminated by individual ions, contributing to the measured backscattered yield. Since the period of any thermal vibrations ( $\sim 10^{-12}$ – $10^{-13}$  s) is much longer than the ion interaction time ( $\sim 10^{-15}$  s), the atoms in the surface will effectively remain ‘frozen’ in position for the duration of an ion transit. Figure 3.15 shows a set of ion trajectories for a harmonically vibrating lattice with atom displacements randomly sampled from a Gaussian probability distribution. In reality, each ion will see a different state of the thermally vibrating crystal. Experimental determination of  $N$  relies on measurement of the area of the ‘surface peak’ of a MEIS energy spectrum. A theoretical calculation of  $N$  is cumbersome, and hence Monte Carlo simulation is often used, aggregating over a large number of randomly generated trajectories to gain statistical significance. Such a computational approach is used in the VEGAS code, discussed in the following chapter and used for simulation work in this thesis.

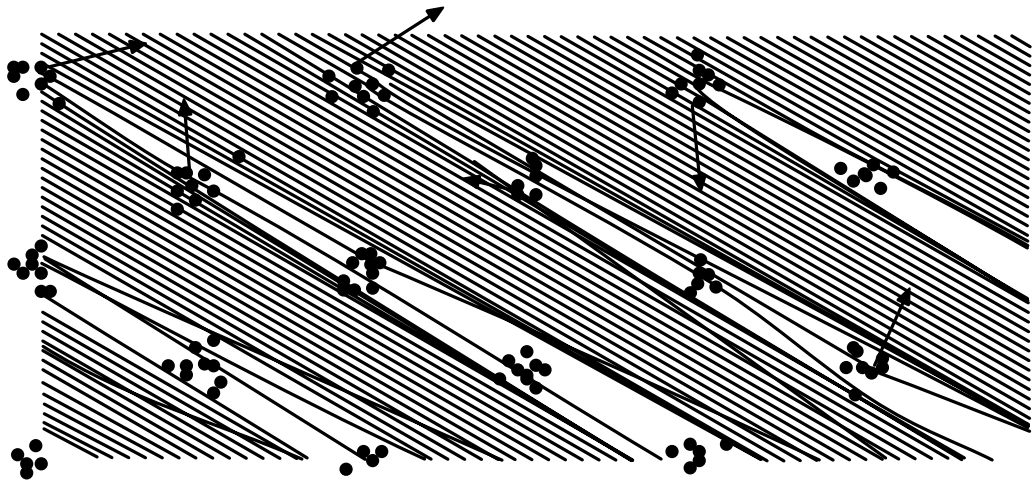


Figure 3.15: Computer-generated ion trajectories for a thermally vibrating lattice. Note that scattering events occur from many sub-surface atoms which were shadowed in the ideal lattice [c.f. figure 3.13].

Whilst as indicated above, shadowing effects from relaxations and reconstructions may affect the backscattering yield profile, and hence be used as a test for structural models, it is much harder to use them for an *ab initio* structure determination. In particular, it is difficult to distinguish reconstruction effects from surface vibrational effects. However, the combination of shadowing with blocking can facilitate direct structure determination.

If the backscattering atom is located beneath the surface layer, then scattered ions may be blocked from exiting the surface by other atoms. The backscattering atom may therefore be considered as a point source of ions. Detecting ions across a range of scattering angles will show a range of blocking minima. Since shadowing theory describes blocking equally well (as the two processes are time-reversed equivalents) there is no increased complication in analysis. In a so-called *double alignment* geometry, the incident beam is aligned along a low-index shadowing direction and the backscattered ion detector is rocked about a suitable blocking direction. Equivalent information about shifts in atomic position is obtained to that from shadowing alone, however the incident beam alignment means that only the topmost layers contribute to the backscattered yield, giving surface specificity.

In the case of surface reconstruction rather than simple relaxation, the re-arrangement of surface atoms from their bulk sites will result in imperfect shadowing and much greater illumination of the sub-surface. The result is an increased scattering yield  $N$  compared to a

bulk-terminated surface. Consideration of  $N$  alone may therefore provide a measurement of the state of reconstruction. Copel and Tromp used MEIS to examine the Si(111)- $(\sqrt{3} \times \sqrt{3})R30^\circ$ -Ag surface and found that  $N$  was much higher than expected for a bulk-terminated surface or a primitive adlayer reconstruction. They therefore concluded that several previously-proposed models were less likely than others involving substantial reconstruction of the topmost layers.<sup>82</sup>

From equation 3.25, it is clear that providing there is sufficient mass separation, MEIS can resolve blocking features from different elements within a surface, enabling element-specific structural information. Heavier incident ions increase the mass resolution, although at the expense of increasing the likelihood of sputtering. From the same equation it is clear that there is a characteristic fall-off in energy with scattering angle. This may be readily observed in experimental data (as seen in subsequent chapters).

In addition there is an energy dependence with depth, as used in depth profiling studies.

The energy  $E$  at perpendicular depth  $z$  is

$$E(z) = K \left[ E_0 - \frac{z}{\cos \theta_{in}} \left( \frac{dE}{dx} \right)_{in} \right] - \frac{z}{\cos \theta_{out}} \left( \frac{dE}{dx} \right)_{out} \quad 3.32$$

where  $K$  is the kinematic factor from equation 3.25 and  $dE/dx$  is the stopping power<sup>83</sup> evaluated at the ion energies along the incident and backscattered tracks. The stopping power depends on  $E$ ,  $Z_1$  and  $Z_2$  as well as the atomic density of the target. In addition to enabling compositional depth profiling, the energy dependence with depth allows the surface peak to be isolated from any bulk contributions in low-index aligned geometries, thus enhancing surface specificity.

Assuming that the detector measures all scattered particles (which for MEIS and HEIS is not unreasonable since the probability of neutralization is low) and that the potentials are screened Coulombic in nature, the detected ion flux  $I$  over the solid angle  $\Delta\Omega$  is given by

$$I = NQ \left( \frac{d\sigma}{d\Omega} \right) \Delta\Omega \quad 3.33$$

where  $N$  is the number of atoms contributing to the backscattering for incident ion flux  $Q$ .  $d\sigma/d\Omega$  is the differential Rutherford scattering cross-section (as mentioned in §3.4.3.4), given by

$$\frac{d\sigma}{d\Omega} = \xi \left[ \frac{Z_1 Z_2 e^2}{4E \sin^2(\theta/2)} \right]^2 \quad 3.34$$

where  $E$  is the incident ion energy and  $\xi$  is an electronic screening parameter, such that typically  $0.85 \leq \xi \leq 1$ . In the Molière approximation<sup>84</sup>

$$\xi_{TFM} = 1 - \frac{0.042 Z_1 Z_2^{4/3}}{E [\text{keV}]} \quad 3.35$$

Since the Rutherford scattering cross-section decreases with increasing scattering angle, there is a characteristic decrease in yield, in addition to a fall-off in energy at higher scattering angles. These essentially classical relations enable quantitative analysis with HEIS techniques such as RBS. Whilst they usually require subtle modifications, they are accurate enough, verbatim, for many quantitative MEIS studies as well. In the LEIS regime however, the assumptions of negligible neutralization and simple screened potentials do not hold true, and the scattering cross-section is therefore not well-known. The additional complications of multiple scattering discussed at the start of this chapter mean that despite better inherent surface specificity, quantitative analysis using LEIS is relatively more difficult than for MEIS. Nonetheless, the relative ease of production of ions at these lower energies means that LEIS remains a key tool in surface analysis in the laboratory.

The use of MEIS in semiconductor studies was pioneered by the FOM-AMOLF group in Amsterdam, who also developed the VEGAS software for MEIS simulation, discussed in depth in the following chapter. An example of their studies is the analysis of Sb<sub>4</sub> deposition on Si(001) at varying substrate temperatures.<sup>85</sup> In this work, MEIS was used to determine surface coverages to an accuracy of 5%. At substrate temperatures below 570 K, Sb cluster formation was observed, whilst at higher temperatures, only two-dimensional growth was possible, the surface saturating with a coverage of between 0.7 and 0.9 ML. A study by Noakes et al compared nominally identical Si/SiGe layer structures grown by MBE and

CVD.<sup>86</sup> It was found that a much greater concentration of Ge was incorporated into the layer structures by MBE than CVD. The NTT Lab in Tokyo used MEIS to investigate the oxidation of a thin SiGe layer on Si(001).<sup>87</sup> Upon oxidation at 525 K, the predominant oxide formed is SiO<sub>2</sub>, with a small amount of GeO. Following oxidation, the MEIS data shows evidence of Ge in-diffusion towards the SiO<sub>2</sub>/SiGe interface. The same group has also studied dimerization of simple semiconductor structures by geometric analysis of asymmetries in the blocking dips. Surfaces studied by this approach include Ge/Si(001) and Sb/Si(001) surfaces<sup>88</sup> and the GaAs(001)-(2×4) reconstruction.<sup>89</sup>

### 3.5 References

- <sup>1</sup> J.W. Rabelais and D. Marton: *Nucl. Instr. Meth. B* **67** (1992) 287
- <sup>2</sup> J. C. Tully: *Phys. Rev. B* **16** (1977) 4324
- <sup>3</sup> H.D. Hagstrum: *Phys. Rev.* **123** (1961) 758
- <sup>4</sup> J. W. Rabalais: *Crit. Rev. Solid State and Mater. Sci.* **14** (1988) 319
- <sup>5</sup> C.E.C. Wood, K. Singer, T. Ohashi, L.R. Dawson and A.J. Noreika: *J. Appl. Phys.* **54** (1983) 2732
- <sup>6</sup> J. F. Ziegler, J. P. Biersack and U. Littmark: *The Stopping and Range of Ions in Solids*, Vol. 1 (Pergamon, New York, 1985)
- <sup>7</sup> P. Sigmund: *Phys. Rev.* **184** (1969) 383
- <sup>8</sup> D.A. Thompson: *Rad. Eff.* **56** (1981) 105
- <sup>9</sup> J.B. Malherbe: *Crit. Rev. Solid State and Mater. Sci.* **19** (1994) 55 and 129 *et loc. cit.*
- <sup>10</sup> D.P. Woodruff, T.A. Delchar: *Modern Techniques of Surface Science* (Cambridge, 1994) 298
- <sup>11</sup> A. Takamori, S. Sugata, K. Asakawa, E. Miyauchi and H. Hashimoto: *Jpn. J. Appl. Phys.* **26** (1989) L142
- <sup>12</sup> N. Kondo and Y. Nanishi: *Jpn. J. Appl. Phys.* **28** (1989) L7
- <sup>13</sup> S. Sugata, A. Takamori, N. Takado, K. Asakawa, E. Miyauchi and H. Hashimoto: *J. Vac. Sci. Technol. B* **6** (1988) 1087
- <sup>14</sup> J.F. Klem, J.Y. Tsao, J.L. Reno, A. Dayte, S. Chadda: *J. Vac. Sci. Technol. A* **9** (1991) 2996
- <sup>15</sup> A. Munoz-Yague, J. Piqueras, N. Fabre: *J. Electrochem. Soc.: Solid State Sci. Technol.* **128** (1981) 149
- <sup>16</sup> I. Suemune, Y. Kunitsugu, Y. Kan and M. Yamanishi: *Appl. Phys. Lett.* **55** (1989) 760
- <sup>17</sup> T. Sugaya and M. Kawabe: *Jpn. J. Appl. Phys.* **30** (1991) L402
- <sup>18</sup> Y.J. Chun, T. Sugaya, Y. Okada and M. Kawabe: *Jpn. J. Appl. Phys.* **32** (1993) L287
- <sup>19</sup> G.R. Bell and C.F. McConville: *Appl. Phys. Lett.* **69** (1996) 2695
- <sup>20</sup> G.R. Bell, N.S. Kaijaks, R.J. Dixon and C.F. McConville: *Surf. Sci.* **401** (1998) 125 *et loc. cit.*
- <sup>21</sup> EPI Application Note 3/98: *Recent Results using the EPI Atomic Hydrogen Source* (1998)
- <sup>22</sup> J.T. Wolan, C.K. Mount and G.B. Hoflund: *J. Vac. Sci. Technol. A* **15** (1997) 2502
- <sup>23</sup> J.T. Wolan, W.S. Epling and G.B. Hoflund: *J. Appl. Phys.* **81** (1997) 6160
- <sup>24</sup> K. Röhhel and H.L. Hartnagel: *Int. J. Electron.* **6** (1986) 663
- <sup>25</sup> M. Yamada: *Jpn. J. Appl. Phys.* **35** (1996) L651

- 26 D.P. Woodruff, T.A. Delchar: *Modern Techniques of Surface Science* (Cambridge, 1994) *et loc. cit.*
- 27 C.J. Davisson and L.H. Germer: *Phys. Rev.* **30** (1927) 705
- 28 C.J. Davisson and L.H. Germer: *Nature* **119** (1927) 558
- 29 W.L. Bragg: *Proc. Cambridge Phil. Soc.* **17** (1913) 43
- 30 J.J. Quinn: *Phys. Rev.* **126** (1962) 1453
- 31 E. Conrad: *Diffraction Methods*, Chapter 7 in *Physical Structure, Handbook of Surface Science, Volume 1* (Elsevier, 1996) *et loc. cit.*
- 32 L.E. Davis, N.C. MacDonald, P.W. Palmberg, G.E. Riach and R.E. Weber: *Handbook of Auger Electron Spectroscopy* (2nd edn., Physical Electronics Inc., MN, 1976)
- 33 L.A. Harris: *J. Appl. Phys.* **39** (1968) 1419
- 34 H. Niehus, W. Heiland and E. Taglauer: *Surf. Sci. Reports* **17** (1993) 213
- 35 G. Molière: *Z. Naturforsch.* **2a** (1974) 133
- 36 S. A. Cruz, E. V. Alonso, R. P. Walker, D. J. Martin and D. G. Armour: *Nucl. Instr. Meth.* **194** (1982) 659
- 37 O. B. Firsov: *Sov. Phys.-JETP* **33** (1957) 696
- 38 J. Lindhard, M. Scharff and H. E. Schiott: *K. Dan. Vidensk. Selsk. Mat. Fys. Medd.* **33** (1963) No. 14
- 39 D. J. O'Connor and J. P. Biersack: *Nucl. Instr. Meth. B* **15** (1986) 14
- 40 O. S. Oen: *Surf. Sci.* **131** (1983) L407
- 41 M. Kato, R. S. Williams and M. Aono: *Nucl. Instr. Meth. B* **33** (1988) 462
- 42 T. Fauster: *Vacuum* **38** (1988) 129
- 43 M. Aono and R. Souda: *Jpn. J. Appl. Phys.* **24** (1985) 1249
- 44 M. Aono, C. Oshima, S. Zaima, Z. Otani and Y. Ishizawa: *Jpn. J. Appl. Phys.* **20** (1981) L829
- 45 E. Taglauer and W. Heiland: *Appl. Phys.* **9** (1976) 261
- 46 E. Hulpke: *Surf. Sci.* **52** (1975) 615
- 47 H. Niehus: *Nucl. Instr. Meth.* **218** (1983) 230
- 48 H. Niehus: *Surf. Sci.* **166** (1986) L107
- 49 H. Niehus: *Appl. Phys. A* **53** (1991) 388
- 50 M. Beckshulte, D. Mehl and E. Taglauer: *Vacuum* **41** (1990) 67
- 51 M. Shi, O. Grizzi, H. Bu and J.W. Rabelais: *Surf. Sci.* **235** (1990) 67
- 52 H. Bu, M. Shi, K. Boyd and J.W. Rabelais: *J. Chem. Phys.* **95** (1991) 2882
- 53 R. Margraf, J. Leyrer, H. Knözinger and E. Taglauer: *Surf. Sci.* **108/109** (1987) 842
- 54 H.H. Brongersma and T.M. Buck: *Surf. Sci.* **53** (1975) 649
- 55 P. Weigand, P. Novacek, G. van Husen, T. Neidart and P. Varga: *Surf. Sci.* **269/270** (1992) 1129
- 56 P.R. Watson: *J. Phys. Chem. Ref. Data* **19** (1990) 85
- 57 M. Aono, M. Katayama, E. Nomura, T. Chassé, D. Choi, M. Kato: *Nucl. Instr. Meth. B* **37/38** (1989) 264
- 58 M. Aono and M. Katayama: *Proc. Jpn. Acad. B* **65** (1989) 137
- 59 M. Katayama, E. Nomura, H. Soejima, S. Hayashi and M. Aono: *Nucl. Instr. Meth. B* **45** (1990) 408
- 60 R. M. Charatan and R. S. Williams: *Surf. Sci.* **264** (1991) L207
- 61 J. W. Rabalais: *J. Vac. Sci. Technol. A* **9** (3) (1991) 1293
- 62 R. Spitzl, H. Niehus and G. Comsa: *Rev. Sci. Instr.* **61** (1990) 760
- 63 R. Spitzl, H. Niehus and G. Comsa: *Surf. Sci. Lett.* **250** (1990) L355
- 64 H. Niehus: *J. Vac. Sci. Technol. A* **5** (1987) 751
- 65 Y. Wang, M. Shi and J.W. Rabelais: *Nucl. Instr. Meth. B* **62** (1992) 505
- 66 J.W. Rabelais, H. Bu and C. Roux: *Nucl. Instr. Meth. B* **64** (1992) 559

- <sup>67</sup> S. Nakanishi, K. Kawamoto and K. Umezawa: *Surf. Sci.* **287/288** (1993) 974
- <sup>68</sup> M. Aono and R. Souda: *Nucl. Instr. Meth. B* **27** (1987) 55
- <sup>69</sup> Y. Wang, S.V. Teplov, O.S. Zaporozchenko, V. Bykov and J.W. Rabelais: *Surf. Sci.* **296** (1993) 213
- <sup>70</sup> Y. Wang, S.V. Teplov and J.W. Rabelais: *Nucl. Instr. Meth. B* **90** (1994) 237
- <sup>71</sup> Y. Wang, H. Bu, T.E. Lytle and J.W. Rabelais: *Surf. Sci.* **318** (1994) 83
- <sup>72</sup> M. Katayama, T. Nakayama, C.F. McConville and M. Aono: *Nucl. Instr. Meth. B* **99** (1995) 598
- <sup>73</sup> R.J. Dixon, C.F. McConville, S.J. Jenkins and G.P. Shrivastava: *Phys. Rev. B* **57** (1998) 12701
- <sup>74</sup> T.C.Q. Noakes, D.A. Hutt and C.F. McConville: *Surf. Sci.* **309** (1994) 101
- <sup>75</sup> M. Katayama, M. Aono, H. Oigawa, Y. Nannichi, H. Sugahara and M. Oshima: *Jpn. J. Appl. Phys.* **30** (1991) L786
- <sup>76</sup> N. Sugiyama, A. Hashimoto and M. Tamura: *J. Vac. Sci. Technol. A* **10** (1992) 29
- <sup>77</sup> A. Hashimoto, N. Sugiyama and M. Tamura: *Jpn. J. Appl. Phys.* **30** (1991) 3755
- <sup>78</sup> T. Saitoh, A. Hashimoto, S. Ohkouchi and M. Tamura: *J. Cryst. Growth* **127** (1993) 1018
- <sup>79</sup> M. Tamura, T. Saitoh, N. Sugiyama, A. Hashimoto, S. Ohkouchi, N. Ikoma and Y. Morishita: *Nucl. Instr. Meth. B* **85** (1994) 404
- <sup>80</sup> J.F. van der Veen: *Surf. Sci. Rep.* **5** (1985) 199
- <sup>81</sup> I. Stensgaard: *Rep. Prog. Phys.* **55** (1992) 989
- <sup>82</sup> M. Copel and R.M. Tromp: *Phys. Rev. B* **39** (1989) 12688
- <sup>83</sup> Stopping powers can be calculated for a range of different substrates and ions using the package SRIM, available from <http://www.research.ibm.com/ionbeams/>
- <sup>84</sup> J. L'Ecuyer, J.A. Davies and N. Matsunami: *Nucl. Instr. Meth.* **160** (1979) 337
- <sup>85</sup> W.F.J. Slijkerman, P.M. Zagwijn, J.F. van der Veen, D.J. Gravesteijn and G.F.A. van de Walle: *Surf. Sci.* **262** (1992) 25
- <sup>86</sup> S. Sugden, C.J. Sofield, T.C.Q. Noakes, R.A.A. Kubiak and C.F. McConville: *Appl. Phys. Lett.* **6** (1995) 2849
- <sup>87</sup> K. Prabhakaran, T. Nishioka, K. Sumitomo, Y. Kobayashi and T. Ogino: *Jpn. J. Appl. Phys.* **33** (1994) 1837
- <sup>88</sup> K. Sumitomo, T. Nishioka and T. Ogino: *Appl. Surf. Sci.* **130–132** (1998) 133
- <sup>89</sup> K. Sumitomo, H. Yamaguchi, Y. Hirota, T. Nishioka and T. Ogino: *Surf. Sci.* **355** (1996) L361

## 4 • Computational techniques

### 4.1 Introduction

Although some information about surface structure can be found from a simple geometric analysis of MEIS spectra, such calculations are limited to only the simplest cases. Usually, quantitative study requires compute-intensive simulation of scattering data for model structures and comparison with experimental data to seek a best-fit solution based on some quantifiable quality-of-fit criterion. The work in this thesis uses the VEGAS simulation code initially developed by Tromp *et al* and the FOM-AMOLF group in Amsterdam.<sup>1,2</sup> The VEGAS code was written to simulate the backscattering of ions in MEIS experiments. It functions by determining the hitting probability for each atom in a model given the geometry and other parameters of the incident ion beam. The detection probability is then calculated for a range of detector angles on the basis of time-reversal, and a value for the elemental backscattered yield thus derived. Optimizations enable the calculation of detection probabilities for a range of structural and vibrational models related to the basic structure without greatly increasing the compute-time.

More recently, the VEGAS code has been revised, and fitting code developed by Paul Bailey of the MEIS facility at CLRC Daresbury Laboratory. This development has continued at Warwick with work to transfer the code to another operating system, and to enable model visualization.

### 4.2 VEGAS simulation

#### 4.2.1 Double-alignment geometry

If only shadowing is considered (single-alignment), then the backscattering intensity can be calculated exactly if two atoms are involved, as the elastic scattering cross-sections for ions are well-known from equation 3.34. In the case of double-alignment, with both blocking and shadowing, three atoms and their positions must be considered.

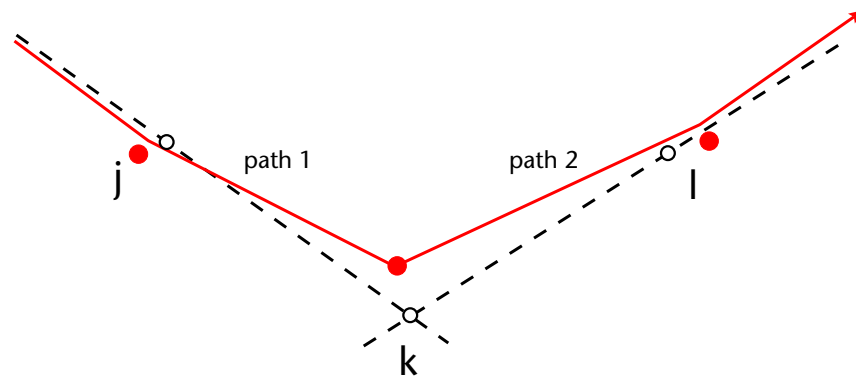


Figure 4.1: Schematic of the scattering process for a double-alignment condition in a three-atom geometry. The open circles represent the equilibrium positions of the crystal atoms and the dashed lines indicate crystallographic directions. The solid circles are ‘frozen’ atom positions, and the solid line shows the ion trajectory [after Tromp and van der Veen<sup>1</sup>].

As mentioned in §3.4.3.2, the velocity of MEIS incident ions is large enough, compared to the phonon frequency of a crystal (by around three orders of magnitude), that the atoms can be considered as effectively ‘frozen’ in their thermally displaced positions at the time of collision. The result of this is that each ion sees a different ‘snapshot’ of the vibrational state of the crystal. Furthermore, the high energy of the ions means that their trajectories can be considered as a series of binary elastic collisions connected by straight line segments. The three-atom case for a double-alignment geometry is shown in figure 4.1. In the double-alignment condition, the incident beam and exit trajectory are both aligned on major crystallographic directions. The scattering process can be considered in two stages:

- i) An ion enters the crystal along path 1 (the shadowing or channelling direction), passing atom  $j$  and being scattering from atom  $k$ .
- ii) The ion exits the crystal, where it may be blocked by atom  $l$ .

Since collisions are considered essentially instantaneous, atom  $k$  is in the same position for both stages, thus they may be considered as correlated. Monte Carlo methods are generally used to generate ion trajectories, based on the assumption that the thermal vibrations of the lattice follow a Gaussian probability distribution. Since the probability of large-angle backscattering events is quite small, a *nuclear encounter probability* concept is used rather than waiting for and measuring backscattering events, as the latter would require excessive computational time.

### 4.2.2 Hitting and detection probabilities

For path 1 in figure 4.1, the probability of the ion colliding with atom  $k$  at position  $x_k$  may be defined as  $P^1(x_k)$ , and for path 2, the probability of the ion leaving atom  $k$  at position  $x_k$  and reaching the detector as  $P^2(x_k)$ . If  $G_k(x_k)$  is the Gaussian probability density function for the thermal displacement of atom  $k$  to position  $x_k$ , then the hitting probability of atom  $k$  along path 1 is given by

$$P^h = \int_{-\infty}^{\infty} P^1(x_k) G_k(x_k) dx_k \quad 4.1$$

The ‘snapshot’ model of the collision means that by time reversal, the detection probability  $P^d$  is equal to the hitting probability of an ion travelling towards  $x_k$  along path 2

$$P^d = \int_{-\infty}^{\infty} P^2(x_k) G_k(x_k) dx_k \quad 4.2$$

This is an important equivalence, enabling the independent calculation of blocking and shadowing probabilities by the same Monte Carlo methods. Integrating over the probability distribution of  $x_k$ , the double-alignment probability  $P^{da}$ , that the ion is backscattered from atom  $k$  and detected, is given by

$$P^{da} = \int_{-\infty}^{\infty} P^1(x_k) G_k(x_k) P^2(x_k) dx_k \quad 4.3$$

In practice, this is often approximated to

$$P^{da} \approx P^d P^h \quad 4.4$$

which has been shown by Tromp and van der Veen to be reasonable (within  $\sim 2\%$ ) for many cases<sup>1</sup>, despite the correlation between the incident and exit trajectories being ignored. As a result of this approximation, the hitting probabilities for incident and exit geometries may be calculated entirely independently and multiplied to give the double-alignment probability and thus the backscattered yield.

### 4.2.3 The single-row approximation

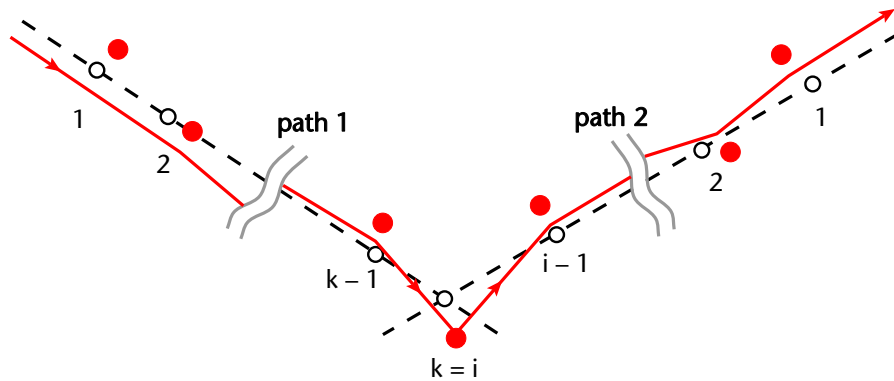


Figure 4.2: Schematic of the scattering process for a double-alignment condition in the general  $n$ -atom geometry, where the number of crystal atoms in paths 1 and 2 are not necessarily equal. [after Tromp and van der Veen<sup>1</sup>.]

The approach outlined for the three-atom geometry above can be extended to the more general  $n$ -atom geometry, shown in figure 4.2. Since the shadow cones for MEIS are narrow, it is reasonable to assume that ions are affected only by atoms within the chain (or row) of atoms, as implicit in a three-atom geometry. Hence, this approach is known as the *single-row approximation*. The first stage, as before, is to determine the hitting probability for atom  $k$ , now being the  $k$ th atom along the incident path 1.

Tromp and van der Veen have developed a particularly efficient method for this calculation. Atom  $k$  is shadowed from the ion beam by atoms 1, 2, ...,  $k - 1$ , the same atoms that deflect the ion trajectory. Let the atoms occupy positions  $x_1, x_2, \dots, x_k$  at the time of interaction. In general, an arbitrary ion track will not coincide with  $x_k$ , but will pass it at a separation of  $\delta x_k$ , perpendicular to the ion beam incident direction. On this basis, a collision would have occurred had the atom positions and ion track all been displaced by  $-\delta x_k$ . Therefore, the probability density for a collision, where the ion track passes through  $x_k$ , is given by the probability density  $P_k$  for the atoms  $j = 1$  to  $k - 1$  to occupy positions  $(x_1 - \delta x_k, x_2 - \delta x_k, \dots, x_{k-1} - \delta x_k)$  instead of  $x_1, x_2, \dots, x_k$ . Hence

$$P_k = \prod_{j=1}^{k-1} G_j(x_j - \delta x_k) \quad 4.5$$

where  $G_j$  is the Gaussian probability density which must be integrated over all possible atom positions for  $x_1$  through  $x_{k-1}$ .  $G_j$  includes information on the equilibrium positions and thermal vibrations of atom  $j$ . It is possible to correlate vibrations between atoms.

However, for the simple case of mutually independent  $G_j$  values

$$P_k(x_k) = \int_{-\infty}^{\infty} \dots \int_{-\infty}^{\infty} \prod_{j=1}^{k-1} G_j(x_j - \delta x_k) dx_j \quad 4.6$$

This function is then substituted into equation 4.1, integrating over all possible positions of the final atom  $x_k$  to give the hitting probability  $P^h$ . Since all the integration variables are independent, a Monte Carlo approach can be used, where uniform random values of  $x_k$  are chosen according to the Gaussian probability distribution.  $P^h$  may then be obtained by averaging over a large number of samples.

This approach differs from Barrett's (the 'standard') method for calculating hitting probabilities<sup>3</sup>, where the probability density is calculated per ion track, rather than for a specific target atom position  $x_k$ . Although the final results have been proved to be identical, Tromp and van der Veen's method is more efficient, in particular facilitating the time-reversed approach to calculating  $P^d$  used in equation 4.2 and thus the backscattered yield via equation 4.4. Another important implication is that for a given sample set of ion trajectories, the hitting probability can be calculated for a number of different crystal parameters (for example vibration amplitudes or atom equilibrium positions) by altering the Gaussian probability distribution function  $G(x)$ , which is not used until after the calculation of ion trajectories. This has a significant impact on the computation time required for evaluating hitting and detection probabilities, accelerating them by around 25–100 times, as the generation of random ion tracks is perhaps the most compute-intensive part of the simulation procedure. This feature of the VEGAS code makes it particularly well-suited to multiparameter analysis of, for example, surface reconstructions. The surface atom positions and thermal vibrations can be varied programmatically in a so-called 'multimodel' calculation, where backscattered yields are calculated using a single set of calculated ion trajectories, rather than repeating the entire process for each parameter.

#### 4.2.4 The complete crystal method

If ions interact with atoms in other rows, then the single-row approximation is no longer valid. This is particularly likely in situations such as with an off-axis (non-channelled) incident ion beam. If the atom rows are equivalent, then this failure of the approximation may be overcome by imposing periodic boundary conditions on the ion trajectory, such that its position is always defined with respect to the nearest atom row. However, in the case that atom rows are not equivalent, such as in surface reconstruction, periodic boundary conditions cannot be applied. In such circumstances, a *complete crystal* approach may be used, and this is the method used within the VEGAS code. A complete crystal slab is constructed using rectangular periodic boundary conditions in both  $x$ - and  $y$ - directions parallel to the surface plane. Its dimensions are chosen according to the surface unit cell, or in the case of a non-rectangular unit cell from a combination of two or more. The thickness of the slab is equal to the depth which the ions traverse in the calculation. The atoms within the slab may occupy strongly irregular equilibrium positions and be subject to isotropic or anisotropic thermal vibrations. Hitting and detection probabilities are then calculated using the Monte Carlo methods described previously.

In the single-row approximation, the sequence of atom interactions is defined intrinsically by their planar order. In the complete crystal, this order is lost, and the collision sequence must be calculated for each ion individually. For a complicated unit cell, the slab may contain many atoms (e.g. in excess of 50–100), and hence an *auxiliary lattice* is constructed, tailored to the surface structure, to reduce the number of possible collision partners. The atoms are grouped into near-neighbours, defining  $x$ ,  $y$  and  $z$  planes with co-ordinates equal to the average  $x$ ,  $y$  and  $z$  co-ordinates of the atoms in each group. The auxiliary lattice of planes is at least as regular as the atomic arrangement within it, has approximately the same number of points as atoms in the slab, but will be rectangular, regardless of the real crystal structure. Each atom is assigned to a single lattice point ( $x$ -,  $y$ - and  $z$ -group), although the equilibrium position of a given atom need not be exactly coincident. Although some lattice points may remain empty, none can accommodate more than one atom.

The ion tracks are calculated by first deciding whether the ion moves primarily in the  $x$ ,  $y$  or  $z$  direction. The ion path is then constructed in terms of intersections with planes of that direction. The typical nearest-neighbour separation in a crystal is  $2 \text{ \AA}$ . For an appreciable deflection, the impact parameter must be less than  $\sim 0.5 \text{ \AA}$ . Since the ion is not moving at a grazing angle relative to the plane (if its primary direction of travel is perpendicular), it can only encounter at most one atom in each plane. By definition, there can only be four lattice points close to the intersection, as shown in figure 4.3. If atoms are assigned to these points, the contributions of the ion track to their hitting probabilities are calculated, a possible collision partner selected and a deflection angle determined. If no sufficiently close encounter occurs, the ion path is simply extrapolated to the next plane and the procedure repeated. The auxiliary lattice must have interplanar separations of at least  $0.1 \text{ \AA}$  in order for the assumptions about the number of possible collision partners to be true, and thus for the ion tracking procedure to be successful. Although this might appear to be a limitation of the complete crystal method, it has not proved so in a number of successful studies including those of  $\text{Si}(111)-(7 \times 7)^4$ ,  $\text{Si}(111)-(2 \times 1)^5$ ,  $\text{GaSb}(110)^6$ ,  $\text{InAs}(110)^7$  and  $\text{GaAs}(110)^8$ .

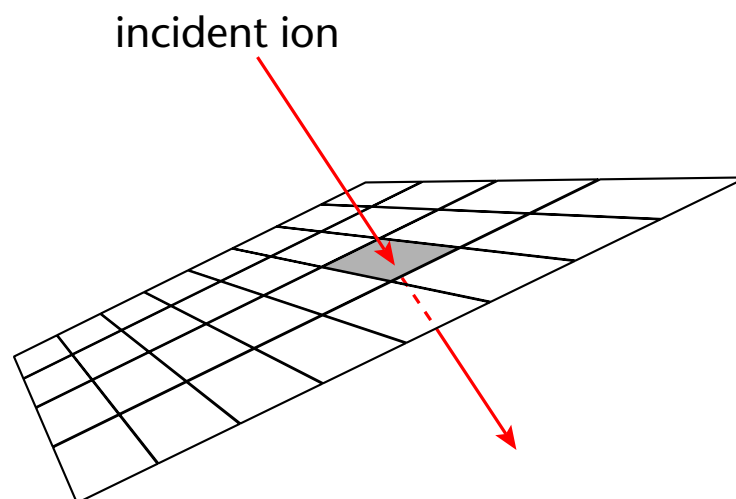


Figure 4.3: Intersection of an ion with one of the  $z$ -planes of the auxiliary lattice. In this  $z$ -plane, only the four lattice points at the corner of the marked square are close enough to the ion track to be considered [after Frenken<sup>2</sup>].

#### 4.2.5 Ion track correlation and connection

As has been established, there is an inherent correlation between incident and exit trajectories for a collision, since the target atom must occupy the same position for both tracks. If  $P^1(x_k)$  and  $P^2(x_k)$  strongly vary with  $x_k$  close to the equilibrium position, then the approximation of equation 4.3 to equation 4.4 is no longer valid. A simple example is that shown in figure 4.4, where the incident track would be expected to completely shadow sub-surface atoms in a bulk-like crystal, but due to surface relaxation, the ion beam illuminates the atoms at the edge of the shadow cones. As the atoms vibrate about their equilibrium position, they enter and leave the shadow cones. Since, by definition, no collisions can occur within the shadow cone, the average emission point for collisions is displaced away from the cone and from the equilibrium position, tilting the angle of the surface blocking minimum away from that expected for an uncorrelated collision. In this scenario, equation 4.4 is not an accurate approximation.

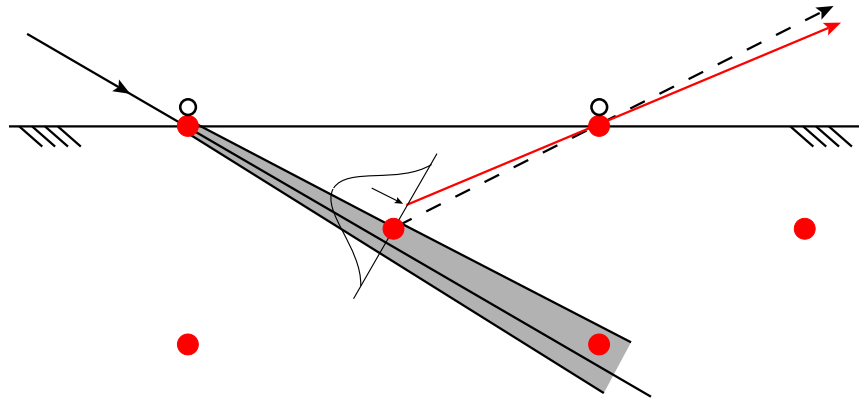


Figure 4.4: Schematic of a scattering plane perpendicular to a contracted surface. Open circles indicate the bulk-like position of the top layer. The Gaussian probability distribution  $G(x)$  is shown in a direction perpendicular to the ion beam, whilst the position at which backscattering is most likely is arrowed. The differing blocking directions thus determined from equations 4.3 (solid line) and 4.4 (dashed line) are shown [after Frenken<sup>2</sup>].

Two distinct solutions have been proposed. Firstly, a Monte Carlo method has been presented by Tromp and van der Veen. Incident (shadowing) tracks are first calculated by the standard method. The termination point  $x_k - \delta x_k$  of this calculation is then used as a new target atom position  $x_k$  for the detection probability calculation using Tromp and van der Veen's approach. The disadvantage of this method is that most of the ion tracks

generated are improbable, as the shift required to correlate the tracks  $\delta x_k$  is usually large compared to the vibration amplitudes of the atoms. The alternative solution uses a fine-mesh grid created around the atom in a plane perpendicular to the ion beam. Ion tracks are generated as before, but instead of evaluating the contributions of each ion track to the hitting probability of the atom, the probability distribution  $P^1(x_k)$  is determined by summing the ion tracks passing through each square of the grid. This procedure, when repeated to determine the time-reversed detection probability along the exit track, results in the space around  $x_k$  being divided into parallelepipeds which may be used in the numerical integration of equation 4.3. Substitution into equations 4.1 and 4.2 enables the solution of the approximated equation 4.4 in the same calculation for comparison. Frenken et al demonstrated that this approach added only  $\sim 20\%$  to the total calculation time<sup>2</sup>.

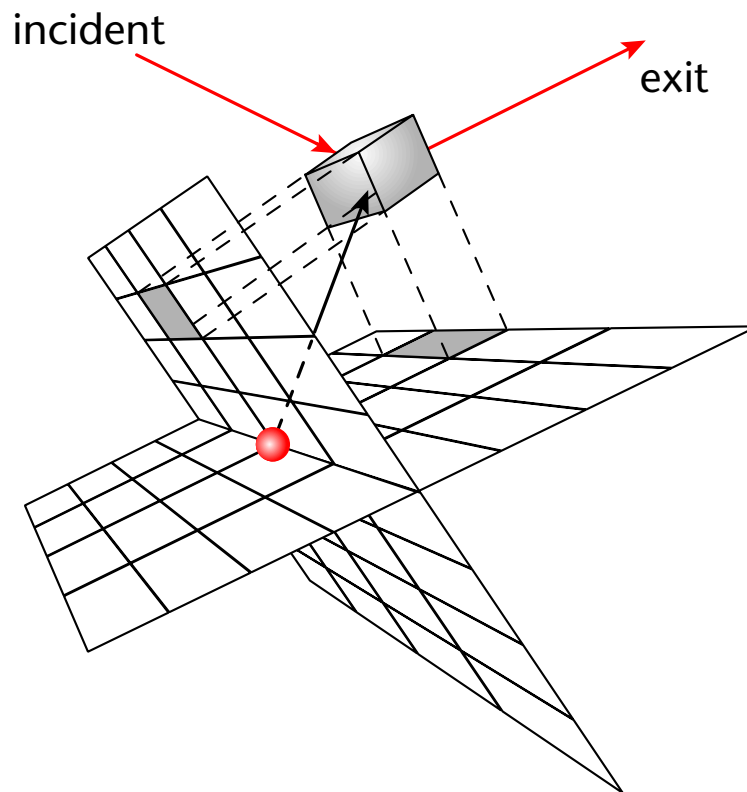


Figure 4.5: Grids perpendicular to the incident and detected beams for the accumulation of collision probability distributions around atom  $x_k$ . For one thermally displaced combination of grid points, the corresponding volume element is highlighted [after Frenken<sup>2</sup>].

### 4.3 Structural optimization

In simulating MEIS surface structure determination experiments, a crucial issue is the approach to structural optimization and evaluation of structural parameters. Whilst it is possible to make subjective judgments about the quality of fit for a given parameter set, it is clearly desirable to find an objective test of the result of our simulations.  $R$ -factors (or reliability factors) have been calculated in ISS for this purpose. In MEIS (and HEIS),  $R$ -factors have generally been based on a sum of squared deviations between experimentally measured and theoretically computed intensities  $I_e$  and  $I_s$ , after appropriate weighting and normalization. Three such  $R$ -factors are<sup>9,10</sup>

$$R_\chi = \frac{1}{N} \sum_i^N \frac{(I_e - I_s)^2}{I_e} \quad 4.7$$

$$R_{SQ} = \frac{1}{N} \sqrt{\sum_i^N (I_e - I_s)^2} \quad 4.8$$

$$R_{QS} = \frac{100}{N} \sqrt{\sum_i^N \left( \frac{(I_e - I_s)^2}{I_e} \right)} \quad 4.9$$

These  $R$ -factors are sensitive to the absolute intensity value, a parameter which is considered important in HEIS and is also well-known, since scattering cross-sections are Coulombic and known to a high degree of accuracy. In MEIS, absolute intensities are considered important, but are relatively less well-known due to imprecisions in the scattering cross-sections, instrumental factors and some charge transfer and neutralization effects as discussed in §3.4.6. A scaling factor is therefore generally required in fitting to the simulated intensities.

Although absolute intensities are important, the angular location of the blocking dips are often of greater interest.  $R$ -factors sensitive to dip and peak positions have been devised for a variety of surface crystallographic methods, including quantitative LEED, such as

$$R_{Pm} = \frac{\sum_i^N (I_e - I_s)^2}{\sum_i^N (I_e^2 + I_s^2)} \quad 4.10$$

This relation has been used in LEED, but with the intensities replaced by the logarithmic derivative  $I'/I$  of the intensities.<sup>11</sup> This  $R$ -factor,  $R_p$  entirely removes sensitivity to the absolute intensity. Alternative approaches replace the intensity with its derivative  $I'$  alone, retaining some intensity sensitivity, or with a factor  $\chi = (I - I_0)/I_0$ , where  $I_0$  is a smooth spline through the curve to be fitted.<sup>12</sup> The  $R$ -factor  $R_m$  resulting from this latter substitution is sensitive to both peak positions and absolute values of intensity modulations, but not to the intensities themselves. All of these alternative  $R$ -factors and substitutions have been studied and compared in the evaluation of MEIS structure analysis of a well-known metal surface, Ni(100)-c(2×2)-O. The results of this study were that, at least for this surface, any of the  $R$ -factors could be used to identify a best-fit structure.<sup>13</sup>

In the context of the work presented in this thesis, the  $R$ -factors were mostly determined using the wave analysis package Igor Pro<sup>14</sup>, running on a desktop PC. The chi-squared  $R$ -factor given in equation 4.7 above was used within a series of macros devised by Paul Bailey of CLRC Daresbury Laboratory (and amended and adapted by the author), which allowed the multiparameter datasets produced by the VEGAS code to be compared in sequence with stored experimental data and a best-fit solution selected by minimizing the  $R$ -factor.

It is important to note that the datasets collected were not calibrated to give absolute yields to allow direct comparison with simulations. Therefore, an  $R$ -factor obtained from a given experiment cannot be compared with that from other datasets or scattering geometries. Comparison of these  $R$ -factors is only meaningful within a single dataset.

The macros also determined a value for the experimental error  $\sigma$  for the best-fit (minimum)  $R$ -factor from a multiparameter calculation, based on the principle that for a given parameter, the higher the gradient of the  $R$ -factor curve the lower must be the error

$$\sigma = \sqrt{2 \left| \frac{d^2 R_k}{dx^2} \right|_{min}} \quad 4.11$$

## 4.4 Computational developments

### 4.4.1 VEGAS

A number of elements within the computational techniques described above have been developed in the evolution of this thesis. The most significant was the porting of the VEGAS code to the modern PC platform. The original VEGAS code was developed in Fortran 77 for the VAX 11/785 mainframe platform. The code at this point (in 1986) typically took 1 CPU hour to generate  $\sim 10^6$  complete ion tracks (hitting/detection probability pairs)<sup>2</sup>. This code was passed to Paul Bailey at the MEIS facility at CLRC Daresbury Laboratory, who made amendments to enable it to run on a Sun workstation running the Solaris operating system, with not dissimilar timescales for simulation.

Whilst this version was functional, its restriction to the Solaris platform had several disadvantages. Firstly, Solaris workstations are relatively rare compared to Windows/Intel ('Wintel') workstations, the global penetration of Wintel platforms currently representing around 90% of the desktop market worldwide. Solaris machines are also significantly more expensive. These two factors alone represent an impetus to convert or 'port' VEGAS to Wintel—making the code available to a greater number of potential users at much lower cost. As a further result of its ubiquity in the marketplace, the Wintel platform is under constant competitive development, with an approximate doubling of raw processing power in around an 18 month timeframe. This means that there should continue to be reductions in simulation time, enabling still more complex and thorough analyses.

The original Solaris code was split into two distinct parts; a 'front-end' program for building crystal structures and defining parameters, and a 'back-end' (multicalc) program which performed the actual multiparameter calculations. Separate back-end programs for single parameter and connected ion-track calculations existed but were not used or developed in this work.

Fortran 77 does not support dynamically generated arrays, where their dimensions can be specified in code at run-time rather than needing to be fixed before compilation. Therefore in the Solaris code, the front-end had to recompile the back-end at run-time before each simulation could begin, in order that the arrays could be statically-dimensioned. This resulted in a time overhead for each run, and furthermore required that a Fortran compiler be present on every machine running VEGAS. A port of VEGAS to Wintel gave the opportunity to take advantage of innovations brought in the Fortran 90 and 95 standards such as dynamic arrays, removing this dependency on recompilation and enabling some of the dimensional limits of the previous version to be raised. Another Warwick postgraduate, Paul Quinn, was writing a new Wintel-based VEGAS front-end for his work on metal adsorbate reconstructions, so there was already an investment in collaborating to develop the software at Warwick.

The opportunity was taken to rewrite some of the compute-intensive routines in the multicalc back-end program to be more efficient. Some optimizations, whilst relatively minor, were in routines that were run many millions of times in a simulation, thus presenting a noticeable increase in overall speed. A sample simulation was of a complex 117 atom unit cell. This was analysed over 151 distinct blocking angles with a total of  $\sim 1.3 \times 10^6$  ion tracks generated. This simulation took 11 hours plus recompilation time to complete on a Sun UltraSparc 1-143 workstation. Running in Windows 98 on a 533 MHz Pentium III processor, the same simulation took 9½ hours to complete, a saving of around 14% computation time. This saving could be increased further by running in a 'full-screen' mode on a dedicated PC.

A final area of change was the user interface. The command-line based approach was retained for familiarity, simplicity during porting, and partly to enable re-porting back to other console-based platforms should it be desired. A visual interface with the same level of functionality would realistically have required conversion to another development language and considerably more time. Certainly, this would be a useful avenue for future work. Instead, amendments were made to increase productivity in preparation of

simulations with the minimum of re-learning. Greater use was made of defaults, enabling standard parameter values or responses to decision queries to be given by a single key-press. Also, 'magic' values were allowed in certain routines, which if entered would enable back-tracking. Thus single data-entry errors, which would previously require the entire parameter set to be re-entered, could be corrected simply at source.

#### 4.4.2 Visualization

Another area of development undertaken by the author was in the area of visualization. The output of the VEGAS code includes information about the hitting and detection probabilities, simulation parameters used and, crucially, the final equilibrium positions of the atoms. However, there was no method available for visualizing this information graphically. This was the impetus for my developing a Delphi program, VEGASmagic, to extract this positional information from the VEGAS output files.<sup>15</sup> The program exports VEGAS files to two common file formats, that of Tripos' Alchemy and a subset of the Brookhaven Protein Data Bank (PDB) format. These formats are specifically designed for macromolecular description, but are equally well-suited to surface visualization. They can be read by a number of other common programs, including RasMol, a popular freeware molecular visualization tool available on platforms including Wintel, Macintosh, UNIX, RISC OS and VAX/VMS.<sup>16</sup> RasMol can calculate and display the van der Waals radii of atoms and determine the presence of bonds based on interatomic separations and enables interactive, dynamic stereoscopic visualization. It can also be used to produce publication quality colour images directly, as well as prepare VRML files and input files for ray-tracing. From this initial development, VEGASmagic was extended to import both VEGAS input files (the files created by the front-end, with complete simulation parameters) and VEGAS crystal files (a relatively simple format containing only atom positions and atomic numbers). After some use, it became clear that the ability to modify files or even model them entirely in the visualization environment, and import them back into VEGAS could prove useful. Hence, VEGASmagic was again updated to allow back-conversion from appropriate subsets of PDB and Alchemy format into VEGAS crystal files.

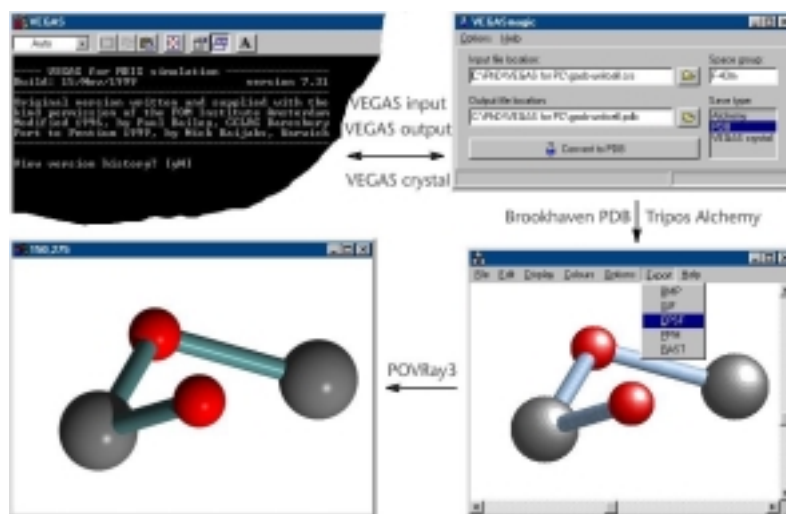


Figure 4.6: Workflow from VEGAS simulation to POVRay3 ray-traced rendering via the VEGASmagic conversion utility and RasMol molecular visualization software.

At the same time, the facility to transpose crystal symmetries (by reflecting in the  $xy$ -plane or  $z$ -plane) was added to simplify conversions between co-ordinate systems. Amendments to the RasMol source itself were also instigated to improve its export facilities. In particular, it was desirable to enable better PostScript colour reproduction and also to modify the representation of bonds when exported to POVRay3, a freeware ray-tracing and model-rendering package available for a number of platforms including Wintel, Macintosh, Linux and Solaris.<sup>17</sup> The combination of VEGASmagic, RasMol and POVRay3 has been used throughout this thesis to generate positionally-accurate ball-and-stick crystal representations based on VEGAS simulation results, with shadowing to provide depth-cueing. This subtle feature has a surprisingly large effect in accelerating the comprehension of three-dimensional models by visual interpretation of two-dimensional plan and side views. To demonstrate this, figure 4.7 shows a section of a relatively complex surface model (a GaAs(001)- $c(4\times 4)$  reconstruction) rendered relatively simply in RasMol and with realistic shadowing by POVRay3.

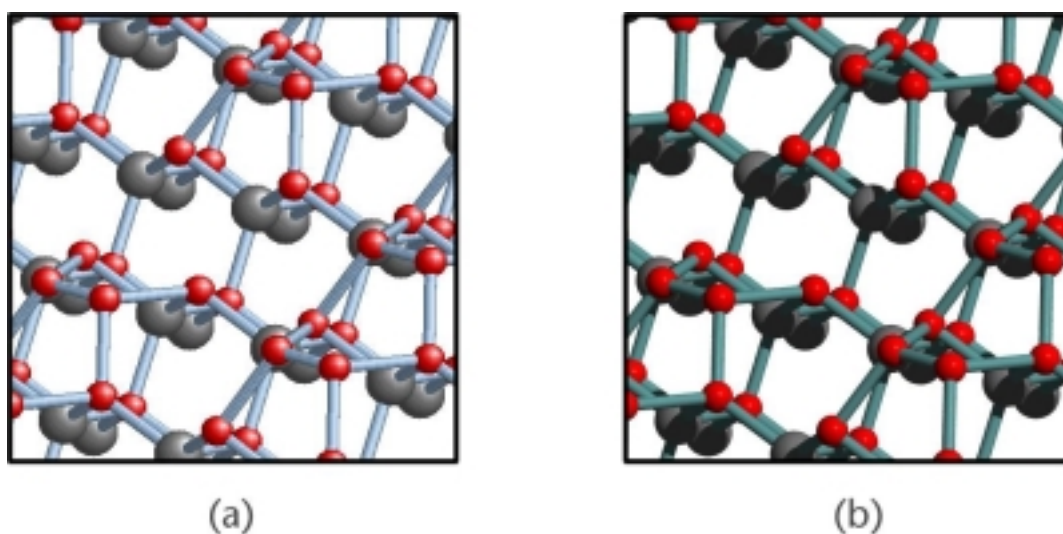


Figure 4.7: A model for the GaAs(001)-c(4x4) reconstruction rendered using (a) RasMol and (b) POVRay3. Note the shadowing providing depth-cueing information in the fully ray-traced representation.

## 4.5 References

- <sup>1</sup> R.M. Tromp and J.F. van der Veen: *Surf. Sci.* **133** (1983) 159
- <sup>2</sup> J.F. Frenken, J.F. van der Veen and R.M. Tromp: *Nucl. Instr. Meth. B* **17** (1986) 334
- <sup>3</sup> J.H. Barrett: *Phys. Rev. B* **3** (1971) 1527
- <sup>4</sup> R.M. Tromp and E.J. van Loenen: *Surf. Sci.* **155** (1985) 441
- <sup>5</sup> L. Smit, R.M. Tromp and J.F. van der Veen: *Surf. Sci.* **163** (1985) 315
- <sup>6</sup> L. Smit and J.F. van der Veen: *Phys. Rev. B* **29** (1984) 4814
- <sup>7</sup> L. Smit and J.F. van der Veen: *Surf. Sci.* **166** (1986) 183
- <sup>8</sup> L. Smit, T.E. Derry and J.F. van der Veen: *Surf. Sci.* **150** (1985) 245
- <sup>9</sup> Y. Kuk, L.C. Feldman, I.K. Robinson: *Surf. Sci.* **138** (1984) L168
- <sup>10</sup> Y. Kuk, L.C. Feldman: *Phys. Rev. B* **30** (1984) 5811
- <sup>11</sup> J.B. Pendry: *J. Phys. C: Solid State Phys.* **13** (1980) 937
- <sup>12</sup> D.P. Woodruff and A.M. Bradshaw: *Rep. Progr. Phys.* **57** (1994) 1029
- <sup>13</sup> T.C.Q. Noakes, P. Bailey and D.P. Woodruff: *Nucl. Instr. Meth. B* **136-138** (1998) 1125
- <sup>14</sup> Igor Pro, ©1997 WaveMetrics Inc., available for Windows and Macintosh platforms, information from <http://www.wavemetrics.com/>
- <sup>15</sup> VEGASmagic (current version 1.21 at time of writing) is freeware, downloadable from <http://www.kajjaks.co.uk/>
- <sup>16</sup> RasMol (current version 2.7.1 at time of writing) is freeware with source, downloadable from <http://www.iucr.ac.uk/iucr-top/cif/software/rasmol/>
- <sup>17</sup> POVRay (current version 3.1g at time of writing) is freeware, downloadable from <http://www.povray.org/>

## 5 • GaSb(001) surface reconstructions

### 5.1 Introduction

An important aim of this work was to examine a number of the commonly occurring surface reconstructions of the clean GaSb(001) surface. Whilst GaSb has been the subject of a number of studies in the past, its surface structures are by no means fully understood, and are far less well-known than the comparable surfaces of GaAs, for example. Indeed, whilst structural models have been proposed for a number of GaSb(001) reconstructions on the basis of STM data, no quantitative study of these structures has been performed to date. Fundamentally, our current understanding of GaSb(001) reconstructions are largely extrapolated from the broader body of knowledge of GaAs. Compared to metal surfaces, even the surface of GaAs has been the subject of relatively few structural determination studies. To contextualize this work it is therefore appropriate to begin by reviewing the major reconstructions of GaAs(001). Current models for GaSb(001) are reviewed, followed by details of the experimental work performed on GaSb surfaces. Discussion of the results includes quantification of structural parameters for some of the models proposed for common reconstructions and the identification of a new surface reconstruction.

### 5.2 GaAs(001) surface reconstructions

A number of different reconstructions have been found on the clean polar (001) surfaces of III–V semiconductors. These III–V surface reconstructions typically exhibit large unit cells and dimerized structures with or without missing rows. The nature of the preparation conditions (both temperature and techniques) and relative concentrations of group III and group V elements at the surface are the primary factors in determining which particular reconstruction is exhibited. Studies have been performed using a number of analytical techniques, mostly STM to gain real space (visual) and electronic information, LEED or RHEED for translational periodicity information and surface x-ray diffraction (SXRD) for atomic structural information. Almost all of these surfaces have been prepared by IBA, which, as discussed in §3.3.1, frequently sputters group V atoms preferentially from the

surface resulting in a group III-terminated surface unless an over-pressure of the group V element is maintained. This section outlines the presently accepted structural models for some of these surfaces. All of these GaAs(001) reconstructions and the history of their analyses are discussed in a recent review by Xue.<sup>1</sup> The principal reconstructions of GaAs(001) are, in order of decreasing arsenic concentration;  $c(4\times 4)$ ,  $(2\times 4)/c(2\times 8)$ ,  $(4\times 6)$  and  $(4\times 2)/c(8\times 2)$ .<sup>2,3,4</sup>

The most As-rich is the  $c(4\times 4)$ , observed under extreme conditions of low temperature and arsenic flux during MBE growth. On the basis of RHEED, photoemission and STM studies, the  $c(4\times 4)$  is believed to be an overlayer-derived phase based on chemisorbed As, trigonally-bonded to a complete layer of As atoms in the second layer.<sup>5,6</sup> The models shown in figure 5.1 maintain the two-fold symmetry expected from the dangling-bond structure but also have the required square unit cell and (as do all the GaAs reconstructions discussed here) satisfy the ECM. These  $c(4\times 4)$  domains are not mutually-exclusive, and may therefore co-exist in different regions of a surface. These structures are also viable with individual missing atoms, explaining the variety of AES-measured coverages of As that have been reported, from around 0.86 ML to 1.75 ML.

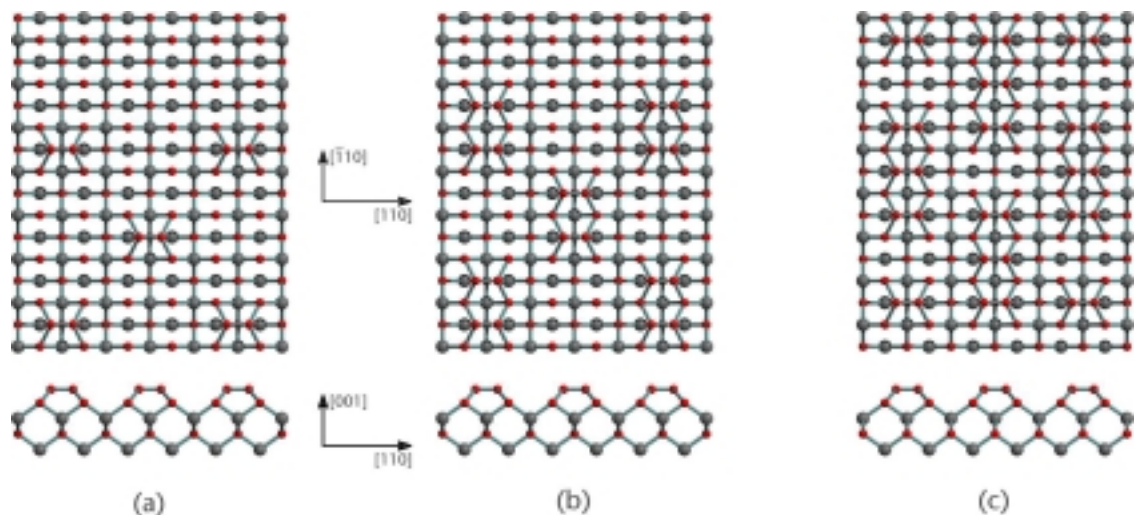
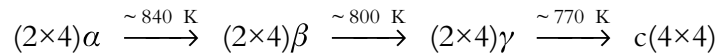


Figure 5.1: GaAs(001)- $c(4\times 4)$  structural models. All three are based on a complete As layer adsorbed with extra As. The As atoms are shown as red, Ga atoms as grey.

The  $c(2\times 8)$  reconstruction is common over a range of growth temperatures, and as such has been the subject of much study. Various models have been proposed, largely featuring dimerized structures based on  $(2\times 4)$  blocks with neighbouring rows translated by a half-unit to give the  $c(2\times 8)$  structure. The first model, based on HREELS data, consists of top-layer blocks each containing three As dimers and one dimer vacancy as shown in figure 5.2(b).<sup>7</sup> Later STM analysis and tight-binding total-energy calculations suggested two other structures where the  $(2\times 4)$  blocks are built from pairs of As dimers and pairs of dimer vacancies, differing in the presence or absence of a second layer As dimer, as shown in figure 5.2(a) and (d).<sup>8,9,10</sup> Further studies have concluded that these models, sometimes modified by the addition of extra As dimers atop the existing dimer structure, as in figure 5.2(c), are essentially consistent with experimental results. Three identifiable phases ( $\alpha$ ,  $\beta$ ,  $\gamma$ ) have been observed under different annealing conditions



with distinct RHEED intensity patterns and differing forms visible in STM. All require As flux during heating to avoid non-congruent sublimation to the more Ga-rich reconstructions described hereafter.

A MEIS study has reported contrasting data, consistent with a three-dimer model, but with some degree of substitution of Ga for As in the top layer.<sup>11</sup> The conclusion from this and other studies is that although the surface reconstruction is based upon  $(2\times 4)$  blocks with As dimers and dimer vacancies, there may not only be differences between surfaces prepared under different conditions but significant variations within a given surface.

A final important factor to note is that many  $c(2\times 8)$  reconstructions have been reported as having  $(2\times 4)$  symmetry on the basis of RHEED studies alone, since RHEED is not as sensitive to the disorder in the  $[110]$  direction as LEED. Hence in this thesis, the notation  $(2\times 4)/c(2\times 8)$  is used to represent both reported symmetries as essentially the same reconstruction.

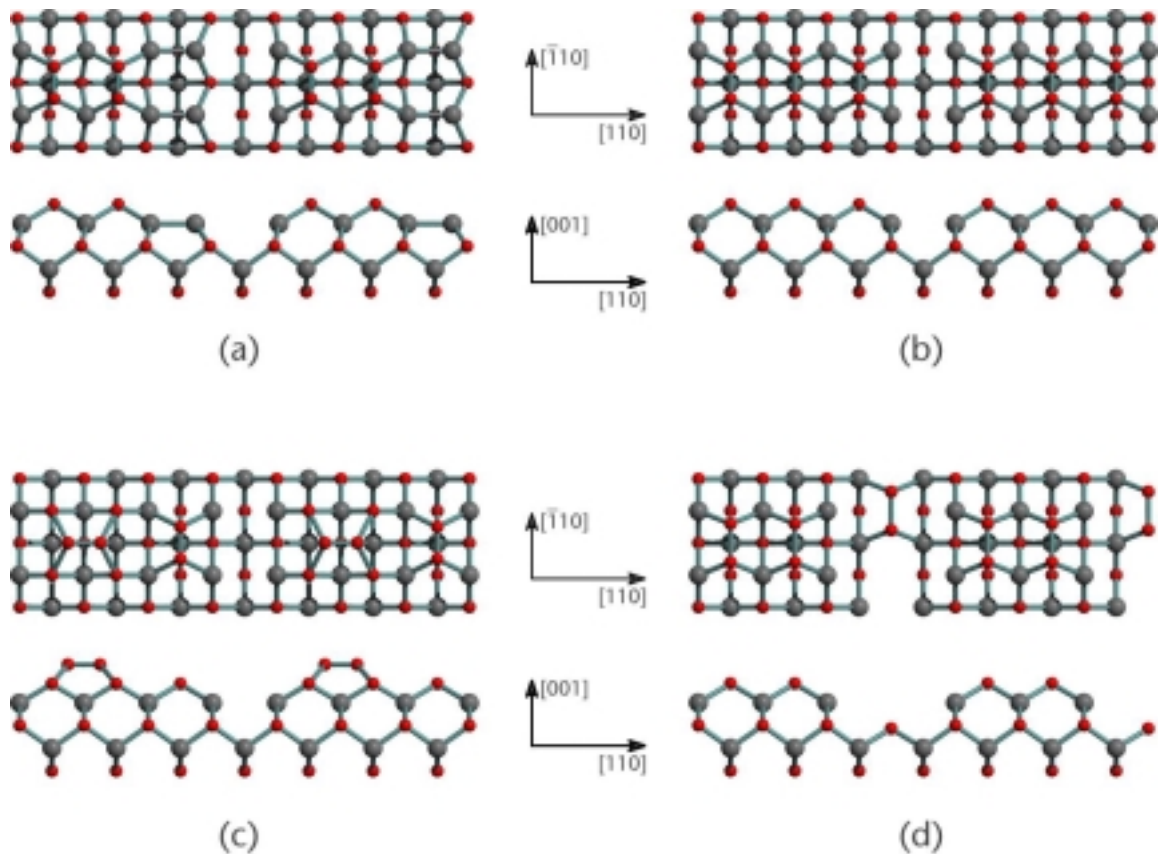


Figure 5.2: GaAs(001)-(2×4) structural models, which form  $c(2\times 8)$  when blocks align in antiphase. (a) two As dimer model with second-layer Ga dimers ( $\alpha$ -phase), (b) three As dimer model ( $\beta$ -phase), (c) extra As dimer model ( $\gamma$ -phase), (d) bilayer two As dimer model.

There are a number of transient phases of GaAs(001) with near-equal Ga–As surface ratios. A (1×6) reconstruction may be prepared on a surface cleaned by argon IBA with an anneal temperature of around 770 K.<sup>4</sup> Alternatively, it may be approached from the Ga-rich (4×2)/ $c(8\times 2)$  surface by cooling under a low As pressure<sup>2</sup>, or by thermal desorption of As from the  $c(4\times 4)$  or (2×4)/ $c(2\times 8)$  under UHV.<sup>12</sup> The basic (1×6) symmetry of the LEED or RHEED pattern is always modified by disorder lines or streaks, which have led to it being reported as having (2×6), (3×6) or (6×6) symmetry. STM studies have shown that this reconstruction is intrinsically irregular whilst energetic considerations suggest that the (1×6) is probably only a metastable, transient reconstruction. A proposed model is shown in figure 5.3.

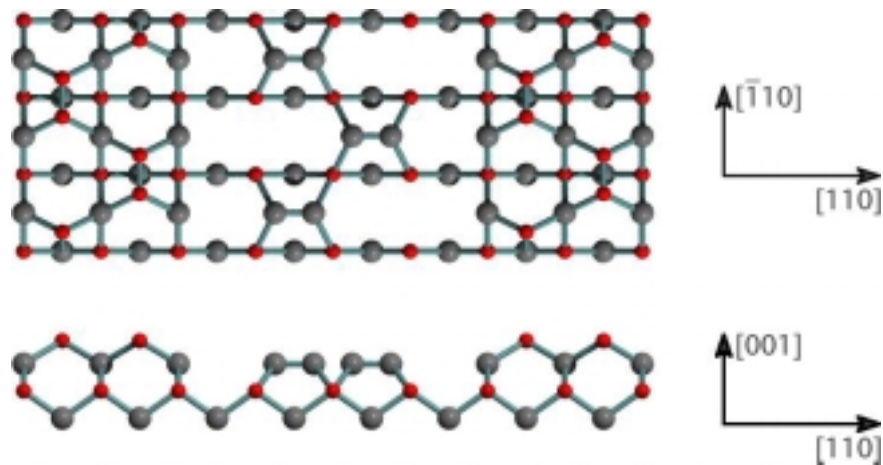
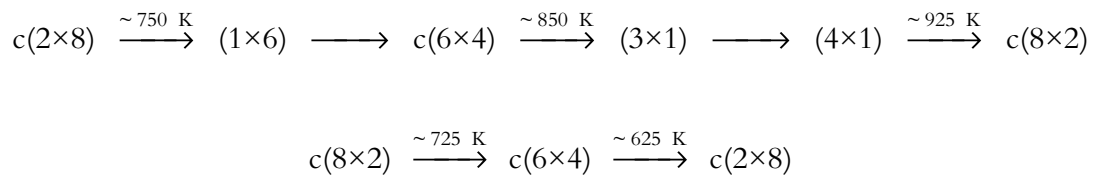


Figure 5.3: (1×6) metastable reconstruction of GaAs(001).

Although it is not a commonly observed reconstruction, the GaAs(001)-c(6×4) surface is of particular interest in relation to the work performed on GaSb(001) in this thesis. The GaAs(001)-c(6×4) appears to be another metastable state, seen during the transition from the c(2×8) to the c(8×2) type reconstructions under UHV heating<sup>13</sup> and in the reverse cooling process



Some related structural models have been proposed for this phase, with staggered Ga dimers (as shown in figure 5.4).<sup>14</sup>

Based on this model, it has been suggested that the (3×1) phase sometimes reported is merely a disordered form of the c(6×4), retaining only the threefold periodicity from the interlocked dimers. Other metastable structures reported include a (2×3) reconstruction composed of domains of (4×3) and c(4×6).<sup>15</sup> Models are shown in figure 5.5.

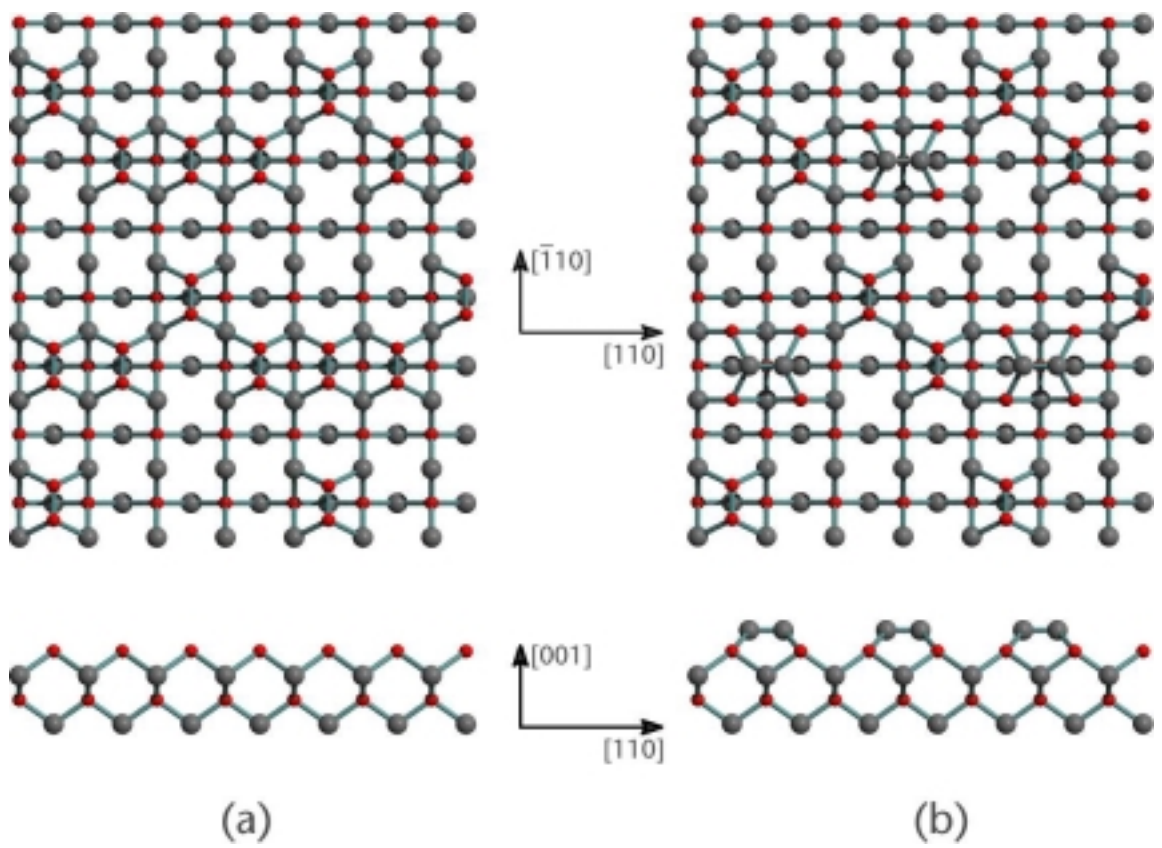


Figure 5.4: Metastable phases of GaAs(001). Proposed structural models for the  $c(6 \times 4)$  reconstruction.

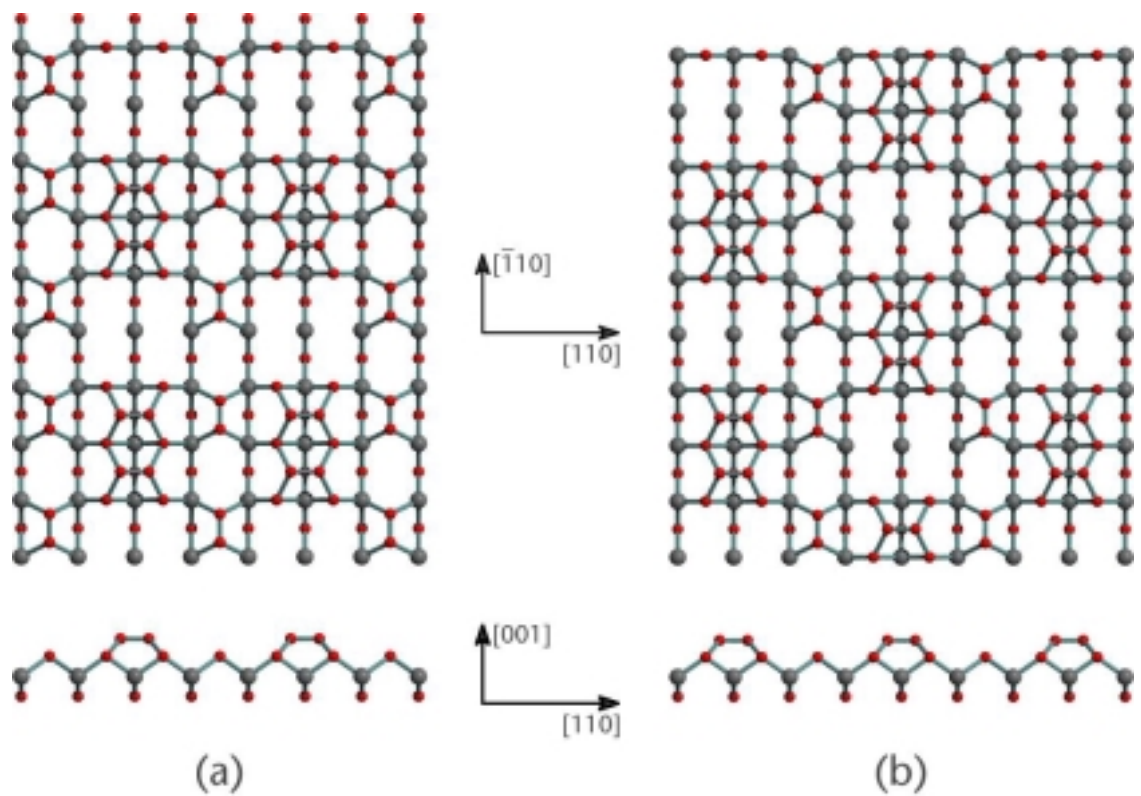


Figure 5.5: Ga-rich metastable reconstructions of GaAs(001). (a)  $(4 \times 3)$  and (b)  $c(4 \times 6)$  models.

The  $c(8\times 2)$  is a Ga-terminated reconstruction, readily obtained by annealing an MBE-grown substrate or an IBA-treated sample under UHV (without As flux). Although first observed in the 1960s with LEED and RHEED in the same initial studies as of the  $(2\times 4)/c(2\times 8)$  phase<sup>16,17</sup>, a structural model was not proposed until 1987, to explain the results of HREELS studies.<sup>7</sup> This model concluded that the four-fold periodicity was most likely to be due to a  $(4\times 2)$  block containing three Ga dimers and a single missing-dimer, rotated by  $90^\circ$  compared to the  $(2\times 4)$  block structure, as in figure 5.6(a). As in the case of the As-rich  $(2\times 4)/c(2\times 8)$ , further studies by other techniques have supported the case for a dimer vacancy-based model, although a two-dimer bilayer structure, modelled in figure 5.6(b), seems to be most consistent with the results of both STM and theoretical studies.<sup>10,18</sup> Unlike the As-rich  $(2\times 4)/c(2\times 8)$ , there is no characteristic RHEED intensity variation behaviour for the  $c(8\times 2)$ .<sup>19</sup> The single-phase  $(4\times 2)$  is difficult to isolate and it can therefore be inferred that it has only a relatively narrow range of stable composition (at  $\sim 0.75$  ML Ga).

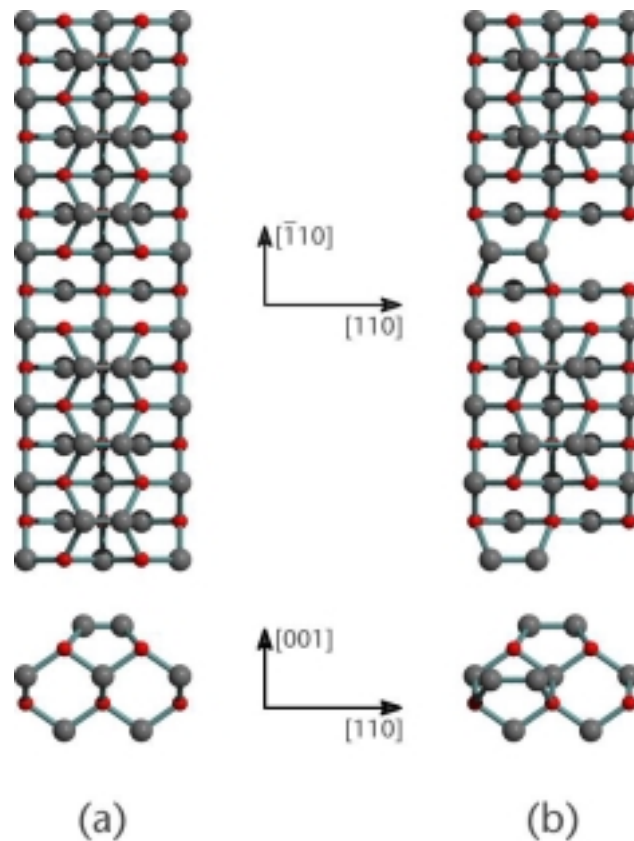


Figure 5.6: GaAs(001)- $(4\times 2)$  structural models, blocks of which form a  $c(8\times 2)$  reconstruction when laid adjacent with antiphase alignment. (a) three Ga dimer model and (b) bilayer two Ga dimer model.

An important implication of these models for the As-rich  $c(2\times 8)\beta$  and Ga-rich  $c(8\times 2)$  is that ignoring atom species, the two models are mirror-symmetric. The  $(2\times 4)$  unit cell has two surface As dimers and one third-layer As dimer, thus containing  $\frac{3}{4}$  ML of As on the surface. The  $(4\times 2)$  unit cell has two surface Ga dimers, and one third-layer Ga dimer, resulting in  $\frac{3}{4}$  ML of surface Ga. Addition of 1 ML of Ga to the As-rich  $(2\times 4)$  surface results in the Ga-rich  $(4\times 2)$  surface and vice-versa. This relationship between the surfaces may have significant implications for control of GaAs(001) epitaxial growth.

A primitive  $(4\times 6)$  reconstruction has long been observed by electron diffraction studies, but for many years, no structural models were proposed due to the large and complicated unit cell. The absence of a complete LEED pattern and variations in reported surface stoichiometry (from 0.33 ML to 1 ML Ga) led to the belief that the structure was composed from a combination of  $(1\times 6)$  and  $(4\times 2)$  domains, with or without disordered regions (depending on the preparation method and conditions).<sup>4</sup> The existence of such a ‘pseudo’  $(4\times 6)$  has been confirmed by STM, although a distinct and apparently ‘genuine’  $(4\times 6)$  structure has since been isolated. This surface has been prepared by annealing at 875 K or MBE growth in a Ga flux at 775 K, a higher temperature than that required to form the  $(4\times 2)/c(8\times 2)$ .<sup>9</sup> STM study suggests that the structure is the most Ga-rich reconstruction of GaAs(001), and is again a bilayer dimer-vacancy reconstruction. However, it is distinguished from a  $(4\times 2)$  structure by Ga clusters or droplets at the unit cell corners, each estimated to contain around 6–8 atoms, as shown in figure 5.7. On the basis of this model, the reconstruction is metallic in nature, with a Ga coverage of 1–1.2 ML. It has since been established that some reported ‘pseudo’  $(4\times 6)$  reconstructions are actually a combination of the  $(1\times 6)$  and the ‘genuine’  $(4\times 6)$  phases. Annealing the  $(1\times 6)$  reconstruction to around 925 K or depositing around 2 ML Ga leads to a  $(4\times 1)$  reconstruction. Like the  $(4\times 6)$ , this is based on a  $(4\times 2)$  block, with large, superimposed clusters of Ga. Annealing to 975 K leads to surface roughening and decomposition, suggesting that these clustered reconstructions are the last stable single-phase Ga-rich structures of the GaAs(001) surface.

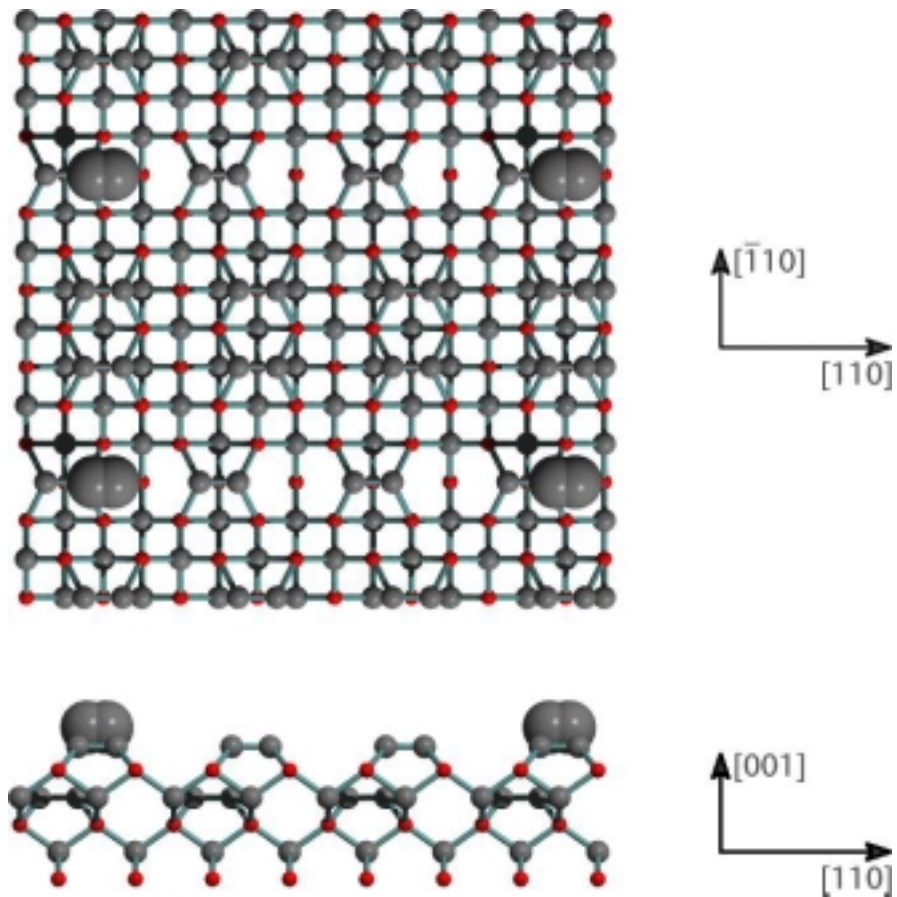


Figure 5.7: Structural model for the 'genuine' GaAs(001)-(4×6) reconstruction.

In summary, the GaAs(001) surface exhibits a variety of stable reconstructions reproducible across a broad range of preparation conditions. The electron counting model, discussed in §2.3.2 applies to all the models discussed, and almost all are consistent with a dimer/dimer-vacancy model, largely based around blocks with a (4×2) or (2×4) unit cell. Dimerization reduces the number of surface dangling bonds, whilst missing-dimers maintain overall charge-neutrality. The variety of different structural models is due to the relatively small energy differences between different arrangements of the blocks, and of the atoms within these blocks. A number of metastable reconstructions can also be observed in the transitions between the more stable reconstructions, some of which account for less-commonly reported phase symmetries, both alone and in combination with other phases.

### 5.3 GaSb(001) reconstructions

The surface reconstructions of GaSb(001) are in some respects quite different from GaAs, although dimerization remains a central factor. One particularly interesting feature of GaSb is that even the most Ga-rich reconstruction reported, the  $(1\times 3)$ , still has more Sb than Ga at the surface.<sup>20</sup> To date, no Ga-terminated phase has been reported for GaSb(001). In order of decreasing antimony concentration, the principal phases of GaSb(001) have  $(2\times 5)$ ,  $(1\times 5)/c(2\times 10)$ ,  $c(2\times 6)$  and  $(1\times 3)$  symmetry.

The GaSb(001)- $(1\times 3)$  reconstruction is the most Ga-rich to have been reported. It has been generated during MBE growth, by IBA (500 eV Ar<sup>+</sup>, 775 K anneal) and by AHC (150 kL H<sub>2</sub> dose at 675–750 K substrate temperature).<sup>21</sup> A structural model consisting of  $\frac{2}{3}$  ML dimerized Sb and  $\frac{1}{3}$  ML Ga atop a complete monolayer of Sb has been proposed, based on photoemission spectroscopy (PES) and STM study, with one Sb dimer per unit cell.<sup>20</sup> It is worth noting that it is reproduced differently in the review by Xue<sup>1</sup>, with the Ga in the second rather than first layer. This difference is unqualified and nonphysical, suggesting an error in drafting. The model is consistent with the ECM and is shown in its original form in figure 5.8. The Sb–Sb trigonal bonding is an important structural feature, similar to the As–As bonding proposed for the Ga-rich GaAs(001)- $c(4\times 4)$  reconstruction discussed in the previous section, and also occurs in other antimonides such as AlSb and InSb. Although the surface is considered Ga-rich, the coverage remains relatively low, compared to group III-terminated surfaces of other III–V materials.

The  $c(2\times 6)$  has been prepared by annealing the  $c(2\times 10)$  reconstruction at above around 675 K or by annealing the  $(1\times 3)$  phase below 775 K in Sb flux. It has a similar proposed structure; indeed many studies do not distinguish between them, assuming that they are the same reconstruction with different degrees of disorder. However, a PES study has shown that the  $c(2\times 6)$  has no top layer Ga, unlike the  $(1\times 3)$  phase. It is suggested that the weak two-fold symmetry sometimes observed in RHEED study of the  $(1\times 3)$  surface could be due to lateral buckling of the Ga atom chains, which may have caused confusion

between the phases. The model for the  $c(2\times 6)$  reconstruction (shown in figure 5.8) ascribes the two-fold symmetry to staggered Sb dimers in the second layer between the parallel Sb dimer chains.<sup>22</sup> This model has been supported by further studies with LEED and STM<sup>23</sup> and is consistent with the ECM. In summary, both the  $(1\times 3)$  and  $c(2\times 6)$  phases are based on continuous Sb dimer chains atop a complete Sb overlayer. The centred reconstruction is due to antiphase second layer dimerization normal to top layer dimers.

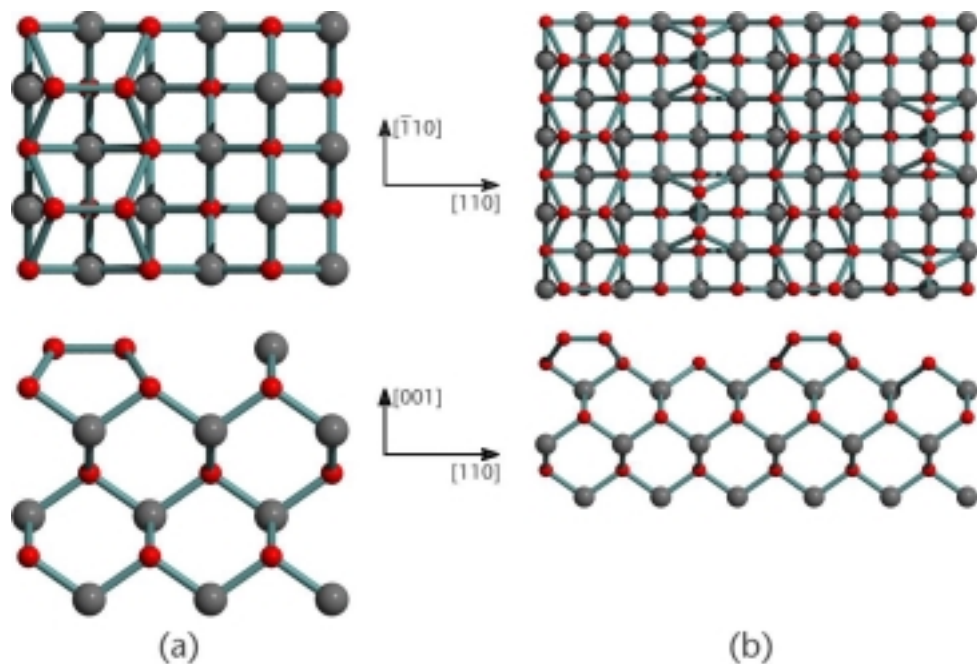


Figure 5.8: Structural models for (a) GaSb(001)- $(1\times 3)$  and (b)  $c(2\times 6)$  reconstructions. Sb atoms are shown as red, Ga atoms as grey.

The  $c(2\times 10)$  phase has been observed by RHEED after MBE growth and annealing at around 475 K with an Sb flux. It is stable and indeed improves in quality upon cooling to room temperature, even without Sb flux. PES demonstrated it to be an extremely Sb-rich reconstruction ( $\sim 2.2$ – $2.6$  ML surface coverage).<sup>22</sup> Based on this, a structural model was proposed (shown in figure 5.9), with triple Sb dimer blocks (similar to the GaAs(001)- $c(4\times 4)$  phase), each with a  $(2\times 5)$  unit cell, staggered to give the centred symmetry. However, a major argument against this model is that multiple layers of Sb would be more likely to bond trigonally throughout, not solely in the top layer as suggested.<sup>5</sup>

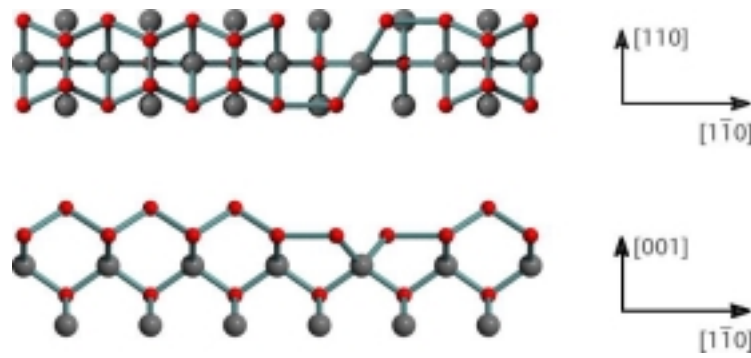


Figure 5.9: Initial structural model for GaSb(001)-(2×5), forming the c(2×10) when staggered.

More recent STM study also suggests a different structure. Two related models have been proposed for the c(2×10) symmetry, also based on (1×5) or (2×5) blocks (shown in figure 5.10) with different amounts of adsorbed Sb.<sup>24</sup>

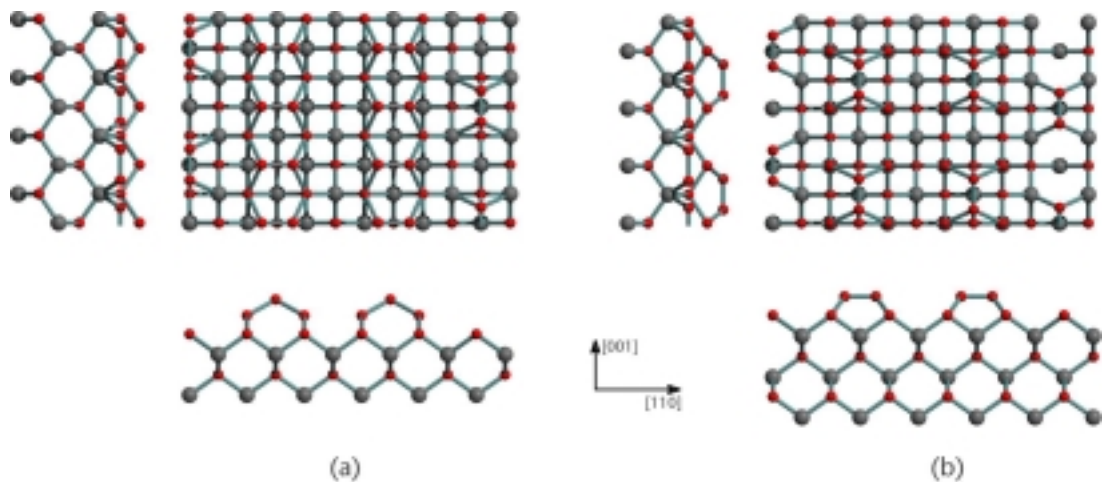


Figure 5.10: Alternative structural models for (2×5) and (1×5) blocks that form the c(2×10) reconstruction of GaSb(001).

Unlike all other III–V semiconductors studied to date (including AlSb, GaAs and InAs), the (001) surface of GaSb does not reconstruct to c(4×4) at any substrate temperature or Sb<sub>4</sub> coverage. Instead, (*n*×5) reconstructions are formed which, given the absence of surface Ga, are weakly metallic and violate the ECM.<sup>25</sup> For each (2×5) unit cell, there are three valence electrons remaining which must therefore occupy midgap or conduction band states. Hence the surface is expected to be metallic, and this is indeed observed in STM. The question of why these (*n*×5) structures form instead of the more common c(4×4) is answered by consideration of the strain induced by lattice mismatches; the formation of surface dimers induces strain. For example, surface Sb dimerization on GaSb

will result in a shift in the Sb atoms from their bulk separation of 4.3101 Å towards the natural Sb–Sb bond length of 2.9 Å, a 30% displacement. However, the lattice parameter of trigonally-bonded elemental Sb, at 4.3083 Å, is nearly equal to that of bulk GaSb(001) (with only 0.04% difference). Hence, formation of a double surface layer of trigonally-bonded Sb greatly reduces the strain within this system. The subsurface layer remains in bulk-like positions, whilst the top layer forms continuous dimer chains free of strain, with the lattice well-enough matched for further unstrained overlayers of rotated Sb dimers. By contrast, for most III–V surfaces this close lattice matching does not exist. Instead, missing dimers and surface relaxation relieve the strain, resulting in the  $c(4\times 4)$  reconstruction.

## 5.4 Experimental work

### 5.4.1 The Warwick CAICISS system facilities

The CAICISS apparatus at Warwick was designed, built and commissioned in-house.<sup>26</sup> It consists of a Nielson ion source generating He<sup>+</sup> or Ne<sup>+</sup> ions in the range 1–4 keV. The beam is electrostatically filtered to remove neutrals and multiply-charged ions by steering it through an aperture before being directed along an ion column onto a sample mounted on a manipulator with two rotational and three translational degrees of freedom. Ions backscattered at  $179\pm 1^\circ$  pass along the ion column striking an annular microchannel plate detector mounted coaxially around the ion beam.

The system is pumped at the ion source and in the scattering chamber, which is also equipped with a ‘hot cathode’ ion gun (ISIS 3000 from PSP Ltd) for IBA, a hydrogen thermal cracker source (Atom–H from EPI Ltd) for AHC, as described in §3.3.2, a reverse-view LEED optic (Omicron GmbH), electron gun and concentric hemispherical analyser (from VG Ltd) for AES. Spectra are recorded using a proprietary Wintel PC-based data acquisition system. The ion beam is pulsed by electrostatic deflection to enable time-of-flight (TOF) measurement of backscattered ion yield. A multi-channel analyser records the yield, across a user-defined window of ion times-of-flight, typically over a period of three minutes. From this, the backscattered ion energy can be derived via equation 3.27.

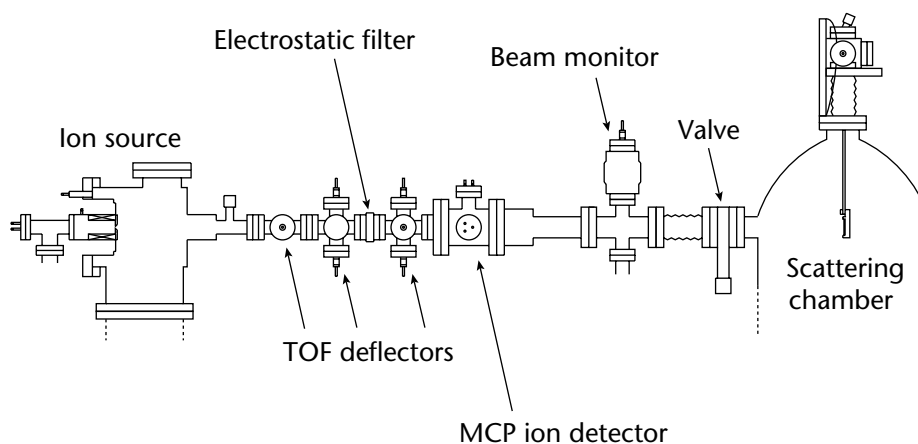


Figure 5.11: Profile schematic of the Warwick CAICISS ion column (approximately 1.5 m in length). Other analytical equipment present on the scattering chamber is not shown. The system is diffusion-pumped (with additional titanium sublimation pumping) at the ion source and scattering chamber, with an additional getter-ion pump in the scattering chamber. The ion column vacuum is maintained by a turbomolecular pump.

A significant effort was made during this studentship to both renovate and develop the CAICISS apparatus. In order to meet increasing safety standards, significant electrical and plumbing work was required, whilst a number of components needed maintenance and renovation. This included a complete overhaul of the AES system and rectifying a problem of occasional fluctuations in the ion source energy. At first, it was presumed to be an intermittent fault in the electrical supply to the source. Investigating the supply proved difficult, as it was designed to match the ion source load, and its characteristics changed completely under different loading. It was eventually concluded that the supply was operating correctly. Attention was therefore turned to the source itself, which had not been vented to atmospheric pressure for some years. Upon inspection, it was found that metallic deposits had accumulated on the ceramic insulators within the source, probably a result of evaporation from both the titanium sublimation pump and molybdenum filament. These deposits provided an electrical path across the surface of the insulators, which would certainly account for the observed fluctuations. After cleaning, the source was re-assembled with a new filament fitted. The source documentation did not specify the dimensions of the filament and the original filament did not survive venting and disassembly intact, making determination of the correct parameters difficult. Several cycles of filament winding and fitting, pumping, baking and degassing were required to create a filament that did not fail during re-commissioning capable of obtaining experimental information.

#### 5.4.2 The MEIS facility at CLRC Daresbury

The Medium-Energy Ion Scattering (MEIS) facility at CLRC Daresbury Laboratory was officially opened in 1996. It is a unique facility in the UK, developed as a joint venture between the Universities of Warwick and Salford and CLRC Daresbury Laboratories, based on the design of the FOM/AMOLF group in Amsterdam.

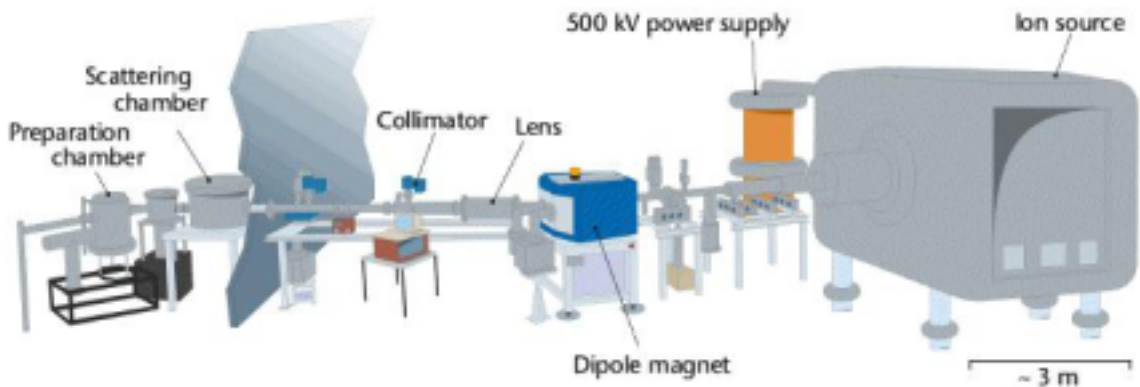


Figure 5.12: Schematic of the Daresbury MEIS beamline (~ 12 m in length from source exit to scattering chamber).

$H^+$  or  $He^+$  ions are accelerated to an energy selectable between 50–400 keV and focused along a beamline of some 10 m in length, onto a sample in a UHV scattering chamber. The spot size at the sample is 1 mm horizontal by 0.5 mm vertical, with divergence  $< 0.1^\circ$ . When not actually recording data, the sample is shielded from the beam by a Faraday cup. The sample is mounted on a motor-driven goniometer with three rotational and three translational degrees of freedom. Scattered ions are collected by a toroidal electrostatic analyser (TEA) with a pass energy selectable from 0–400 keV and energy resolution of  $dE/E = 2.4 \times 10^{-3}$ . A position-sensitive detector, consisting of a chevron array of anodes with micro-channel plates, integrates ion yield over time across a range of scattering angles of  $\sim 24^\circ$  (with  $< 0.3^\circ$  resolution) and an energy window of 2% of the pass energy (shown in schematic in figure 5.13). The result is a two-dimensional ‘tile’ spectrum of yield against energy and scattering angle. A current monitor measures and maintains a constant total detected dose for each tile (typically  $4 \mu C$  for this work on GaSb). It is normal practice to move the sample (by around 1 mm) between data collection for each tile, in order to avoid localized beam damage of the surface.

Tiles can be recorded for various backscattered energy windows, from near the primary beam energy (representing surface elastic scattering events) to much lower energies (due to scattering events from deeper in the bulk). Also, tiles can be recorded across a range of different detection angles. These tiles can be ‘stitched’ together with software to give an overall 2D spectrum of the yield across the whole dataset. The source, ion beam transport, sample alignment and data acquisition are all fully remotely controlled using a Solaris-based computer system. A sample spectrum from this study, of a GaSb(001)–(1×3) reconstruction, is shown in figure 5.14. From this 2D spectrum, yield profiles in energy (and hence depth) or scattering angle can be derived by simply taking appropriate cross-sections.

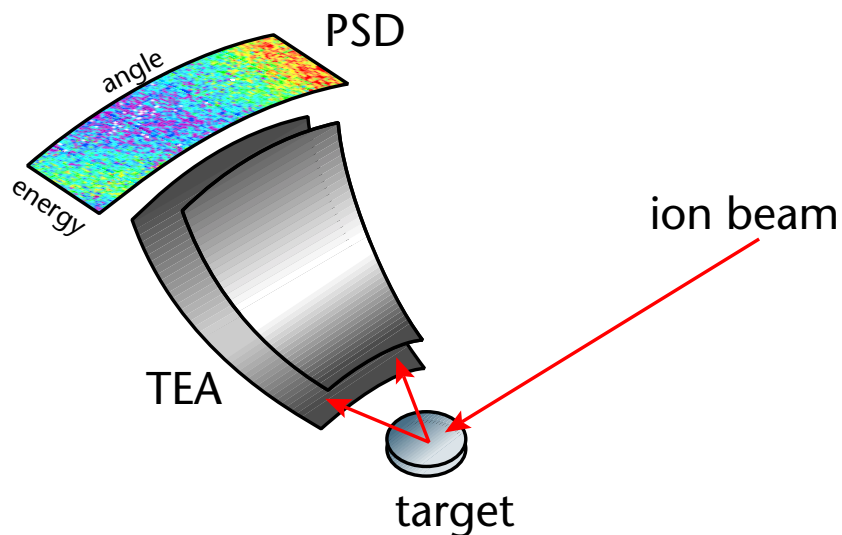


Figure 5.13: Schematic of the Daresbury MEIS detector, showing the toroidal electrostatic analyser (TEA) and position sensitive detector (PSD) in relation to the sample and beam. A sample tile image is superimposed on the PSD to indicate the type and form of data recorded.

In addition, the MEIS facility has three other chambers, for sample loading, storage and preparation. All four are separately pumped and separated by gate valves, but are interconnected *in vacuo* by transfer arms enabling straightforward sample movement between them. The loading chamber has a load-lock enabling fast pumping-down from atmospheric pressure to  $\sim 10^{-6}$  mbar, and a filament-heated sample mount for preliminary degassing. Samples may then be moved to the storage chamber where further degassing is possible, thence to the preparation chamber where filament or  $e^{-}$  beam annealing is

possible. This chamber is also fitted with a reverse-view LEED optic, electron gun and concentric hemispherical analyser for AES (all equipped by VG Ltd) and several spare ports. The hydrogen cracker source and an antimony-filled k-cell (Oxford Instruments Ltd) were both brought from Warwick and fitted to the preparation chamber for the work presented in this thesis.

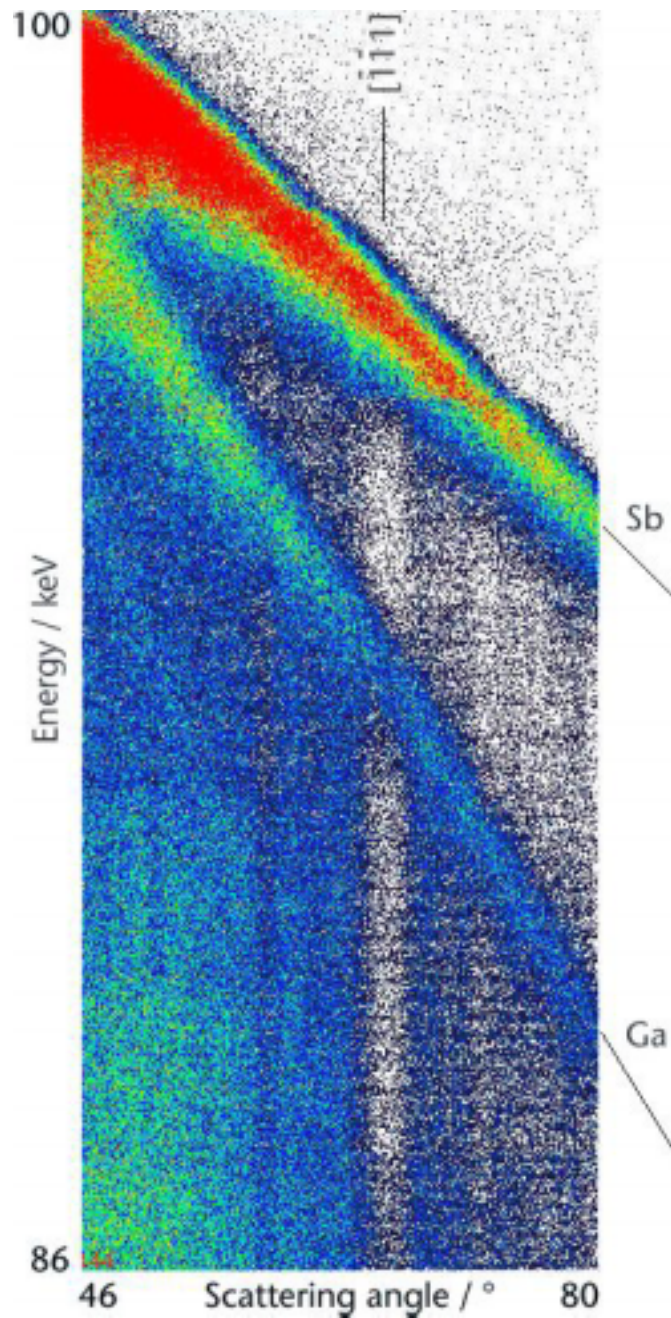


Figure 5.14: A sample 2D MEIS spectrum stitched together from several individual tiles for a partially AHC-cleaned GaSb(001)-(1×3) sample, with incident ion beam along the  $[111]$  channelling direction. Increasing scattered intensity is represented as a colour change from white through blue to red. The Sb and Ga surface peaks (labelled) are angled because there is a characteristic fall-off in energy with scattering angle (from equation 3.25).

### 5.4.3 Experiments

The experiments performed on GaSb(001) fell into two main classes. In the first type, CAICISS was used as a real-time analytical technique for monitoring surface condition and then decomposition upon annealing of AHC-prepared surfaces. In the second type, MEIS was used to analyse the surface structure of GaSb(001) reconstructions produced by AHC and Sb<sub>4</sub> deposition at elevated temperatures. In both series of experiments, LEED and AES were used to provide additional symmetry and compositional information.

The samples of GaSb(001) were Te-doped to a bulk carrier concentration of  $n \sim 5 \times 10^{17} \text{ cm}^{-3}$  and mechanically polished and chemically etched by the manufacturer, MCP Wafer Technology Ltd. Each wafer sample was cut, cleaned and mounted onto a sample holder prior to introduction to the chamber. Once *in vacuo* the samples were degassed thoroughly for at least one hour. Experiments were performed with a scattering chamber base pressure below  $10^{-9}$  mbar and a preparation chamber base pressure below  $10^{-8}$  mbar. During AHC, the chamber pressure was typically  $5 \times 10^{-5}$  mbar, with dose times between 15–45 minutes. Molecular hydrogen was supplied from a low pressure cylinder (Messer Gresheim GmbH) and thermally-cracked by a tungsten filament at  $\sim 2100$  K surrounded by a water-cooled jacket, as shown schematically in figure 5.15.

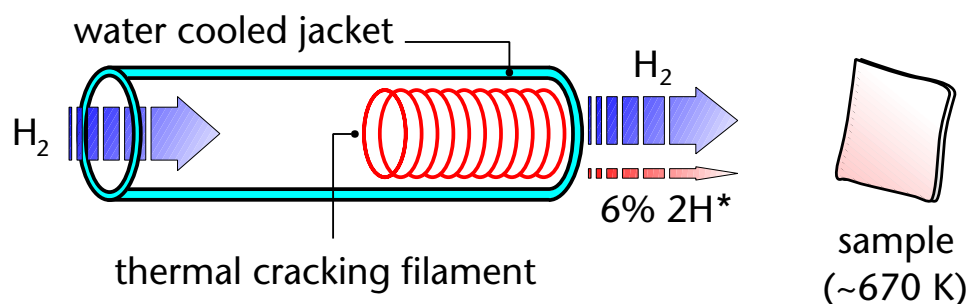


Figure 5.15: Schematic diagram of the thermal cracker source for AHC. Molecular hydrogen is introduced to the water-cooled source, where it is partially cracked by a tungsten filament to produce some 6–7 % H\*. This non-energetic atomic flux cleans the surface which is usually held at an elevated temperature.

Exposure is measured in Langmuirs, (where  $1 \text{ kL} = 10^{-3} \text{ Torr seconds}$ ), with the atomic hydrogen dose estimated to be 6–7% of the molecular hydrogen exposure on the basis of the previously calculated cracking efficiency (discussed in §3.3.2). A typical molecular

exposure was therefore in the range  $\sim 35$ – $100$  kL, with corresponding atomic hydrogen dose of  $\sim 2.1$ – $7$  kL. Hereafter, only molecular hydrogen exposures are cited. Surface temperatures were measured using a chromel–alumel thermocouple in direct contact with the sample.

In the first set of experiments, using the Warwick CAICISS apparatus, GaSb(001) samples were annealed to 600 K, then exposed to sequential doses of atomic hydrogen at between 670 K and 740 K, forming a  $(1\times 3)$  reconstruction with a sharp LEED pattern. Exposures up to 92 kL of  $H_2$  were used. At each stage, AES derivative spectra were recorded for Ga, Sb and the major contaminants C and O. CAICISS spectra were recorded for a polar angle of  $54.7^\circ$  relative to the surface normal (aligned with a bulk  $\langle 111 \rangle$  channel), along two perpendicular azimuths, using 4 keV  $He^+$  incident ions. These azimuths were determined by LEED to be along the  $[110]$  azimuth, parallel with the top layer dimers as shown in the model of figure 5.8(a) and along the  $[\bar{1}10]$  azimuth, normal to the top layer dimers. The sample was then annealed in UHV through a range of temperatures up to 875 K, with further CAICISS and AES spectra recorded to examine the decomposition behaviour. In further experiments at CLRC Daresbury Laboratory, GaSb(001) samples were prepared by AHC in combination with  $Sb_4$  flux and various substrate and annealing temperatures. A number of different surface reconstructions were produced and identified by LEED, including the  $(1\times 3)$ ,  $c(2\times 6)$  and a previously unreported  $c(6\times 4)$ . The  $(2\times 5)/c(2\times 10)$  reconstruction was also observed, but the MEIS data was noisy and gave inconclusive results upon analysis. This is attributed to a combination of surface disorder and a large unit cell making simulation difficult. For each surface, exposures of  $H_2$  up to 150 kL were used and AES spectra of Ga, Sb, N, C and O recorded. The LEED patterns were photographed and MEIS was used to analyse the surface atomic structure. For the MEIS experiments, 100 keV  $He^+$  ions were used rather than  $H^+$ , in order to maximize the mass resolution. Generally, a double alignment geometry was used, with the ions incident along a  $\langle 111 \rangle$  bulk channel and detected around a  $\langle \bar{1}\bar{1}1 \rangle$  direction.

## 5.5 Results and discussion

### 5.5.1 Efficacy of atomic hydrogen cleaning

A plot of the surface composition determined from peak-to-peak height measurements from the normalized AES derivative spectra is shown in figure 5.16. After annealing to 600 K for one hour without atomic hydrogen present, the carbon contamination was significantly reduced, although it remained the dominant species followed closely by oxygen. Exposure to atomic hydrogen at 670 K with a total H<sub>2</sub> dose of 72 kL dramatically reduced both the C and O levels to only a few percent of a monolayer. A final dose of 20 kL H<sub>2</sub> was then sufficient to reduce both contaminant signals to the detection limit of AES (approximately 1–2 % of a monolayer), leaving a surface with an Sb:Ga ratio of ~ 2:1 and a sharp symmetric (1×3) LEED pattern.

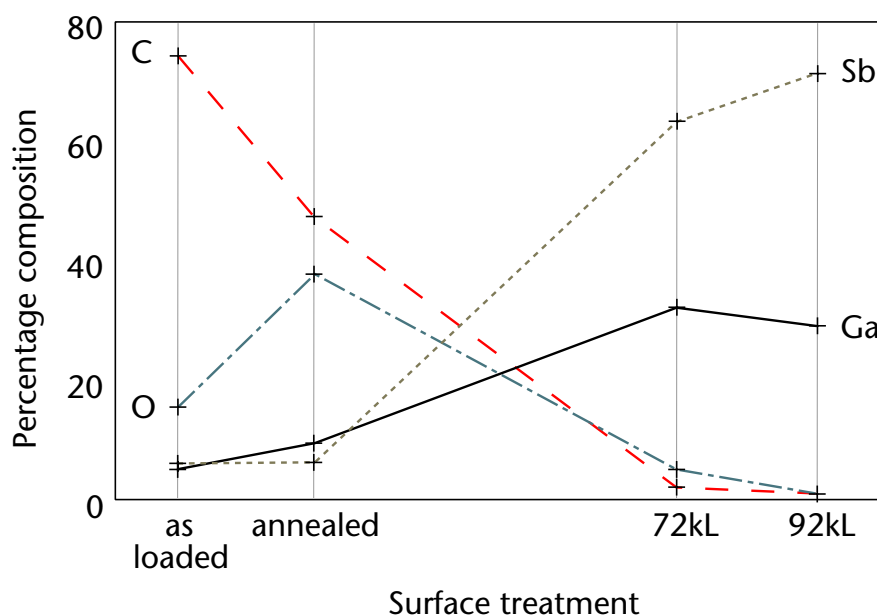


Figure 5.16: Surface composition determined from AES for GaSb(001) during AHC.

Further experiments using HREELS were performed to examine the same preparation conditions, details of which are reported elsewhere.<sup>27</sup> The results indicated that oxide vibrational modes were persistent after even 92 kL H<sub>2</sub> at 670 K, and remained after further doses, as shown in figure 5.17(a). This was attributed to the presence of an ordered low coverage oxide phase. However, after only a further 20 kL dose at 740 K, the oxide loss

peak disappeared. It was concluded that essentially all atmospheric oxygen contamination was efficiently removed without loss of surface stoichiometry. It was also concluded from bulk carrier concentration simulations that there was no significant reduction in the conduction band electron concentration as a result of dopant passivation by the atomic hydrogen, as shown in figure 5.17(b).

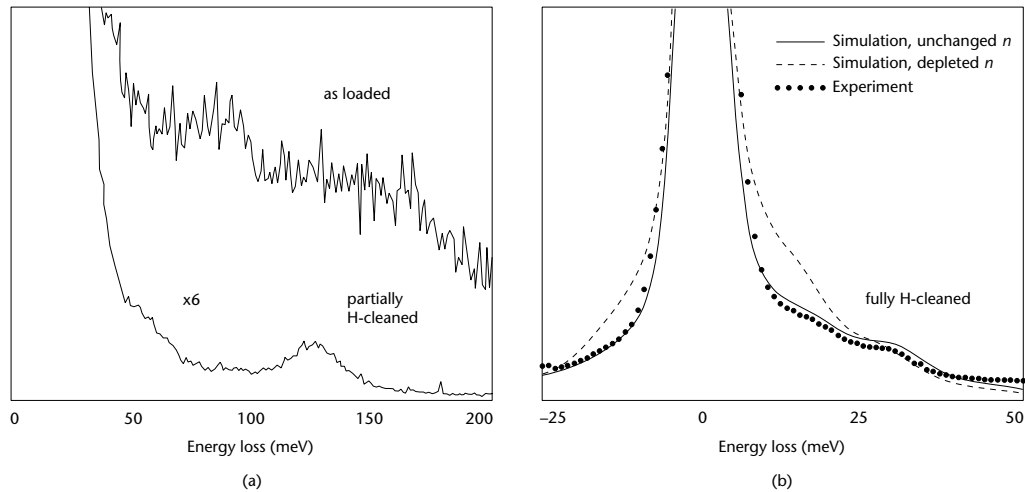


Figure 5.17: Specular HREEL spectra (at 30 eV) from GaSb(001) at different stages of AHC. (a) shows data from a sample as-loaded and partially-cleaned (50 kL at 670 K). The intensity of the cleaned sample has been multiplied by six. (b) shows data from the fully-cleaned sample (solid circles, 100 kL total dose, completed at 740 K), alongside simulated spectra for a similar bulk carrier concentration (solid curve,  $n = 4 \times 10^{17} \text{ cm}^{-3}$ ) and a significantly reduced concentration as expected if passivation had occurred (dashed curve,  $n = 2 \times 10^{17} \text{ cm}^{-3}$ ).

As a result of these experiments it is clear that AHC is an effective and efficient technique for surface preparation and removal of atmospheric contaminants from GaSb(001).

Thermal desorption at 870 K under an  $\text{Sb}_4$  over-pressure can remove the native oxide layer but results in significant surface roughening.<sup>28</sup> Low energy IBA has been the traditional technique for producing clean, well-ordered GaSb(001) reconstructions.

However, in related III–V materials, IBA has been shown to result in residual electronic damage that cannot be repaired by annealing. For example, in *n*-type GaAs, a high concentration of acceptor-like defects occurs, resulting in strong near-surface carrier depletion.<sup>29</sup> Meanwhile in both *p*- and *n*-type InSb, the residual defects are donor-like, resulting in a subsurface layer of enhanced electron concentration.<sup>30</sup> No electronic defects of this type were evident using HREELS after AHC.

### 5.5.2 Thermal decomposition of GaSb(001)

Stacked CAICISS spectra taken over a range of temperatures are shown in figures 5.18 and 5.19 for both the  $[\bar{1}10]$  and  $[110]$  azimuths. These data were for a GaSb(001)-(1×3) reconstruction, as identified by LEED, which was found by AES to be free of atmospheric contamination after AHC. The CAICISS peaks can be readily identified using equation 3.25, with Sb surface scattering preceding the Ga peak. The large Ga peak visible in the  $[\bar{1}10]$  direction at 625 K was relatively unpronounced in the  $[110]$  azimuth. This is consistent with the top layer Sb dimer chains of the (1×3) reconstruction shadowing the Ga atoms between them, as shown in figure 5.20.

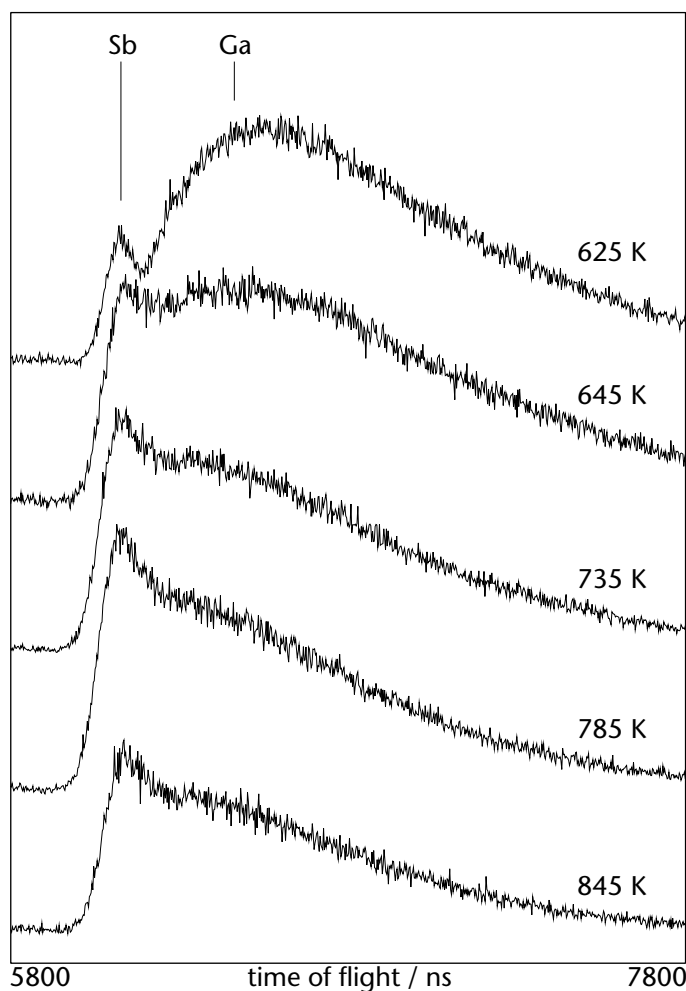


Figure 5.18: Stacked CAICISS spectra for the  $[110]$  azimuth of the GaSb(001)-(1×3) reconstruction, showing the variation of intensity (and indirectly of composition) with anneal temperature.

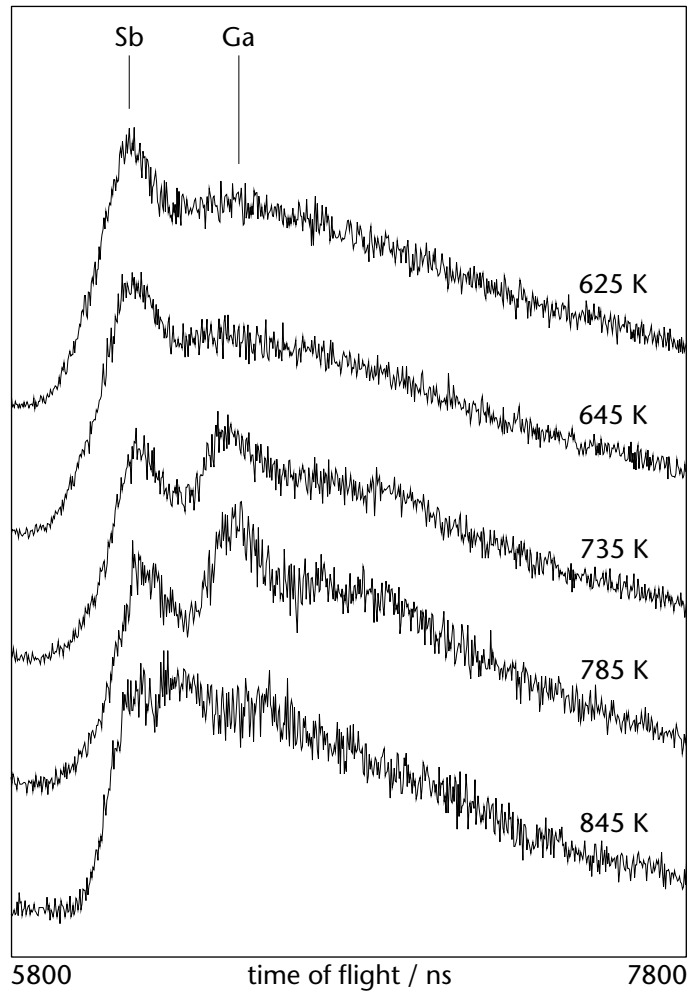


Figure 5.19: Stacked CAICISS spectra for the  $[110]$  azimuth of the GaSb(001)-(1 $\times$ 3) reconstruction, showing the variation of intensity (and indirectly of composition) with anneal temperature.

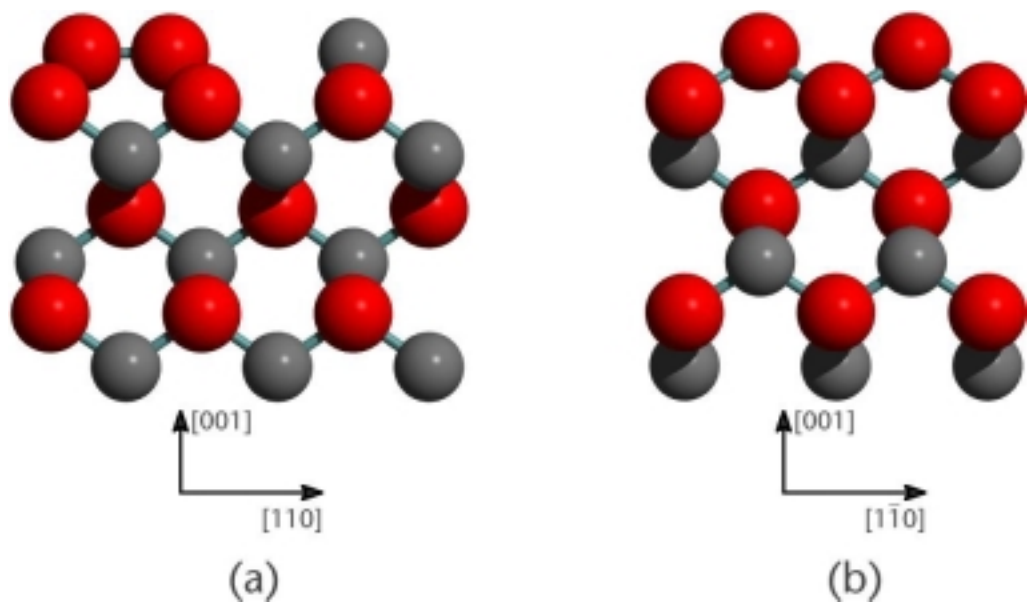


Figure 5.20: GaSb(001)-(1 $\times$ 3) structural model (space-filled representations using covalent radii) showing views along (a) the  $[1\bar{1}0]$  azimuth and (b) the  $[110]$  azimuth. The Ga atoms (grey) are illuminated in (a) but shadowed by the Sb dimers (red) in (b) [c.f. figures 5.18 and 5.19].

Quantitative calculations based upon this CAICISS data are difficult. In principle, the elemental composition could be determined from the intensity of scattered ions as a function of energy at the given scattering angle. However, the scattered intensity is correlated with the scattering cross-section, as discussed in §3.4.3.4. For the CAICISS energy range, the interaction potential is not simply Coulombic and therefore scattering cross-sections and compositional calculations are imprecise. Additionally, the overlap of the two peaks at this energy makes deconvolution of the Ga elastic scattering intensity from that of Sb inelastic collisions difficult. The Sb and Ga peaks were fitted using Gaussian curves, and their integral areas scaled to account for differing scattering cross sections (using equation 3.34), in order to give an approximate relative composition. This value was normalized to the unconvoluted, and therefore more precise AES data, in order to make comparison of the compositional trends more straightforward. It is clear from figure 5.21 that there was an initial drop in Sb recorded from the  $[110]$  azimuth in both CAICISS and AES between 625 and 645 K. However, there was a relatively large rise in the Sb signal recorded by CAICISS along the perpendicular  $[\bar{1}10]$  azimuth as can be seen in figure 5.18. This behaviour might be explained by non-congruent sublimation below the  $T_{cs}$  of 728 K. Indeed, it has been reported that an Sb capping layer can be thermally removed by anneal temperatures as low as 575 K, and that higher decapping temperatures can result in surface degradation.<sup>31,23</sup> However, a more likely explanation, given the disparity between the azimuthal data, is the onset of a change of surface reconstruction from the  $(1\times 3)$  towards the  $c(2\times 6)$ . This latter phase is known to be a less Ga-rich reconstruction. The drop in the  $[\bar{1}10]$  Ga intensity is consistent with the loss of the inter-dimer Ga which had been illuminated by the ion beam, as seen in figure 5.20(a). Whilst a phase transition was not observed by LEED, the pattern became much less distinct, consistent with partial reconstruction of the surface. This  $(1\times 3) \rightarrow c(2\times 6)$  transition has been previously reported to occur under an Sb flux, as discussed in §5.3. It appears that it may also be achievable simply by annealing.

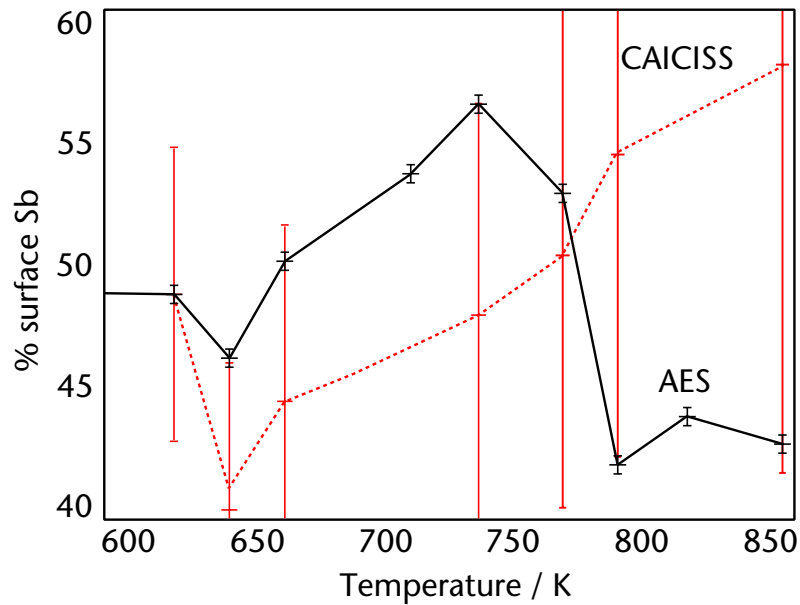


Figure 5.21: Surface Sb percentage determined from AES (black) and CAICISS (red) for GaSb(001) during thermal decomposition. Noise and the convolution of Ga and Sb CAICISS peaks results in a relatively very poor discrimination of composition compared to AES.

The Sb signal increased again between 650 and 725 K, which can be ascribed to continuing reconstruction of the surface. Above around 735 K, a sharp drop in Sb is visible in AES, ascribed to non-congruent sublimation of Sb. Over the same range, the CAICISS signal became noticeably noisier (making the curve-fit less reliable). This was accompanied by a deterioration in the quality of the LEED pattern symmetry and visible surface cloudiness. As cited before, similar studies indicate that this cloudiness is the result of roughening at the atomic level. It can be concluded, therefore, that in UHV without an Sb flux, surface decomposition begins with non-congruent sublimation at around 735 K, progressing rapidly above 785 K, but still well below the GaSb melting point at 985 K.

### 5.5.3 GaSb(001)–(1×3) reconstruction

The (1×3) reconstruction was further examined during the experiments at CLRC Daresbury Laboratories, along with approaches to generating a variety of GaSb(001) reconstructions through the combination of AHC and annealing with or without antimony flux. A sample of GaSb(001) was loaded and degassed in HV before bringing to UHV. At this point, AES was performed to determine the surface stoichiometry of the as-loaded sample, in terms of gallium, antimony, carbon and oxygen (as seen in figure 5.22).

Using equation 3.10, it was determined that the surface region had a composition of 62.4% C, 28.3% O, 5.65% Sb and 3.64% Ga. This result, consistent with our earlier work, is a good demonstration of the degree of contamination resulting from atmospheric reaction alone.

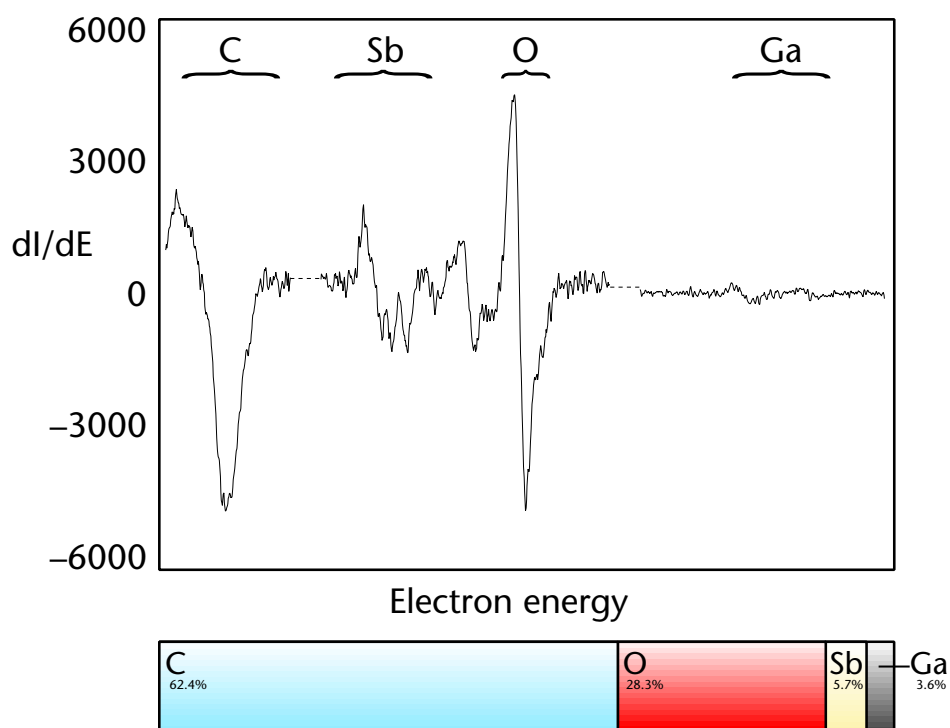


Figure 5.22: AES spectra and the composition determined for the as-loaded GaSb(001) sample.

A diffuse  $(1 \times 3)$  LEED pattern was produced by a 75 kL  $H_2$  dose (taking  $\sim 30$  minutes) with a substrate temperature of 575 K. The quality of the pattern was further improved by the use of an Sb flux, dosing for 30 minutes at  $7 \times 10^{-7}$  mbar chamber pressure with the k-cell at 730 K, and annealing to a substrate temperature of 675 K. The result was a sharp  $(1 \times 3)$  LEED pattern, as shown in figure 5.23. This reconstruction was found to be Sb-rich (54.7% surface composition), with levels of carbon and oxygen below the detection limits of AES (as shown in figure 5.24).

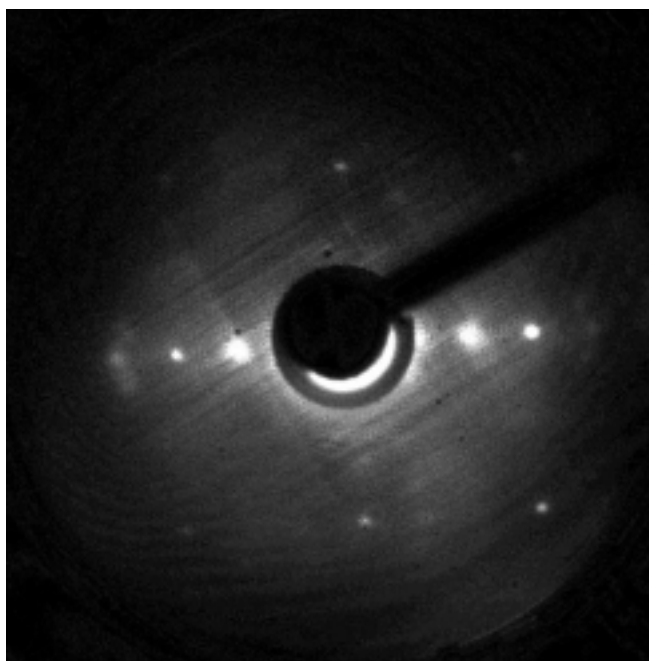


Figure 5.23: GaSb(001)-(1×3) reconstruction produced by AHC and observed by LEED (54 eV beam energy).

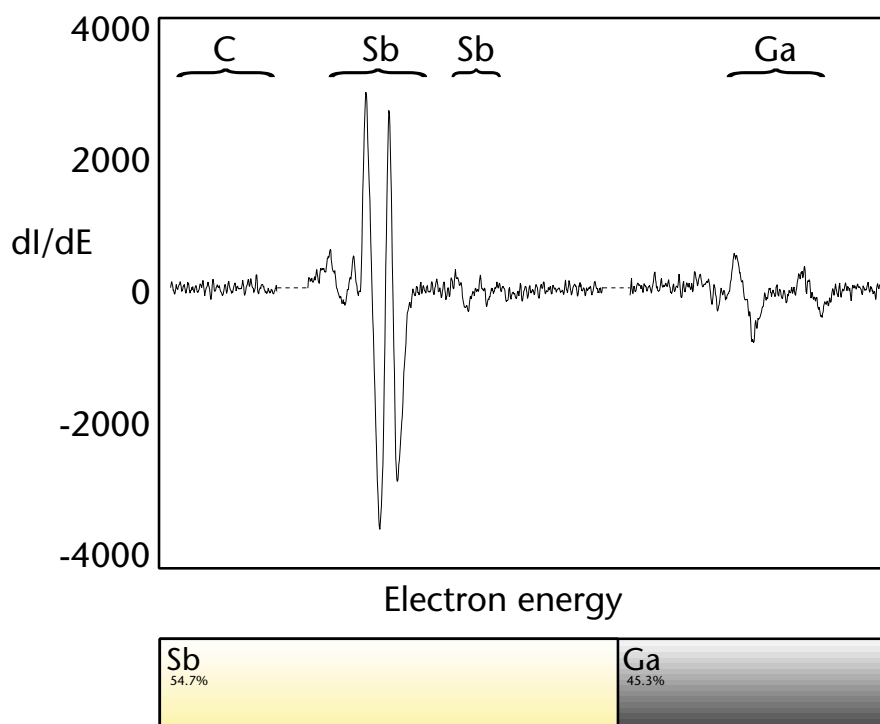


Figure 5.24: Concatenated AES spectra for the GaSb(001)-(1×3) reconstruction produced by AHC.

Two such  $(1 \times 3)$  reconstructed samples were examined by MEIS in order to collect sufficient data for a detailed structural analysis. The ball-and-stick model shown in figure 5.20 is the proposed structure for this reconstruction, and is well-supported by STM, LEED and RHEED data. However, there has, to date, been no effort to quantify the model. The experimental data recorded (and shown in figure 5.26) was therefore simulated in VEGAS using the simple model shown, which has dimerized Sb atoms in the top layer with a dimer length of  $2.31 \text{ \AA}$ , compared to the Sb–Sb separation of  $4.31 \text{ \AA}$  of the unreconstructed GaSb surface. In order to evaluate the likely atom positions, the dimer length (centred about the initial dimer position) and its height above the second layer were both systematically varied through a range of  $\pm 0.5 \text{ \AA}$ . The height of the second layer Ga atoms between the dimer rows was then varied systematically, and this process repeated iteratively, evaluating the best-fit simulation to refine these parameters. The global best-fit was for the model shown in figure 5.25, with structural parameters given in table 5.1.

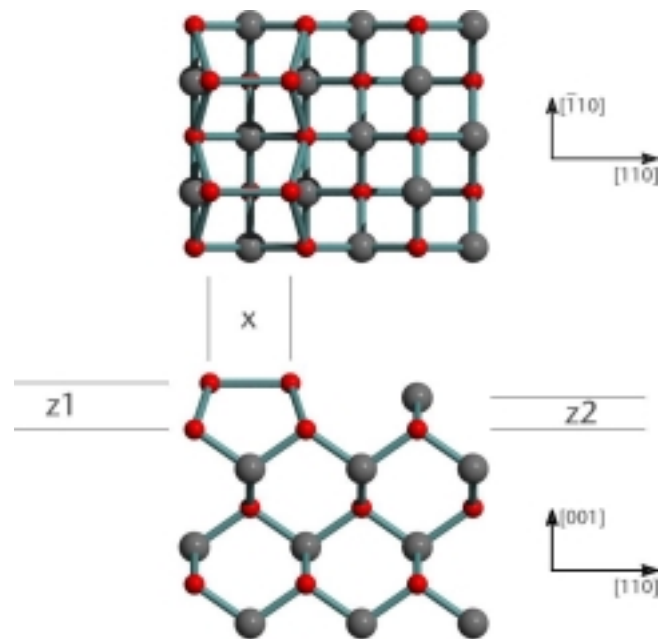


Figure 5.25: Structural solution for the GaSb(001)– $(1 \times 3)$  reconstruction.

x	z1	z2
3.11	1.81	1.24

Table 5.1: Parameters for the GaSb(001)– $(1 \times 3)$  structural solution shown in figure 5.25. All values are in  $\text{\AA}$ , with an estimated error of  $0.05 \text{ \AA}$ .

Variations of this model gave local minima for  $R$ -factors across the eight datasets (combinations of two each of samples, elements and azimuths), in the range 1.7–5.0 with the exception of the  $[111]$  Ga data, which exhibited a relatively poor  $R$ -factor of  $\sim 35$ . As was noted in §4.3 though,  $R$ -factors from different datasets cannot be compared directly, so this was not considered an undue cause for concern. No single model gave a best-fit for more than two datasets. However, the model cited above was judged to have the most consistently low  $R$ -factor. The  $R$ -factors for this specific model are shown in table 5.2, and the fits shown in figure 5.26.

$[111]$ Sb	$[1\bar{1}1]$ Sb	$[111]$ Ga	$[1\bar{1}1]$ Ga
4.99	1.93	35	2.81

Table 5.2: Calculated  $R$ -factors for the GaSb(001)–(1×3) structural solution.

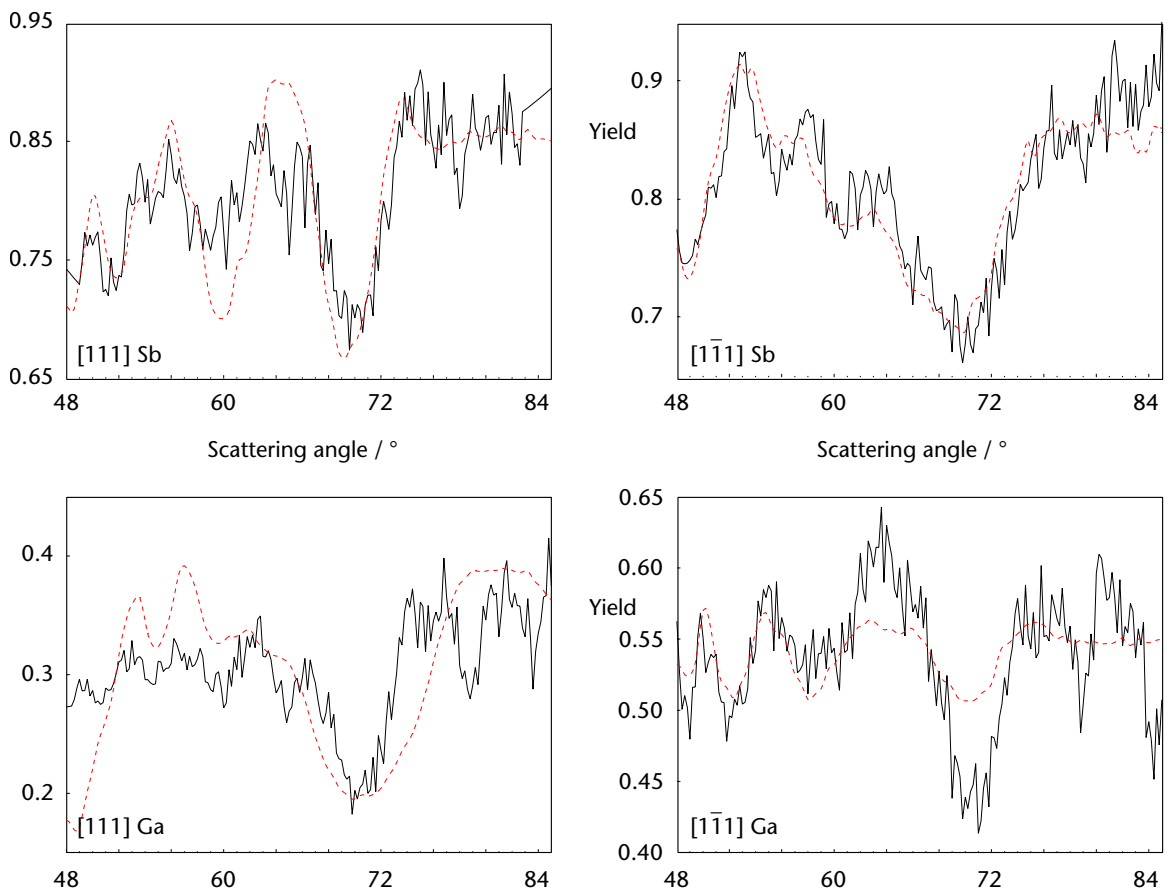


Figure 5.26: Simulated (red, dashed line) and experimental MEIS data (black, solid line) for the GaSb(001)–(1×3) model.

#### 5.5.4 GaSb(001)-c(2×6) reconstruction

The c(2×6) reconstruction was prepared both by AHC and the more traditional technique of IBA. Two cycles of IBA were performed using 1 keV Ar<sup>+</sup> ions at a grazing incidence angle ~ 30°, followed by annealing at 625 K. The resulting surface had a reasonably sharp LEED pattern. Whilst IBA successfully removed the carbon, there was still some residual oxygen after the treatment, as discernible in figure 5.27.

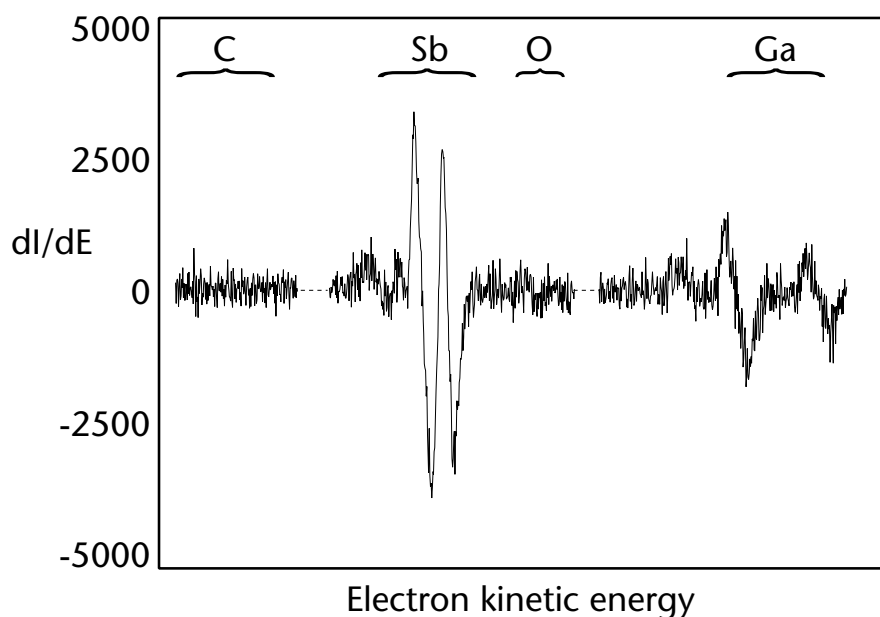


Figure 5.27: Concatenated AES spectra for the GaSb(001)-c(2×6) reconstruction produced after two cycles of IBA.

The same reconstruction was also produced by AHC (75 kL exposure) at 575 K, followed by 5 minutes Sb deposition at a substrate temperature of 525 K. AES indicated a similar surface composition, although this time free from atmospheric contamination by carbon or oxygen. The AES signal was also less noisy, more like the (1×3) reconstruction in character. The LEED pattern, shown in figure 5.28, was also a clearer c(2×6) symmetry than that produced by IBA. Both LEED and AES suggest a greater degree of disorder in the IBA-produced surface. MEIS data also supported this view; it can be seen by inspection of the ion yields from the two samples (shown in figure 5.29) that the surface prepared by AHC must have a greater scattering cross-section, consistent with a less rough and less damaged surface.

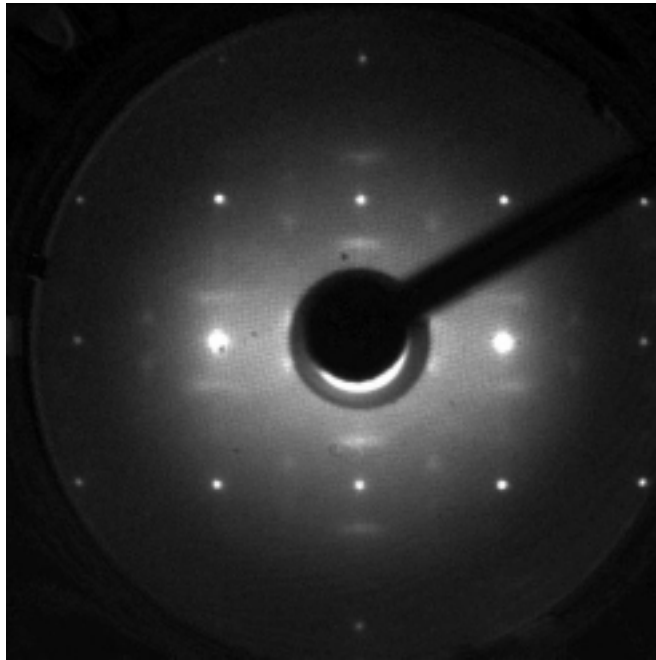


Figure 5.28: GaSb(001)-c(2×6) reconstruction produced by AHC and observed by LEED (84 eV beam energy).

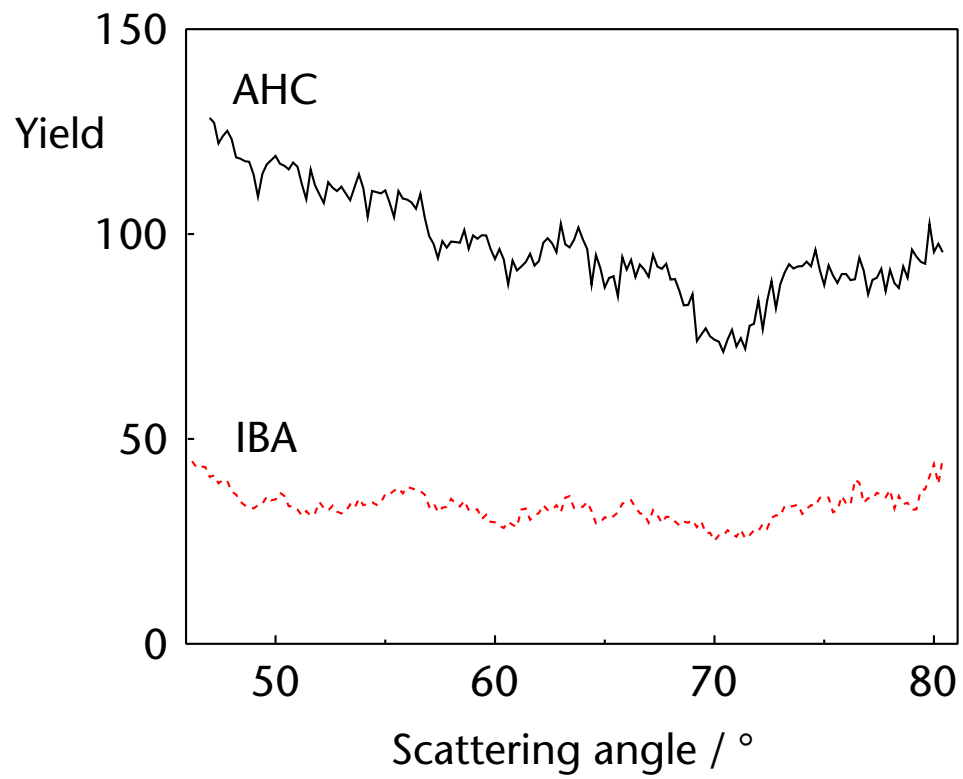


Figure 5.29: Comparison of ion yields scattered from Ga along the  $[\bar{1}10]$  azimuth of the GaSb(001)-c(2×6) reconstruction prepared by AHC (black, solid line) and IBA (red, dashed line). Note the doubling of yield from the AHC-prepared sample.

A structural analysis was performed on the AHC sample using MEIS, based on the model shown in figure 5.8(b). As before for the  $(1 \times 3)$  phase, top layer Sb dimer height and length parameters were varied systematically to make a first order determination of the parameters. In this model, the antiphase Sb dimers in the second layer were also varied in height and length. These two sets of dimer parameters were varied alternately and iteratively to refine their values. A local minimum of  $R_{Sb} = 8.98$  (from an initial best-fit value of 14.06) was found after ten iterations, in a model with a reduced dimer height. However, a problem visible in the Sb data was a significant offset between the position of the main  $\langle 111 \rangle$  blocking dip in the simulated and MEIS data, as shown in figure 5.30.

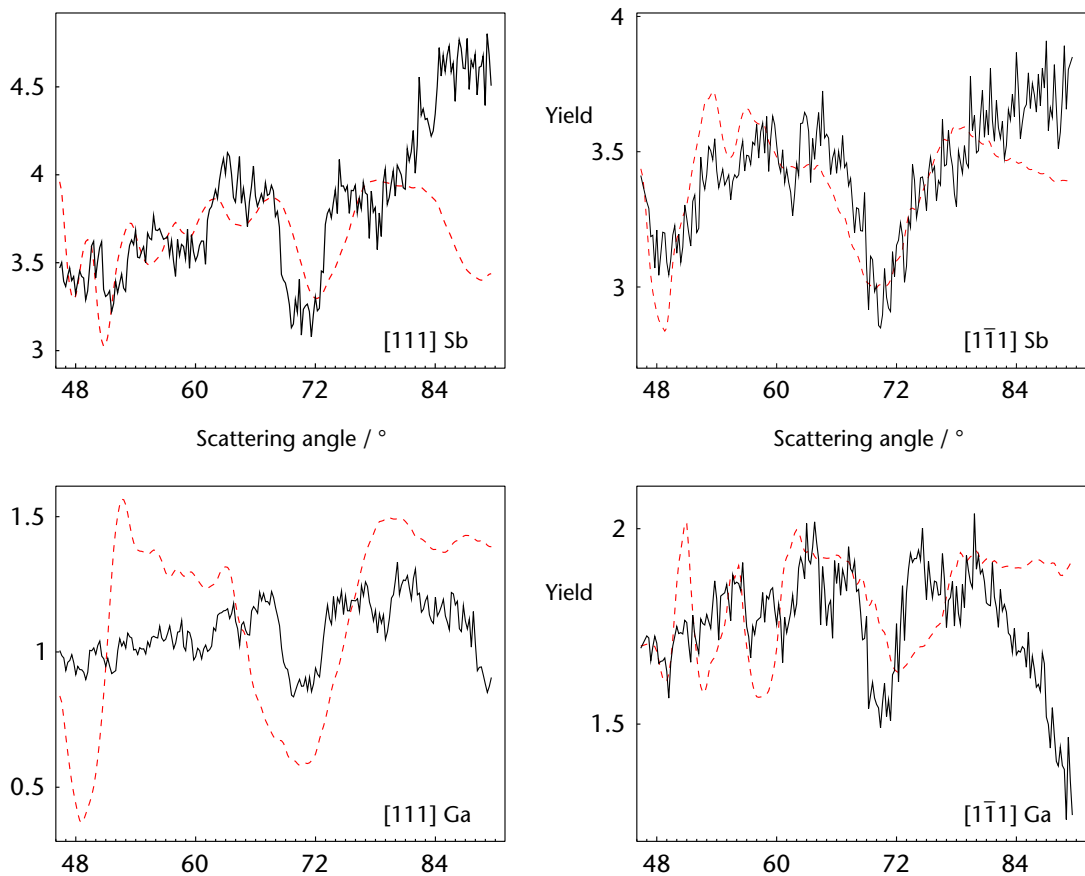


Figure 5.30: Best-fit MEIS simulation data for GaSb(001)- $c(2 \times 6)$  with  $R_{Sb} = 8.98$  after ten iterations.

Possible variations in the model were therefore considered. It was recognized that the dimerization in the second layer would be likely to have an effect on the position of the top layer atoms, most likely to be manifested as a staggering of the top layer dimers away from the electron orbital concentration of the second layer dimers. Hence, the model was

modified systematically to stagger the dimer centre positions. After several iterations, an improved local minimum was found, with  $R_{Sb} = 4.36$ . The experimental and best-fit simulated data for both Ga and Sb along the  $\langle 111 \rangle$  azimuth are plotted in figure 5.31.

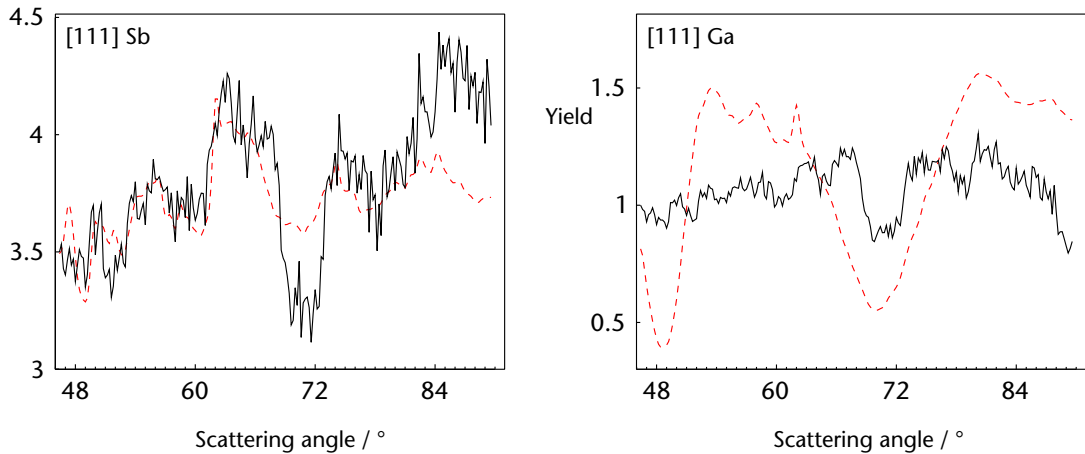


Figure 5.31: Best-fit MEIS simulation data for GaSb(001)-c(2x6) with  $R_{Sb} = 4.36$ .

However, when this best-fit simulation was visualized using VEGASmagic and RasMol, it was immediately evident that the model was not physical. The process of refinement, by use of the  $R$ -factor criterion for quality of fit, had led to a model where the top layer dimers were depressed vertically to be almost in-plane with the second layer atoms. Meanwhile, as shown in figure 5.32, the second layer dimers were elevated above their neighbours. Additionally, there was enormous inconsistency between the dimer parameters in the two layers. The dimer lengths were  $1.695 \text{ \AA}$  and  $3.11 \text{ \AA}$  for top and second layer, a difference of 90%. Clearly this model, with an interatomic separation sometimes less than  $0.4 \text{ \AA}$ , was a highly improbable solution.

A model with a similar dimer length but more realistic interlayer separations was therefore created. This was a significantly worse fit both in terms of visual inspection of the peak matching and in terms of  $R$ -factor ( $R_{Sb} = 6.34$ ). The model was again modified systematically to shift both the centre position and now the length of the top layer dimers whilst initially keeping their height constant. The  $R$ -factor was improved by this, and hence this model was used as the basis of further refinement. Systematically, all top and second layer dimer parameters were varied until a satisfactory best-fit was obtained.

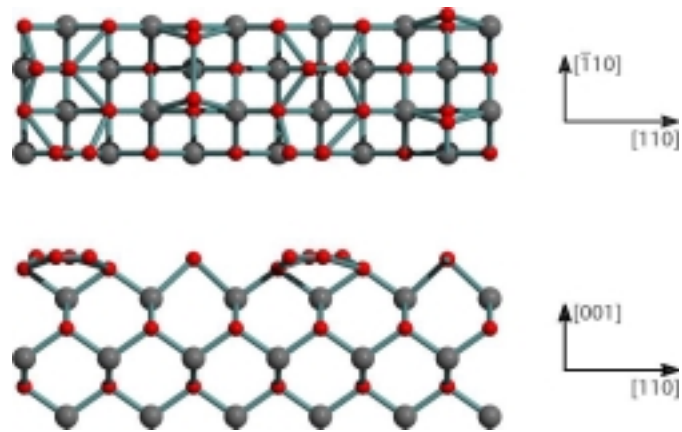


figure 5.32: GaSb(001)-c(2×6) model with  $R_{sb} = 4.36$ . This was considered improbable due to inconsistencies in dimer height and differences between the dimer lengths in opposite azimuths.

Finally, surface vibration enhancement was examined for this bilayer model. It is common practice in the MEIS community to enhance the thermal vibrations of the top two layers by a factor of  $\sqrt{2}$ . Such an enhancement has physical justification, as there is inevitably a greater degree of freedom of motion in the surface layers than in the bulk. There are several effects of this enhancement. Firstly, there is an increase in absolute yield, as sub-surface shadowing becomes less efficient when atoms are displaced from their equilibrium positions. This itself results in attenuation of the bulk blocking features relative to the surface blocking features. Although the intensities vary as a result of the surface vibration enhancement, the positions of blocking features does *not* vary, so the effect is minimal on distinguishing between different parameters. However, it does improve the overall quality of fit and thus reduces the value of the  $R$ -factor determined. For this reconstruction, the degree of vibration enhancement was varied separately for the top layer and second layer dimers through a range of one to two times bulk amplitude. The result for this was that the best-fit was for bulk-like vibrations in both layers. The final model is shown in figure 5.33, with parameters in table 5.3 whilst best-fits for the data are shown in figure 5.34 with  $R$ -factors in table 5.4.

x	z1	y	z2
2.35	1.57	3.11	2.02

Table 5.3: Parameters for the GaSb(001)-c(2×6) structural solution shown in figure 5.33. All values are in Å, with an estimated error of 0.05 Å.

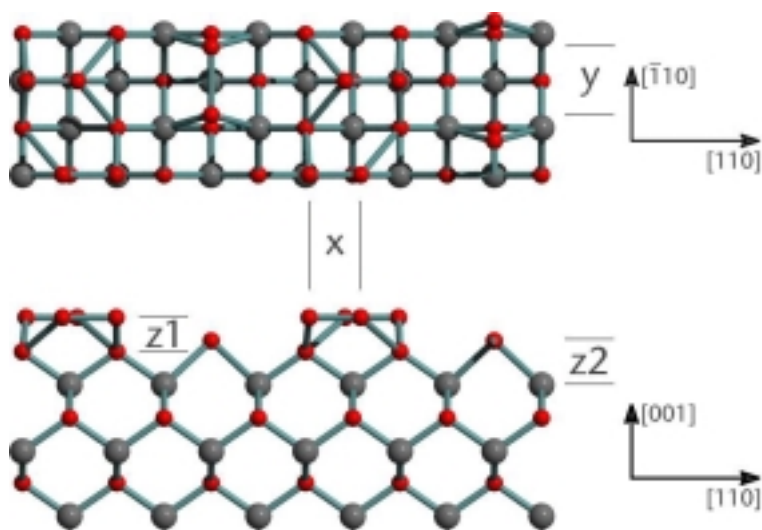


Figure 5.33: Structural solution for the GaSb(001)- $c(2 \times 6)$  reconstruction.

$[111]$ Sb	$[1\bar{1}1]$ Sb	$[111]$ Ga	$[1\bar{1}1]$ Ga
5.27	6.65	122.13	8.83

Table 5.4:  $R$ -factors for the GaSb(001)- $c(2 \times 6)$  structural solution.

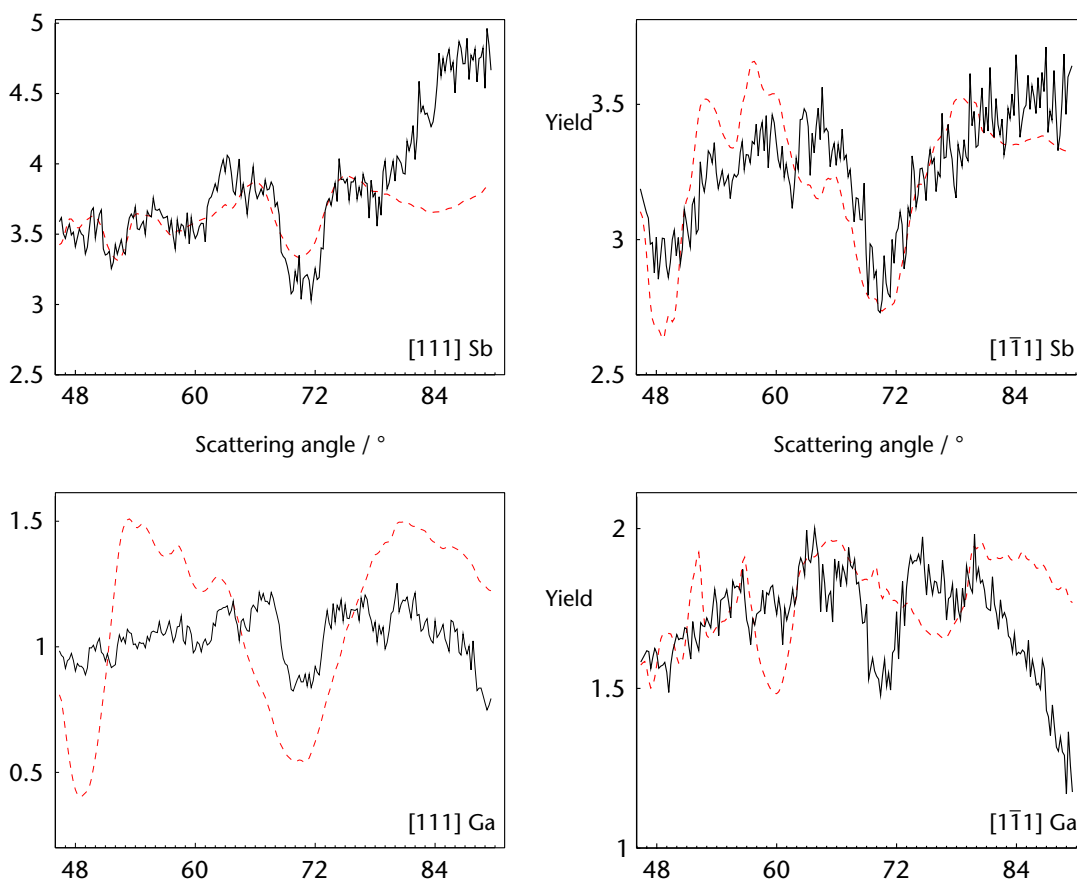


Figure 5.34: Best-fit MEIS simulation data for the GaSb(001)- $c(2 \times 6)$  reconstruction.

The  $c(2\times 6)$  reconstruction proved harder to model than the  $(1\times 3)$  phase for a number of reasons. The first and most obvious is the four-fold increase in the number of atoms in the model. This also results in a quadrupling of the number of atoms to be considered in the surface unit cell, and a commensurate increase in the number of permutations of atomic positions. Of course, the simulations are also based on two fundamental assumptions; that the surface was entirely free of disorder (thermal vibration excepted), and that the model proposed is indeed an accurate representation of the reconstruction. Obviously, the first of these assumptions is unlikely to hold true on the microscopic scale in a real crystal. Instead, there has to be a further assumption that deviations from the model structure are normally distributed about the ideal, and therefore average out macroscopically over the  $0.5\text{ mm}^2$  illuminated area of the crystal. The second assumption is perhaps more troublesome. As can be seen from the results above, in this example, the value of the  $R$ -factor obtained from a relatively nonphysical model was lower than that obtained in the best-fit eventually obtained. The conclusion must therefore be that although MEIS results can be successfully simulated using VEGAS, the use of  $R$ -factors cannot be relied upon when refining models towards a physical solution. Whilst a valuable criterion for evaluating quality of fit, it cannot be used alone.

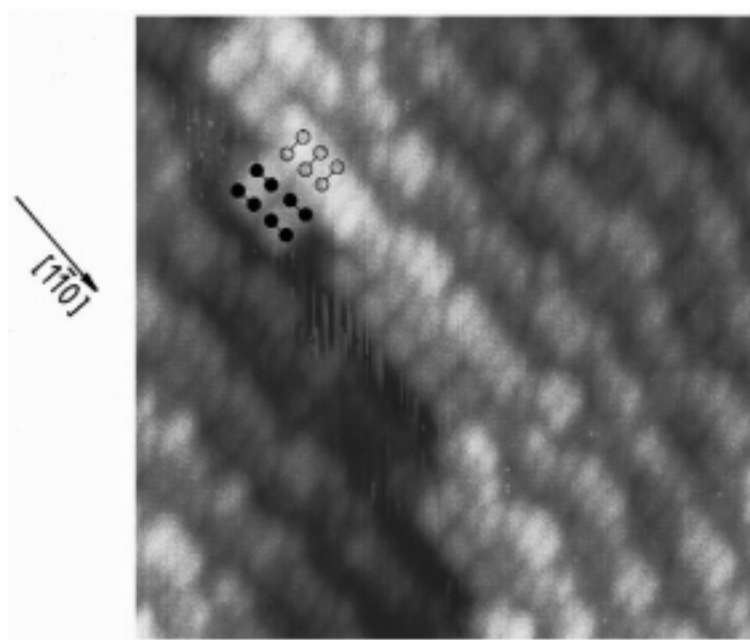


Figure 5.35: High-resolution STM image ( $105\times 105\text{ \AA}^2$ , sample bias  $-2.18\text{ V}$ ) of the GaSb(001)- $c(2\times 6)$  reconstruction [from Resch-Esser et al<sup>23</sup>]

The structural solution obtained for the  $c(2\times 6)$  reconstruction is interesting, in that it exhibits marked staggering of the Sb dimers. Whilst this behaviour has been observed in STM studies of some other III–V materials, it has not been particularly emphasized in studies on GaSb(001) to date, although it is evident in the recent work by Resch–Esser et al, shown in figure 5.35. An interesting point was that the dimer lengths determined here for the two layers differed by some 30%. That the best-fit dimer length was 2.35 Å for the top layer is perhaps surprising, particularly given the good agreement between the dimer length of 3.11 Å found in the second layer and the  $(1\times 3)$  reconstruction. Nevertheless,  $R_{Sb}$  for a top layer dimer length of 3.11 Å was 11.45, more than double that for a 2.35 Å dimer length, with a visibly poorer fit. The shorter dimer length is more consistent with the MEIS results recorded. Overall, there is good matching of the Sb peak positions in both azimuths. Furthermore, there is good quantitative agreement, except for some dip splitting and broadening at a scattering angle around 63°, between the  $[\bar{2}\bar{3}3]$  and  $[\bar{4}\bar{5}5]$  azimuths, as shown in figure 5.36. As discussed in §3.4.6, blocking dip splitting is often an indication of dimerization, and geometric consideration of the MEIS data is consistent with this.

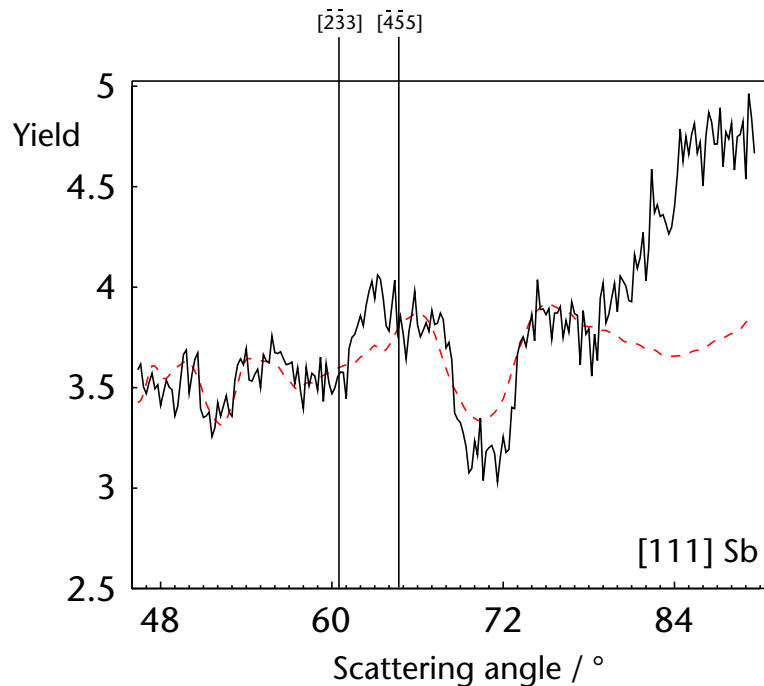


Figure 5.36: Inconsistencies between the best-fit simulation and MEIS experiment for the GaSb(001)– $c(2\times 6)$  reconstruction for  $[111]$  incident Sb data. Dip splitting and broadening around the  $[\bar{2}\bar{3}3]$  and  $[\bar{4}\bar{5}5]$  azimuths is evident.

Consideration of both the cited STM data and MEIS results suggest that this inconsistency would be accounted for by a greater degree of irregularity at the surface. Top layer dimer staggering is physically consistent with the presence of second layer dimerization, alternating in phase between adjacent  $(1 \times 3)$  blocks. However, whilst staggering is evident in the STM data, it does not appear between adjacent  $(1 \times 3)$  blocks, but between dimer chains of irregular length. As can be seen in figure 5.37, the difference in dip profile between the  $[\bar{2}\bar{3}3]$  and  $[\bar{4}\bar{5}5]$  azimuths is geometrically consistent with such disorder in the dimer staggering. This would be impossible to model in VEGAS, given the size of unit cell that would be required. It is clear though, from the simulation, that the average long-range periodicity is more consistent with dimer staggering than with straight dimer chains.

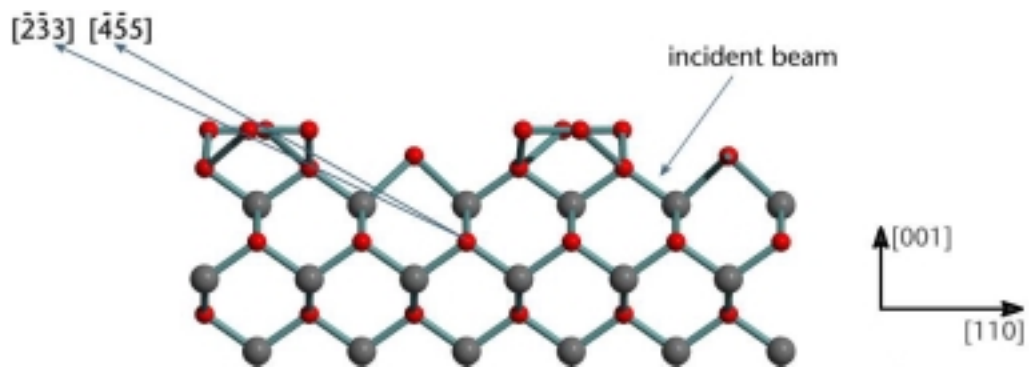


Figure 5.37: Inconsistencies between the best-fit simulation and MEIS experiment for the GaSb(001)- $c(2 \times 6)$  reconstruction for  $[111]$  incident Sb data. The best-fit model with  $[\bar{2}\bar{3}3]$  and  $[\bar{4}\bar{5}5]$  azimuths superimposed. Variation in dimer staggering would affect the yield from third layer Sb at around this angle.

By comparison, the Ga fits were relatively poor, with a high  $R$ -factor for the  $[111]$  direction, and inconsistencies in the fit for the  $[\bar{1}\bar{1}1]$  azimuth. As has been stressed before, different data-sets cannot be compared directly. However, even a cursory inspection of the fits in figure 5.34 will show that the Ga signal is much more poorly matched by the simulations. A number of factors may affect this. The first and perhaps most important is that Ga is lighter than Sb. The result is that the Ga scattering signal lies at a lower energy than Sb, as can be seen in figure 5.14. It is inevitable that there will be some convolution of sub-surface and bulk Sb scattering events with near-surface Ga scattering. Simple subtractive deconvolution is used in this case, which inevitably means that there is some degradation of the Ga signal. This is further exacerbated by the relatively low scattering

cross-section of Ga compared to Sb (a factor of  $\sim 2.7$ ). This results in a lower ion yield, and hence greater signal/noise ratio for the Ga signal. It is probably inevitable from an instrumental perspective that the quality of fit for the Ga data will be worse. These factors probably explain the relatively poor Ga fit in one azimuth for the  $(1\times 3)$  reconstruction. However, the problem is less significant there since there are contributions to the Ga signal from the top layer Ga atoms in the  $(1\times 3)$  model, as seen in figure 5.25.

Another factor in the consideration of Ga fits for the  $c(2\times 6)$  reconstruction is that no variation in their positions were considered in the simulations performed. It is expected that there would be less deviation from bulk-like locations for the Ga atoms in the subsurface, particularly when compared to the effects of dimerization on Sb positions in the Sb-terminated surface. Furthermore, the number of variations that would need to be considered would have a dramatic effect on the simulation time. In this analysis alone, six parameters were varied to attain these fits, taking over 120 hours of CPU time. Whilst it might be considered desirable to increase the number of variables to improve the fit, it must be borne in mind that changes in even a single parameter will almost certainly affect the scattering behaviour, such that the remaining parameters no longer provide the best-fit. This interdependency is further complicated since the software does not allow the evaluation of more than three parameters in any single simulation. A balance must be struck between perceived quality of fit and complexity of simulation. Given the instrumental limitations and the inherent complexity of the large unit cell model, it was considered acceptable to allow relatively greater disparity between the Ga simulated and experimental results.

#### 5.5.5 GaSb(001)- $c(6\times 4)$ reconstruction

Whilst the reconstructions described elsewhere in this chapter are all well-known and have been the subject of studies by various techniques, a previously unreported GaSb(001)- $c(6\times 4)$  reconstruction was also observed as a result of AHC. It was initially prepared by a 75 kL dose at a substrate temperature of 575 K, and again prepared on

several other occasions. The LEED pattern observed after such cleaning was, however, relatively diffuse. Flash annealing to 795 K sharpened the pattern, resulting in a clear  $c(6\times 4)$  pattern, a typical example of which is shown in figure 5.38.

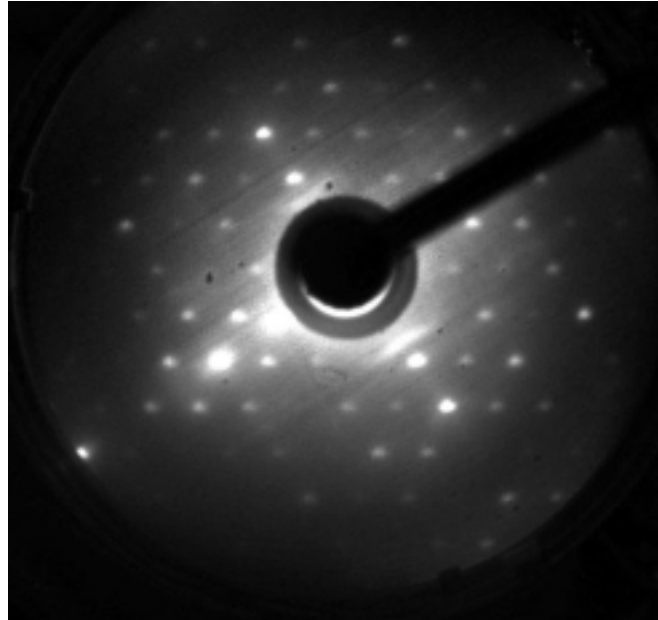


Figure 5.38: GaSb(001)- $c(6\times 4)$  reconstruction produced by AHC and observed by LEED (31 eV beam energy).

The quality of the LEED pattern and its reproducibility makes it seem extremely unlikely that it is anything other than a genuinely novel GaSb(001)- $c(6\times 4)$  reconstruction.

Previously, Waterman et al has reported the presence of a Ga-rich  $(4\times 3)$  RHEED pattern during the Ga deposition phase of MBE growth of GaSb on an GaAs substrate<sup>32</sup>, whilst Ludeke reported a Ga-rich  $(2\times 3)$  RHEED pattern after heating GaSb to 775 K in UHV.<sup>33</sup> However, it was indicated that these reconstructions are not stable. Sieger et al did not observe a  $(2\times 3)$  phase, but did observe a faint  $c(4\times 4)$  or  $c(4\times 12)$  using RHEED. Unable to distinguish it adequately from the  $c(2\times 6)$ , they did not consider it further.<sup>22</sup>

Anneal temperatures up to 875 K (which resulted in melting of regions of the surface in the earlier CAICISS experiments) were used in UHV to attempt a transition to more common reconstructions. It was found that flash annealing to 840 K retained the sixfold symmetry, whilst only a substrate temperature as high as 855 K resulted in a breakdown of the LEED pattern to one with more  $(1\times 3)/c(2\times 6)$  character. This pattern was diffuse and

streaky, and it is therefore reasonable to assume that the condition of the surface after such treatment was very poor. However, annealing in Sb flux did result in transition to a  $(1\times 3)$  or  $c(2\times 6)$  reconstruction.

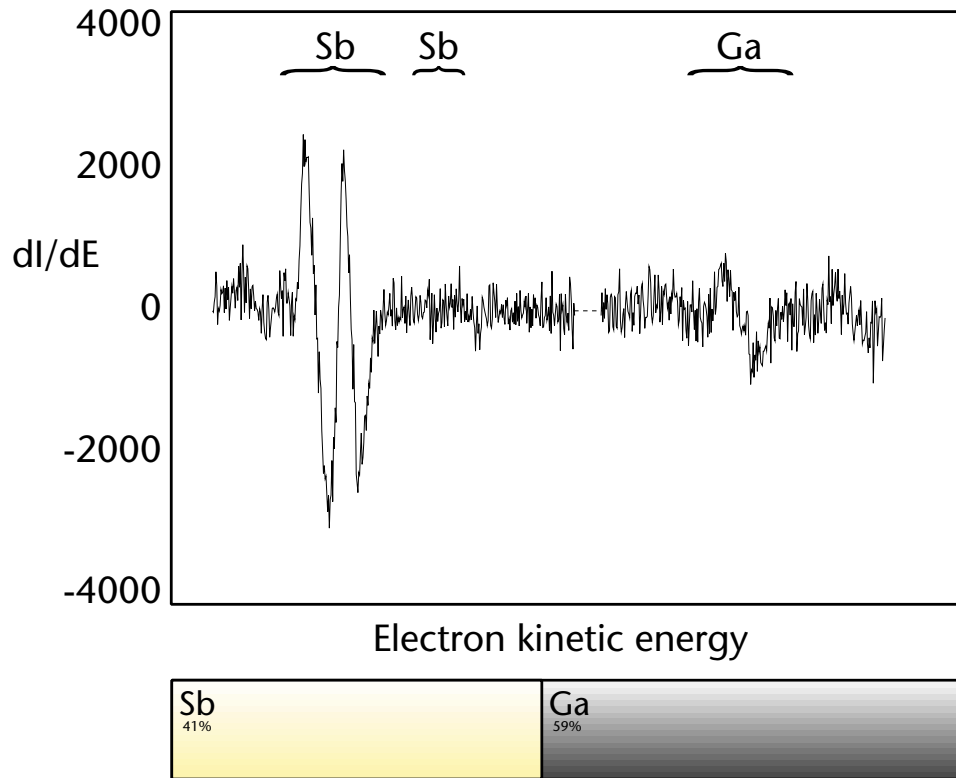


Figure 5.39: AES spectra and composition for the GaSb(001)- $c(6\times 4)$  phase shown in figure 5.36, produced by AHC.

It is therefore proposed that the  $c(6\times 4)$  is a stable, Ga-rich GaSb(001) reconstruction. AES indicated a surface composition of between 57–59% Ga, with a typical spectrum shown in figure 5.39. It is probable that it has not been observed before because non-energetic surface preparation techniques have not been available in the past. IBA produces a clean surface by first sputtering the existing surface, whether it be contaminated by atmospheric pollutants or otherwise. A clean, well-ordered surface is then achieved by annealing to repair the damage. However, it is well-established that in IBA of III–V materials, as discussed in §3.3.1, preferential elemental sputtering is possible. In a study of IBA on InP(001), it was found that the lighter element, In was preferentially sputtered.<sup>34</sup> It is quite probable that IBA will result in a Ga-rich phase losing Ga and reconstructing to become Sb-rich. However AHC, as a non-energetic technique, would maintain the Ga coverage.

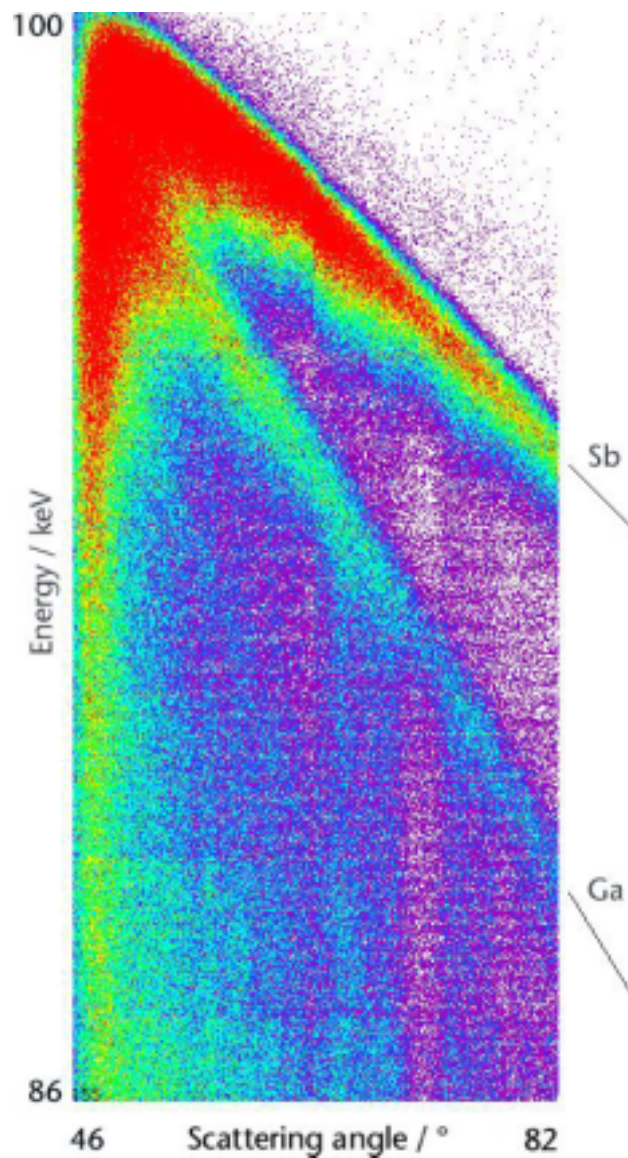


Figure 5.40: Tiled MEIS spectrum for the GaSb(001)-c(6×4) reconstruction.

This reconstruction was analysed in MEIS (a sample spectrum shown in figure 5.40), with a view to attaining a structural solution. This would require modelling and simulation, just as in the case of the c(2×6) before. However, no model for this or indeed any Ga-rich surface of GaSb(001) was extant, and with a unit cell area twice as large again as the c(2×6), this task was to prove difficult. The only models that could be identified for a related c(6×4) reconstruction were those for GaAs(001), discussed in §5.2, and shown again in figure 5.41. These were used as the basis for VEGAS simulation, using a similar pattern of dimer parameter variation as before, varying the atomic positions of the dimer atoms starting from bulk-like sites.

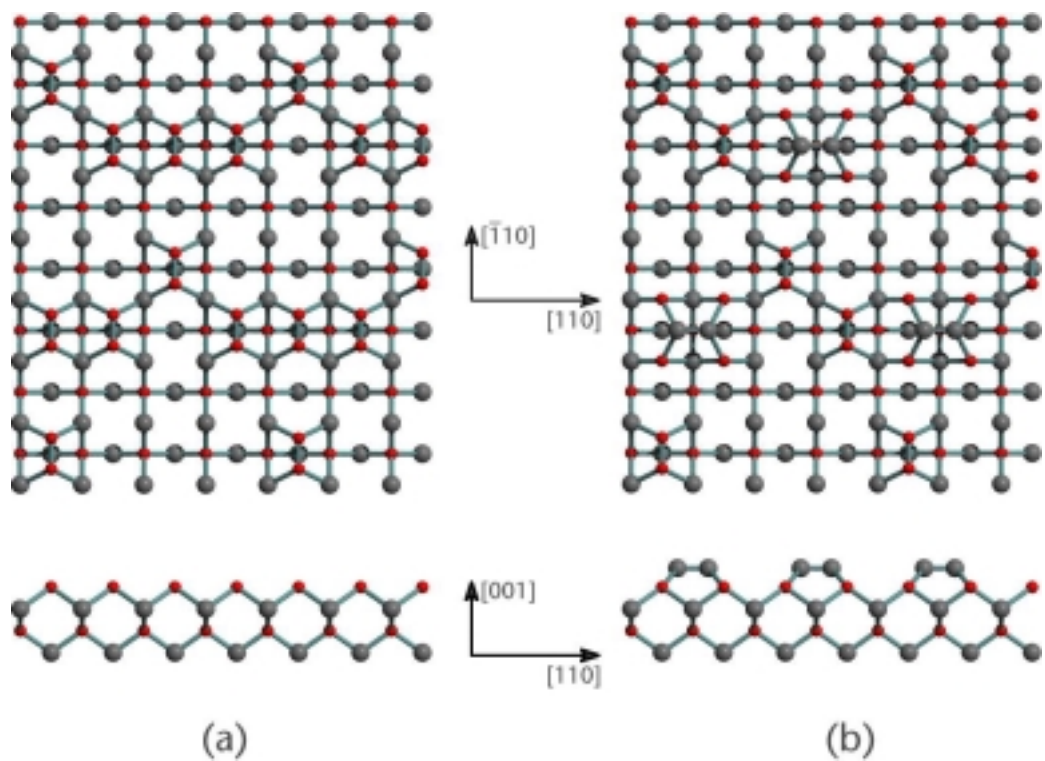


Figure 5.41: Alternative models for the GaSb(001)-c(6x4) reconstruction, based on those proposed for GaAs(001), as shown in figure 5.4. Note that the GA model (b) has Ga dimers surmounted atop the Sb dimer chains. These Ga dimers are not present in the NGA model shown in (a).

Whilst simulations initially succeeded (albeit with each requiring many hours of compute time), it was found that attempts to refine them failed, with the VEGAS program crashing catastrophically. Much time was spent in trying to resolve this. It was considered almost certain to be a memory issue, with some parameter being too large in the simulation. As described in §4.4.1, efforts were made to streamline the code, reducing both the time taken and the memory requirements during simulation. One of the advantages of the changes made was that it should have reduced the likelihood of crashes due to memory allocation failure. By removing the arbitrary dimensioning of the internal arrays and replacing them with dynamic allocations, memory use should have been more efficient. Any failure to allocate memory should produce a well-defined exception, which could be trapped and dealt with elegantly. However, this was clearly not occurring in this case. Investigation of the error indicated that it happened under several different conditions during calculation of hitting probability. The actual crash occurred when writing data to arrays. There was no evidence that it was due to a problem at the time of memory

allocation. The inconsistency in the timing of the crash (at any point in the hitting probability calculations) suggests that it is somehow related to the randomness of the ion trajectories. However, since such an error does not generally occur in other, smaller models, it is thought unlikely to be an arithmetic overflow. Such an exception might lead to an attempted write of an unreasonable value to the array. However, overflow exceptions can be handled, and indeed VEGAS already deals with hitting probabilities which exceed expected norms. This leads to the conclusion that it is a memory problem which is not recognized by the compiler. It may be that a more recent compiler (produced since 1995) might be able to handle the problem more gracefully. However, resources of time and money meant that this problem could not readily be addressed at source level. Therefore, attempts were made to reduce the parametric dimensions of the model. A number of approaches were taken, including reduction in the range of detection angles, the number of z-layers, the number of incident ions and the number of 'multimodel' variations (as discussed in §4.2.3). Unfortunately, none of these measures proved enough to enable a simulation to run to completion. Even reducing the number of parameters to a level comparable to the much simpler models already described was unsuccessful. Further tests on a larger machine resulted in a curiously inconsistent behaviour. The simpler NGA (no gallium atop) model, shown in figure 5.41(a), ran to completion although the results were void. The more complex GA (gallium atop) model, shown in figure 5.41(b), failed as before.

It was eventually identified that the cause of the problem was the number of groups of atoms in the  $x$ - and  $y$ -planes. In constructing the original model with bulk-like atomic positions, the number of groups forming the auxiliary lattice was low enough for the model to run. However, as the dimer atoms were moved closer together, the VEGAS software considered them to reside in separate planes from the bulk atom planes. In the case of the simpler model, this resulted in an immediate increase in the number of  $y$ -planes to be modelled from 17 to 27. The three extra dimers in the GA model resulted in an additional increase in the  $x$ -plane from 14 to 20 planes. A net increase of 220% in the array

size over the bulk-like model would therefore be required in this case. The fact that this is a problem is not flagged at the time of model generation, since the calculation of the auxiliary lattice does not take place until the back-end multicalc program is run. Further evidence of the scalability problems inherent in large unit cell models is in the size of the input files. For example, the input file for a typical simulation of the  $(1\times 3)$  surface was 10 kilobytes, and for the  $c(2\times 6)$  phase, it was 33 kilobytes. For the  $c(6\times 4)$  model, a similar input file was 359 kilobytes.

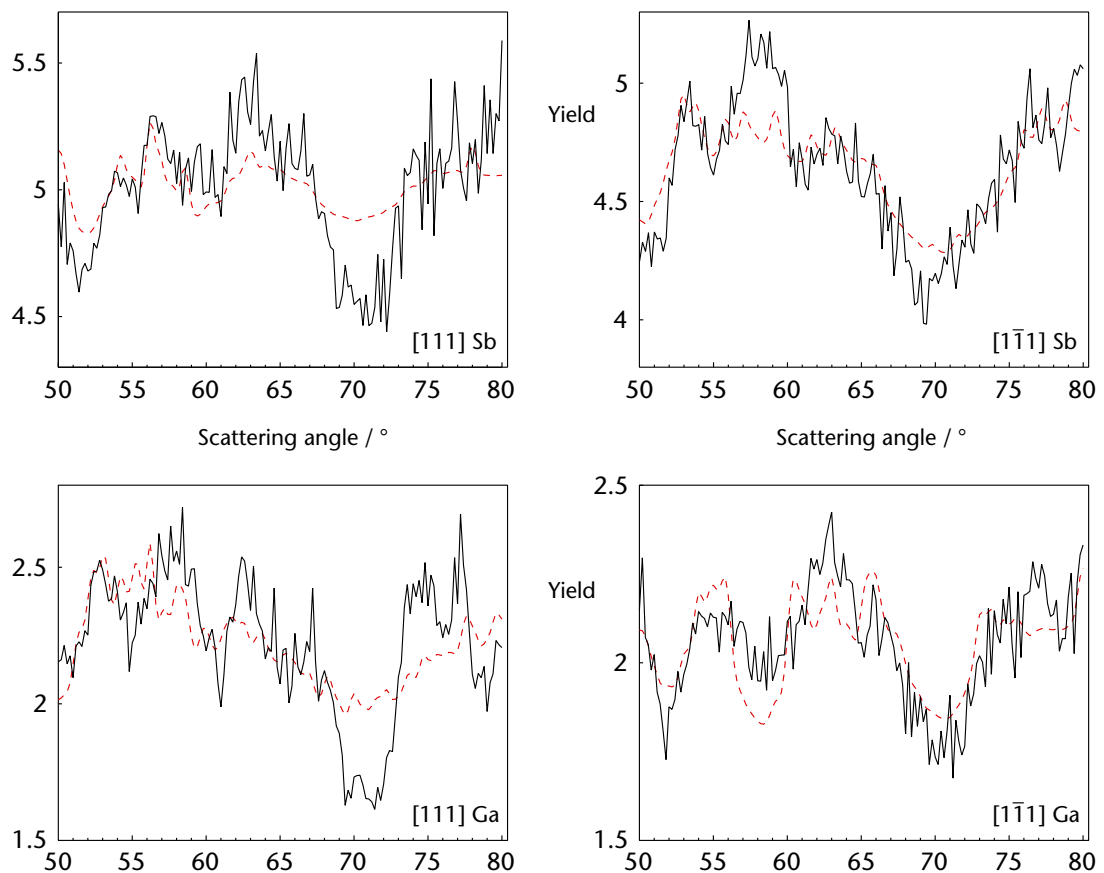


Figure 5.42: Best-fit MEIS data for the GaSb(001)- $c(6\times 4)$  reconstruction, NGA model, as shown in figure 5.41(a).

Although a complete structural solution was not possible, some useful qualitative information can be gleaned from the simulations that did succeed. Best-fit simulations are shown alongside the relevant data in figures 5.42 (NGA) and 5.43 (GA model). It should be noted that the raw MEIS data is scaled and skewed using an empirical calibration factor to account for intensity variations in the experimental data not modelled in the simulation. The yields plotted should therefore not be treated as absolute.

It is visually evident from these simulations based on near-bulk atom positions that the GA model is a much poorer fit than the NGA model. The best-fit  $R$ -factors bear out this conclusion, and are shown in table 5.5.

model	$[111]$ Sb	$[1\bar{1}1]$ Sb	$[111]$ Ga	$[1\bar{1}1]$ Ga
GA	5.29	8.27	6.80	9.24
NGA	2.82	2.50	4.28	2.53

Table 5.5: Best-fit  $R$ -factors for the two models proposed for the GaSb(001)- $c(6\times 4)$  reconstruction.

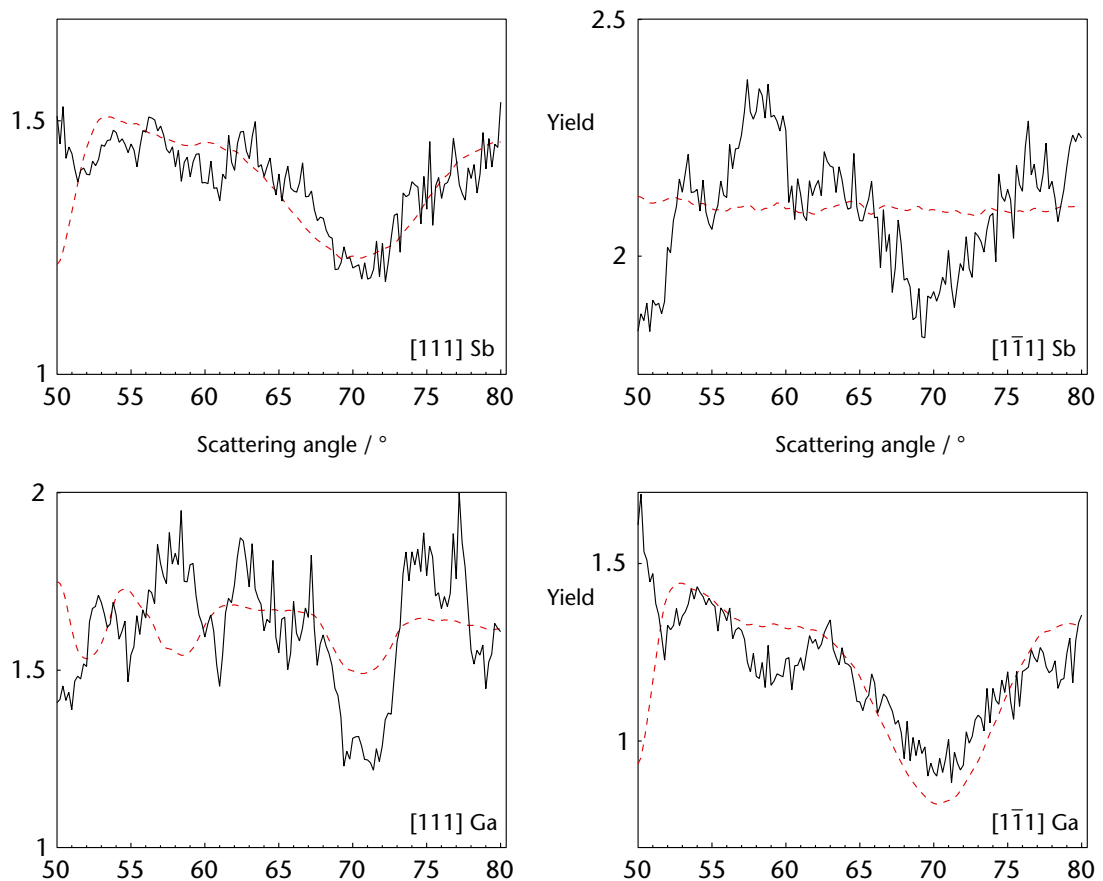


Figure 5.43: Best-fit MEIS data for the GaSb(001)- $c(6\times 4)$  reconstruction, GA model, as shown in figure 5.41(b).

In the NGA model, shown in figure 5.42, there is excellent matching of the peak locations, particularly in the  $[1\bar{1}1]$  azimuth. Note also that although the agreement between simulated and experimental yield is relatively poor in the  $[111]$  Ga data (indeed this azimuth had the poorest  $R$ -factor for this model), the splitting of the main  $[1\bar{1}1]$  blocking dip (at around  $69^\circ$  and  $72^\circ$ ) is in excellent alignment. By comparison, the best-

fits for the GA model, shown in figure 5.43 have markedly worse  $R$ -factors, clearly poorer dip alignment and markedly different yield profiles. The simulated data are relatively featureless compared to the NGA fits, particularly in the case of the  $[1\bar{1}1]$  Sb fit, for which the yield is almost constant. The  $[111]$  Ga simulation has a completely different blocking profile, with complete misalignment of all but the  $[\bar{1}\bar{1}1]$  blocking dip at  $70.52^\circ$ . Although these results are for near bulk-like dimer positions, the GA model of figure 5.39(b) is much less consistent with the MEIS data recorded.

### 5.5.6 Summary

- i) The (001) surface of GaSb has been cleaned by exposure to atomic hydrogen at elevated temperatures. CAICISS and AES were used to investigate transitions of the surface with increasing temperature. LEED, AES and MEIS were used to study the atomic hydrogen cleaning (AHC) process and the surface reconstructions thereby formed.
- ii) Exposure to atomic hydrogen at 670 K with a total  $H_2$  dose of  $< 100$  kL reduced atmospheric contamination to the detection limit of AES without physical damage to the surface or sub-surface. This is consistent with earlier work demonstrating that no measurable electronic damage resulted from AHC.
- iii) Annealing a  $(1\times 3)$  reconstruction to 645 K led to the onset of a transition to a  $c(2\times 6)$  reconstruction. Above 735 K non-congruent sublimation of Sb was observed by AES with rapid surface decomposition occurring above 785 K.
- iv) A  $(1\times 3)$  reconstruction was prepared by AHC and found to have a surface composition of around 45% Ga. A structural solution by MEIS using VEGAS Monte Carlo simulations was performed, using a model based on STM and PES data. Parameters were determined for Sb dimer length and height and interdimer Ga height.

- v) A  $c(2 \times 6)$  reconstruction was prepared by both argon ion-bombardment and annealing (IBA) and AHC. MEIS, LEED and AES data were all consistent with the hydrogen-cleaned surface having less disorder and less contamination. Structural analysis supported a model based on staggered Sb dimer chains interspersed by antiphase second layer Sb dimers, but with some degree of disorder. This is consistent with reported STM evidence.
- vi) A previously unreported stable  $c(6 \times 4)$  reconstruction was clearly observed using LEED after AHC with a 75 kL dose of  $H_2$  and a substrate temperature of 575 K. AES suggests it is a Ga-rich phase, with around 59% Ga. It is proposed that it has not been previously observed because IBA will preferentially sputter surface Ga. Due to the large unit cell, simulation to determine a structural solution proved unsuccessful. However, it was possible to demonstrate that of two models based on a similar GaAs phase, one based on staggered Sb dimers without top layer Ga dimers was more consistent with the MEIS data.

## 5.6 References

- <sup>1</sup> Q. Xue, T. Hashizume, T. Sakurai: *Progress in Surf. Sci.* **56** (1997) 1
- <sup>2</sup> A.J. van Bommel, J.E. Crombeen and T.G.J. van Oirschot: *Surf. Sci.* **72** (1978) 95
- <sup>3</sup> P. Drathen, W. Ranke and K. Jacobi: *Surf. Sci.* **77** (1978) L162
- <sup>4</sup> J. Massies, P. Etienne, F. Dezaly and N.T. Linh: *Surf. Sci.* **99** (1980) 121
- <sup>5</sup> P.K. Larsen, J.H. Neave, J.F. van der Veen, P.J. Dobson and B.A. Joyce: *Phys. Rev. B* **27** (1983) 4966
- <sup>6</sup> M. Sauvage-Simkin, R. Pinchaux, J. Massies, P. Calverie, N. Jedrecy, J. Bonnet and I.K. Ro: *Phys. Rev. Lett.* **62** (1989) 563
- <sup>7</sup> D.J. Frankel, C. Yu, J.P. Harbison and H.H. Farrell: *J. Vac. Sci. Technol. B.* **5** (1987) 1113
- <sup>8</sup> D.J. Chadi: *J. Vac. Sci. Technol. A* **5** (1987) 834
- <sup>9</sup> D.K. Biegelsen, R.D. Bringans, J.E. Northrup and L.E. Swartz: *Phys. Rev. B.* **41** (1990) 5701
- <sup>10</sup> Q. Xue, T. Hashizume, J.M. Zhou, T. Sakata, T. Ohno and T. Sakurai: *Phys. Rev. Lett.* **74** (1995) 3177
- <sup>11</sup> J. Falta, R.M. Tromp, M. Copel, G.D. Pettit and P.D. Kirchner: *Phys. Rev. Lett.* **69** (1992) 3068
- <sup>12</sup> R. Duszak, C.J. Palmstrom, L.T. Florez, Y-N. Yang and J.H. Weaver: *J. Vac. Sci. Technol. B*(1992) 1891
- <sup>13</sup> W. Mönch: *Semiconductor surfaces and interfaces* (Springer, 1993)
- <sup>14</sup> H.H. Farrell, M.C. Tamargo and J.L. de Miguel: *Appl. Phys. Lett.* **58** (1991) 355

- 15 I. Chizhov, G. Lee, R.F. Willis, D. Lubyshev and D.L. Miller: *Phys. Rev. B* **56** (1997) 1013
- 16 F. Jona: *IBM J. Res. Develop.* **9** (1965) 375
- 17 A.Y. Cho: *J. Appl. Phys.* **42** (1971) 2074
- 18 J.E. Northrup and S. Froyen: *Phys. Rev. Lett.* **71** (1993) 2276
- 19 H.H. Farrell, J.P. Harbison and L.D. Peterson: *J. Vac. Sci. Technol. B* **5** (1987) 1482
- 20 G.E. Franklin, D.H. Rich, A. Samsavar, E.S. Hirschorn, F.M. Leibsle, T. Miller, T-C. Chiang: *Phys. Rev. B* **41** (1990) 12619
- 21 G.R. Bell and C.F. McConville: *Appl. Phys. Lett.* **69** (1996) 2695
- 22 M.T. Sieger, T. Miller and T-C. Chiang: *Phys. Rev. B* **52** (1995) 8256
- 23 U. Resch-Esser, N. Esser, B. Brar and H. Kroemer: *Phys. Rev. B* **55** (1997) 15401
- 24 P.M. Thibado, B.R. Bennett, B.V. Shanabrook and L.J. Whitman: *J. Cryst. Growth* **175/176** (1997) 317
- 25 L.J. Whitman, P.M. Thibado, S.C. Erwin, B.R. Bennett, B.V. Shanabrook: *Phys. Rev. Lett.* **79** (1997) 693
- 26 T.C.Q. Noakes: *PhD Thesis* (University of Warwick, 1995)
- 27 G.R. Bell, N.S. Kaijaks, R.J. Dixon and C.F. McConville: *Surf. Sci.* **401** (1998) 125
- 28 F.W.O. Da Silva, C. Raisin, M. Silgs, M. Nouaoura and L. Lassabatere: *Semicond. Sci. Technol.* **4** (1989) 565
- 29 L.H. Dubois and G.P. Schwartz: *J. Vac. Sci. Technol. B* **2** (1984) 101
- 30 T.S. Jones, M.Q. Ding, N.V. Richardson and C.F. McConville: *Surf. Sci.* **247** (1991) 1
- 31 M. Dumas, M. Nouaoura, N. Bertru, L. Lassabatère, W. Chen and A. Kahn: *Surf. Sci. Lett.* **262** (1992) L91
- 32 J.R. Waterman, B.V. Shanabrook and R.J. Wagner: *J. Vac. Sci. Technol. B* **10** (1992) 895
- 33 R. Ludeke: *IBM J. Res. Develop.* **22** (1978) 304
- 34 W.O. Barnard, J.B. Malherbe and G. Myburg: *S. Afr. J. Phys.* **14** (1991) 22

## 6 • Surface preparation and the (4×2) reconstruction of InAs(001)

### 6.1 Introduction

The preparation of clean, crystalline and stoichiometric III–V semiconductor surfaces is important both for surface science studies and for device growth. It is only in recent years that UHV growth techniques such as MBE have enabled such clean surfaces to be prepared *in-situ* with analytical apparatus. In many laboratories, it remains important to be able to prepare clean and well-ordered crystals from initially contaminated and disordered samples, whilst it is equally essential to have well-prepared substrates for MBE growth. Various cleaning techniques to achieve these aims were discussed in chapter 3, in particular focussing on atomic hydrogen cleaning (AHC) and ion-bombardment and annealing (IBA). This chapter examines the effects of IBA and AHC on InAs(001) using LEED, AES and MEIS, as well as comparing models for the InAs(001)–(4×2) reconstruction and presenting structural parameters for the most likely model.

### 6.2 Experimental details

Work had already been performed using HREELS and AES to examine the electronic effects of AHC on InAs(001).<sup>1</sup> As with GaSb(001), a dose of less than 100 kL H<sub>2</sub> resulted in the removal of almost all surface atmospheric contamination at a substrate temperature of 670 K, with a sharp LEED pattern and AES results indicating an In-rich surface. HREELS simulations confirmed a surface region free of electronic damage. It is assumed that the mechanism for oxide desorption is similar to that described for GaAs in §3.3.2. Annealing above 700 K resulted in rapid degradation of the surface, it becoming cloudy in appearance and showing a significantly higher indium content in AES. Atomic force microscopy (AFM) images of these samples showed the presence of large droplets of metallic indium (~ 3 μm in width and ~1 μm in height) distributed evenly across the cloudy regions of the surface. Therefore, substrate temperatures during AHC were maintained below 670 K for the work presented in this thesis.

The InAs(001) samples used in this work were bulk-grown, polished and etched by the manufacturer, MCP Wafer Technology Ltd. They were S-doped, with a carrier density of  $\sim 10^{18} \text{ cm}^{-3}$ . These experiments were performed at the MEIS facility of CLRC Daresbury Laboratories, using the apparatus as described in §5.4.2. An AG10 ‘cold cathode’ ion gun (supplied by VG Ltd) was fitted for IBA. This ion gun could be used to accelerate ions through an energy range between 0.5 and 4 keV. The angle of incidence of the ions could be varied between normal and grazing incidence with an uncertainty of  $\pm 2^\circ$ . High purity argon from a low pressure cylinder was used, with the gas supply lines pumped to  $\sim 1 \times 10^{-7}$  mbar before gas admittance through a leak valve.

The samples were introduced into the loading chamber before pumping down, outgassing and annealing for typically one hour at  $\sim 500$  K. Both IBA and AHC were performed in the preparation chamber, with bombardment energies for IBA varied systematically over a range from 0.5–4 keV at  $45^\circ$  incidence. AES measurements of the surface composition were made both before and after annealing at 600 K for thirty minutes. MEIS was performed with 100 keV  $\text{H}^+$  ions, normally incident, along an  $\langle 001 \rangle$  axis, and detected around a  $\langle 111 \rangle$  direction. This geometry results in greater mass resolution, but at the expense of a much lower yield than for the  $\langle 111 \rangle$  incidence used in the GaSb(001) work of the previous chapter. This is due to the much greater backscattering angle (around  $90\text{--}140^\circ$  instead of  $40\text{--}80^\circ$ ), resulting in a relatively low Rutherford scattering cross-section (as defined in §3.4.6). The use of  $\text{H}^+$  ions instead of  $\text{He}^+$  was primarily to reduce the likelihood of damage due to the analysing beam. In addition to depth profiling by MEIS, a structural study of the AHC-prepared InAs(001)–(4×2) surface was performed using MEIS, LEED and AES.

### 6.3 Structural analysis of InAs(001)–(4×2)

InAs is a low band gap semiconductor ( $E_g = 0.36$  eV, compared to 1.42 eV for GaAs), promising for applications in high-speed transistors, infrared detectors and lasers. The reconstructions of its (001) surface are similar to GaAs(001), but relatively simple and few

in number, with mainly As-rich (2×4) and In-rich (4×2) phases reported.<sup>2</sup> The structure and stoichiometry has been little investigated, with STM being the primary technique used so far. As with GaAs(001) reconstructions in the previous chapter, Xue offers a good review of the work performed on InAs(001) to date.<sup>3</sup>

The As-rich (2×4) surface may be prepared by decapping at 530 K or by annealing in As flux.<sup>4,5</sup> Models proposed are very similar to those for GaAs(001)–(2×4), with STM results to date being most consistent with a bilayer model as shown in figure 6.1.

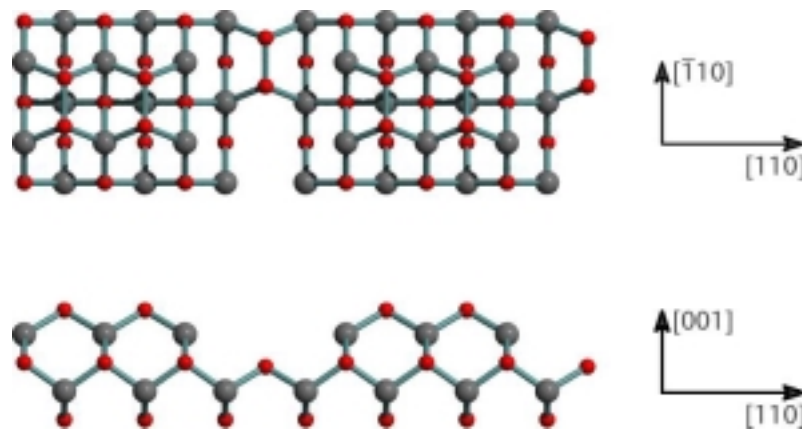


Figure 6.1: Models for the As-rich InAs(001)–(2×4) reconstruction. As atoms are shown as red, In atoms as grey.

The In-rich (4×2) phase is readily prepared by annealing, IBA or MBE growth.<sup>6,7</sup> Indications from STM are that the structure is consistent, by whichever method the surface is prepared, and is extremely well-ordered. It is believed to be a missing-row dimer structure, and three distinct models have been proposed; a two In dimer bilayer model (hereafter, 2DB) similar to that proposed for GaAs(001)<sup>8</sup>, a one In dimer bilayer model (1DB)<sup>9</sup> and a two In dimer model with perpendicular As dimerization (2DR)<sup>10</sup>. Each model is shown in figure 6.2.

As with other III–V semiconductor surfaces, there is a related  $c(8\times 2)$  phase, derived from a shift in the In dimers, either in the top or the third layer.<sup>7</sup> Although this phase was observed, beam-time limitations prevented a structural analysis by MEIS.

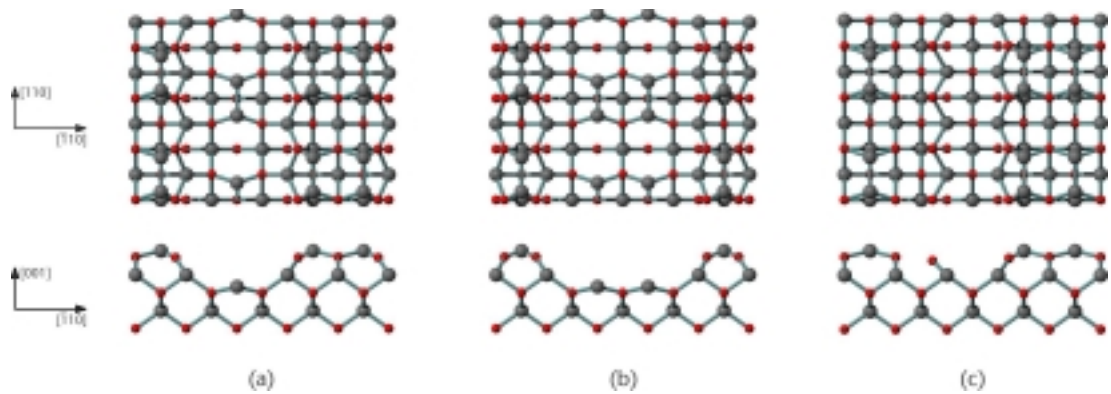


Figure 6.2: Models for the In-rich InAs(001)-(4×2) reconstruction. (a) two-dimer bilayer model (2DB), (b) one-dimer bilayer model (1DB), (c) two-dimer rebonded-As model (2DR). As atoms are shown as red, In atoms as grey.

The observed contrast difference in the STM images of figure 6.3, along lines L1 and L2 (the [110] direction) is relatively low indicating corrugation much less than the 3 Å which would be expected for the 1DB model, given the large gap between dimer chains. This suggests a two-dimer model is more likely. However, for both the 2DB and 1DB models, the In coverage is 0.75 ML, whilst the STM experimental results are more consistent with the 0.5 ML coverage of the 2DR model.

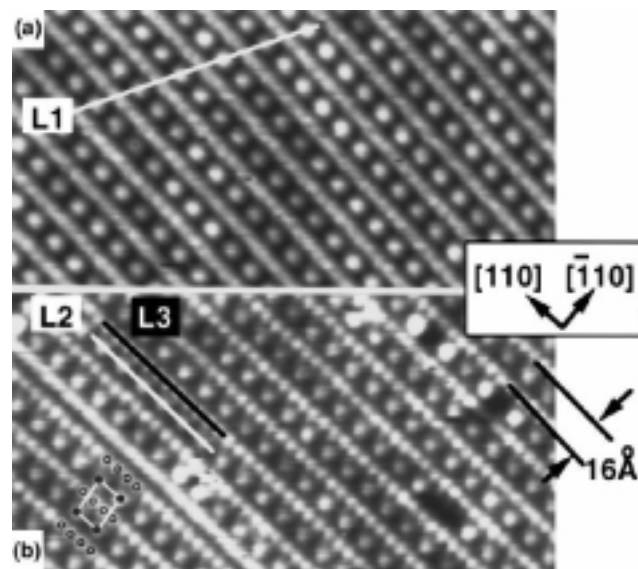


Figure 6.3: Filled states STM images of the InAs(001)-(4×2) surface taken at bias voltages of (a) -2.2 V and (b) -1.6 V [from Xue et al<sup>10</sup>].

Models for all three (4×2) structures were created in VEGAS, and iterative simulations performed in order to determine the atomic positions of the dimerized atoms, following a similar pattern to that described in the previous chapter. The structural parameters varied

were the lengths and heights of the In dimers in the top and third layer as well as the positions of the As atoms in the second layer separating the dimer chains. As before, the limitation of the software to analysis of only three simultaneous parameters meant that variations had to be simulated cyclically.

After several iterations of simulation and model refinement, the structural parameters were examined. The  $R$ -factors for the best-fit 2DB model, shown in table 6.1, were noticeably worse than for the other two models. The structure itself was nonphysical, with a top layer dimer length of 1.12 Å, as shown in figure 6.4. This is consistent with the appraisal based on STM data, and therefore the 2DB model was discounted and not examined further.

$[111]$ In	$[1\bar{1}1]$ In	$[111]$ As	$[1\bar{1}1]$ As
16.79	3.34	6.16	2.88

Table 6.1: Best-fit  $R$ -factors for the InAs(001)-(4×2) reconstruction, 2DB model.

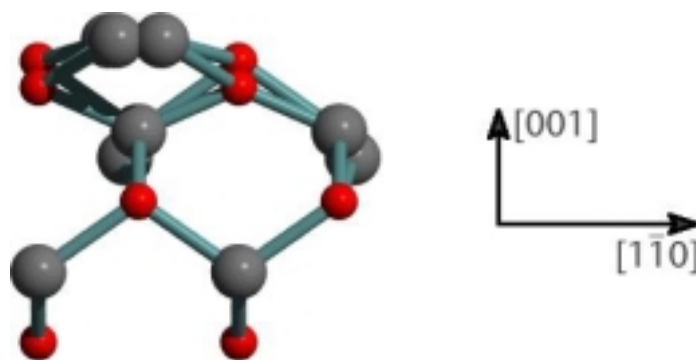


Figure 6.4: Best-fit structural solution for the InAs(001)-(4×2) reconstruction, 2DB model. The top layer dimer length for this solution is 1.12 Å.

The 1DB model provided a much better fit to the data. However, the model was still not particularly physical, particularly in the value of  $x$  as shown in figure 6.5. The structural parameters obtained are shown in table 6.2. The global best-fit simulations and MEIS data for the 1DB model are shown in figure 6.6. Whilst some dips, such as the  $[\bar{2}33]$  dip at  $115.24^\circ$  in the  $[1\bar{1}1]$  As azimuth, are not well matched the overall closeness of the yield profile is good, with consistently reasonable  $R$ -factors, listed in table 6.3.

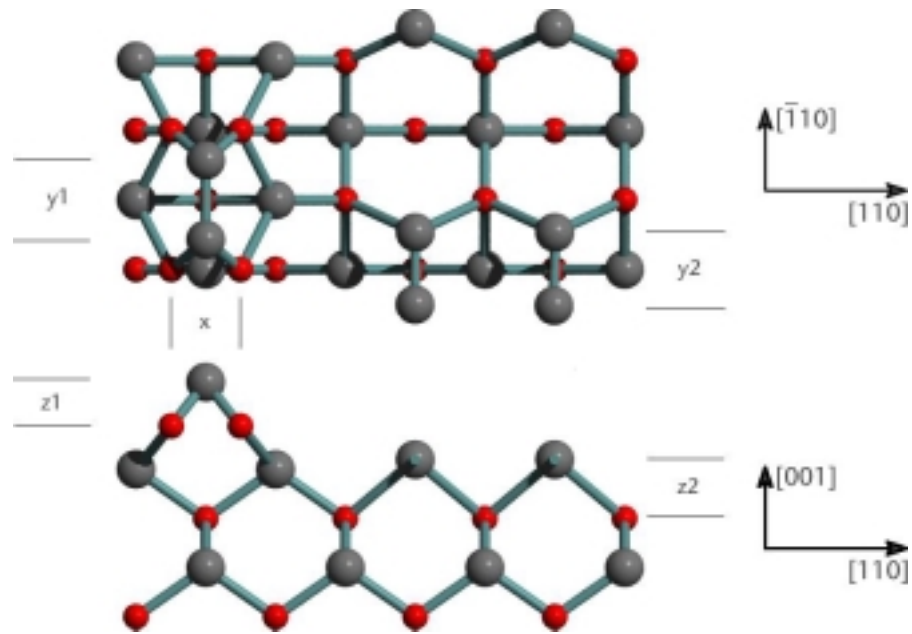


Figure 6.5: Best-fit structural solution for the InAs(001)-(4×2) reconstruction, 1DB model.

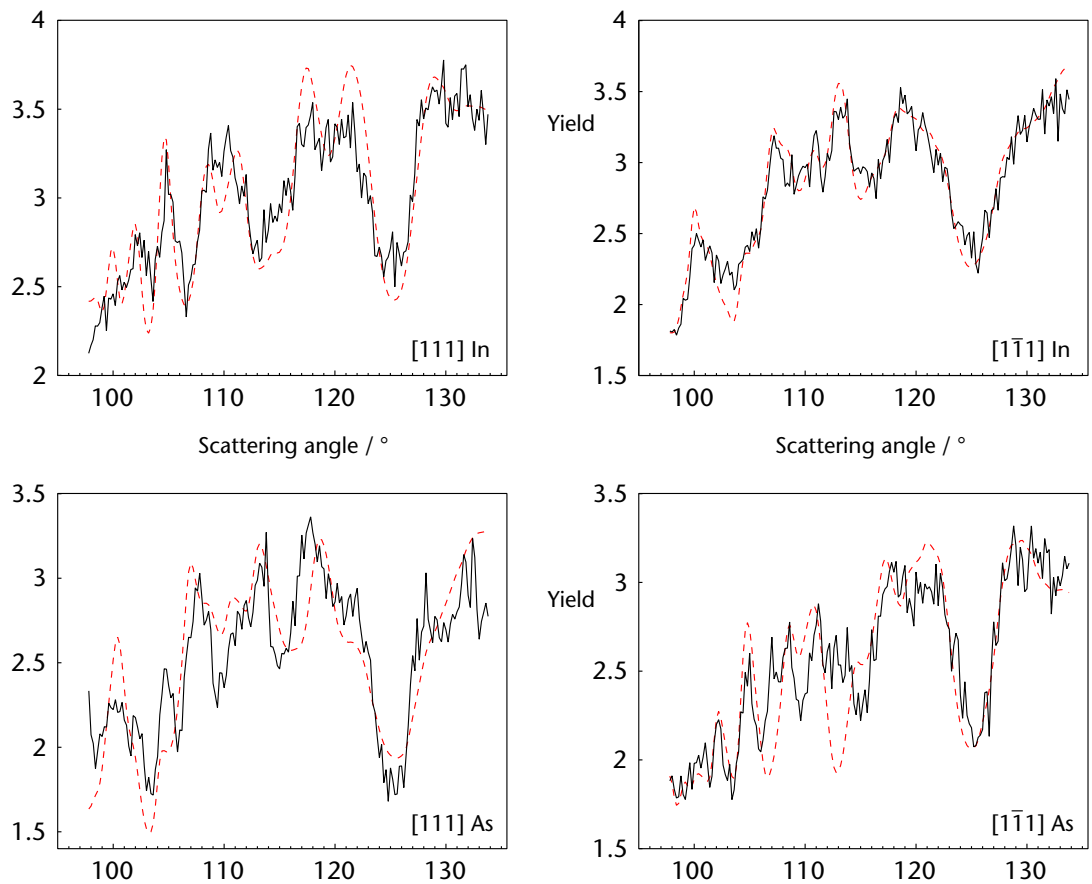


Figure 6.6: Best-fit MEIS simulation data for the InAs(001)-(4×2) reconstruction, 1DB model.

y1	z1	y2	z2	x
2.45	1.35	2.29	1.82	2.13

Table 6.2: Structural parameters for the InAs(001)–(4×2) reconstruction, 1DB model. All figures are in Å, with an estimated error of 0.05 Å.

$[111]$ In	$[1\bar{1}1]$ In	$[111]$ As	$[1\bar{1}1]$ As
4.81	2.49	4.80	3.81

Table 6.3: Global best-fit  $R$ -factors for the InAs(001)–(4×2) reconstruction, 1DB model.

The 2DR data again demonstrated that use of  $R$ -factors as a criterion of fit quality must be tempered by consideration that comparisons cannot be made across datasets, even within a single experiment. After a number of iterations, best-fits were obtained for In and As datasets. The best-fit for the different datasets was for different parametric variations of the model. In and As fits for the  $[1\bar{1}1]$  azimuth are shown in figure 6.7. The difference in the position of the second layer rebonded atom between these two fits was 0.7 Å, and the best-fit  $R$ -factors were  $R_{As} = 2.32$ , and  $R_{In} = 4.23$ . However, the best-fit for the As simulation fails to match a number of experimental peaks. For example, as with the 1DB model, the  $[\bar{2}33]$  dip at  $115.24^\circ$  in the experimental data is not present in the simulation, whilst conversely a dip at around  $112^\circ$  is visible in the simulation but not in the data. Although the  $R$ -factor is almost twice as large for the In simulation, the matching of the peak locations is visibly better, and therefore it was used as the basis for further refinement.

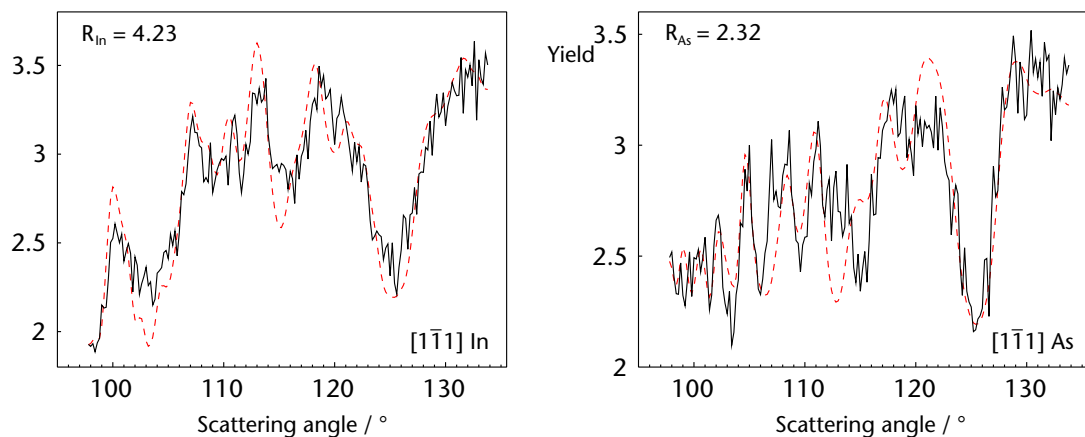


Figure 6.7: Best-fit MEIS simulation data after several iterations for InAs(001)–(4×2), 2DR model,  $[1\bar{1}1]$  azimuth.

The best-fit solution for the 2DR model is shown in figure 6.8 and structural parameters given in table 6.4. The simulation fits are shown in figure 6.9; the  $R$ -factors obtained are given in table 6.5. As can be seen by comparison with the  $R$ -factors for the 1DB model in table 6.3, this model is not dissimilar in terms of global quality of fit. However, whilst the individual  $R_{In[111]}$  is relatively poor, the overall parity in dip position, yield profile and  $R$ -factors are much greater than for the 1DB model. Perhaps more pertinent though, is that the model is physical, with a structure consistent with the STM data already reported.<sup>10</sup> It is therefore proposed that the 2DR structural model for the InAs(001)-(4×2) reconstruction, shown in figure 6.2(c), is the most consistent with the results of these MEIS experiments, with structural parameters as given in table 6.4.

There is one caveat in this analysis, which is that more parameters needed to be varied in order to produce a solution for the 2DR model than for the 1DB. This gives a greater degree of freedom, and so more potential for a parametric (if nonphysical) solution to the data. Conversely though in this case, the 1DB model with fewer degrees of freedom produced a less physical model. This supports the 2DR as the most viable solution.

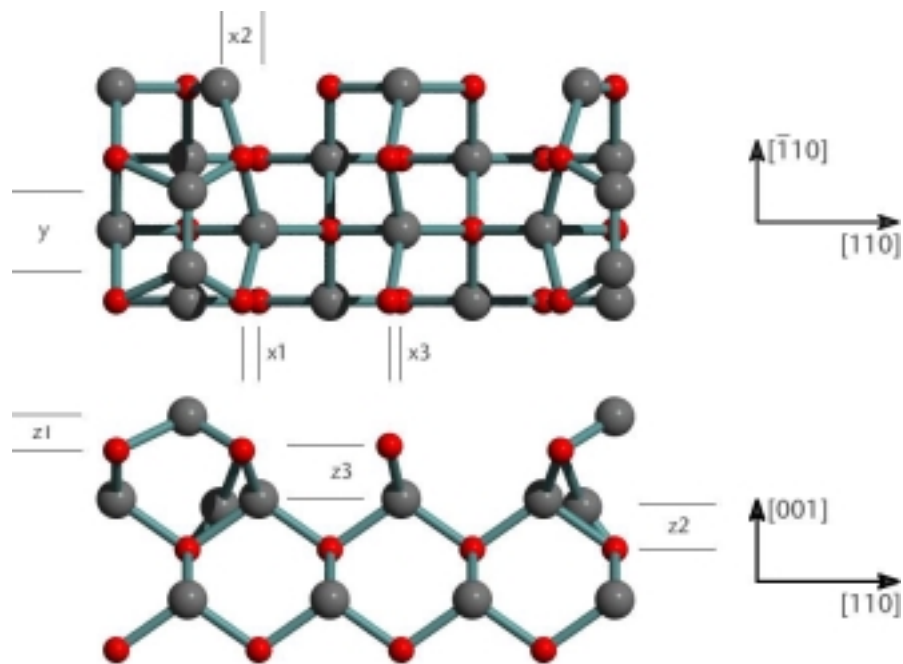


Figure 6.8: Best-fit structural solution for the InAs(001)-(4×2) reconstruction, 2DR model.

y	x1	z1	x2	z2	x3	z3
2.35	0.51	1.03	1.16	1.28	0.35	1.60

Table 6.4: Structural parameters for the InAs(001)–(4×2) reconstruction, 2DR model. All figures are in Å, with an estimated error of 0.05 Å.

$[111]$ In	$[\bar{1}\bar{1}1]$ In	$[111]$ As	$[\bar{1}\bar{1}1]$ As
7.49	3.87	3.79	3.44

Table 6.5: Best-fit *R*-factors for the InAs(001)–(4×2) reconstruction, 2DR model.

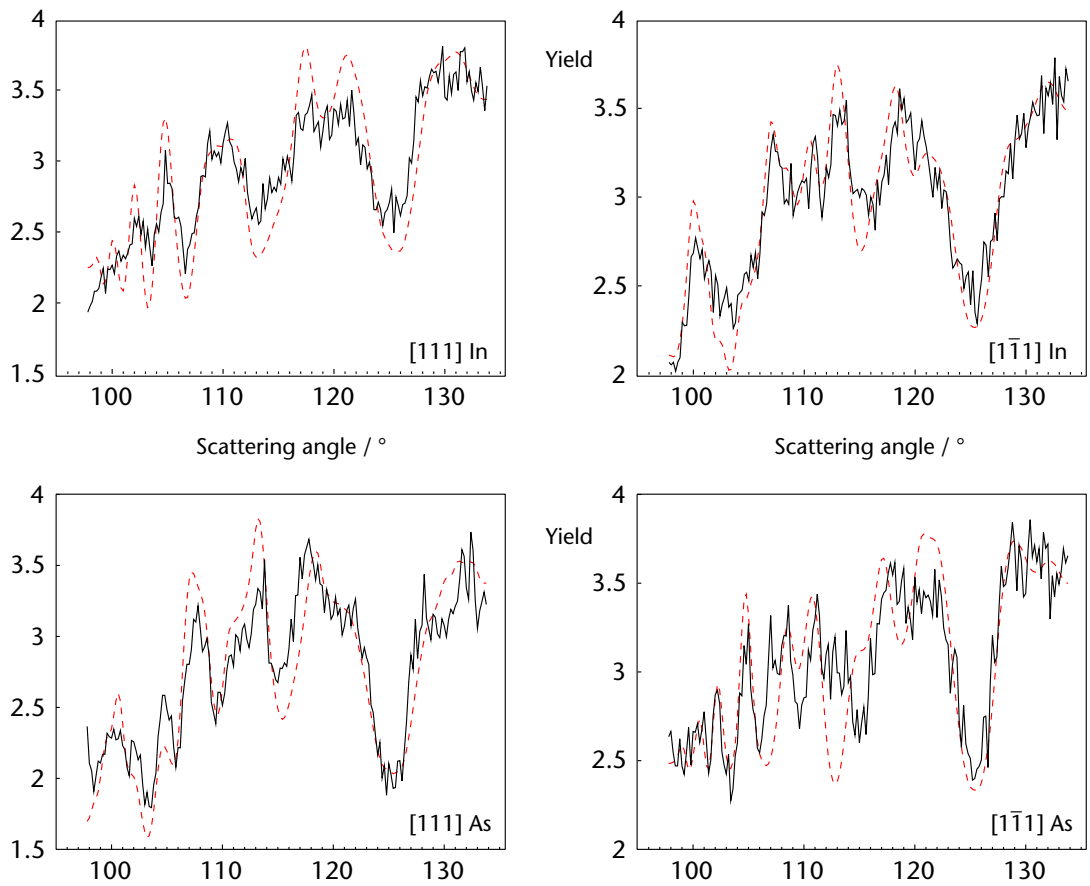


Figure 6.9: Best-fit MEIS simulation data for the InAs(001)–(4×2) reconstruction, 2DR model.

## 6.4 Beam damage induced by ion bombardment of InAs(001)

Perhaps the first consideration in the MEIS study of ion beam damage due to IBA was to establish whether the ion beam used to probe the sample during analysis could cause damage itself, and if so, to what extent. A conscious decision was made to use  $H^+$  ions rather than  $He^+$  in order to reduce the likelihood of damage, despite the resultant loss of mass resolution. However, even a proton beam may cause damage when incident with 100 keV energy. The MEIS system at CLRC Daresbury Laboratories uses a Faraday cup in the beamline to capture ions before they reach the sample when data is not actually being collected. Therefore no damage can occur from an idle beam. In order to quantify the damage that the ion beam could occur, an InAs(001) sample was analysed using MEIS over an incremental beam dose, as integrated using the sample current monitor. The results are shown in figure 6.10.

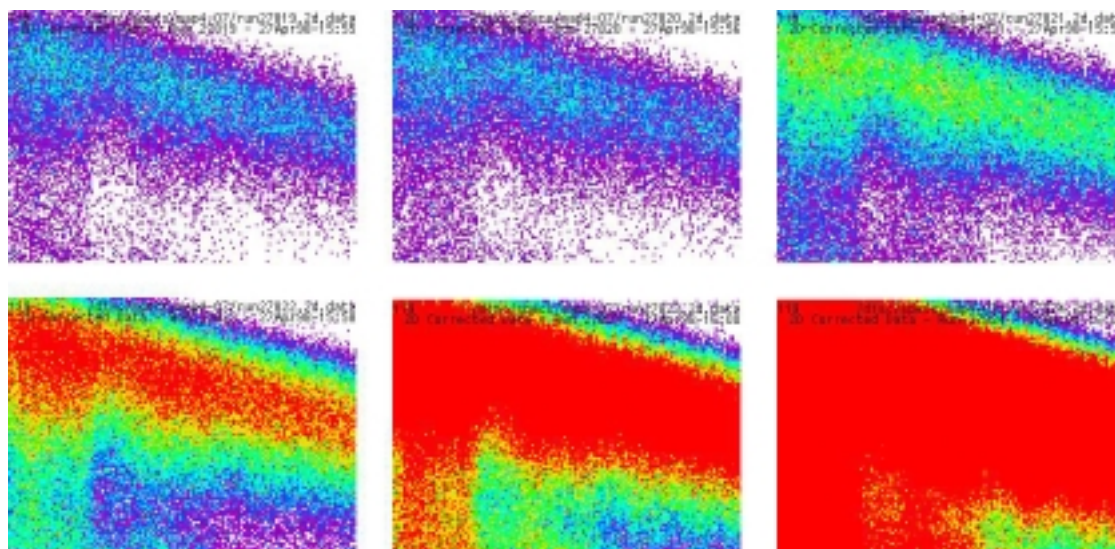


Figure 6.10: Beam damage induced by the 100 keV MEIS  $H^+$  ion beam after ion doses of (top row, left to right) 1, 2, 4  $\mu C$  and (bottom row) 8, 16 and 32  $\mu C$  on an InAs(001) surface. The beam is normally incident, with the detector centred on a  $\langle 233 \rangle$  azimuth. The backscattered energy range displayed is 98.2–96.44 keV.

It was clear from these data that doses over 2  $\mu C$  cause discernible changes in the backscattered yield, evidence of amorphization of the near-surface. During subsequent MEIS analysis, a dose of  $< 2 \mu C$  was used to minimize such damage. Also, between tiles the sample was moved so the beam was incident on previously unilluminated areas.

It was an aim of this work to examine directly whether any physical damage occurred due to AHC. Work using HREELS had already shown that no discernible electronic damage was evident as a result of AHC.<sup>1</sup> However, quantitative examination of surface damage proved difficult due to a persistent problem with antimony contamination. It appeared that the tip of the atomic hydrogen source had become contaminated with Sb from the k-cell during the previous experiments on GaSb(001). As a result, most AHC-treated InAs(001) samples had some surface Sb adsorbed from the atomic hydrogen source, in some cases comprising up to 34% of the surface composition as measured by AES. Despite attempts to outgas the source, clean it *in-situ* by sputtering and clean it chemically *ex-situ*, the problem was only resolved on the penultimate day of the allocated time at the MEIS facility. MEIS results from such an Sb-free H\* cleaned InAs(001)–(4×2) surface were used for the structural analysis in the previous section. There was no evidence of sub-surface damage as a result of AHC with a dose of 75 kL and substrate temperature of 600–630 K. A typical LEED pattern after AHC is shown in figure 6.11. It features some spot streaking, consistent with a well-ordered surface composed of both (4×2) and c(8×2) phases. The surface composition of the surface (without Sb contamination) was 43.5% indium, as measured by AES, with atmospheric contamination reduced to below detectable limits. Sample AES and MEIS spectra for the H\* cleaned InAs(001) surface are shown in figures 6.12 and 6.13 respectively.

For the samples prepared earlier in the experimental period by IBA, it was attempted to maintain a consistent ion dose at all energies by measuring and summing the sample current manually during the bombardment, adjusting the ion gun supply to counteract drift in the flux over the 5–30 minute bombardment timescales used. Analysis of the MEIS data taken after bombardment made it clear that manual management of dose was inaccurate, leading to a variation of up to a factor of two in the total ion dose. This made quantification more difficult, although some normalization was possible.

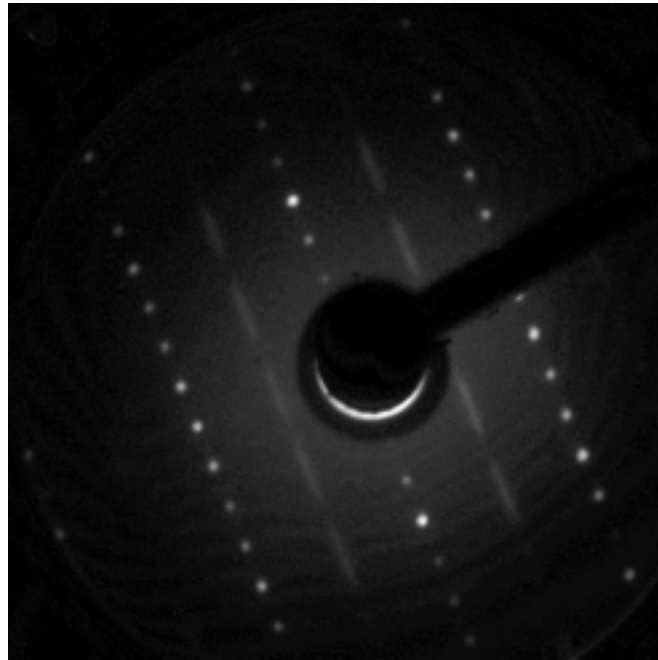


Figure 6.11: LEED pattern for an InAs(001)-(4×2)/c(8×2) reconstruction prepared by AHC (65 eV beam energy).

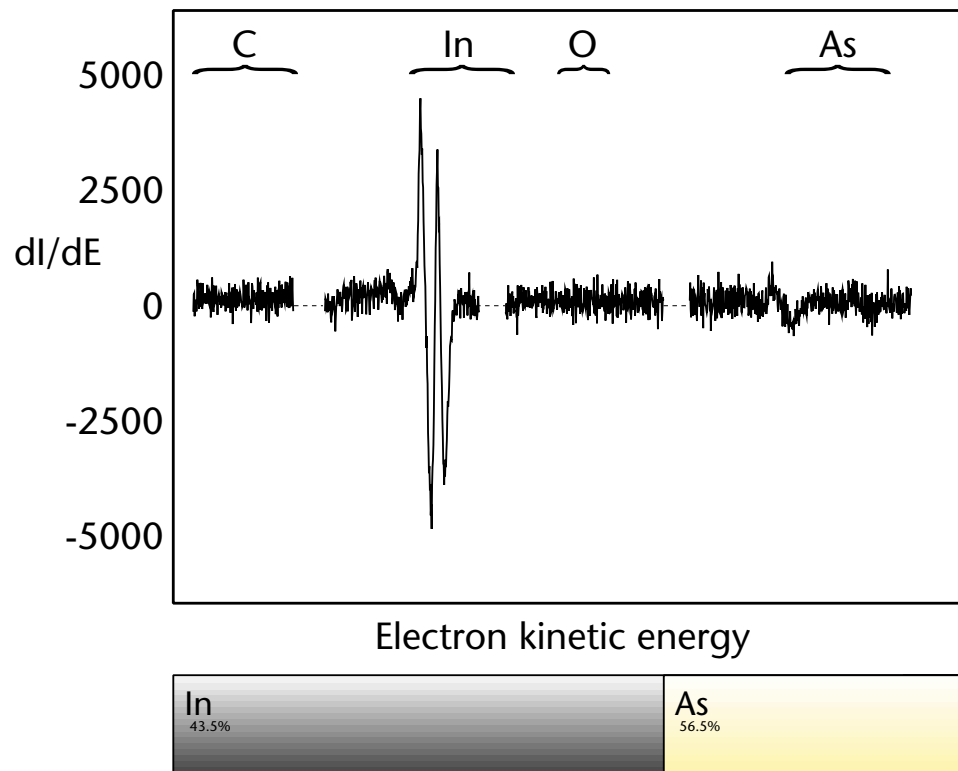


Figure 6.12: AES spectra and surface composition determined for the InAs(001)-(4×2)/c(8×2) reconstruction.

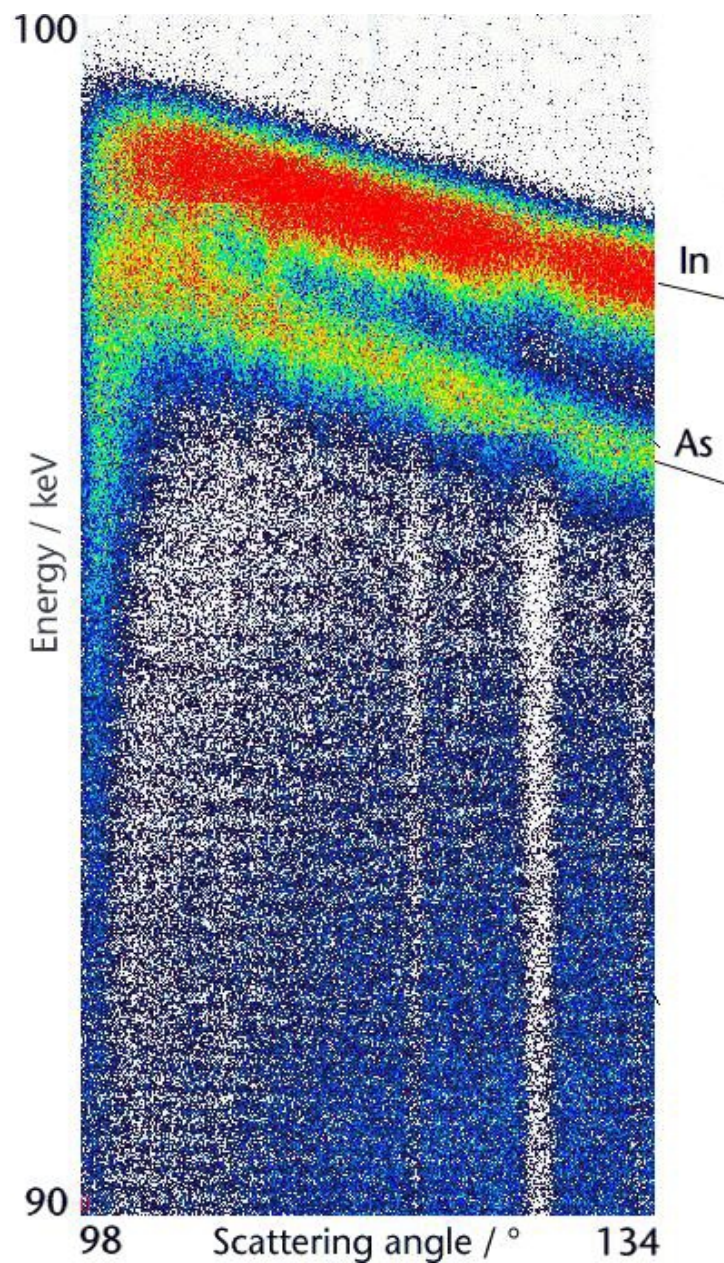


Figure 6.13: A tiled MEIS spectrum from an InAs(001)-(4×2) sample prepared by AHC.

Some simple peak height calculations for the surface MEIS data after bombardment and before annealing were performed in order to determine ratios of In/As at the top surface layer for a selection of bombardment energies. These data are summarized in figure 6.14. The unannealed data (red line) shows an decrease in relative In concentration above 0.5 keV ion energy. This is consistent with calculations of the In/As ratio after low kV ion bombardment based on Sigmund preferential sputtering theory<sup>11</sup>

$$\frac{C_{In}^s}{C_{As}^s} = \frac{C_{In}}{C_{As}} \left( \frac{m_{In}}{m_{As}} \right)^{2k} \cdot \left( \frac{U_{In}}{U_{As}} \right)^{1-2k} \quad 6.1$$

where

$$U_{In} = H_{In}^s + \frac{1}{2}(\epsilon_{In} - \epsilon_{As})^2$$

$$U_{As} = \frac{1}{2}D_{In-As} + \frac{1}{2}D_{As-As} - \frac{1}{2}(\epsilon_{In} - \epsilon_{As})^2 \quad 6.2$$

Here  $H_{In}^s$  is the sublimation enthalpy of In,  $\epsilon$  are Pauling electronegativities,  $D$  are diatomic bond energies and  $k$  is an empirical cross-section factor, of  $\sim 0.165$  for typical bombardment energies.  $C_{In}^s/C_{As}^s \sim 0.9$ , indicating slight preferential sputtering of In.

The data post-anneal (blue line) shows an essentially equal elemental ratio at the surface, consistent with surface repair following sublimation of As. Assuming that the annealed sample is stoichiometric, the variation in ratio is consistent with differences in the degree of surface repair following differing ion doses during bombardment. It is estimated that the actual ion dose was approximately twice as large for 2 keV incident energy as for 1 keV. The unannealed data was therefore normalized to account for this (black line). These results are consistent with the data of figure 3.4 for sputter yield at increasing energies.

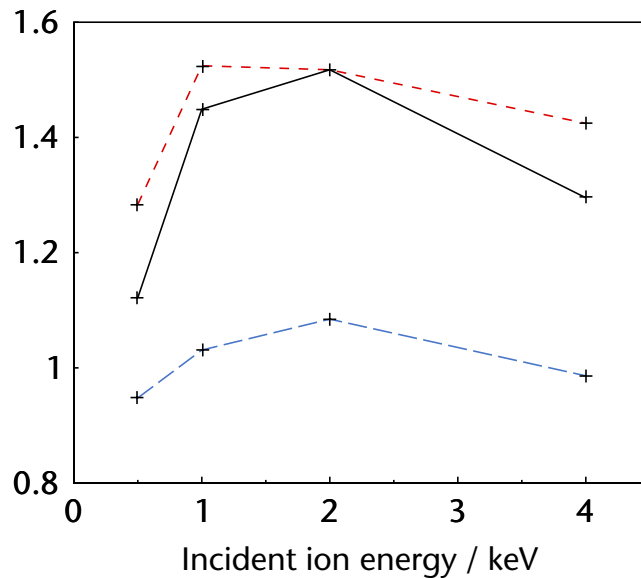


Figure 6.14: As/In ratios for InAs(001) after ion bombardment at varying energies (red) and post-annealing (blue). The unannealed data is also shown normalized to an assumed equal As/In ratio after annealing (black).

Having established that MEIS can demonstrate that surface damage and stoichiometric changes induced by ion bombardment are indeed removed by annealing, the sub-surface effects of IBA were examined by depth profiling with MEIS, using a normal incidence direction, detecting ions backscattered with an energy down to 89 keV, which enabled analysis to a depth of around 200 Å along an  $\langle 001 \rangle$  channel. The depth profiles are taken as an energy cross-section of the MEIS spectra (consider a vertical cross-section through figure 6.13). The profiles for the different bombardment energies are shown in figure 6.15, with surface In and As peaks evident at high energy as well as damage-induced peaks at lower energies in the background. Data for the sample prepared by IBA at 0.5 keV was used as a background function and subtracted from the data for more energetic IBA treatments. Curve-fits were performed and the backscattered energy converted to an equivalent depth by use of a constant stopping power. The approximation of a constant stopping power is adequate for 100 keV  $H^+$  ions over this relatively narrow energy range. The results are shown in figure 6.16.

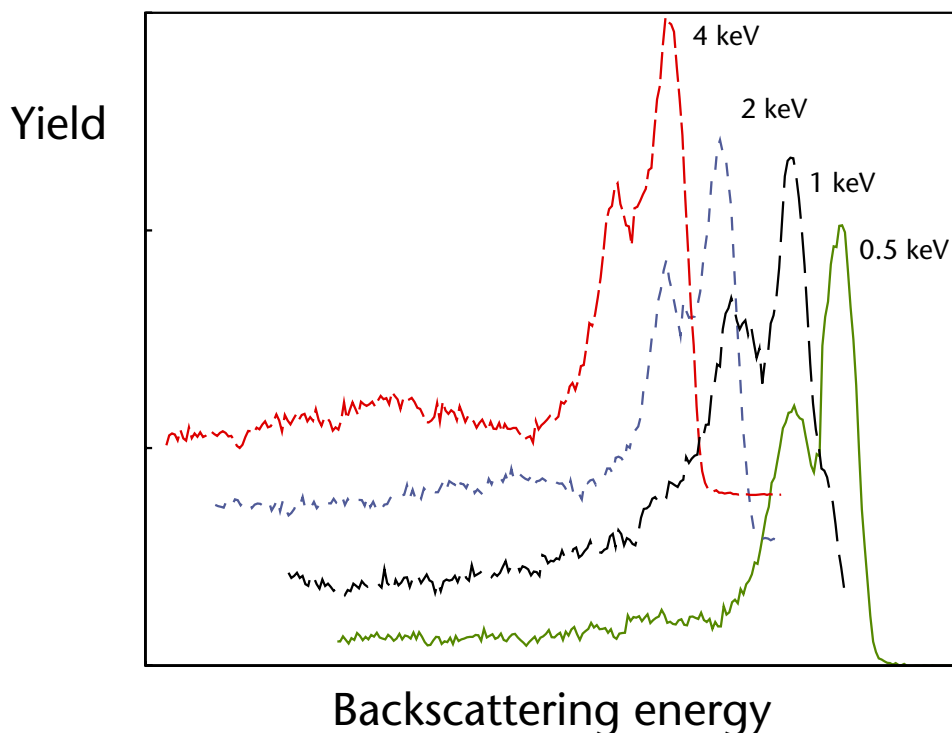


Figure 6.15: Stacked MEIS depth profiles for InAs(001) after  $Ar^+$  IBA at 0.5 (green), 1 (black), 2 (blue) and 4 keV (red) incident ions. The backscattered energy range is from 90–100 keV. The profiles are displaced both vertically and horizontally for clarity.

For all three incident ion energies there was an increased intensity peak in backscattered yield at a depth related to the energy. The peaks were centred at 76 Å depth for 1 keV, at 110 Å for 2 keV and at 145 Å for 4 keV ions. These depths are greater than would be expected from calculations using SRIM.<sup>12</sup> For 5 keV Ar<sup>+</sup> ions, the typical stopping distance would be expected to be ~ 60 Å for normal incidence. The 45° incidence used in this work would result in a still lower stopping distance, although collision cascades might result in some deeper damage. The reason for this disparity is that SRIM assumes an amorphous target. Channelling effects in a crystalline sample can cause considerable deviation from the simple Gaussian distribution which is adequate for an amorphous material. SRIM uses empirical potentials for its calculations, which give more realistic results, but the situation is further complicated because the amount and depth of channelling will inevitably decrease non-linearly as ion damage increases amorphization within the target.

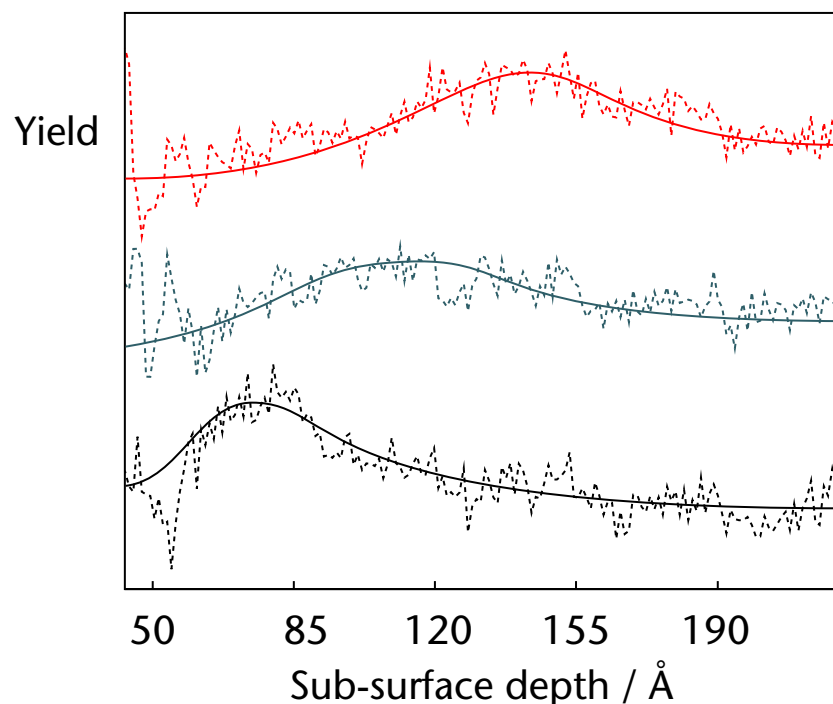


Figure 6.16: Stacked curve-fits and background-subtracted MEIS depth profiles of InAs(001) after IBA, for 1 (black), 2 (blue) and 4 keV (red) incident ions.

Since a channelling incident direction for analysis was chosen, the sub-surface backscattering events observed can only be due to regions of physical defects. It is clear

from these results that although the surface region is rendered essentially defect-free by annealing after ion bombardment, there remains an amorphized sub-surface region at a depth dependent on the energy used for bombardment. No such sub-surface damage was observed for samples prepared using atomic hydrogen cleaning. If narrow band gap III–V semiconductor materials are to make a broader contribution to electronic devices, the cost-effectiveness of processing must be improved and the material and electronic properties must be controlled in a uniform and reproducible way. It is clear from this work that even in the energy range from 1–5 keV, IBA is a less than ideal technique for the preparation of damage-free materials with well-ordered surfaces.

## 6.5 Summary

- i) The (001) surface of InAs has been cleaned by exposure to atomic hydrogen at elevated temperatures. LEED, AES and MEIS were used to study the (4×2) reconstruction formed. Exposure to atomic hydrogen at 670 K with a total H<sub>2</sub> dose of < 100 kL reduced atmospheric contamination to the detection limit of AES without physical damage to the surface or sub-surface. This is consistent with earlier work showing no measurable electronic damage from AHC.
- ii) MEIS results for three different structural models for the InAs(001)–(4×2) reconstruction were simulated. One model, based on double In dimers with perpendicular As dimerization was found to offer excellent agreement with the experimental data, in terms of blocking dip position and calculated backscattered yields. The structural parameters determined for this model were physical and in good agreement with a previous STM study.
- iii) MEIS was used to examine the damage induced in InAs(001) by ion bombardment with energies of between 1 and 4 keV. It was found that preferential sputtering of As from the surface was repaired by subsequent annealing. However, sub-surface physical damage remained even after annealing, at a depth of between 75 and 200 Å.

## 6.6 References

- <sup>1</sup> G.R. Bell, N.S. Kaijaks, R.J. Dixon and C.F. McConville: *Surf. Sci.* **401** (1998) 125
- <sup>2</sup> H. Yamaguchi and Y. Horikoshi: *Phys. Rev. B* **45** (1992) 1511
- <sup>3</sup> Q. Xue, T. Hashizume, T. Sakurai: *Progress in Surf. Sci.* **56** (1997) 1
- <sup>4</sup> H. Yamaguchi and Y. Horikoshi: *Phys. Rev. B* **48** (1993) 2807
- <sup>5</sup> S. Ohkouchi, N. Ikoma and I. Tanaka: *J. Vac. Sci. Technol. B* **12** (1994) 2033
- <sup>6</sup> S. Ohkouchi and N. Ikoma: *Jpn. J. Appl. Phys.* **33** (1994) 3710
- <sup>7</sup> C. Kendrick, G. Lelay and A. Khan: *Phys. Rev. B* **54** (1996) 17877
- <sup>8</sup> D.K. Biegelsen, R.D. Bringans, J.E. Northrup and L.E. Swartz: *Phys. Rev. B.* **41** (1990) 5701
- <sup>9</sup> N. Ikoma and S. Ohkouchi: *Jpn. J. Appl. Phys.* **34** (1995) 5763
- <sup>10</sup> Q.K. Xue, Y. Hasegawa, T. Ogino, H. Kiyama and T. Sakurai: *J. Vac. Sci. Technol. B* **15** (1997) 1270
- <sup>11</sup> J.B. Malherbe: *Crit. Rev. Solid State and Mater. Sci.* **19** (1994) 129
- <sup>12</sup> Stopping powers can be calculated for a range of different substrates and ions using the package SRIM available from <http://www.research.ibm.com/ionbeams/>

## 7 • Conclusions and future work

### 7.1 Conclusions

Some of the surface reconstructions of GaSb(001) and InAs(001) produced by cleaning with atomic hydrogen have been studied using low energy electron diffraction (LEED), Auger electron spectroscopy (AES) and two varieties of ion-scattering spectroscopy (ISS); coaxial impact collision ion-scattering spectroscopy (CAICISS) and medium energy ion-scattering spectroscopy (MEIS). Structural studies have been performed with the aid of the VEGAS simulation code for MEIS, developed by the FOM/AMOLF Institute in Amsterdam, and further developed during the course of this work by the author. MEIS has also been used to characterize sub-surface damage of InAs(001) samples prepared by AHC and argon ion-bombardment and annealing (IBA).

A significant part of the work in this thesis was performed to convert the VEGAS code from UNIX into a functional form for use on Wintel PCs. This effort will enable access to the code to a wider user base, and take advantage of the rapid and continuing increase in compute power available on that platform. It is salient to note that in the time since this computational work was started, the raw processor power of Wintel PCs has doubled, whilst since this studentship began it has increased five-fold. The opportunity was also taken to address the issue of self-compilation. The original version of the VEGAS code recompiled part of itself every time a simulation was started, in order to set the fixed dimensions of a large number of arrays. Revision from FORTRAN 77 to FORTRAN 90 that formed part of the conversion to the Wintel platform enabled the use of dynamically-generated arrays instead of this cumbersome self-compilation. Whilst it would ultimately be desirable to replace the command-line based VEGAS user interface with a graphical manager and model designer, such an undertaking was not feasible in the timescale of this project. What was feasible was a number of minor changes to enable correction of input errors and speed data entry by supply of default values, neither of which was possible before. Instead of building a new graphical interface, the program VEGASmagic was

written to enable straightforward conversion between VEGAS' own file formats and common macromolecular formats such as Brookhaven Protein Databank (PDB) and Tripos' Alchemy format. This relatively quick solution facilitates the visualization of VEGAS models using a range of publicly available open standard software, such as RasMol and POVRay, with advantages in analysis of the physical viability of structural models.

Annealing under a flux of atomic hydrogen radicals ( $H^*$ ) has previously been shown to enable desorption of surface contaminants such as oxides and hydrocarbons from a variety of polar III–V semiconductor surfaces at lower temperatures than previously required for oxide desorption, even with a group V over-pressure. Previous work using HREELS at Warwick has shown that the resulting surface and near-surface region are free from electronic damage. In the work presented here, the atomic hydrogen cleaning (AHC) technique has been used to form both recognized and novel reconstructions of GaSb(001). Exposure to atomic hydrogen at 670 K with a total  $H_2$  dose of  $< 100$  kL reduced atmospheric contamination to the detection limit of AES. Thermal decomposition of  $H^*$  cleaned GaSb(001)–(1 $\times$ 3) was also examined using CAICISS and AES. The onset of reconstruction to the c(2 $\times$ 6) phase was observed at 645 K. That this reconstruction was underway could be determined from the change in surface elemental composition measured by AES and by the anisotropic change in backscattering profile along different azimuths in CAICISS. Reconstruction to a c(2 $\times$ 6) phase has previously been reported under Sb flux at similar temperatures, but it appears to be possible by annealing under UHV conditions alone. It is probable, though, that maintenance of an Sb flux would result in a less disordered (albeit perhaps non-stoichiometric) surface. Non-congruent sublimation of Sb occurred above 735 K followed by rapid surface degradation above 785 K, well below the melting point of GaSb at 985 K.

A GaSb(001)–(1 $\times$ 3) reconstruction was prepared by AHC and identified by LEED. It was found by AES to have a surface composition of around 45% Ga. A structural solution by MEIS using VEGAS Monte Carlo simulations was performed, using a model based on STM and PES data composed of single Sb dimer chains separated by Ga atoms. Structural

parameters were determined for Sb dimer length and height and interdimer Ga height, by iterative refinement of simulation parameters based upon consideration of  $R$ -factor criteria for quality-of-fit. A dimer length of 3.11 Å was determined, which is quite physical, falling between the 4.31 Å bulk bond length of GaSb and the natural Sb–Sb bond length of 2.9 Å. A GaSb(001)- $c(2\times 6)$  reconstruction was prepared by both argon ion-bombardment and annealing (IBA) and AHC. The MEIS, LEED and AES data were all consistent with the hydrogen-cleaned surface having less disorder and no residual contamination.

Structural analysis in MEIS supported a model based on staggered Sb dimer chains interspersed by antiphase second layer Sb dimers, but with some degree of disorder. This is consistent with STM evidence. The  $c(2\times 6)$  reconstruction caused some difficulties in simulation compared to the  $(1\times 3)$  phase. This is largely attributable to the four-fold increase in the scale of the model with an inevitable increase in the permutations of possible atomic positions. Such increases in complexity inherently magnify the effects of simplifications in the model. For example, the simulations assume that the equilibrium arrangement of the surface atoms is perfectly ordered. For a real crystal, however, there has to be an assumption that deviations from the model structure are normally distributed about this ideal, and therefore average out over the relatively large illuminated area of the crystal. However, such an assumption is not necessarily valid. The solution of this reconstruction also demonstrated another problem with this approach to the analysis. The value of the  $R$ -factor obtained from a relatively nonphysical model was lower than that obtained in the best-fit eventually obtained. The conclusion must therefore be that although MEIS results can be successfully simulated using VEGAS, the use of  $R$ -factors cannot be solely relied upon when refining models towards a physical solution.

A previously unreported stable  $c(6\times 4)$  reconstruction was clearly observed using LEED after AHC with a 75 kL dose of H<sub>2</sub> and a substrate temperature of 575 K. AES suggests it is a Ga-rich phase, with around 59% Ga. It is proposed that it has not been previously observed because most traditional surface preparation techniques such as IBA or ECR atomic hydrogen cleaning are energetic and will therefore preferentially sputter the lighter

surface element, Ga. Thermally produced H<sup>•</sup> is non-energetic and hence does not sputter. Due to the large unit cell, simulation to determine a structural solution proved unsuccessful. However, it was possible to demonstrate that of two models based on a similar GaAs phase, one based on staggered Sb dimers without top layer Ga dimers was more consistent with the MEIS data.

A (4×2) reconstruction of the (001) surface of indium arsenide was prepared by AHC and analysed by MEIS, LEED and AES. Three previously proposed models have been compared and evaluated. It was found that a model based on In dimer pairs separated by second layer dimers was relatively inconsistent with the MEIS data recorded. A model based on single In dimers separated by second layer two-dimer chains was consistent with MEIS results, but structural parameters determined were nonphysical. A model without dimerization in the second layer was found to be in best agreement with the experimental results, as well as being physical and consistent with previously reported STM data. Structural parameters for this model were determined.

A study of the effects of argon ion-bombardment and annealing (IBA) on the H<sup>•</sup> cleaned InAs(001) surface was performed using MEIS, LEED and AES. The potential for beam damage by the MEIS analysis beam was examined, and the conclusion drawn that ion doses < 2 μC had no measurable effect on the surface. It was found that preferential sputtering of As from the surface resulting from 45° Ar<sup>+</sup> ion bombardment was repaired by subsequent annealing. However, sub-surface physical damage remained, even after annealing, at a depth of between 75 and 200 Å. It was found that a layer with a high defect density was produced, with a depth directly dependent on the incident ion energy. No such sub-surface damage was found in samples prepared by AHC.

Aside from the materials aspects, another aim of this work was to use and evaluate a combination of techniques for surface preparation and analysis. The primary preparation technique used was atomic hydrogen cleaning (AHC), and this work has confirmed its value as a technique for producing well-ordered surfaces free of both physical damage and

atmospheric contamination. It has complemented well the earlier work presented in the thesis of G.R. Bell (University of Warwick, December 1996) using HREELS to examine the effects of AHC on electronic structure.

The final aim of the work was to assess the suitability of a promising structural technique such as MEIS for the study of common III–V binary semiconductor surfaces. The conclusion of this work must be that MEIS cannot be used in isolation as a technique for surface structural studies of III–V materials. The low scattering cross-section compared to metals means that backscattered yields are relatively low. This means that signal/noise ratios are relatively poor. In order to compensate for this, it would be desirable to use a higher dose. However, since III–V materials are soft, significant doses are likely to result in surface damage which would destroy the surface under investigation. Another limitation of MEIS is that the achievable mass resolution prevents study of GaAs and InSb, two of the most commonly utilized III–V semiconductor surfaces. Generally, like LEED I–V, MEIS suffers the difficulties of *ab initio* analysis resulting from dynamical scattering when modelling semiconductor surfaces. The large surface unit cells often exhibited by the various reconstructions of these materials are in many ways better suited to analysis by techniques which give real space information without the necessity for a trial-and-error model simulation approach. The immediate visual nature of STM and the Fourier transform solution enabled by a kinematical approach in SXRD both have advantages when analysing novel reconstructions. When working within the confines of a trial-and-error approach, large unit cells cause a great deal of problems. The many degrees of freedom resulting from having a large number of parameters to fit makes simulation intrinsically difficult. Aside from VEGAS, the limitation of the analysis routines to three independent parameters means that time-consuming iteration is required to refine models. It is not uncommon for a round of such iterations to lead to a model which is a significantly poorer fit to the data than before. In several of the models analysed in this thesis, it has been amply demonstrated that whilst *R*-factors are often useful criteria for refining parameters, they can sometimes be a hindrance. They provide some indication of a defined reliability,

but no guarantee of physicality. Furthermore, without absolute calibration of the MEIS data, they are of limited value in discriminating between models. It is important, however, to stress that MEIS can excel both in the calculation of structural parameters for well-known models and in its ability to combine surface structural and compositional information with sub-surface depth profiling. In combination with other structural and chemical techniques, MEIS is versatile and productive, offering information that cannot easily be determined by other means.

## 7.2 Future work

For the IBA analysis of the InAs data, the problems of Sb contamination reduced the breadth and depth of investigation possible. It would be interesting to see a more complete study of the effects of IBA on the sub-surface of III–V semiconductors using MEIS, particularly at the lower energy range, where physical damage is likely to be shallower and segregated to the surface upon annealing. Analysis using secondary ion mass spectrometry (SIMS) would also be interesting as a comparative depth-profiling technique. In the area of AHC, it would be interesting to examine the use of an electron-stimulated desorption hydrogen source, which by virtue of its reported greater efficiency and lower operating temperature appears to offer the potential for much faster cleaning, clearly a factor of importance in industrial applications.

In computational terms, it would be of great benefit for the MEIS community as a whole to see more work on the VEGAS simulation code. There is a strong argument for rewriting it in a visual environment such as C++ or Delphi, with the advantages of a more accessible graphical user interface, a modern optimizing compiler and a better structured, more flexible language. In the short-term there are features of the VEGAS code which might be worth investigating, depending on the timescale involved in a full rewrite. These include the facility to connect incident and exit trajectories in multiparameter calculations and investigating the memory limitations on large numbers of  $x$ - and  $y$ -groups. This latter point may require as simple a solution as a newer version of the Fortran compiler.

MEIS data was collected for a structural study of the GaP(111)–(2×2) reconstruction. At the time of submission, however, analysis of this data is incomplete. It is desirable to complete this study, since there is an extant structural solution based on  $R$ -factor analysis of LEED I–V experiments. It would be interesting to compare the structural parameters obtained by these distinct experimental techniques but using a similar computational approach. Such comparative studies has been made in the past between LEED I–V and MEIS solutions for metal–adsorbate reconstructions, but not yet for a III–V semiconductor surface.

Experimentally, it is crucial for more work to be performed on the GaSb(001)–c(6×4) reconstruction. In particular, *ab initio* investigation by SXRD and STM would be useful to gain a foothold on how the reconstruction actually appears. Other analytical techniques such as LEED I–V and PES would also be of value, as might further opportunities for investigation with MEIS, perhaps using a number of different azimuths and ion species to gain a broader range of information. The structural models proposed would certainly have benefited from a more rigorous theoretical analysis, perhaps using total energy calculations. The same arguments would indeed apply to the other reconstructions observed in GaSb(001). The more information can be gleaned from more techniques, the better will be our understanding of these surfaces.

## Index

### A

AES 6, 10–11, 29, 31, 39, 43–44, 91–105, 108, 119, 125–126, 128–129, 138–139, 145–149  
 AHC 11, 29, 37–38, 88, 91–105, 108–110, 117–119, 125–126, 128–129, 138–140, 145–151  
 Atomic hydrogen cleaning *see* AHC  
 Auger electron spectroscopy *see* AES  
 Auxiliary lattice 68–69, 122–123

### B

Blocking 48–53, 57–58, 63–65, 70, 72, 75, 112, 115, 124–125, 145

### C

CAICISS 7, 10–11, 53–54, 91–92, 96–97, 100–103, 118, 125, 146–147  
 Coaxial impact collision ion scattering spectroscopy *see* CAICISS

### D

Daresbury 63, 73–74, 93–94, 97, 103, 129, 137  
 Double-alignment 49, 63–66

### E

ECM 21–24, 80, 88–90  
 Electron counting model *see* ECM  
 electron-stimulated desorption *see* ESD  
 ESD 38, 151

### G

GaAs 1–2, 10, 17–18, 129  
     (1×6) 82–83, 86  
     (2×3) 83  
     (2×4)/c(2×8) 60, 80–86, 130  
     (3×1) 83  
     (4×1) 86  
     (4×2)/c(8×2) 80–86, 130  
     (4×3) 83–84  
     (4×6) 80, 86–87  
     c(4×4) 77–78, 80–82, 88–91  
     c(4×6) 83–84  
     c(6×4) 83–84, 120–121, 126, 149  
     growth 1, 25–26, 54, 118  
     reconstruction 23–24, 54, 69, 79–90, 99, 129–130, 150  
     surface preparation 34–38, 128  
 Gallium antimonide *see* GaSb  
 Gallium arsenide *see* GaAs  
 Gallium nitride *see* GaN  
 GaN 2

GaSb 1–3, 10–11, 18, 96, 129, 138, 147  
 (1×3) 10, 88–89, 97–107, 118, 147  
 (1×5)/c(2×10) 88–90  
 (2×3) 118  
 (2×5) 88–90  
 (4×3) 118  
 c(2×6) 10, 88–89, 102, 108–119, 148  
 c(6×4) 117–124, 148, 152  
 reconstruction 10, 69, 79, 83, 88–96, 103–120, 146–147, 152  
 surface preparation 34, 37, 96–104, 108, 119, 125, 128

## H

H<sup>\*</sup> cleaning *see* Atomic hydrogen cleaning  
 High resolution electron energy loss spectroscopy *see* HREELS  
 HREELS 8, 81, 85, 98–99, 128, 138, 147, 150

## I

IBA 11, 29–30, 33–38, 58, 79, 82, 85, 88, 91, 99, 108–109, 119, 125–130, 137–151  
 III–V semiconductors 1, 3–5, 144, 150  
   band gaps 2, 18  
   crystallography 3, 10–21, 54, 150–152  
   growth 26, 54  
   reconstruction 20, 24, 79, 90–91, 115, 119, 130  
   surface preparation 33–35, 99, 128, 147, 150–151  
 InAs 1–3, 10–11, 18, 138  
   (2×4) 130  
   (4×2) 10, 128–141, 145  
   beam damage 137, 142–146  
   growth 54, 129  
   reconstruction 69, 90, 128–130, 146  
   surface preparation 34, 37, 128, 145, 149, 151  
 Indium arsenide *see* InAs  
 Ion-bombardment and annealing *see* IBA

## K

k-cell 26, 95, 104, 138  
 Knudsen cell *see* k-cell

## L

LEED 5–15, 20, 29, 39–43, 72–73, 79–82, 85–91, 95–109, 118, 125–129, 138–139, 145–152  
 Low energy electron diffraction *see* LEED

## M

MBE 22, 26–27, 37–38, 54, 59–60, 80, 85–89, 118, 128, 130  
 Medium energy ion scattering spectroscopy *see* MEIS  
 MEIS 7, 10–11, 43–50, 55–66, 72–74, 81, 93–97, 106–116, 120, 123–152  
 Molecular beam epitaxy *see* MBE

**N**

Non-congruent sublimation 33–36, 81, 102–103, 125, 147

**P**

PES 88–89, 125, 147, 152

Photoemission spectroscopy *see* PES

POVRay3 77–78

**R**

RasMol 76–78, 111, 147

RBS 55, 59

Reciprocal lattice 5–6, 14–15, 39–42

Reconstruction 3, 10, 17–26, 56–58, 67–68, 75–91, 94–109, 112–136, 139, 145–152

Reflection high energy electron diffraction *see* RHEED

RHEED 9, 27, 79–82, 85, 88–89, 106, 118

Rutherford backscattering spectroscopy *see* RBS

Rutherford scattering cross-section *see* Scattering cross-section

R-factor 6–7, 43, 72–73, 111–116, 123–124, 132–136, 148, 152

**S**

Scanning tunnelling microscopy *see* STM

Scattering cross-section 9, 50–51, 55, 59, 63, 72, 102, 108, 116, 129, 150

Shadow cone 45–57, 63–66, 70, 77, 112

Shadowing *see* Shadow cone

Sputtering *see* IBA

STM 9–10, 13, 19–20, 79–82, 85–90, 106, 114–116, 125–126, 130–132, 135, 145–152

Surface x-ray diffraction *see* SXRD

SXRD 8–9, 79, 150, 152

**U**

UHV 4–5, 26–27, 38, 82–85, 93, 97, 103, 118, 128, 147

Ultra-high vacuum *see* UHV

**V**

VEGAS 11, 56, 59, 63, 67–68, 73–77, 106, 114, 116, 120–122, 125, 131, 146–151

    multicalc 67, 73–75, 123, 151

    VEGASmagic 76–77, 111, 146

**W**

Warwick 11, 63, 75, 91–97, 147, 150

**Z**

Zinblende 2, 16, 20, 33